Fluid flow induced by travelling waves in beam-like structures: modelling, simulation and experimental validation

Skriptyan Noor Hidayatullah Syuhri

Submitted in fulfilment of the requirements for the

Degree of Doctor of Philosophy

James Watt School of Engineering

College of Science and Engineering

University of Glasgow

November 2022

Abstract

The configuration of a beam submerged in liquid can offer many advantages in engineering applications by providing an ability to generate alternative propulsion systems. These are achieved via travelling waves that propagate through the beam and, interacting with the surrounding fluid, generate thrust. Numerous concepts and implementations have been proposed differing in general arrangements that lead to different structural and fluid characteristics. Understanding the characteristics and limitations of travelling waves on the beam can provide advantages toward more effective and efficient actuations. The aim of this thesis is to provide insight into the mechanisms that allow structural travelling waves induced through electromagnetic actuation to interact with the surrounding fluid. This study would contribute to the development of controllable devices capable of self-propulsion.

In this thesis, the dynamic behaviours of a cantilever beam submerged in a fluid is approximated by simplifying fluid effects with hydrodynamic forces. Accordingly, the Galerkin-based model for fluid structure interaction can be derived and solved with a linear approximation method. This technique allows to investigate the vibration patterns of the beam under hydrodynamic loads that can be used to provide an assessment into factors affecting modal parameters and influencing the generation of travelling waves.

Advanced experimental techniques using Laser Doppler Anemometry (LDA) in conjunction with numerical simulation of fluid-structure interaction (FSI) models are used to provide a thorough and systematic characterisation of the fluid-structure interactions that constitute the fundamental of the correlation between structural travelling waves and thrust generated by a beam submerged in a viscous fluid. The discussion is expanded to consider the potential use of an additional mechanical element in attempting to improve features that promote travelling waves and large beam displacements without necessarily inducing high input power in a contactless actuation system.

Contents

List of Tables

List of Figures

Acknowledgements

All praise is for Allah – Lord of all worlds.

First and foremost, I would like to extend my deepest gratitude to my supervisor, Dr Andrea Cammarano, for his invaluable advice, guidance and technical support. He has given me the opportunity to learn about structural dynamics, fluid dynamics and electro-magnetic fields, making this project truly multidisciplinary. He has been a very supportive mentor that allowed me to develop into an enthusiastic and motivated researcher. I would also like to thank my co-supervisor, Dr Hossein Zare-Behtash, for his guidance and wisdom in my research and for the numerous opportunities he has given me to expand my work particularly in the field of fluid dynamics.

I would like to extend my appreciation to Dr David Pickles for helping me with conducting LDA measurements in the de Havilland low speed National Wind Tunnel Facility, and Dr Alexander Elliot for his guidance in the area of structural dynamics.

Most importantly, I would like to thank my parents, Ahmad and Nurkhayati, for their constant support, encouragement and believing in me from the beginning of my odyssey. My special thank goes to my wife, Bela, and daughter, Briena, for enabling me to pursue my dream. Being 7600 miles away from home without them has never been more challenging. I extend my thanks to my brothers, my parents-in-law and my relatives.

Finally, I would like to express my thanks to Saif Alshammari who has helped me countlessly and made my stay in Glasgow more enjoyable. I would also like to thank my friends, particularly in JWSE – Amir Khfagi, Abdulaziz, Gaddafi, Isam – for their support and encouragements. There are so many to name for the limited space.

This work would not have been possible without my main funding: Islamic Development Bank (IsDB) Scholarship through PIU-UNEJ. Moreover, I gratefully acknowledge financial support from the James Watt School of Engineering (JWSE), and also Dr David K Brown Scholarship to allow me for conducting research in structural dynamics.

Author's Declaration

I declare that the work in this this was carried out in accordance with the regulations of the University of Glasgow. The work is original except where indicated by special reference in the text and no part has been submitted for any other degree.

Any views expressed in the dissertation are those of the author and in no way represent those of the University of Glasgow.

The thesis has not been presented to any other University for examination either in the United Kingdom or overseas.

Signed: ……

Skriptyan Noor Hidayatullah Syuhri

Dated: November 2022

Nomenclature

Chapter 1

x	Location along the beam length
t	Time
F	The forcing function applied to a structure
φ	The mode shape function of a system
ω	The frequency of a system
w_{mc}	The modal contribution at a particular vibration mode for the displacement response of the beam
ω_i	The natural frequency of a structure
ω_f	The forcing frequency of a structure

Chapter 2

General nonlinear beam equations

$w(x,t)$	Total (absolute) displacement of a beam structure
L	Total beam length
x	Physical coordinate system
z	Physical coordinate system
E	Modulus of elasticity of a material
I	Second moment of inertia
μ	Linear mass per unit beam length
$w_b(x,t)$	Local displacement of the clamped-free beam
$w_r(x,t)$	Displacement motion of the base
A_f	The base amplitude
$\delta(x)$	The Dirac-delta function
ψ	Beam slope
s	The length along the beam
$\partial\blacksquare$	Derivative function
Δw	The small segment of beam displacement
Δx	The projection of the deflected beam along the x-axis

Δs	The small length of beam
$\varphi_i(x)$	The mode-shape of the system at the *i*-th mode
$q_i(t)$	The modal displacement at the i-th mode
β_i	A constant associated with the spatial function of the beam equation
F_f	The total fluid force acting on the beam
ρ_f	The fluid density
b	The beam width
C_d	The drag coefficient
C_m	The inertia coefficient
$\lvert\blacksquare\rvert$	Absolute sign
C_{ld}	The linear damping due to the material
M	The added mass due to fluid force
C_{qd}	Damping coefficient due to fluid force
$\dot{\blacksquare}$	First derivative of ■ with respect to *t*
$\ddot{\blacksquare}$	Second derivative of ■ with respect to *t*
i	Number of harmonics in trial solution
j	Number of harmonics in trial solution
k	Number of harmonics in trial solution
$\blacksquare''''$	Fourth derivative of ■ with respect to *x*, equal to $\partial\blacksquare/\partial x^4$
dx	Integral over the length of the beam
$\zeta_{ld,i}$	The *i*-th element of damping ratio due to beam's material
ψ_{jki}	Parameter used to denote the integral of the product of arbitrary mode shape
$Q_i(t)$	The *i*-th element of the weighted forcing function in the modal coordinate equation after applying the Galerkin approximation
ρ	Beam's material density
∞	The infinity symbol
π	A constant to represent a half-rotation around a circle in radians

Linear approximation

ζ_i	The *i*-th element of damping ratio
f_0	The forcing function in the linear approximation of the Euler-Bernoulli beam equation

ω_{ni}	The *i*-th element of the natural frequency of a system
χ_i	The correction factor for damping in the linear model
$q_{NL,i}(\omega)$	The frequency series of the modal coordinate of the nonlinear model
$w_t(x,t)$	The total solution of the steady-state vibration of the beam using the linear approximation method
lp_i	Parameter used to define modal coordinates that have a sine function
rp_i	Parameter used to define modal coordinates that have a cosine function

Modal analysis using numerical approaches

μ	The eigenvalue of a system
$[M]$	A mass matrix
$[C]$	A damping matrix
$[K]$	A stiffness matrix
$\{\phi\}$	The eigenvector of a system
i	Imaginary unit, i.e. $\sqrt{-1}$
m_α	The generalised mass associated with mode α
ϕ_α^N	An $N \times 1$ vector of the eigenvector for mode α
$M^{N\,M}$	An $N \times M$ matrix of the structure's mass
ϕ_α^M	An $M \times 1$ vector of the eigenvector for mode α
$\Gamma_{\alpha i}$	The *i*-th element of the modal participation factor
T_i^M	The magnitude of the rigid body response of degree of freedom M in a system
$m_{\alpha i}^{eff}$	The effective mass for mode α

Chapter 3

$U(\beta x)$	Parameter used to denote the spatial function related to the sine function of the modal coordinate equation
$V(\beta x)$	Parameter used to denote the spatial function related to the cosine function of the modal coordinate equation
U_1, U_2	Amplitudes of the spatial function $U(\beta x)$
V_1, V_2	Amplitudes of the spatial function $V(\beta x)$
d_1, d_2, d_3	Parameters used to denote the dipping depth of the beam
f	Frequency in Hz

γ_i	A correction factor used in the model validation

Nonlinear identification parameters

t_{fi}	The *i*-th element of the time when the vibration amplitudes cross the zero point
$f(t_{fi})$	The instantaneous frequency of a decay response
t_{Ai}	The *i*-th element of the time at the local minima or maxima of the decay responses
$A(t_{Ai})$	The instantaneous amplitude a decay response
A_0	Initial amplitude of a decay response
$\zeta(t)$	Damping ratio of a decay signal
k_1, k_2, k_3	Parameters used to denote a cubic equation

Chapter 4

c	1 chord length equal to the total beam length
G1	The coarse mesh grid
G2	The medium mesh grid
G3	The finest mesh grid
w_{b1}	The base input motion at $x = 0$
w_{b2}	The base input motion at $x = L$
θ_1	Phase of the base input w_{b1}
θ_2	Phase of the base input w_{b2}
$\delta(x)$	The spatial function of the base motion for the clamped-clamped beam configuration

Chapter 5

k	Spring constant
Cl	Total length of the coil
Cw	Coil width
Bl	Bobbin length
Bw	Bobbin width
b	Winding width
h	Winding height

d	Wire diameter
n	Number of turns
FF	Coil fill factor
L_{total}	Total wire length
L_{avg}	The average length of the coil and bobbin
W_{avg}	The average width of the coil and bobbin

Polynomial fit

$F(x, y)$	Mechanical force
x	Current
y	Gap between the coil and magnet
p	Parameter used to denote the polynomial terms

List of Abbreviations

AC	Alternating current
AFM	Atomic force microscopy
AWG	American wire gauge
CAD	Computer-aided design
CFD	Computational fluid dynamics
FE	Finite element
FFT	Fast-Fourier transform
FRF	Frequency response function
FSI	Fluid-structure interaction
FV	Finite volume
LDA	Laser Doppler anemometry
LED	Light-emitting diode
PC	Personal computer
PLA	Polylactic acid
RANS	Reynolds-Averaged Navier-Stokes
RDM	Resonance decay method
RMSE	Root-mean square error
SA	Signal analyser
SG	Signal generator
SNR	Signal-to-noise ratio
SST	Shear stress transport
USB	Universal serial bus

Chapter 1. Introduction

The arrangement of a beam submerged in liquid can provide many advantages in engineering applications by offering an ability to generate thrust. This is achieved via travelling waves that propagate through the beam and, interacting with the surrounding fluid, generate thrust. Numerous concepts and implementations have been proposed differing in general arrangements that lead to different structural and fluid characteristics. However, the relation between travelling waves and their capacity to generate thrust is not well understood. In addition, the onset of travelling waves is depending on a multitude of conditions that are not fully investigated. Therefore, the purpose of this project is to provide insight into the mechanisms that allow structural travelling waves induced through electromagnetic actuation to interact with the surrounding fluid. This study is pivotal to the development of controllable devices capable of self-propulsion.

Section 1.1 shows the relation of this work in comparison with the existing literature. A brief overview of the development of beams submerged in viscous fluid throughout the last century is then discussed in Section 1.2. A more focussed discussion is given to outline the most recent study and understanding of the travelling wave phenomena afterwards. The scope and targeted contributions of this work are then presented in Section 1.3. It is expected that the methodology and the wide-ranging investigation through analytical, numerical and experimental approaches make this research a deep contribution to the understanding of the submerged beam performance, structural dynamics, electromagnetic actuations and extended effects into the fluid dynamics. Section 1.4 provides a detailed outline of this thesis.

1.1. Research motivation

Existing and potential applications of beam submerged in a viscous fluid are presented in this section. The technical shortcomings of existing solutions to address the problems and trends in research are also presented.

1.1.1. Artificial swimmers

Artificial swimmers are devices that use undulatory locomotion to create travelling waves along their body and generate propulsive forces. This type of locomotion can be observed particularly in some microorganisms [1, 2] and aquatic animals such as eels [3, 4], lampreys [5, 6] and snakes [7]. The recent development in wave identification allowed the researchers [8, 9] to implement mechanical wave decomposition techniques to estimate the travelling wave content in fish locomotion. This is achieved by applying, for instance, the complex orthogonal decomposition analysis to the midline motions of swimming fish which result in the ratio of the magnitude of travelling waves to standing waves, commonly known as the travelling index. Reported in reference [9], the midline motions of eels and lampreys demonstrate wave motions with high travelling index ranging from 75% to 90%. Since the body motion of these living creatures in the swimming mode can be modelled as bending (transverse) vibrations of infinite thin and flexible structures performing progressive (travelling) waves with particular amplitude and frequency [10-13], this leads to massive interests in the research community for emulating undulatory motion using continuous or distributed-parameter system configurations. Ramananarivo et. al. [14], for instance, reproduced undulatory swimming by using an elastic beam with a permanent magnet attached to one tip as an actuator that was achieved by inducing electromagnetic fields around the structure. Subsequently, such studies have been carried out numerically and experimentally by many researchers to further the understanding of the dynamic characteristics and propulsive phenomena of beam structures submerged in viscous fluid [15-20].

It is noted that travelling waves in the beam only occur in particular conditions, mostly due to phase shift induced by the contribution of the damping forces [18]. Accordingly, some studies in [21, 22] have implemented alternative techniques for manipulating boundary conditions of the beam to maximise the travelling wave generation. However, the travelling waves generated by altering the forcing functions do

not produce maximum thrust [23]. Understanding how to generate travelling waves that can be used for propulsion purposes is the main motivation of this study: this will be achieve by investigating the correlation between structural travelling waves and the thrust generated by a beam submerged in a viscous fluid. Advanced experimental techniques as well as numerical simulations will be used to provide a thorough and systematic characterisation of the fluid structure interactions that constitute the fundamental of this phenomenon.

1.1.2. Robotic fish applications

This study is strongly connected with the design of robotic fish, devices that use oscillatory motion to generate propulsion. This swimming motion is commonly found in the thunniform fish [24, 25]. According to references [8, 9], the wave decomposition of the midline motions of the thunniform fish exhibit low travelling index with an estimated value of 36%. This means that the remaining 64% of the midline motion of the thunniform fish forms standing waves. Studies for understanding the body and propulsive dynamics of this locomotion have been widely performed. The propulsion in this type of fish is achieved due to the movement of their tip rather than their body. Nevertheless, the travelling waves along their body are still observed in their swimming mode which are indicated with phase delay between the head and tail.

Due to similar characteristics of the first and second mode shape of cantilever beam models, researchers [17, 26-28] have attempted to replicate this motion using slender beam structures. Subsequently, fluid dynamics of the beam tip have been thoroughly investigated [17, 28-31]. A parametric study has been conducted to address the influence of beam geometries to the propulsive performance of the beam [26, 27]. The use of smart materials to actuate and mimic the fin and tail characteristics of a fish has been attempted in recent times [26, 32-35]. However, it is noticed that high tip velocities are limited around the resonant frequencies. Therefore, this study will investigate the potential use of an additional mechanical element in attempting to improve the tip velocity of the beam which, in turn, can induce more fluid flow over wide range of frequencies. Furthermore, the contribution of travelling waves particularly in the first two mode shapes of the beam has not been clearly understood. Accordingly, this will be addressed in this study by using a mechanism capable of generating pure travelling waves in the beam.

By contributing to the development of artificial swimmers and robotic fish, these configurations can be used in drug delivery systems. These can be achieved by miniaturizing the size of these mechanisms to the order of microns, which will allow for creating micro-robots to deliver drugs directly to the target. Micro-robots are usually released inside a blood vessel for administering pharmaceutical compounds onto targeted cells or organs [36]. By taking advantage of self-propulsion mechanism using travelling wave generations, tiny magnets attached to micro-beams can be used as micro-robots. The magnetic field will be induced by an electromagnet from outside the patient to control the robots. The application of this technology is not only limited to deliver drugs, but it would also allow doctors to move diagnostic and surgical tools remotely with minimal invasion [37]. This, however, requires an understanding of non-contact actuations in the beam motion which will be covered in this study.

1.1.3. Pumping devices

The need for devices capable of delivering tiny volume of fluid and transporting different type of fluid viscosity and temperature has guided a number of inventions in the pumping systems [36]. Current development in the pumping devices must also consider about miniaturisation of their system to allow for developing micro-pumps [38]. These requirements lead to the use of travelling waves on the beam to push the liquid around the structure. Ogawa et. al. [39] first introduced a liquid pumping device by utilising a clamped-clamped beam configuration actuated with nine piezoelectric patches distributed evenly along the beam length. Travelling waves are induced by applying sinusoidal voltages with a phase difference of 120° for each piezoelectric. The bending travelling waves on the beam surface are then used to carry the liquid. This configuration has attracted interest from researchers to further improve the system performance by modifying the beam surface [40, 41] and fluid chambers [42-44]. Furthermore, these improvisations also lead to valveless pumping systems.

Following this investigation, the performance of travelling wave-based pumping devices is further improved in references [45, 46] by using magnetic-based actuators to replace the piezoelectric patches. The magnetic actuator is achieved by mounting four cylindrical magnets on the beam surface that are separated equally along the beam length. Furthermore, the poles are also arranged in a way to create a 90-degree phase delay. This

actuator generates more force for the beam which, in turn, produce higher flow rate than the piezoelectric-based actuator [40, 45, 46]. However, the use of four magnets on the beam surface can limit their miniaturisation capability. Therefore, this study will investigate the use of two magnets to generate pure travelling waves on the beam which can potentially be used to reduce the size of the system. Furthermore, features that promote large displacements without necessarily inducing high input power will also be explored in the study to increase the efficiency of the system.

By contributing to the development of liquid pumping devices based on travelling waves, these configurations can be used in many engineering applications. Since the material properties of the beam can be chosen in a way to be corrosion and heat resistance, those configurations can be used in drug delivery systems as implantable devices, offering noticeable advantages including localised drug exposure, precise drug dosage, limited unwanted systemic side effects and minimalized invasive surgery [47]. Miniaturisation in the order of micron also makes these configurations a good candidate to be used for chemical industries. In fact, micro-beams permit to transport prescribed quantities of reagents to a precise location in a reactor and enhance delivery, mixing and ultimately reaction between different chemical species. This will reduce the amount and the frequency of sampling in the reactions to ensure homogeneity and quality in the chemical production [48, 49]. Pumping tiny volume is also the main concern for energy-related industries. A small amount of fuel is required to circulate in fuel cell systems for portable electronic devices such as laptops, digital cameras, cell phones, etc [50]. Furthermore, it is also the fundamental part in cooling devices for keeping temperature low in electronic systems [51]. By surrounding chips with micro-channels, bending travelling waves can be used to force the coolant to circulate through the channels.

1.1.4. Sensing devices

Modal parameters and dynamic behaviours of beam submerged in liquid can depend on the fluid properties. This dependency is used by researchers [52-56] to develop sensing devices for measuring fluid properties. These devices usually comprise of two piezoelectric patches to sandwich the beam. One piezoelectric is used as the actuator and the other one for reading the output voltage due to bending vibration. This configuration requires an accurate modal analysis to estimate the changes in the natural frequencies and

damping values which are then used to determine the mass density and viscosity of the liquid. For fully submerged beam, the relationship of modal parameters and fluid properties can be conveniently obtained by analytical approaches using small displacement assumption [57]. However, the dynamic properties of partially submerged beam configurations are complex and need to be measured experimentally to create database for correlating the beam and fluid properties [55]. Therefore, some experimental works in this study will be dedicated to investigating the characteristics of natural frequencies and steady-state responses of partially submerged beam configurations to allow recommendations to be made for improving analytical approaches. The use of nonlinear identification parameters in this work can also provide alternative techniques for estimating modal parameters particularly from free vibration signals. Furthermore, the changes in the added mass can also be used for damage identification of structures [58].

Note that the configuration for sensing liquid by utilising two piezoelectric materials to actuate and detect dynamic properties of the beam is also used in the Atomic Force Microscope (AFM) system to measure topography surfaces and mechanical forces in miniature scale. One of techniques to scan physiological samples is the tapping mode procedure where the beam is actuated at the resonant frequency to allow intermittent contact with the sample surface [59, 60]. Researchers [61-67] have anticipated in case the sample surface immersed in liquid by investigating the changes in the modal properties and dynamic behaviours of fully submerged beam configurations specifically for the AFM. Furthermore, the work in this thesis will allow to expand the estimation of natural frequencies and steady-state properties of the beam that is partly submerged in liquid.

1.1.5. Other relevant applications

For the case of flow-induced vibration, the submerged beam configuration can be utilised as check valve systems to prevent reversed flow [68, 69]. This configuration takes advantages of highly deflective cantilever beam model with a constraint around the beam tip. The beam can only deflect to one side to generate forward flow. Otherwise, the beam tip hits the stopper, closing the channel. The other possible configuration to regulate the flow is the snap-through system studied in references [70-72]. Since dynamic responses of the beam can become rich of nonlinear phenomena due to the impact to the boundary particularly for the case of inviscid fluid [73], it is important that the practitioner is aware

of the potential shortcomings of these techniques. The generality of the methodology in this study will allow to design the optimal parameters by considering the modal properties and operating frequencies that are associated with the mode shape of the system.

Due to the massive development of piezoelectric materials, bending vibration of submerged beam configurations from fluid flow are used not only for sensors, but also for energy harvesters [74-77]. To generate more electrical energy, these require a design and understanding of particular mode shapes that can induce more bending vibration over wide range frequencies. Therefore, a mechanism developed in this thesis can potentially be used to extend the frequency bandwidth of the existing energy harvesters based on the bending vibration that are immersed in viscous fluid for maximising the output power.

1.2. Literature review

Review related to characteristics of travelling waves, techniques for actuating beam structures, modal parameters that promoting travelling waves and analytical approaches capable of correlating beam and fluid parameters to travelling wave phenomena are presented. Moreover, this review is also used as the basis to develop experimental setup.

1.2.1. Travelling waves on beam structures immersed in a fluid

In cases of inviscid fluids, beam structures do not accommodate themselves to produce pure travelling waves due to insignificant damping values and boundary conditions. Accordingly, the beam requires adjustments in the boundary conditions to cancel standing wave generation [78]. Theoretically, the boundary conditions need to be designed in a way to achieve a beam equation containing two main functions as follows:

$$w_{mc}(x,t) = F_1\varphi_a(x)\sin\omega t + F_2\varphi_b(x)\cos\omega t \tag{1.1}$$

where F is the forcing function including the modal participation factors, φ is the mode shape, ω is the frequency, x and t is the location along the beam length and time, respectively; whereas $w_{mc}(x,t)$ is the modal contribution at a particular vibration mode for the displacement response of the beam. Note that the displacement responses are summation of many vibration modes. To realise Eq. (1.1), Loh and Ro [79] introduced a two-mode excitation where two forces arranged in a symmetrical form along the beam length are set at the same amplitude and frequency with a phase difference of 90 degrees.

This configuration creates a modal contribution, $w_{mc}(x,t)$, in the beam equation of the form (after simplification) [21],

$$w_{mc}(x,t) = \frac{F_i \varphi_i(x)}{\omega_{n,i}^2 - \omega^2} \sin \omega t + \frac{F_{i+1} \varphi_{i+1}(x)}{\omega_{n,i+1}^2 - \omega^2} \cos \omega t \tag{1.2}$$

where the subscript i denotes the i-th element of the natural frequency values starting from 1 to ∞; whereas ω_n and ω are the natural frequency and forcing frequency, respectively. The optimal travelling waves are achieved when the beam is actuated halfway between two resonant frequencies. When the forcing frequency is set around the resonant frequency, for instance $\omega \approx \omega_i$, the modal contribution responsible for creating travelling waves will be dominated only by the sine function, resulting in the pure standing wave form. Furthermore, pure travelling waves in the beam can only be achieved when the hyperbolic part of the mode shape is approximately zero. This condition occurs only in higher mode shapes.

This technique is considered easy to be implemented in the real engineering applications and has been expanded in many successive works such as [21, 22, 78, 80-84]. However, manufacturing imprecision, structural instability and discrepancy in the actuator can impair the pure travelling wave generation. Another method to produce the travelling wave was developed by Kuribayashi et. al. [85] based on the principle of impedance matching. This actuation also utilises two actuators: one actuator is functioned as the source of excitation and the other is used to prevent the reflection wave when the propagating wave collides with boundaries. This technique requires careful tuning of the actuators because the impedance values depends on the amplitude load and frequency [86]. Furthermore, Tanaka and Kikushima [87] proposed an active sink method, which is based on the elimination of the reflecting wave at the other boundary utilising damping mechanisms. This method is principally the same as the impedance matching technique where the exact wave elimination must match with the damper requirements. Also, the damper only works effectively in a certain range of frequencies.

Some researchers have attempted to improve the travelling wave generation based on these three fundamental methods. For instance, Ghenna et. al. [88] proposed a vector control method in order to improve the travelling wave generation using the two-method excitation. Improvement in the impedance matching method was performed in [89] by

adding a spring at each end of the beam to eliminate the reflection effect. Blanchard et. al. [90, 91] further investigated the effect of adding a spring and damper to improve the active sink method. They further varied the positions to find the optimum value for reducing the standing wave and enhancing the travelling wave generation. Furthermore, a tuning method based on a wave identification scheme was proposed by Minikes et. al. [92] that can be implemented with real-time control strategy to obtain pure travelling waves.

In cases of beam submerged in a viscous fluid, strong damping induced from fluid loading can generate phase delay along the beam length that leads to travelling wave phenomena in the vibration pattern. Accordingly, passive travelling waves can be produced by implementing single excitation such as a cantilever beam configuration subjected to base motion. Since the damping function is 90 degrees out of phase to the stiffness and mass per unit length functions, the beam equation for this configuration eventually fulfils Eq. (1.1). With the development of wave identification, the content of mechanical waves can be decomposed to give a travelling index which describes a measurable quality metric on a scale from 0 (pure standing waves) to 1 (pure travelling waves). Study in [22] demonstrates that the travelling index of a cantilever beam configuration subjected to base motion vary depending on the frequency with the highest index values observed around the third resonant. Although the variation in the travelling index of the cantilever beam can be eliminated by implementing the two-mode excitation technique as investigated in [22, 23], understanding the characteristics and limitations of passive travelling waves, which are the main focus of this work, can offer benefits towards more effective and efficient actuations.

1.2.2. Features of modal parameters that promote travelling waves

It has been described in the previous subsection that a cantilever beam configuration submerged in a fluid subjected to its base motion can generate passive travelling waves when there is a presence of strong damping [18]. The passive travelling waves are also determined by the location of natural frequencies [22]. In an inviscid fluid, the modal parameters of the beam – the natural frequency and damping – are dependent variables dictated by the geometric and material properties of the beam. In cases of viscous fluids, modal parameters become complex due to the interaction between the beam displacement

and fluid force. This problem requires solutions from coupling equations of structural mechanics and fluid dynamics. Therefore, this section provides an insight into factors affecting to the modal properties due to the presence of fluid that can influence to the generation of passive travelling waves.

In stationary (quiescent) flow, the presence of fluid in the surrounding beam can be modelled as two force components containing an inertial force and drag force [93]. The inertial force is in phase with the local beam acceleration and directly influences the mass per unit length of the beam. The drag force corresponds to the local beam velocity which contributes to increasing the total dissipative force on the beam [94]. Therefore, the general contribution of fluid loading to the modal parameters is expected to decrease the natural frequencies and increase the damping values of the beam. In small displacements, a complex hydrodynamic function was introduced in [95] by neglecting the convective term in the Navier-Stokes equations and considering the 2D unsteady Stokes flow model to linearise the fluid-structure interaction (FSI) problem. The real and imaginary parts of the complex function therefore represent the added mass and damping, respectively. Although these procedures were proposed for circular cross-section, Sader [65] extended the work by providing correction factors for the hydrodynamic function which can be used for rectangular cross-section.

The methodology developed in [65] is expanded by the author to further investigate the characteristics of a slender beam submerged in a viscous fluid vibrating with small displacements by considering experimental verifications [61], torsional vibrations [62, 96], compressible fluids [67] and vibration near a solid surface [63, 97]. From these consecutive studies, it is noticed that decreasing the cross-section of a slender cantilever beam can increase the viscous damping value [65]. The frequency response of a rectangular cantilever beam is relatively insensitive to the presence of an infinite planar surface when the separation between the two is greater than the width of the cantilever beam [63]. The presence of a solid surface close to the vibrating beam also leads to an increase in the hydrodynamic loading. In particular, the damping component of the loading increases dramatically for the Reynolds numbers and the ratio of the wall distance to the beam width less than equal to unity [97]. It should be noted that Reynolds number, Re, in this case is adapted from the nonlinear convective inertial term of the Navier stoke equation given by [65]

$$Re = \frac{\rho_f \omega b^2}{4\eta} \tag{1.3}$$

where ρ_f is fluid density, η is the fluid viscosity and b is the beam width. Equation (1.3) assumes that the oscillation beam amplitude, A_f, is small compared to the beam width. Another pertinent approach for defining the Reynolds number is by associating the nondimensional frequency parameter and oscillation amplitude to give $Re = \rho_f \omega b A_f / (2\pi\eta)$ that has been used, for instance, in references [98-101].

With increasing oscillation amplitudes, the prediction of hydrodynamic functions using the methodology in [65] becomes underestimated. This is due to neglecting the advection term from the Navier-Stokes equation that limits the capability of estimating the vortex shedding and advection-driven phenomena [102]. To alleviate this issue, a correction factor is implemented in the hydrodynamic function to take the nonlinearity caused by oscillation amplitudes into account [103]. It was also found that the oscillation amplitude only affects significantly to the damping force rather than the added mass of the beam. This study is extended in [104] to include the effect of the thickness-to-width aspect ratio of the beam. As anticipated, increasing the aspect ratio enhances the natural frequency of the beam while no appreciable effects are observed on the damping value. Furthermore study regarding the length-to-width aspect ratio of the beam is thoroughly performed in reference [105]. The added mass and damping coefficients for the first two natural frequencies due to the variation of the length-to-width aspect ratio are obtained by fitting the frequency response function (FRF) of the experimental data to the analytical model. It is noticed that the inertia and drag coefficients converge towards a constant value for the aspect ratio greater than approximately 5, making these coefficients insensitive to the changes of the aspect ratio.

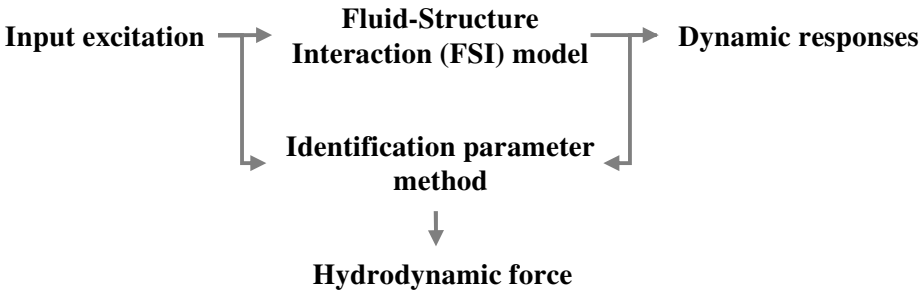

Figure 1.1. Schematic diagram for identifying hydrodynamic forces from experiments

For some numerical and experimental studies, the changes in the hydrodynamic loading are examined by using identification parameter methods. Figure 1.1 depicts the schematic diagram commonly used for identifying hydrodynamic forces by considering input and output responses of the system. The most common technique for calculating the damping is the quadrature peak picking method [106] (or the half-power point method in [107]) which is based on the frequency series and is largely used in FSI characterisations such as [27, 108-111]. Study in [111] used this method to demonstrate the effect of the narrow fluid gap between a submerged beam and finite wall. Note that the beam configuration in this study differs from references [63, 97]. The results indicate that the presence of the narrow fluid gap introduces complicated relationships between Reynolds number, gap height, and the corresponding fluid added mass and damping. The variation in the Reynolds number is achieved by using two different fluid media: water and vegetable oil – with two different beam thicknesses. In general, both added mass and damping tend to increase with decreasing Reynolds number and decreasing gap height.

The peak picking method is also used in references [55, 112, 113] to conduct extensive numerical analyses for investigating modal parameters of a beam submerged partially in viscous fluid. It is found that the resonant frequency of the beam was found to be decreased with the increasing fluid density and viscosity. Conversely, the Q-factor decreased with the increase in fluid viscosity, but was unaffected by the fluid density [112]. Note that the Q-factor is inversely proportional to two times of the damping ratio [107]. The most sensitive changes in the resonant frequency and Q-factor values are found when the beam was submerged by one-third of its length [113]. The numerical model with dimension in micro scale was found more sensitive with viscosity and density compared to the original model at macro scale [55].

It is worth mentioning that the peak picking method is not free from errors. Some low excited modes can create a distorted peak in the frequency response function which leads to an error in the quadrature peak picking method. Due to the rapid development of the nonlinear identification method, there are currently many tools readily available for extracting modal parameters containing nonlinearities. For this reason, Vu et al. [114] used an advanced modal parameter, based on the time domain method utilising multivariable autoregressive model, to review the damping changes in the vibration modes of a submerged vibrating plate. The study demonstrates that the damping ratio at a particular vibration mode is not constant, and the damping value can be higher when a

noticeable excitation is applied. Furthermore, the nonlinearity in the damping ratio will be further studied in this work using another nonlinear parameter identification method. Finally, this review provides the basic knowledge regarding the beam and fluid configurations that lead to variation in the modal parameters. This will also be used to determine the experimental setup for this work such as the tank size; distance between the beam and wall; geometric and material properties of the beam; and forcing amplitude and frequency.

1.2.3. Analytical approaches for estimating travelling waves

To allow for understanding factors affecting travelling waves in the beam, the FSI model is decoupled by introducing the hydrodynamic forces: added mass and damping – in the beam equation illustrated in Figure 1.2. There are two most common linear beam theories: the Euler-Bernoulli and Timoshenko beam theory. The latter theory is an improvement which takes the shear deformation into account. Study in [115] demonstrates that the difference between solutions for the two models is too small to be of practical importance if the aspect ratio of the length-to-height is relatively large and only a few modes are significant in a solution. It is also generally considered that a Timoshenko beam is superior to an Euler-Bernoulli beam for determining the dynamic response of beams at higher frequencies but that they are equivalent at low frequencies [116]. These considerations lead to the use of the Euler-Bernoulli theory for approximating slender (elastic) beam models typically vibrating at low frequencies for FSI applications. Furthermore, it is worth mentioning that the linear beam theory does not include damping. The damping element is coupled directly in the beam equation since there is no clear understanding how to derive the mathematical model of damping in finite structures [73].

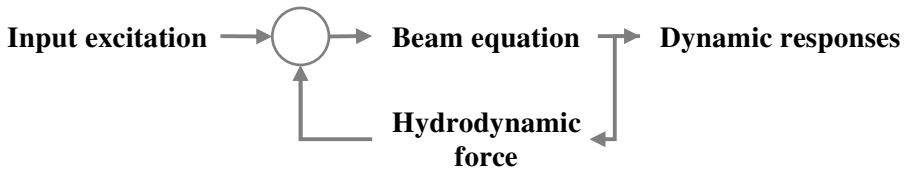

Figure 1.2. Decoupling FSI problem adapted from reference [98]

The estimation of hydrodynamic forces has been presented in the previous section. In cases of small oscillation amplitudes, the damping ratio can be extracted instantly from

the hydrodynamic function [32]. The implementation of damping ratio in the Euler-Bernoulli beam theory can result in the temporal part of the beam equation equal to a lumped mass multi-degree-of-freedom system with spring and damper. This system has an exact analytical solution which can be used to examine the contribution of parameters to the dynamic responses of the beam. In cases of moderately large displacements, the modification of the hydrodynamic function with a correction factor presented in [103] can provide good approximation compared to the standard linearised model. This function can be incorporated with the beam equation using Morison's approaches [117] to give the hydrodynamic forcing per unit length which ultimately leads to a quadratic (nonlinear) damping function. This procedure however complicates the beam equation and requires numerical approaches to obtain the solution. Note that the nonlinearity in the beam equation can also occur due to the boundary conditions such as large deflections of thin beams with distortions [118], sandwich beam configurations with different materials [119] and beam partially submerged in viscous fluid [52, 120].

Since the work in this thesis considers moderately large displacements, the following strategy will be implemented: the quadratic damping approximation will be used along with the estimation of the added mass; then an equivalent damping ratio will be derived to give linear approximations that can be used to decompose the beam equation into mechanical waves. This would allow to understand parameters affecting passive travelling waves. The hydrodynamic parameters provided in [121] will be used in this work to provide assessment of their limitation since we noticed in reference [18] that those parameters provide good approximation only for a certain condition.

1.3. Research aims

To date, there has not been any literature currently available which has assessed the contribution of structural travelling waves induced through electromagnetic actuation to the fluid dynamics. Thus, the aims of this work are:

- To extend and align the usage of analytical approaches used to assess the travelling waves of beam submerged in liquid.

  Although the analytical approaches have been widely used, this requires further assessment in the capability of accurately predicting the propagation wave. This also requires the establishment of an experimental rig capable of capturing

mechanical waves. From this assessment, the correlation between the travelling waves and beam parameters will then be investigated.

- To further the understanding of the contribution of travelling waves to the characteristics of fluid flow.

  This aim requires quantitative methods to provide assessment on the fluid velocity. Thus, an experimental rig capable of measuring fluid velocity around the beam is required to provide initial assessments of the system. Computational methods such as CFD modelling will then be used to further investigate the correlation between travelling waves and fluid flow.

- To investigate the performance of the beam actuated with electromagnetic actuation and contribute to their development.

  In this thesis, a conceptual design of a non-uniform beam model controlled with electromagnetic actuation is introduced. Initially, the influence of this model on the dynamic properties of the beam is assessed. Parameters associated with the performance of mechanical forces in the electromagnetic actuation will then be investigated. The development of an experimental rig is necessary to investigate the potential shortcomings of the proposed design. Finally, this methodology will allow to contribute to the development of controllable devices capable of self-propulsion.

1.4. Structure of thesis

The thesis is divided into the following sections:

Chapter 1 presents the current state of the art on research of beam submerged in viscous fluid and structural travelling waves phenomena.

Chapter 2 describes the derivation of the mathematical models of the beam submerged in liquid. This chapter also provides a description of the computational methodology used to develop the CFD models. Details of the techniques to perform numerical simulations are also presented here.

Chapter 3 provides an overview of the rig and the measurement techniques used in the experimental approaches. By comparing the experimental the measurements provide

the basis to validate the numerical and analytical techniques. A study of the relation between the beam parameters and the development of travelling waves is also provided.

Chapter 4 presents the fluid measurement results from the experimental analysis. The findings for the CFD analysis of cantilever beam submerged in viscous fluid are also elaborated in this chapter. A description of the mesh and physic settings used is provided. A parametric study is also conducted to assess various parameters associated to dynamic properties of the beam with aim to characterising their effect on reducing the mean fluid velocities.

Chapter 5 explores the dynamic properties of the non-uniform beam model. A parametric study for electromagnetic actuation is performed to characterise the different parameters associated to mechanical force. The development of an experimental rig for generating optimum travelling waves is also presented.

Chapter 6 presents the main conclusions of this study, along with recommendations for future work.

Chapter 2. Analytical and numerical approaches

2.1. Introduction

As shown in the previous chapter, the dynamic responses of a beam immersed in a fluid can be approximated by simplifying fluid effects with the hydrodynamic forces that the fluid induces on the beam. Following this approach, analytical techniques that permit to investigate the vibration patterns of the beam under hydrodynamic loads are here described. Using the models developed, this chapter investigates the relationship between the beam parameters and travelling wave phenomena. However, the simplification used in the models do not allow to capture unsteady and complex flow features induced by the motion of the beam. These can be investigated using advanced experimental flow diagnostics such as the Laser Doppler Anemometry (LDA). Although LDA would permit to investigate the fluid velocity induced due internal flow from vibrating beam, this is an expensive and time consuming approach that would allow for a limited number of tests. To overcome these shortcomings, complex FSI problems are usually investigated using numerical models.

Section 2.2 focuses on the analytical approaches of the steady-state vibration of a cantilever beam submerged in a fluid. Sections 2.2.1 and 2.2.2 explore general considerations to be made for modelling the beam and discuss the equation of motion of the undamped beam vibration. Following this, Section 2.2.3 explains the decomposition of beam equations by considering hydrodynamic forces using Galerkin approximations. The temporal solution from this decomposition contains of modal couplings due to nonlinear damping which are further examined in Sections 2.2.4 and 2.2.5. The linear approximation model of the beam equation is derived in Section 2.2.6. Furthermore, the methodologies for performing numerical simulation described in Section 2.3. Finally, Section 2.4 summarises the main findings of the chapter.

2.2. Part I: Analytical approaches

The schematic diagram of the system under consideration is illustrated in Figure 2.1. From the figure, x and z define the physical coordinate system, L is the total beam length, E is the modulus of elasticity, I is moment of inertia, and μ is the linear mass per unit beam length. The beam is attached to the base at one end and free at the other end, satisfying clamped-free boundary conditions. The base is assumed to be fully rigid, such that it only undergoes a rigid body translation in the z direction. Due to the relative motion between the beam and base, the total (absolute) displacement of the beam, $w(x,t)$, can be determined by,

$$w(x,t) = w_b(x,t) + w_r(x,t) \tag{2.1}$$

where $w_r(x,t)$ is the relative displacement of the clamped-free beam and $w_b(x,t)$ is the displacement motion of the base defined as

$$w_b(x,t) = \delta(x) A_f \sin \omega t \tag{2.2}$$

where $\delta(x) = 1$ for the clamped-free beam [122]; whereas A_f and ω are the base amplitude and forcing frequency, respectively.

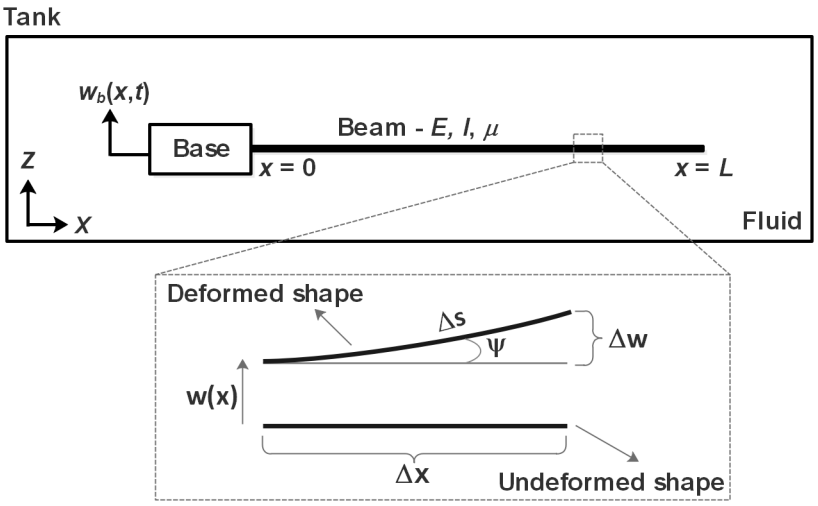

Figure 2.1. Schematic diagram and small section of the beam at the deformed position

2.2.1. General thin-beam theory and Galerkin approximation

The basic modelling assumption is that the beam is assumed to be slender where bending displacement prevails shear deformation. It is also assumed that the displacement

in the z direction is not necessarily large so that the deflection in the x direction and the rotational inertia can be neglected. Another set of assumptions is both the flexural rigidity, and the distribution mass are uniform along the length of the beam. For this system, the Euler-Bernoulli beam theory [73] is considered to approximate the transverse displacement of the beam at any point x along the length of the beam which gives

$$EI\frac{\partial^2}{\partial x^2}\left(\frac{\partial \psi}{\partial s}\right)+\mu\frac{\partial s}{\partial x}\frac{\partial^2 w_r}{\partial t^2}=0 \tag{2.3}$$

where ψ is the beam slope, s is the length along the beam. Note that ψ is a function of time and location.

To illustrate the relationship of the slope angle and transverse displacement of the beam, small beam elements at deformed position are displayed in the inset in Figure 2.1. From the figure, Δw is the small segment of beam displacement, Δx is the projection of the deflected beam along the x-axis and Δs is the small length of beam. By invoking small displacement assumption, the slope can be approximated by writing $\psi \approx \Delta w/\Delta s$ and $\Delta x \approx \Delta s$. Using these approximations, Equation (2.3) reduces to

$$a^2\frac{\partial^4 w_r}{\partial s^4}+\frac{\partial^2 w_r}{\partial t^2}=0 \tag{2.4}$$

where $a=\sqrt{EI/\mu}$.

According to the Galerkin approximation, the solution for Eq. (2.4) can be represented as a series of independent functions containing spatial and temporal parts of the form

$$w_r(x,t)=\sum_{i=1}^{\infty}\varphi_i(x)q_i(t) \tag{2.5}$$

where $\varphi_i(x)$ is the mode-shape of the system and $q_i(t)$ is the modal displacement for the i-th mode.

2.2.2. The spatial functions

Substituting the method of separation variables in Eq. (2.5) into the unforced Euler-Bernoulli beam equation in Eq. (2.4) results in (after arrangement)

$$\frac{a^2}{\varphi(x)}\frac{\partial^4\varphi(x)}{\partial x^4} = -\frac{1}{q(t)}\frac{\partial^2 q}{\partial t^2} = \omega^2 \tag{2.6}$$

where the ω^2 term has been introduced to represent the frequency equation which is associated with the temporal part. Alternatively, Equation (2.6) may be written in two distinct equations as follows:

$$\frac{\partial^2 q_i(t)}{\partial t^2} + \omega_i^2 q_i(t) = 0 \tag{2.7}$$

$$\frac{\partial^4 \varphi_i(x)}{\partial x^4} - \beta_i^4 \varphi_i(x) = 0 \tag{2.8}$$

where

$$\beta_i^4 = \left(\frac{\omega_i}{a}\right)^2 = \frac{\mu\omega_i^2}{EI} \tag{2.9}$$

This temporal equation given in Eq. (2.7) is a set of i uncouple second-order ordinary differential equations which is equivalent to a series of lumped spring-mass systems. It should be noted that the term ω_i in Eq. (2.9) becomes the system natural frequency, $\omega_{n,i}$. The solution of this equation is assumed to be in the form of the trigonometric Fourier series model containing Fourier coefficients such as the fundamental frequency, sine coefficient and cosine coefficient. Both the sine and cosine coefficients can be determined from the initial conditions and the fundamental frequency can be specified by using Eq. (2.9).

For the spatial equation, the variable β_i has been introduced in Eq. (2.8) such that the general solution of the spatial equation can be written as

$$\varphi_i(x) = a_1 \sin\beta_i x + a_2 \cos\beta_i x + a_3 \sinh\beta_i x + a_4 \cosh\beta_i x \tag{2.10}$$

For this system, the boundary conditions require that the deflection and slope must vanish at the clamped end, while the bending moment and shear force must vanish at the free end. Alternatively, these conditions can be written as

$$w_r(0,t) = 0, \qquad \left.\frac{\partial w_r(x,t)}{\partial x}\right|_{x=0} = 0 \tag{2.11}$$

$$\left.EI\frac{\partial^2 w_r(x,t)}{\partial x^2}\right|_{x=L} = 0, \qquad \left.\frac{\partial}{\partial x}\left(EI\frac{\partial^2 w_r(x,t)}{\partial x^2}\right)\right|_{x=L} = 0 \tag{2.12}$$

Implementing these boundary conditions to Eq. (2.10) results in four equations which eventually have a characteristic equation of the form

$$\cos\beta_i L \cosh\beta_i L = 1 \tag{2.13}$$

This equation can now be solved by using a numerical method to obtain the values of $\beta_i L$ or the weighted frequency that are associated with the mode-shape of the clamped-free beam. Using Eqs. (2.10)-(2.13), it is possible to plot the normalised mode shape as depicted in Figure 2.2.

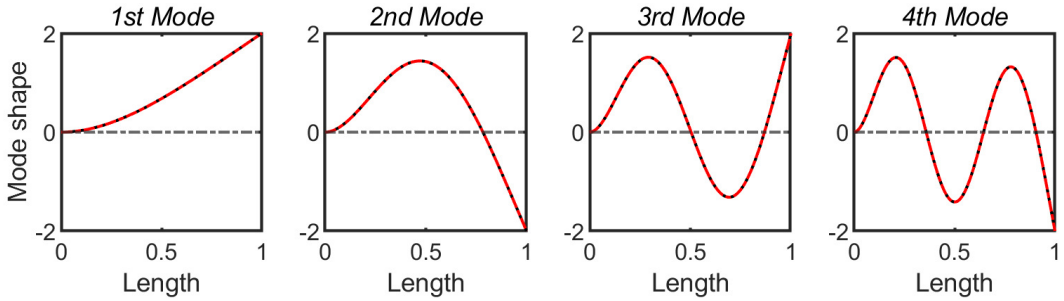

Figure 2.2. First-four mode shapes of a cantilever beam

2.2.3. Galerkin-based model for fluid-structure interaction

The mathematical derivation in the previous section has been independent of damping and forcing functions and is helpful to attain the mode shape of the beam. It is worth mentioning that the numerical modelling of damping mechanisms in finite structures capable of correctly capturing the energy losses as well as the local structural behaviour is quite challenging. In many cases the energy losses are neglected, but in this study the structural damping plays an important role in the generation of travelling waves and therefore removal of the damping would make the beam behaviour unrealistic. It is common practice in models to add viscous damping to each vibration mode to represent the energy dissipation in beam due to material. For the case of beam interacting with

surrounding fluid, the presence of fluid introduces two main effects in the beam equation that can be described as drag and inertia. The overall effect can be expressed as

$$F_f = \frac{\pi}{4}\rho_f C_m b^2 \frac{\partial^2 w_r}{\partial t^2} + \frac{1}{2}\rho_f C_d b \left|\frac{\partial w_r}{\partial t}\right| \frac{\partial w_r}{\partial t} \tag{2.14}$$

where F_f is the total fluid force acting on the beam, ρ_f is the fluid density, b is the beam width, whereas C_d and C_m is the drag and inertia coefficients. The expression in Eq. (2.14) is mainly based on the Morison equation [117] which is originally for a fixed body subject to a fluctuating flow. Since this study considers a vibrating beam in quiescent fluid with no external flow, the flow velocity around the beam is assumed to be equal to the transverse velocity of the beam.

The terms C_d and C_m can be estimated experimentally by using the least square method or the phase-averaging method for periodic flow from the observed forces [123]. In recent studies, the hydrodynamic force can be obtained using a 2D CFD study. The phase shift between the identified force and displacement of a body is used to extract the hydrodynamic force component in phase with the acceleration that is responsible for added mass effects and its out-of-phase component which results into hydrodynamic damping [100, 124]. These components can be adapted to extract the terms C_d and C_m for the Morrison's formula as demonstrated in reference [103].

Depending on the system being considered, the damping term can be integrated with the beam equation before or after applying method of separation variables. In this study, we applied the damping in the beam equation. The reason of this technique is discussed in detail in Section 2.2.5. Incorporating Eq. (2.14) into the Euler-Bernoulli beam equation in Eq. (2.3), and then applying the separation variables from Eq. (2.5) results in

$$\begin{aligned}(\mu + M)\sum_{j=1}^{\infty}\varphi_j(x)\ddot{q}_j(t) + C_{ld}\sum_{j=1}^{\infty}\varphi_j(x)\dot{q}_j(t) \\ + C_{qd}\sum_{j=1}^{\infty}\left|\varphi_j(x)\dot{q}_j(t)\right|\sum_{k=1}^{\infty}\varphi_k(x)\dot{q}_k(t) \\ + EI\sum_{j=1}^{\infty}\frac{\partial^4\varphi_j(x)}{\partial x^4}q_j(t) \;=\; F(x,t)\end{aligned} \tag{2.15}$$

where C_{ld} is the linear damping due to the material, $M = 0.25\pi\rho_f C_m b^2$, $C_{qd} = 0.5\rho_f C_d b$ and $F(x,t) = -(\mu + M)\ddot{w}_b(x,t)$. Multiplying Eq. (2.15) with an arbitrary mode shape and then integrating over the length of the beam, L, yields

$$\begin{aligned}(\mu + M)\sum_{j=1}^{\infty}\int_0^L \varphi_j\varphi_i dx\,\ddot{q}_j + C_{ld}\sum_{j=1}^{\infty}\int_0^L \varphi_j\varphi_i dx\,\dot{q}_j \\ + C_{qd}\sum_{j=1}^{\infty}\sum_{k=1}^{\infty}\int_0^L |\varphi_j|\varphi_k\varphi_i dx\,\dot{q}_k|\dot{q}_j| + EI\sum_{j=1}^{\infty}\int_0^L \frac{\partial^4\varphi_j}{\partial x^4}\varphi_i dx\,q_j \\ = \int_0^L F(x,t)\varphi_i dx\end{aligned} \tag{2.16}$$

The orthogonality conditions for these mode-shapes are given by

$$\begin{aligned}\int_0^L \frac{\partial^4\varphi_j}{\partial x^4}\varphi_i dx = 0 \\ \int_0^L \varphi_j\varphi_i dx = 0\end{aligned} \tag{2.17}$$

for $i \neq j$. When $i = j$, we can express Eq. (2.16) as an infinite series number of independent equations of which the i-th mode is given by

$$\begin{aligned}(\mu + M)\int_0^L \varphi_i\varphi_i dx\,\ddot{q}_i + C_{ld}\int_0^L \varphi_i\varphi_i dx\,\dot{q}_i + C_{qd}\sum_{j=1}^{\infty}\sum_{k=1}^{\infty}\int_0^L |\varphi_j|\varphi_k\varphi_i dx\,\dot{q}_k|\dot{q}_j| \\ + EI\sum_{j=1}^{\infty}\int_0^L \frac{\partial^4\varphi_i}{\partial x^4}\varphi_i dx\,q_i = \int_0^L F(x,t)\varphi_i dx\end{aligned} \tag{2.18}$$

The definitions of mode-shapes satisfy

$$\begin{aligned}\int_0^L \varphi_i\varphi_i dx = L \\ \int_0^L \varphi_i''''\varphi_i dx = \frac{\beta_i^4}{L^3}\end{aligned} \tag{2.19}$$

It is now possible to simplify Eq. (2.18) using Eq. (2.19) to give

$$\ddot{q}_i(t) + 2\zeta_{ld,i}\omega_{ni}\dot{q}_i(t) + \frac{C_{qd}}{(\mu+M)L}\sum_{j=1}^{\infty}\sum_{k=1}^{\infty}\psi_{jki}\dot{q}_k(t)\left|\dot{q}_j(t)\right| + \omega_{ni}^2 q_i(t) = Q_i(t) \tag{2.20}$$

where $\zeta_{ld,i} = C_{ld}/(\mu+M)$ and

$$Q_i(t) = \frac{1}{(\mu+M)L}\int_0^L F(x,t)\varphi_i dx = -\frac{\ddot{w}_b(x,t)}{(\mu+M)L}\int_0^L \varphi_i(x)dx$$
$$\psi_{jki} = \int_0^L \left|\varphi_j(x)\right|\varphi_k(x)\varphi_i(x)dx \tag{2.21}$$

Equation (2.20) contains a nonlinear damping term which requires numerical integration such as Runge-Kutta in order to obtain the solution of $q_i(t)$.

2.2.4. Investigating the nonlinear coefficients

The terms $\psi_{jki}\dot{q}_k(t)\left|\dot{q}_j(t)\right|$ in Eq. (2.20) can lead to multiple coefficients depending on the number of modes used in the simulation. To demonstrate this, the first-two modes, $i = 1,2$, are used to give a two-mode modal coordinate equation in the form of

$$\begin{aligned}
&\ddot{q}_1 + 2\zeta_{ld,1}\omega_{n1}\dot{q}_1 \\
&\quad + \frac{C_{qd}}{(\mu+M)L}(\psi_{111}\dot{q}_1|\dot{q}_1| + \psi_{121}\dot{q}_1|\dot{q}_2| + \psi_{211}\dot{q}_2|\dot{q}_1| \\
&\quad + \psi_{221}\dot{q}_2|\dot{q}_2|) + \omega_{n1}^2 q_1 = Q_1 \\
&\ddot{q}_2 + 2\zeta_{ld,2}\omega_{n2}\dot{q}_2 \\
&\quad + \frac{C_{qd}}{(\mu+M)L}(\psi_{112}\dot{q}_1|\dot{q}_1| + \psi_{122}\dot{q}_1|\dot{q}_2| + \psi_{212}\dot{q}_2|\dot{q}_1| \\
&\quad + \psi_{222}\dot{q}_2|\dot{q}_2|) + \omega_{n2}^2 q_2 = Q_2
\end{aligned} \tag{2.22}$$

It is observed that the first-two modes can result in 8 combinations of the damping terms $\psi_{jki}\dot{q}_k(t)\left|\dot{q}_j(t)\right|$. Therefore, the first-three modes can lead to 27 combinations.

To investigate the influence of the nonlinear coefficient terms on the beam responses, parameters in reference [125] are used to perform simulation for Eq. (2.22). The beam

has a length, width and thickness of 80 *mm*, 12.75 *mm*, and 0.08 *mm*, respectively. The beam density, ρ, is approximately 7200 kg/m^3 and the modulus of elasticity, E, is 240 *GPa*. For the fluid properties, the water density, ρ_f, is 997 kg/m^3 and the drag coefficient, C_d, is 1.8. With these parameters, the nonlinear coefficient value, ψ_{jki}, in Eq. (2.22) can be obtained using Eq. (2.21), and the results are presented in Table 2.1.

Table 2.1. Nonlinear coefficient values of Equation (2.22)

jk	i	$\lvert\dot{q}_j\rvert\dot{q}_k$	ψ_{jki}	jk	i	$\lvert\dot{q}_j\rvert\dot{q}_k$	ψ_{jki}
11	1	$\lvert\dot{q}_1\rvert\dot{q}_1$	0.118225	11	2	$\lvert\dot{q}_1\rvert\dot{q}_1$	-0.03196
12	1	$\lvert\dot{q}_1\rvert\dot{q}_2$	-0.03196	12	2	$\lvert\dot{q}_1\rvert\dot{q}_2$	0.076415
21	1	$\lvert\dot{q}_2\rvert\dot{q}_1$	0.079282	21	2	$\lvert\dot{q}_2\rvert\dot{q}_1$	-0.00707
22	1	$\lvert\dot{q}_2\rvert\dot{q}_2$	-0.00707	22	2	$\lvert\dot{q}_2\rvert\dot{q}_2$	0.103617

It is noted from Table 2.1 that the term ψ_{jki} gives higher values when it satisfies $i = j = k$. Substituting all parameters including the nonlinear coefficient values into Eq. (2.22), the solutions of q_1 and q_2 in time series can be obtained using the Runge-Kutta numerical integration method. To obtain a frequency series focusing on the first-two modes, the forcing frequency is varied from 0.5 *Hz* to 22 *Hz* and the base amplitude is kept constant at a certain value. Since the results from numerical simulation contains transient and steady state parts. The transient parts are neglected, and the maximum value of the steady state responses is estimated and stored each frequency. This technique would allow to obtain the maximum amplitude of the modal coordinate for various forcing frequencies.

Figure 2.3 shows the frequency responses of q_1 and q_2 generated with the base amplitude of 0.1 *mm*. The blue dotted line was obtained by considering all nonlinear coefficients given in Table 2.1. For the red line, only ψ_{111} and ψ_{222} were considered in the simulation. Overall, both models have good agreement. It is observed from Figure 2.3(a) that there are two peaks for q_1, particularly for the blue line, where the second peak is located around the second mode. The small figure inset in Figure 2.3(a) depicts the time responses at $f = 16.15$ *Hz*. The time series of ψ_{jki} with variation j, k, i indicates that the steady state response contains multiple frequencies. The FFT analysis, not shown here for brevity, reveals that the signal consists of the first natural frequency, ω_{n1}, and the forcing frequency 16.15 *Hz*. The reason for this behaviour is due to the cross-coupling

between the variable $\dot{q}_1$ and $\dot{q}_2$. Referring to Eq. (2.22), the maximum value for $\dot{q}_2|\dot{q}_2|$ generated with the base amplitude and forcing frequency of 0.1 mm and 15 *Hz*, respectively, is higher than $\dot{q}_1|\dot{q}_1|$. This happens when the maximum value $\dot{q}_1$ is less than equal to 1. Accordingly, this condition creates a multi-frequency signal in $q_1(t)$. Figure 2.3(b) shows the frequency responses of q_2. It is seen that the blue line superimposes the red line over a range of frequencies. Unlike q_1, the influence of cross-coupling modal terms does not appear in the frequency series of q_2.

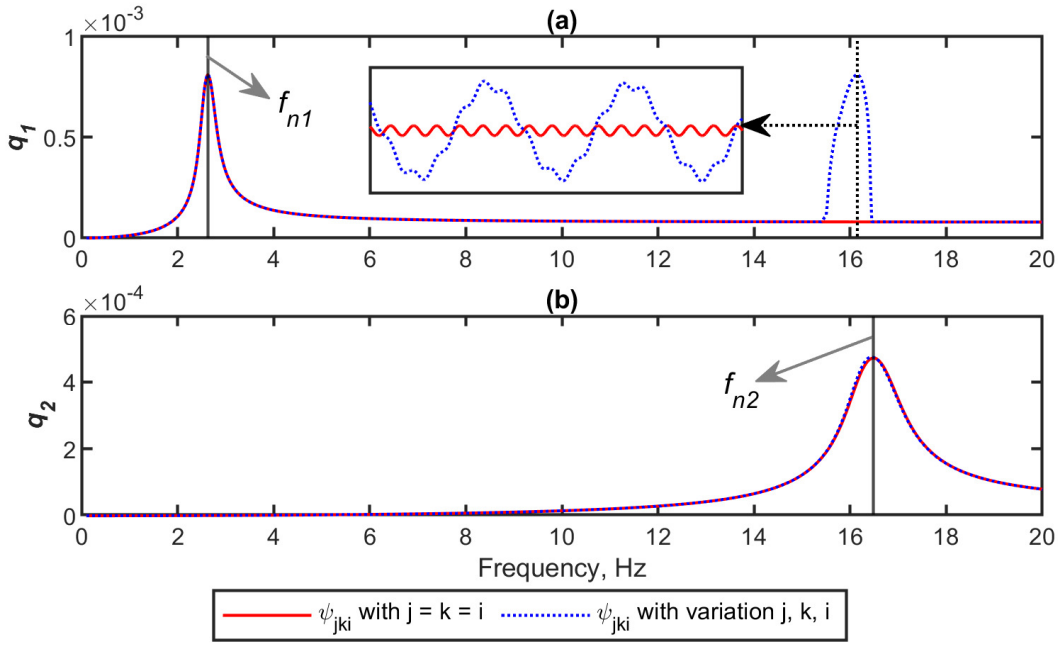

Figure 2.3. Modal coordinate generated with the base amplitude of 0.1 *mm*

Figure 2.4 displays the frequency series of Eq. (2.22) generated with the base amplitude of 2 *mm*. It is observed from Figure 2.4(a) that there is no peak presented around the second mode. Furthermore, the second peak around 16 Hz in Figure 2.4(a) is now vanished compared to that of the base amplitude 0.1 *mm*. This is caused by the square velocity term $\dot{q}_1|\dot{q}_1|$ that gives considerable values to Equation (2.22), eliminating nonlinearities in the time series. Considering phenomena in Figure 2.3(a) and Figure 2.4(a), it can be concluded that the nonlinearities around the second mode in the time series of q_1 vanish with increasing the base amplitude.

Figure 2.4(b) displays the frequency series of q_2. With increasing the base amplitude, the nonlinearities around the second mode become evident. It is noticed that these nonlinearities exist up to 12 *Hz*. Due to the cross-coupling modal terms, the nonlinearities in the time series of q_2 affect to the frequency series of q_1. This evidence is indicated with

"the dent" shown in Figure 2.4(a). These nonlinearities disappear when the base amplitude is set at very low amplitudes, for instance 0.1 *mm*. With low base amplitudes, $\dot{q}_2$ becomes close to zero. Accordingly, the influence of $\dot{q}_2$ in the cross-coupling modal terms become weaker and Equation (2.22) are primarily determined by $\psi_{111}\dot{q}_1|\dot{q}_1|$ and $\psi_{222}\dot{q}_2|\dot{q}_2|$.

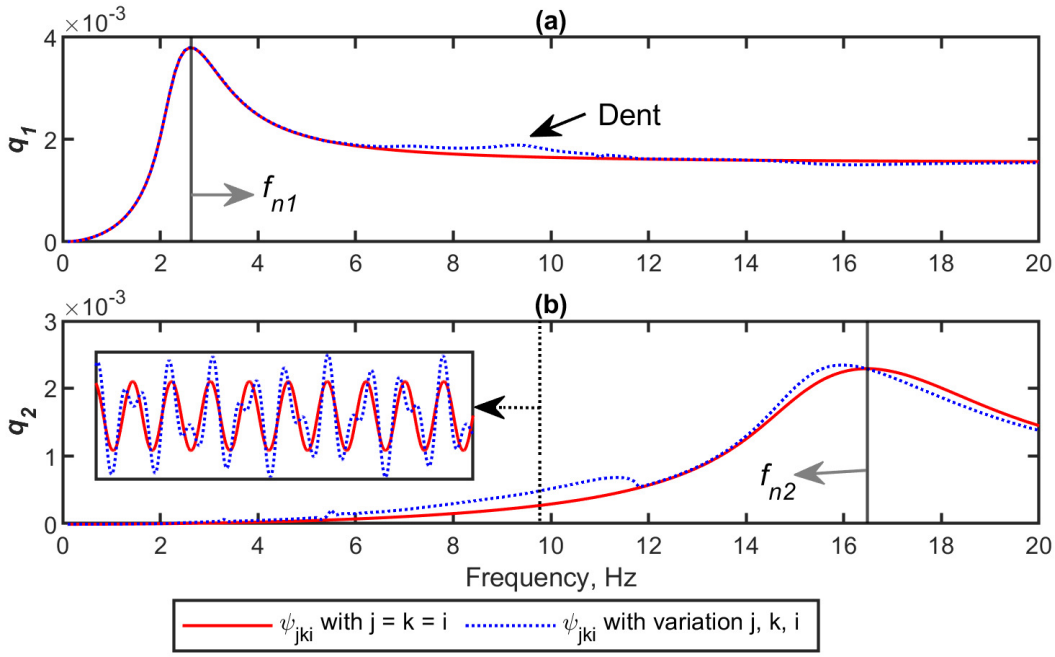

Figure 2.4. The first two modal coordinates generated with the base amplitude of 2 *mm*

It is evident from these investigations that the cross-coupling modal terms with the variation of j, k, i can induce nonlinearities which limit the equation to explore a wide range of problems. It has been demonstrated in Figure 2.3 and Figure 2.4 that removing coefficients $\psi_{121}, \psi_{211}, \psi_{221}, \psi_{112}, \psi_{122}$ and ψ_{212} gives more stable results both in time and frequency series without loss of generality. Therefore, the nonlinear coefficient ψ_{jki} with $j = k = i$ is considered for analysis and validation with experimental models. This will reduce the complexity in the equation, allowing investigation to be carried out in higher modes.

2.2.5. Discussion on incorporating damping into beam equation

It should be emphasised that there is no exact mathematical derivation to integrate damping into the Euler-Bernoulli beam equation. For the case of linear damping, the damping value, denoted as C_{ld}, can be added in the Euler-Bernoulli beam equation as

demonstrated in Section 2.2.3. After applying the method of separation variables and using the orthogonality conditions in Equation (2.19), the linear damping and mass per unit length in the temporal equation become $C_{ld}L$ and $(\mu + M)L$, respectively. To obtain the damping ratio, the linear damping term $C_{ld}L$ is divided by the mass, $(\mu + M)L$. This division removes the influence of the beam length, L, resulting from the separation of spatial and temporal functions. Thus, the damping ratio is independent of the method of separation variables. To remove complexity, Wagg and Neild [73] suggested to use an undamped Euler-Bernoulli beam model and, then, introduce the damping after applying the method of separation variables in the form of damping ratio, denoted as ζ_{ld}, in the modal coordinate.

For the case of quadratic damping, implementing the damping before modal separation can result in the modal interaction between the temporal solution and the spatial function as expressed in Equation (2.20). Due to the modal interaction, ψ_{jki}, the damping coefficient can lead to different values for each mode of the temporal function. Using Equation (2.20) and parameters in Section 2.2.4, the first-three modes of the damping coefficient $C_{qd}\psi_{jki}/(\mu + M)L$ with $jki = [111 \quad 222 \quad 333]$ are 10.05, 8.81 and 8.67, respectively. Accordingly, the damping functions become $10.05\,\dot{q}_1|\dot{q}_1|$, $8.81\,\dot{q}_2|\dot{q}_2|$ and $8.67\,\dot{q}_3|\dot{q}_3|$. Note that due to the orthogonality conditions in the method of separation variables, the mass per unit length, $(\mu + M)$, in the beam equation becomes the unit of mass, $(\mu + M)L$ in the modal coordinate.

It is also possible to add the quadratic damping function after the method of separation variables. Accordingly, Equation (2.18) can be written, after implementing Eq. (2.19),

$$(\mu + M)L\ddot{q}_i + C_{ld}L\dot{q}_i + EI\frac{\beta_i^4}{L^3}q_i = \int_0^L F(x,t)\varphi_i dx \tag{2.23}$$

The quadratic damping function, C_{qd}, from Equation (2.14) can be integrated after the undamped modal coordinate equation is divided by the mass $(\mu + M)L$ to give

$$\ddot{q}_i + \left[C_{qd}|\dot{q}_i| + \frac{C_{ld}L}{(\mu + M)L}\right]\dot{q}_i + \frac{EI\beta_i^4}{(\mu + M)L^4}q_i = \int_0^L F(x,t)\varphi_i dx \tag{2.24}$$

Note that dividing the damping function with the unit of mass would make the damping coefficient 7 times larger than the original value. This becomes overestimated and must be avoided. Accordingly, this would result in the damping value of $0.5\rho_f C_d b = 11.44$ and is constant for all modes, $i = 1,2, \ldots, \infty$. This technique reduces the complexity in the decomposition of the beam equation.

It has been demonstrated that incorporating the quadratic damping before and after the method of separation variables can lead to different damping values. To investigate the influence of these techniques on the modal coordinate, the damping values obtained from these two methods are used to simulate the first-three modes of Equation (2.20). The base amplitude for numerical simulation is 1.5 *mm* and the frequency is varied from 0.5 *Hz* to 60 *Hz*. Following the same procedure for obtaining the frequency series, the maximum amplitude of q_i is taken at the steady states and the results are shown in Figure 2.5. As anticipated, it is seen that there are discrepancies between applying the damping before and after the method of separation variables. Note that the discrepancies occur around the natural frequencies. All models agree when it is actuated away from resonances. As expected, the peaks for the dashed-dotted blue lines are constant, while the red lines vary for q_1, q_2, and q_3 due to decreasing the damping value.

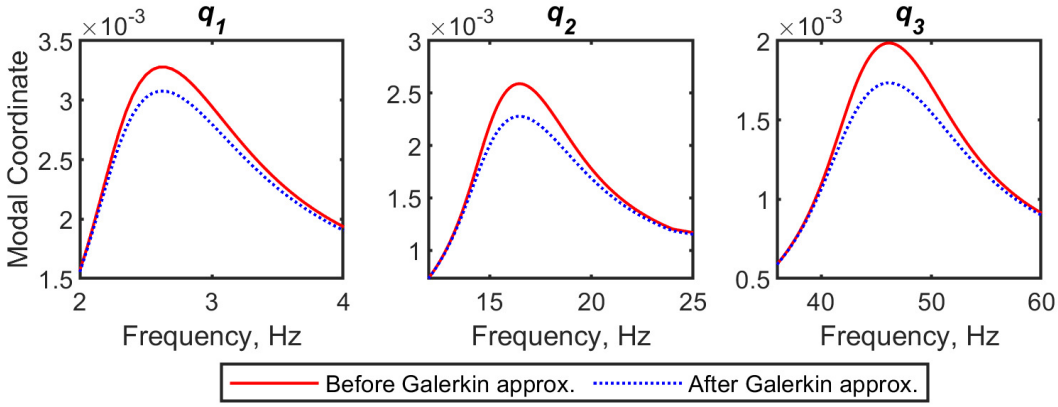

Figure 2.5. Comparison of implementing damping functions before and after the Galerkin approximation

Considering Equations (2.14) and (2.20), the beam velocity increases along with increasing the forcing frequency. This increase can lead to double the damping force where it has a function of the square of velocity. Accordingly, using a constant damping value for all modes can result in overdamped beam responses, particularly at high

frequencies. Therefore, the approximation for applying the damping before the method of separation variables is more appropriate and is used in this study.

2.2.6. Linear approximation

In the case of small displacements, the nonlinear term $|\partial w_r/\partial t|\,\partial w_r/\partial t$ in Eq. (2.14) can be approximated with $A_f\omega\,\partial w_r/\partial t$ [18]. The term A_f is the base amplitude given in Eq. (2.2). Consequently, the damping function due to the material and the surrounding fluid fulfils a linear damping form which can be expressed as $\left(C_{ld} + C_{qd}A_f\omega/L\right)\partial w_r/\partial t$. It has been described in Section 2.2.5 that the linear damping form can be integrated instantly in the modal coordinate after applying the method of separation variables. Using the same procedures, the modal coordinate of the Euler-Bernoulli beam equation becomes a linear second ODE analogous to a linear spring-mass-damper system written as,

$$\ddot{q}_i(t) + 2\zeta_i\omega_{ni}\dot{q}_i(t) + \omega_{ni}^2 q_i(t) = Q_i(t) \tag{2.25}$$

where $\zeta_i = \left(C_{ld} + 0.5\rho_f C_d b A_f\omega\right)/(2(\mu + M)\omega_{ni})$. The exact solution for Eq. (2.25) can be obtained analytically by applying, for instance, the Duhamel integral method to give

$$q_i(t) = \left(-\frac{A_f\omega^2}{(\mu+M)L}\int_0^L \varphi_i dx\right)\left(\frac{(\omega_{ni}^2-\omega^2)\sin\omega t}{(\omega_{ni}^2-\omega^2)^2 + (2\zeta_i\omega_{ni}\omega)^2} + \frac{2\zeta_i\omega_{ni}\omega\cos\omega t}{(\omega_{ni}^2-\omega^2)^2 + (2\zeta_i\omega_{ni}\omega)^2}\right) \tag{2.26}$$

where the first bracket is the forcing function and is constant over time; whereas the second bracket depends on the beam properties and varies over time. Note that the total solution from the Duhamel integral consists of the transient and steady state solution. Equation (2.26) is only the steady-state solution, and the transient response containing the exponential decay is neglected since it is not interest of this study.

The maximum amplitude of Eq. (2.26) can be expressed as

$$q_i(\omega) = \left(\frac{f_0}{\sqrt{(\omega_{ni}^2 - \omega^2)^2 + (2\zeta_i \omega_{ni} \omega)^2}} \right) \tag{2.27}$$

where f_0 is the forcing function defined as

$$f_0 = -\frac{A_f \omega^2}{(\mu + M)L} \int_0^L \varphi_i dx \tag{2.28}$$

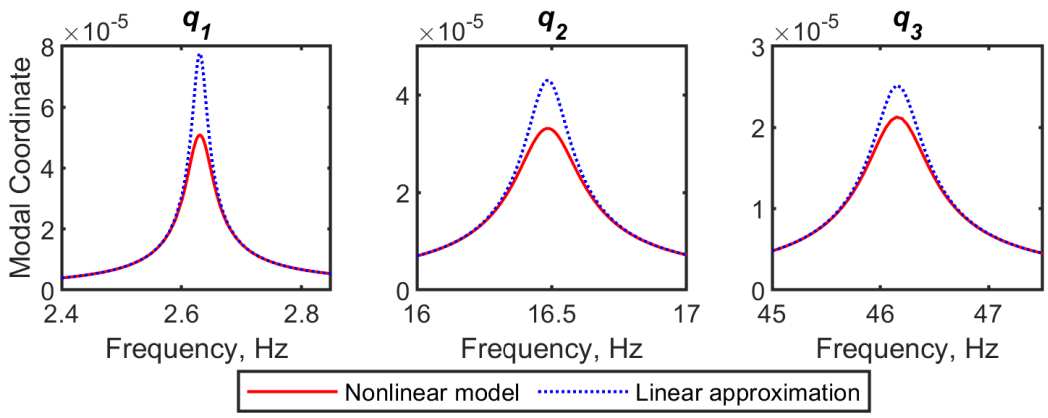

Figure 2.6. Base amplitude 1E-6 *mm*

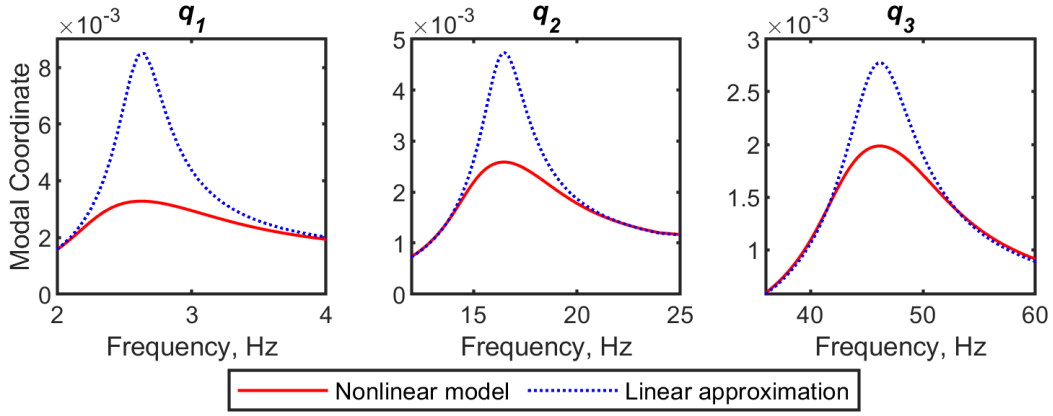

Figure 2.7. Base amplitude 1 *mm*

Equation (2.27) is independent of time and can be used to obtain the frequency series of the linear approximation model by varying the forcing frequency, ω. To investigate the linear model, the frequency series obtained from Eq. (2.27) is compared with the nonlinear model provided in Eq. (2.20) with $j = k = i$. Using the same parameters as in Section 2.2.4, Figure 2.6 shows the comparison between the two models for the first-three modes generated with the base amplitude, A_f, of 1E-6 *mm*. It is seen that the linear model,

the dashed blue line, superimposes the nonlinear model, the solid red line. Figure 2.7 shows the frequency series generated with the base amplitude of 1.5 *mm*. The damping value in the linear approximation model becomes underestimated with increasing the base amplitude, creating discrepancies between the two models. Accordingly, it is evident that the linear approximation term, $A_f \omega \, \partial w/\partial t$, to estimate the nonlinear term, $|\partial w/\partial t| \, \partial w/\partial t$, is valid for the case of the atomic force microscopy where beams vibrate due to thermal driving forces [65].

The exact solution of the modal coordinate from the linear model is paramount to explain the interaction between the beam properties and forcing functions to the beam responses. To alleviate discrepancies between the linear and nonlinear models, the frequency series of the nonlinear model is substituted to Equation (2.27) to obtain the equivalent damping ratio. Then, the correction factor for the linear model can be introduced by dividing the equivalent damping ratio from the nonlinear model with ζ_i which can be expressed as follows:

$$\chi_i(\omega) = \frac{1}{\zeta_i}\left(\frac{\left(f_0/q_{NL,i}(\omega)\right)^2 - (\omega_{ni}^2 - \omega^2)^2}{4\omega_{ni}^2\omega^2}\right)^{\frac{1}{2}} \tag{2.29}$$

where $\chi_i(\omega)$ is the correction factor and $q_{NL,i}(\omega)$ is the frequency series of the modal coordinate of the nonlinear model. The term inside the bracket in Eq. (2.29) is the equivalent damping ratio derived by rearranging Eq. (2.27) and ζ_i is estimated damping ratio from Eq. (2.25).

Using Eq. (2.29), the correction factor for the first-three modal coordinates generated with the base amplitude of 1.5 *mm* is displayed in Figure 2.8. It is seen from the first row of Figure 2.8 that the peaks of the correction factors are obtained around the natural frequencies and the magnitudes of the correction factors gradually become unity when the modal coordinates are actuated away from resonances. Referring to Equation (2.27), the subtraction of $\omega_n^2 - \omega^2$ becomes close to zero as the forcing frequency approaches the natural frequency, $\omega_{ni} \approx \omega$. Consequently, the responses are predominantly composed of the damping function, $2\zeta\omega_n\omega$. On the contrary, when the modal coordinate is forced away from the natural frequencies, the stiffness term, $\omega_n^2 - \omega^2$, outweighs the

damping term, $2\zeta\omega_n\omega$. Therefore, the damping has no significant contribution to the modal coordinates.

Different base amplitudes lead to different $q_{NL,i}(\omega)$ values, requiring re-evaluation of the correction factors. Eventually, the correction factor at a particular mode can be plotted with respect to the base amplitude and forcing frequency. Since the correction factor is a ratio and is a dimensionless number, this must be multiplied with the linear damping function in Eq. (2.25) to give $2\zeta_i\chi_i(\omega)\omega_{ni}\dot{q}_i(t)$. For the second row of Figure 2.8, the results for the linear approximation model with correction factors are superimposed with those of the nonlinear model. Note that the correction factor in the first row of Figure 2.8 is valid only for the base amplitude of 1.5 *mm*.

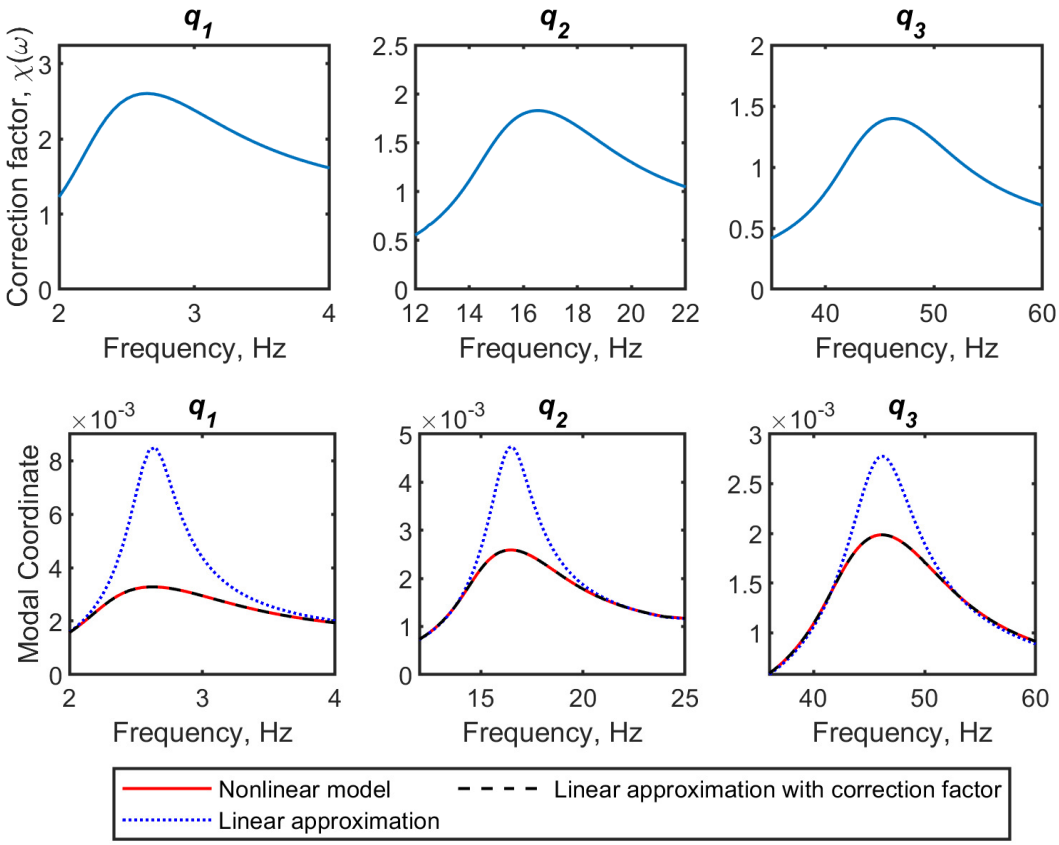

Figure 2.8. First row: Correction factors for the base amplitude 1.5 *mm*; and Second row: Responses of the first three modal coordinate after implementing correction factors

Once the solution of q_i from the linear approximation model is comparable to that of the nonlinear quadratic model, the total solution of the steady-state vibration of the beam, $w(x,t)$, can be realised by multiplying the modal coordinate, $q_i(t)$, with the mode shape, $\varphi_i(x)$, and considering the relative motion in Eq. (2.1) to give

$$w(x,t) = A_f \sin \omega t + (lp_1\varphi_1(x) + lp_2\varphi_2(x) + \cdots) \sin \omega t + (rp_1\varphi_1(x) + rp_2\varphi_2(x) + \cdots) \cos \omega t \tag{2.30}$$

where the terms lp and rp are constants defined as

$$\left.\begin{aligned} lp_i &= \frac{A_f\omega^2}{L} \frac{(\omega_{ni}^2 - \omega^2)}{(\omega_{ni}^2 - \omega^2)^2 + (2\zeta_i\omega_{ni}\omega)^2} f_0 \\ rp_i &= \frac{A_f\omega^2}{L} \frac{2\zeta_i\omega_{ni}\omega}{(\omega_{ni}^2 - \omega^2)^2 + (2\zeta_i\omega_{ni}\omega)^2} f_0 \end{aligned}\right\} i = 1,2,\ldots,\infty \tag{2.31}$$

2.3. Part II: Numerical approaches

This section presents the methodology for numerical approaches to approximate responses of solid structures and fluid dynamics.

2.3.1. FSI simulation

The grid structure is a discretised representation of a geometric computational domain used by physics equations to produce a numerical solution. For FSI simulation, there are two active domains: solid and fluid domain. The solid domain uses the solid stress model to compute the displacement of the solid structure using the finite element method and then calculates the corresponding stresses and strains; meanwhile, the finite volume method is used by the fluid flow solver to compute values at cell centres. The flow domain is replaced with a discrete number of elements, where the governing equations which describe the flow-field behaviour are solved at each individual cell. This means the quality of the CFD grid and the time it takes to complete the simulation depends on the grid resolution at the regions of interest where complex flow physics occur. Different types of grids can be implemented as well as the types of grid refinements which are applied to increase the number of cells in the regions of interest, such as near the aerofoil wall surface boundary.

The two types of grids commonly used in the CFD analysis for various applications include structured and unstructured grids. The structured grid provides a robust and efficient method of producing a high-quality grid for simple and complex grid construction problems [126]. In STAR-CCM+ [127], directed meshing is a method for generating high quality swept meshes on CAD geometries. Directed meshing is effective in providing a structured mesh and is used here to discretise the solid stress model for

finite element stress analysis of the beam. Figure 2.9 depicts an example of the directed meshing procedure applied to a slender beam with a rectangular cross-section.

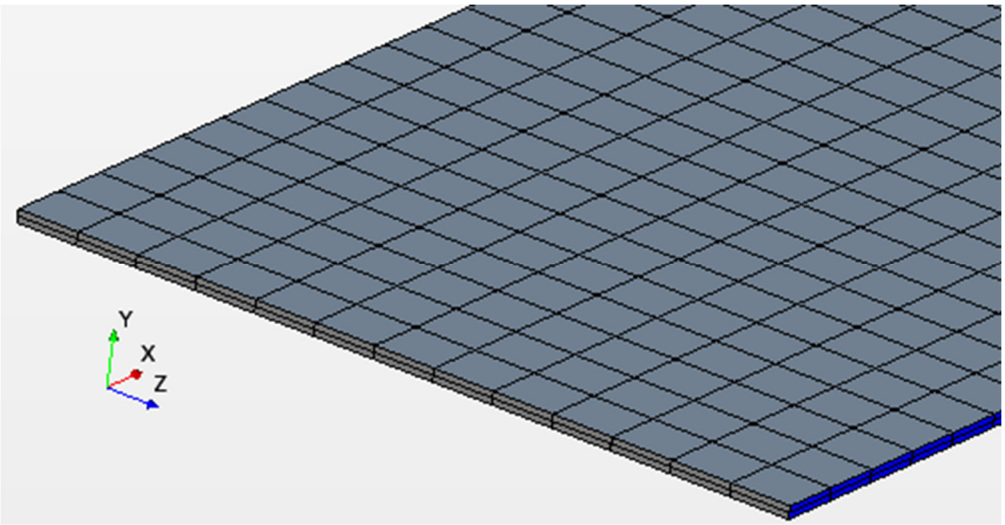

Figure 2.9. Directed meshing procedure applied to a slender beam with a rectangular cross-section. Note that the beam spans along the *x*-axis.

A type of unstructured grid method in STAR-CCM+ uses polyhedral elements which are efficient when applied to complex geometries due to easy adaptability whilst ensuring sufficient grid quality. The geometry can be represented by an unstructured grid as the cells are distributed efficiently throughout the computational domain and provides robust grid refinements at the regions of interest. It is common in computational FSI studies to adopt a hybrid mesh approach which utilises an unstructured grid for the core flow domain and an orthogonal prism layer mesher which grows normal to the direction of the solid surface. The prism layer mesh is part of the hybrid mesh and is used to generate prismatic cells next to wall surfaces or boundaries.

The use of the prism layer mesh also results in the reduction in numerical diffusion near the wall which significantly improves the accuracy as a result. There are multiple ways that the prism layer mesher can be controlled using the built-in mesh feature in STAR-CCM+. A wall thickness distribution method was implemented as this method constructs a structured prism layer mesh from the beam surface based on the total thickness of the prism layers, the total number of prism layers, and the cell height of the initial prism layer from the boundary surface. The size of the prism layer's total thickness should be selected so that it models the boundary layer which develops across the beam surface.

Since the beam vibrates in a particular mode shape depending on the vibration amplitude and frequency, this can deform the mesh in the fluid domain which can generate numerical instability. Figure 2.10(a) and (b) illustrate the deformation of the mesh due to the beam undergoing large displacements. An alternative grid method such as the overset mesh, known as a Chimera or overlapping mesh, can be used to overcome this issue. This grid discretises the computational domain with several different meshes that overlap each other in an arbitrary manner. They are most useful in problems involving multiple moving bodies, as well as optimisation and parametric studies [127]. A key advantage of using overset meshes is that the overset mesh does not require any modifications to the mesh if a body is rotated or translated to a new position, which offers greater flexibility over the standard meshing techniques. This is beneficial in parametric studies which involve vibrating beam in different amplitudes and frequencies which can be easily achieved using an overset mesh; a standard mesh would need further modifications in order to represent the physical geometry change. The implementation of the overset mesh also allows to simulate complex body motions, such as bodies that are close together, or have large, multiple motions applied. Figure 2.10(c) and (d) shows examples of implementing overset mesh for which the background fluid does not deform due to the displacement of the beam.

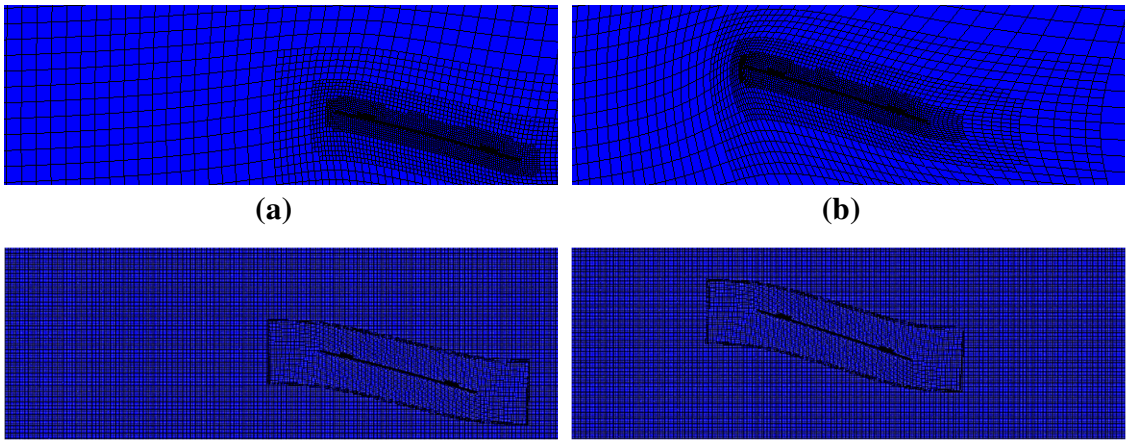

Figure 2.10. Simulation of an elastic beam using (a),(b) the normal mesh and (c),(d) the overset taken at (a),(c) 0.4 *s* and (b),(d) 0.8 *s*

When implementing the overset mesh technique, the flow domain grid is split into two types of mesh: a stationary background mesh which represents the flow-field domain, and an overset mesh which contains a single body such as a beam. The overset mesh is

created using an overset mesh boundary, which is the outer boundary of the overset region that transfers information between the overset mesh and background mesh through interpolation. In an overset mesh, cells for both the background and overset grids are split into active, inactive, or acceptor cells [127]. The discretized governing equations are solved for the cells which are active. For inactive cells, no equations are solved; cells will only become active at certain points if the overset motion has motion applied [127]. The function of the acceptor cells is to separate active and inactive cells in the background region and are attached to the overset boundary in the overset region. Acceptor cells are also used to couple solutions on the two overlapping grids. Variable values at donor cells of one mesh express variable values at acceptor cells in the other mesh through interpolation. The donor cells are the active cells from the other mesh that are closest to the nearest acceptor cell.

A linear interpolation method was selected for the overset mesh which dictates the set of donor cells that are chosen as well as the number of active cells in the donor region around the acceptor cell centroid. This method uses shape functions spanning a tetrahedron defined by centroid of the donor cells. This interpolation option is the most computationally expensive within the CFD solver STAR-CCM+, however it results in a robust and accurate result. A successful coupling of the overset interface between both the background and overset region results in a "hole" being cut in the background mesh. This process is defined as the hole-cutting process. After initialising the overset interface which executes the hole-cutting process, the status of the over mesh cells is determined, i.e. it is determined which cells are active or inactive.

Compared to a standard static mesh, the overset mesh method is not conservative which results in an interpolation error at the overset mesh interface leading to a mass imbalance [127]. It is therefore recommended to have a sufficient number of cells across the overlapping zone. For transient motion simulations, it is recommended that the overset region displacement within one time-step meets the following condition: when the 2nd order implicit time integration scheme is selected for time integration, the maximum movement is half the smallest cell size in the overlapping zone [127]. Moreover, to reduce the discretisation error, the cell sizes for both the background and overset regions should be of similar magnitude in size.

STAR-CCM+ allows for the effect of the fluid forces on the structure displacement and the solid displacement on the fluid flow. Since the beam submerged in a viscous fluid possesses a strongly coupled FSI problems, this requires to solve the flow and structure simultaneously using the two-way coupled FSI model to allows for data exchange fluid forces and solid displacements across the fluid-structure interface. Again, fluid flow and solid displacements are solved using different discretization methods, Finite Volume (FV) and Finite Element (FE) respectively. The different mesh topologies require an interface of type Mapped Contact Interface, which allows for data mapping between the FV and FE meshes. This interface type is a variation of contact interface that relies on an indirect association between faces of the interfacing boundaries for data mappers. Each face of the original boundary is linked with a group of faces on the opposing boundary using a proximity-based algorithm. The main advantage of a Mapped Contact Interface is that it allows for a non-conformal mesh across the interface. This type of mesh is desirable in cases where the interfacing boundaries have different mesh resolutions. For instance, the heat conduction in the solid region requires a coarser mesh compared to resolving the boundary layer in the fluid domain [127].

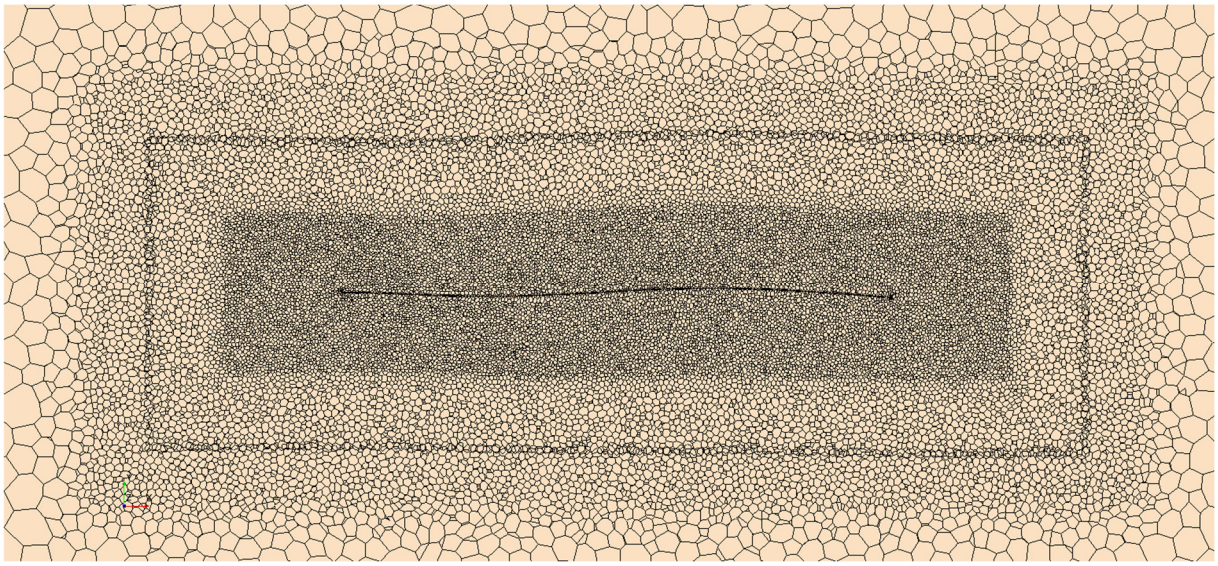

Figure 2.11. Morphing of the fluid mesh based on the motion of the beam

In two-way coupled simulation, the fluid and solid meshes deform due to the displacement of the solid structure. Accordingly, a Solid Displacement motion model is applied to the solid region that allows the sold mesh to deform in real time based on the computed displacements computed by the solid stress solver, while a Morphing motion model is assigned to the fluid region, allowing the fluid mesh to deform based on the

displacements mapped at the interface. Figure 2.11 illustrates the deformation of the fluid mesh due to the displacement of the beam. For solution stabilisation, the solver automatically estimates the volume of displaced fluid per unit area. Then the solver adds a force correction which is proportional to the product of the displaced fluid per unit area and the change in the structure acceleration.

Solid Mechanics studies the displacement of a solid continuum under prescribed loads and constraints. The fundamental laws that govern the mechanics of solids are the same laws that describe the mechanics of fluids, namely, the conservation of mass, linear momentum, angular momentum, and energy. In Solid Mechanics, it is more natural to express the conservation laws using a Lagrangian approach, where the observer follows the solid material as it moves through space and time. In the Lagrangian approach, mass is always conserved. The mass that is contained in any deformed volume is the same mass that was originally contained in the undeformed volume. Since the mass within the volume is conserved, volume changes result in density changes. Linear elastic materials extend proportionally to the applied load and return to the original configuration when the load is removed. The stress-strain relationship for linear elastic materials is linear and is given by Hooke's law.

The motion of a solid body is governed by the principle of virtual work, which expresses the conservation of linear momentum for a continuum. Simcenter STAR-CCM+ calculates the displacement of a solid based on the principle of virtual work, which is discretized using the Finite Element method. This approach follows the total Lagrangian displacement Finite Element formulation by Zienkiewicz and Taylor [128]. The formulation presented in the previous sections does not take into account the damping mechanisms that arise in time-dependent systems. Damping is the dissipation of energy in the solid structure due to a combination of different phenomena, including molecular interaction within the material. In dynamic problems, the contribution of damping forces can be taken into account by including a velocity dependent damping term in the equation of motion. For compressible materials, the only unknown in the governing equations is the displacement field.

2.3.2. Modal analysis

The modal analysis derived from analytical approaches in Section 2.2 is limited for cases of uniform cantilever beam models performing transverse vibration. Thus, numerical approaches are used to extract natural frequencies and corresponding mode shapes of beam structures with nonuniform material properties, complex geometries, and boundary conditions. These problems are found in this thesis particularly in Section 4.3.5 and 5.2. The modal analysis in this work is performed with the commercially available Abaqus software [129]. This type of software has been used extensively for conducting modal analysis with considerably high accuracy. Note that this analysis only considers solid materials without fluid coupling. Therefore, any interaction with an internal or surrounding fluid flow will be ignored.

The frequency extraction using Abaqus is a linear perturbation procedure [129]. The eigenvalue problem for natural modes of small vibration of a finite element model is

$$(\mu^2[M] + \mu[C] + [K])\{\phi\} = 0 \tag{2.32}$$

where $[M]$ is the mass matrix, which is symmetric and positive definite in the problems of interest here; $[C]$ is the damping matrix; $[K]$ is the stiffness matrix, which may include large-displacement effects, such as "stress stiffening" (initial stress terms), and, therefore, may not be positive definite or symmetric; $[\mu]$ is the eigenvalue; and $\{\phi\}$ is the eigenvector—the mode of vibration.

The presence of damping matrix can generate complex eigenvalues and eigenvectors. This system can be symmetrized by assuming that $[K]$ is symmetric and by neglecting $[C]$ during eigenvalue extraction. This technique can lead to real squared eigenvalues, μ^2, and real eigenvectors only. Typically, for symmetric eigenproblems we will also assume that $[K]$ is positive semidefinite. In this case μ becomes an imaginary eigenvalue, $\mu = i\omega$, where ω is the circular frequency, and the eigenvalue problem can be written as

$$(-\omega^2[M] + [K])\{\phi\} = 0 \tag{2.33}$$

Extraction of the eigenvalues and corresponding eigenvectors are performed with the Lanczos method. In theory the basic Lanczos process (in the assumption of "exact" computations without taking into account round-off errors) is able to determine only

simple eigenvalues. In Abaqus, the Lanczos procedure is solved with the SIM architecture to give more efficient computation than the traditional architecture for large-scale linear dynamic analyses. Accordingly, this requires the user to provide the maximum frequency of interest or the number of eigenvalues required.

Although the Lanczos eigensolver in Abaqus can extract coupled vibration modes to fully include structural-acoustic coupling that can affect the natural frequency response of systems, this feature will be ignored since the interest of the study is in the lower frequency modes. In addition to extracting the natural frequencies and mode shapes, the Lanczos eigensolver automatically calculate the generalized mass, the participation factor, the effective mass, and the composite modal damping for each mode; therefore, these variables are available for use in subsequent linear dynamic analyses. For the normalisation, the eigenvectors can be normalized so that the generalized mass for each vector is unity, $m_\alpha = 1$. The generalised mass associated with mode α is

$$m_\alpha = \phi_\alpha^N M^{N\,M} \phi_\alpha^M \tag{2.34}$$

where $M^{N\,M}$ is the structure's mass matrix and ϕ_α^N is the eigenvector for mode α; whereas the superscripts *N* and *M* refer to degrees of freedom of the finite element model.

The modal participation factor is a variable that indicates how strongly motion in the global *x*-, *y*-, or *z*-direction or rigid body rotation about one of these axes is represented in the eigenvector of that mode. The six possible rigid body motions are indicated by $i = 1, 2, \dots, 6.$. The modal participation factor is defined as

$$\Gamma_{\alpha i} = \frac{1}{m_\alpha} \phi_\alpha^N M^{N\,M} \phi_\alpha^M T_i^M \tag{2.35}$$

where $\Gamma_{\alpha i}$ is participation factor for mode α in direction i, T_i^M defines the magnitude of the rigid body response of degree of freedom *N* in the model to imposed rigid body motion (displacement or infinitesimal rotation) of type *i*. Eventually, the effective mass for mode α associated with kinematic direction $i (i = 1,2, \dots ,6)$ is defined as

$$m_{\alpha i}^{eff} = (\Gamma_{\alpha i})^2 m_\alpha \tag{2.36}$$

If the effective masses of all modes are added in any global translational direction, the sum should give the total mass of the model (except for mass at kinematically restrained degrees of freedom).

2.4. Conclusion

The derivation of undamped vibration of the cantilever beam has been presented allowing the spatial function to be obtained. The integration of nonlinear damping due to the presence of fluid in the beam equation has been presented. Using the Galerkin approximation, separation variables of the beam equation result in nonlinear modal coordinate equations containing cross-coupling spatial terms. Further investigation demonstrates that the cross-coupling modal terms can generate a signal with multiple frequencies occurred particularly at resonant frequencies when the beam is actuated at very low oscillation amplitudes. On the contrary, the nonlinearities occur at away from resonant frequencies for cases of moderately large amplitudes. Another technique for implementing nonlinear damping in the beam equation has also been presented which can give constant damping values would be constant for all vibration modes. Finally, the methodologies for numerical approaches to obtain numerical solution particularly for the FSI problems and modal analyses have been presented.

Chapter 3. Characteristics of travelling waves of submerged cantilever beams

3.1. Introduction

This chapter investigates the characteristics of travelling waves of cantilever beams submerged in liquid for various configurations and forcing frequencies. The main objective of this study is to use analytical approaches derived in Chapter 2 to demonstrate how travelling waves are induced by the beam. Accordingly, an experimental investigation is carried out not only to validate the analytical models, but also to study the changes in the beam properties, such as damping and natural frequencies, due to the presence of fluid. This experimental analysis consists of parametric studies examining the influence of the forcing amplitude and frequency, beam dimension, dipping depth of the beam and fluid viscosity. These variables are evaluated against the frequency response function (FRF), transient responses and steady-state responses of the beam. A description of the experimental method is provided as well as the techniques used to post-process the experimental data. In some cases, the FRF and decaying transient responses are used to evaluate the nonlinear damping and natural frequencies of the beam. Furthermore, the experimental test is also used to explore the beam properties in the partially submerged beam.

The steady state responses of the fully submerged beam obtained from the experiment are compared with the nonlinear beam equation. This comparison involves the assessment of the beam envelope over the beam length and the propagation of the maximum amplitude with respect to time and length. Next, the linear approximation beam model is used to approximate the steady state responses of the nonlinear beam equation. Finally, the linear beam equation can be used to elucidate the travelling waves on the beam.

3.2. Mechanical waves in continuous structures

Using Eq. (2.30), it is possible to correlate the beam equation with the mechanical wave phenomena. To illustrate the wave composition in the beam, let the series of $lp_i\varphi_i$ and $rp_i\varphi_i$ in Eq. (2.30) be a function of a single wavelength as follows:

$$\begin{aligned} U(\beta x) &= A_f + \sum_{i=1}^{\infty} lp_i\varphi_i \cong U_1 \cos\beta x + U_2 \sin\beta x \\ V(\beta x) &= \sum_{i=1}^{\infty} rp_i\varphi_i \cong V_1 \cos\beta x + V_2 \sin\beta x \end{aligned} \tag{3.1}$$

Using trigonometric identities, this would allow Eq. (2.30) to be decomposed based on the travelling components to give

$$\begin{aligned} w(x,t) = \frac{1}{2}\big((U_1 + V_2)\sin(\omega t + \beta x) + (V_1 - U_2)\cos(\omega t + \beta x) \\ + (U_1 - V_2)\sin(\omega t - \beta x) + (U_2 + V_1)\cos(\omega t - \beta x)\big) \end{aligned} \tag{3.2}$$

where $(\omega t + \beta x)$ and $(\omega t - \beta x)$ represent the wave travelling in the positive and negative direction, respectively. Therefore, there are three possibilities of mechanical waves that can be generated on the beam based on the definition of Eq. (3.2), namely standing, travelling and hybrid waves.

The pure standing wave is formed when the beam has very little damping influence, $\zeta \approx 0$. Consequently, $rp_i \approx 0$ or $V(\beta x) \approx 0$ since it is proportional to the value of the damping ratio. With the absence of variables V_1 and V_2, the wave in Eq. (3.2) propagates to the positive and negative directions with the same amplitudes. This would create standing waves which are commonly indicated with the node(s) in the beam envelope as illustrated in Figure 3.1. Note that the node position along the beam length can be displaced to the left or right depending on the values of U_1 and U_2.

If the presence of damping is significant, the term $V(\beta x)$ in the wave equation cannot be neglected. The contribution of variables V_1 and V_2 to Eq. (3.2) can result in a percentage between the functions $(\omega t + \beta x)$ and $(\omega t - \beta x)$ in the wave equation. This leads to a hybrid wave formation, which is generally observed by an increase in the amplitude at the node in the beam envelope illustrated in Figure 3.1. For the pure

travelling wave, it requires that the waves travel in one direction either positive or negative. In theory, this can be achieved by invoking the variables $U(\beta x)$ and $V(\beta x)$ to give $U_1 = V_2 = 0$ and $U_2 = V_1 \neq 0$ so that the wave equation in Eq. (3.2) forms in an expression of $\cos(\omega t - \beta x)$. Practically, this can be realised by the manipulating boundary conditions to eliminate reflection waves as presented in references [79, 85-87].

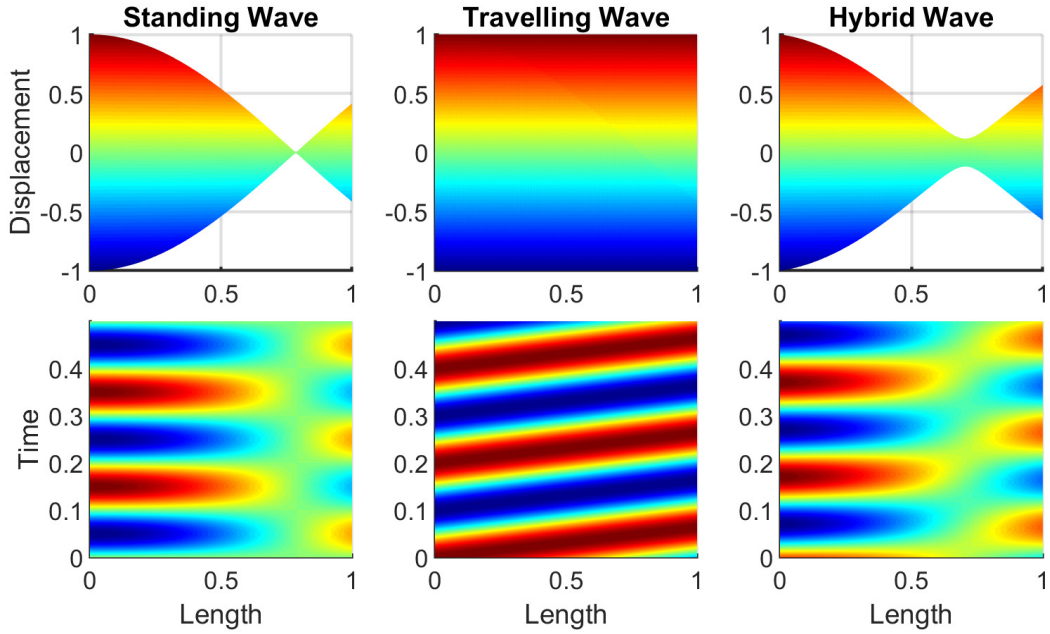

Figure 3.1. Characteristics of mechanical waves in distributed-parameter systems

3.3. Experimental methods

This section describes the experimental apparatus and techniques to post-process experimental data.

3.3.1. Vibration measurements

The schematic diagram of the experimental setup for obtaining the dynamics of the beam is illustrated in Figure 3.2. A desktop PC was utilised not only to generate a command for the signal generator (SG), but also to provide a graphical representation of data from the signal analyser (SA) and camera. Since the signal generator is a USB-powered device, the output power from this device is typically low. Therefore, a 48-Watt LDS PA25E power amplifier was used to enhance the signal before it was connected to an LDS V201 electrodynamic shaker to induce vibrations. The beam was clamped on to the edge of an extension (supporting) plate. The other edge of the supporting plate was

mounted on the shaker. Since the supporting plate transmits vibration from the shaker to the beam, the dimension and material properties of the plate were chosen such a way to not interfere with the working frequency of the beam. Moreover, the supporting plate would allow the beam to be fully immersed inside a tank filled with a liquid. The tank is mounted on an adjustable height table so that the dipping depth of the beam can be varied. The diameter of the tank is 15 *cm* with the height of 28 *cm*.

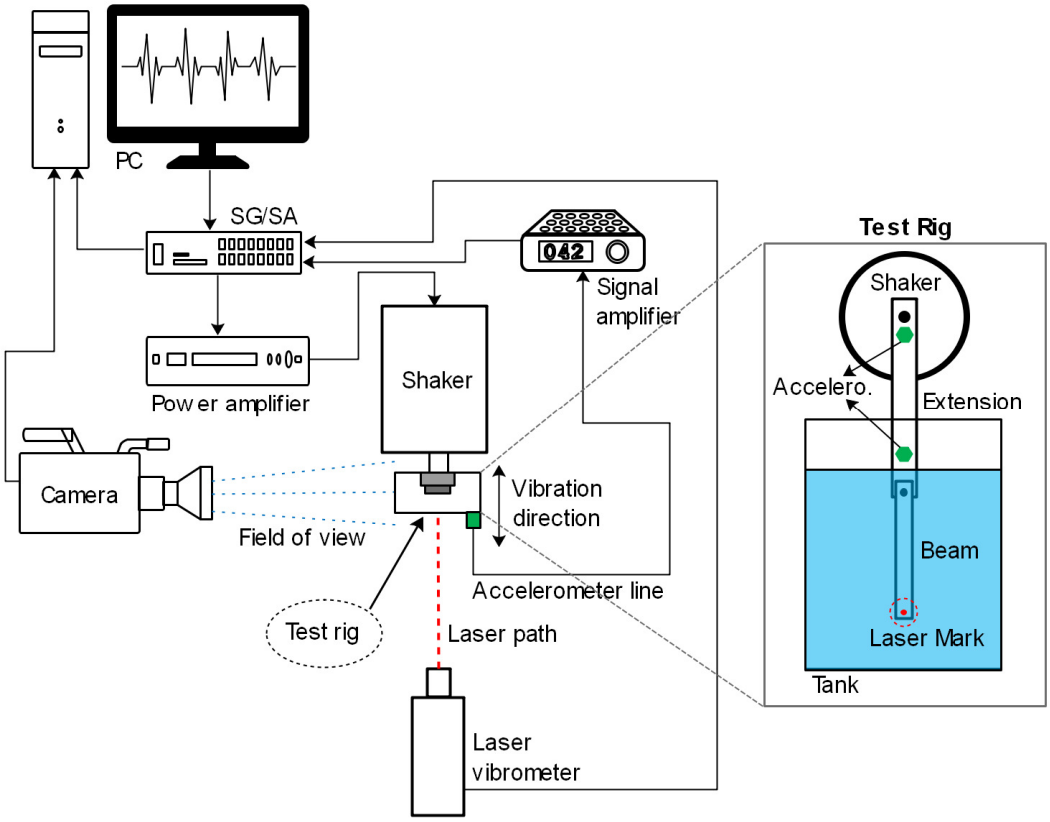

Figure 3.2. The schematic diagram of the experimental investigation

A PCB Piezotronics 352C22 ceramic shear accelerometer was mounted on the shaker to monitor the acceleration of the shaker. The same type of accelerometer was also mounted on the clamped section of the beam to measure the input base acceleration for the beam. The two accelerometers were also used to observe nonlinearities such as multiple frequency phenomena in the extension plate due to interaction between two continuous systems with different geometries and material properties which may influence the motion of the beam. The signals from accelerometers were amplified with a PCB Piezotronics 428C signal amplifier. The velocity responses of the free tip of the beam, indicated by the laser mark in Figure 3.2, were measured by a Polytec PDV100 laser vibrometer. A Photron Fastcam SA1.1 high-speed camera was set perpendicular to

the beam displacement to capture the beam motion over period of time. The physical realisation of the schematic diagram is shown in Figure 3.3. Note that the distance between the camera and test rig shown in Figure 3.3(a) does not represent the real distance when conducting the tests. The wall behind the test rig that is parallel to the field of view of the camera was covered with a white backdrop to anticipate the noise in the captured images. Since the frame rate and shutter speed of the camera were set to 2000 *fps* and 1/2000 *s*, respectively, a 3W LED light was used to illuminate the beam.

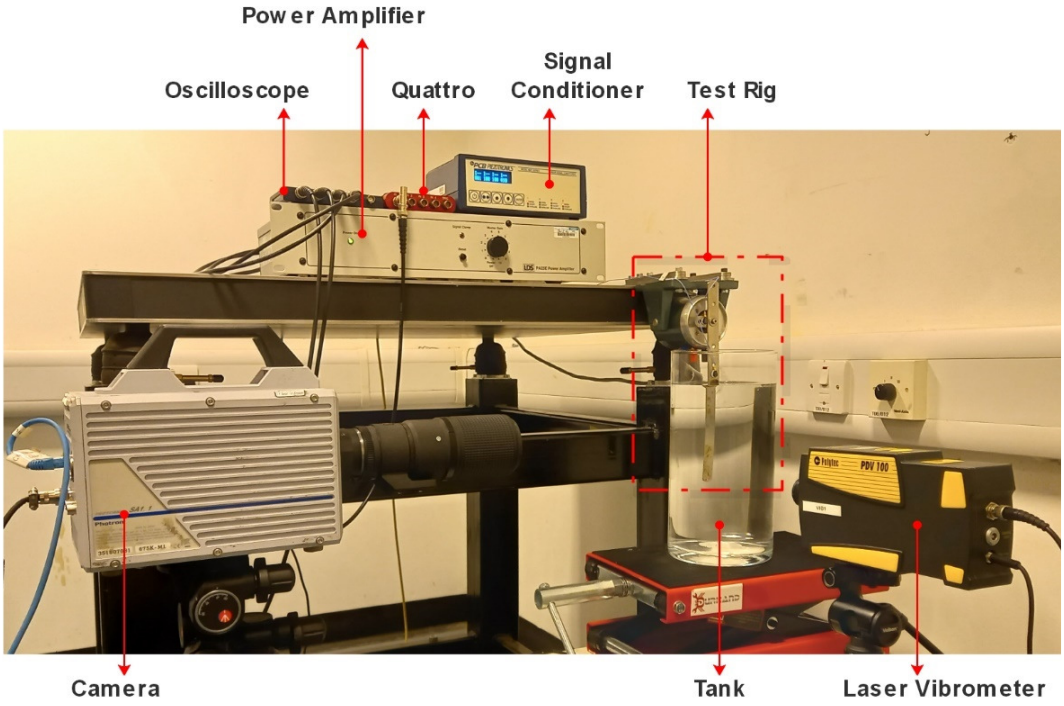

(a)

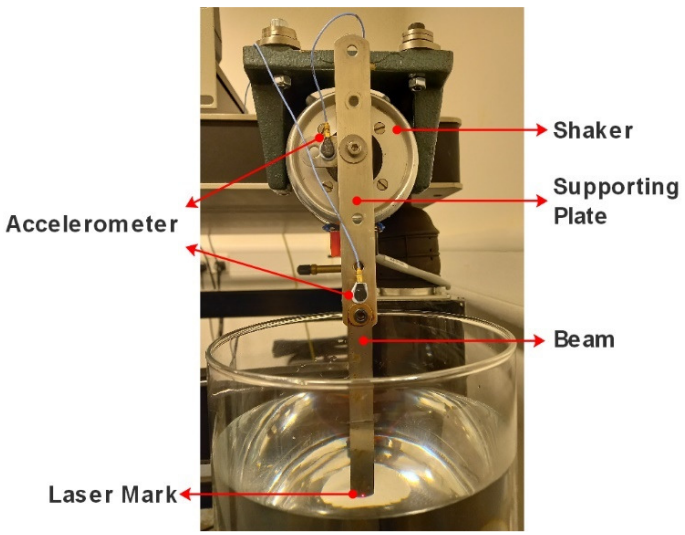

(b)

Figure 3.3. (a) Experimental apparatus and (b) the closer view of the test rig

The USB Oscilloscope and Quattro shown in Figure 3.3(a) are part of the SG/SA system in the schematic diagram. The SG/SA system consists of the software and hardware platform. The software provides control panels to setup parameters, generate input signals and display measurement results. The hardware is equipped with sets of input and output (source) channels, and a USB connectivity to the PC. For time series analyses, the USB Oscilloscope was utilised as the SG/SA device in the experiment to record the measurement data. This digital oscilloscope is capable of recording long time series signals, making it suitable for monitoring transient and steady state vibrations of beams. There are 4 channels available in this model to probe voltages from the power amplifier, laser vibrometer and 2 accelerometers. Moreover, the oscilloscope is featured with signal generator functions which can be used to create specific input signals for the shaker such as the step signal and the derivative of ramp functions signal.

The SignalCalc Ace software powered by the Quattro hardware platform was used to estimate frequency response functions (FRFs) of a system. The signal analyser estimates the transfer function of a system by measuring the amplitude and phase delay between two signals. For example, the FRF of the beam is obtained by connecting the accelerometer and laser vibrometer to the input ports of Quattro. Note that the accelerometer signal is amplified by a signal amplifier before connected to the signal analyser. Therefore, the measurement results are in the form of the amplitude ratio of the laser vibrometer to the accelerometer across a range of frequencies. Depending on the applications, the typical input signals for obtaining the FRF in this study are random and stepped-sine input signals. The random signals are based on the white noise in which the signal amplitudes and frequencies vary between the prescribed values. Accordingly, the random signals have a nonuniform power spectrum across a range of frequencies. On the contrary, the stepped-sine signals generate constant amplitudes across allowable frequencies, providing consistent power spectra. The basic principle of this test is the same as that in Section 2.2.4 for obtaining the frequency series from numerical simulation. In this test, the signal analyser generates a sine wave at one particular frequency and evaluates the transfer function of the two signals. Then, the data is stored, and the signal analyser produces another sine wave based on the prescribed frequency resolution. This process repeats until it reaches the final frequency value. Due to time-consuming, this signal was implemented only for systems that have poor signal-to-noise ratio (SNR).

3.3.2. Test rig examination

Each individual component of the test rig is examined with Quattro to obtain their characteristics over frequencies. This is to identify phenomena that may affect to the beam responses. Figure 3.4(a) shows the FRF of the power amplifier for different gain levels. The FRF magnitude has the unit "V/V" which represents the ratio of the output voltage of the amplifier relative to the signal generator. It is observed that the FRF magnitude converges to a constant value after 10 Hz. This means that the amplifier may not be able to provide a constant amplification for the shaker, particularly for the stepped-sine signals, in frequency up to 10 *Hz*. Moreover, by setting the gain amplifier to 3, the output voltage of the amplifier is about 4 times of that of the input signal. Therefore, the gain indicator does not facilitate a linear magnification for the amplifier.

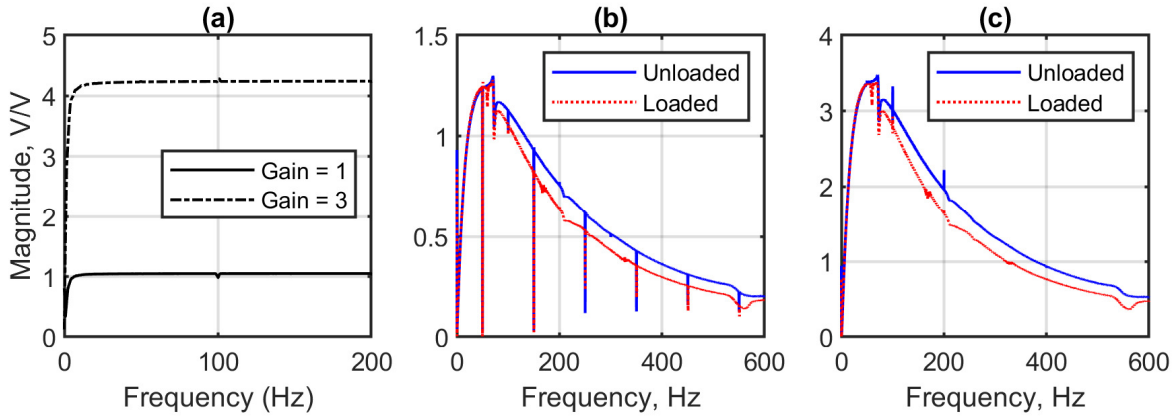

Figure 3.4. Transfer function of (a) the amplifier, (b) the shaker relative to the power amplifier, and (c) the shaker relative to the signal generator

Figure 3.4(b) shows the transfer function of the output voltage of the laser vibrometer to the output voltage of the amplifier. It is observed from the figure that the peak is obtained around 70 *Hz*. When the shaker is loaded with a static mass, indicated with the red dotted line, the FRF magnitude slightly decreases, and the peak remains consistent in the same frequency location. To examine the dependency of the peak to other factors, Figure 3.4(c) displays the FRF of the output voltage of the laser vibrometer relative to the output voltage of the signal generator or Quattro. From the figure, the peak is in the same location as in Figure 3.5(b), indicating that the peak is only mass dependent. Based on the structure of electrodynamic shakers, the moving part of the shaker is attached to a spring mechanism to maintain the position and perform the translation motion. The spring induces a natural frequency in a low frequency range, while the resonant frequency of the moving part exists in a high frequency range [107]. Therefore, it is believed that the peak

in Figure 3.4(b) and (c) corresponds to the natural frequency of the flexible support of the shaker.

Note that aliasing in the FRF signals occurs in Figure 3.4(b). The DC output voltages of the power amplifier interfere with the electrical frequency (AC voltage) of the power amplifier, creating a sudden drop to zero at frequency 50 *Hz*. This magnitude is aliased every 100 *Hz* across frequencies – 150 *Hz*, 250 *Hz*, 350 *Hz*, 450 *Hz* and 550 *Hz*. This argument agrees with the results in Figure 3.4(c) where the aliasing phenomena disappear when the input signal for the signal analyser is replaced with the output signal of Quattro.

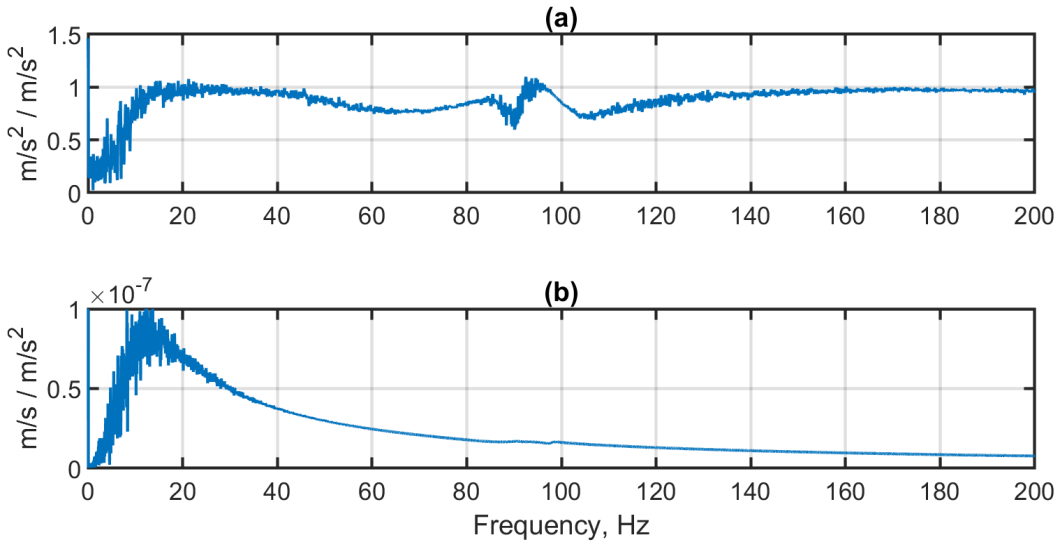

Figure 3.5. Transfer function of (a) the accelerometer 2 to the accelerometer 1, and (b) the accelerometer 2 to the laser vibrometer

To test the sensors, two accelerometers were mounted at one particular location and the laser vibrometer was also pointed to the same location. Figure 3.5(a) shows the transfer function of the two accelerometers. Note that the cut-off frequencies for those accelerometers based on the specification are 1 *Hz*. Therefore, it is expected that the two sensors converge starting from 1 *Hz*. However, it is seen that both accelerometers converge at 1 after it passes 15 *Hz*, meaning that that the two accelerometers have different voltage readings in the range of 1 *Hz* to 15 *Hz*. The same phenomenon is found in Figure 3.5(b) that shows the FRF of the laser vibrometer relative to the one of accelerometers. The cut-off frequency of the laser vibrometer is 0.5 *Hz*. Theoretically, the FRF of the laser and accelerometer starts to decline around 1 *Hz*. In fact, the measurement result shows that the FRF magnitude declines after 15 *Hz*. These phenomena may also be influenced by the characteristics of the shaker and power amplifier. In Figure 3.4, the

shaker produces small displacements in the range up to 15 *Hz*, resulting in poor signal-to-noise ratios for the accelerometers. Since the power of the signal is lower than that of the noise, this can mislead the amplitude of the FFT for estimating the transfer function of the system.

To obtain the characteristics of the extension plate vibrating in air, the plate was mounted on the shaker at one tip and free at the other tip. Figure 3.6 displays the FRF of the extension plate generated with a random signal with the frequency span of 800 *Hz*. The magnitude of the FRF defines the ratio of the tip acceleration relative to the base acceleration of the shaker. It is seen that the first peak is around 80 *Hz*. The discontinuity or the notch around 100 *Hz* may not be related to the responses of the supporting plate. It is believed that the discontinuity is caused by the measuring instruments. The notch around 100 *Hz* appears evidently when using accelerometers as shown, for example, in Figure 3.5(a). The notch becomes vague when using laser vibrometer; see small notches around 100 *Hz* in Figure 3.4(b), (c) and Figure 3.5(b). Moreover, the small notches around 100 *Hz* in the FRF also occurred in the power amplifier of the shaker measurement displayed in Figure 3.4(a). Therefore, the glitch may be from the filtering process of the signal analyser to prevent aliasing from the electrical AC frequency of 50 *Hz*.

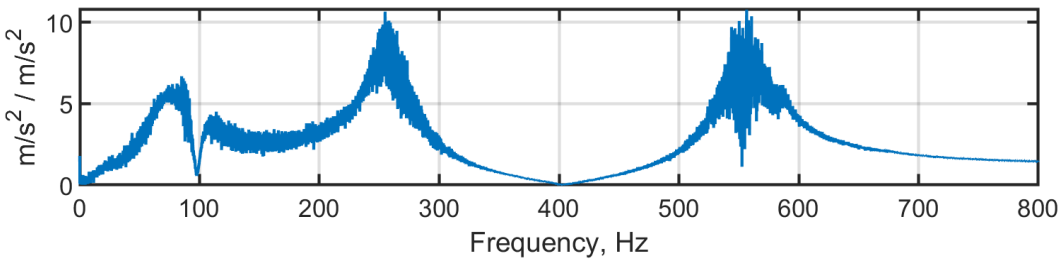

Figure 3.6. The FRF of the supporting plate vibrating in air

Depending on the beams, some parts of the supporting plate can also immerse in liquid. Therefore, it is paramount to examine the supporting plate under different dipping depths. An additional static mass is mounted on the free tip of the plate to replicate a load and induce more contact (interference) with the liquid. The experimental method for testing the plate is displayed in Figure 3.7. The dipping depths were varied indicated with the strip levels marked with d_1, d_2 and d_3. The laser vibrometer was pointed to the end of the supporting plate, indicated with the red point, and the measured FRFs are shown in Figure 3.8. It is observed that the first peak displaced to around 20 *Hz* due to the additional

static mass. There are minor differences in the FRF due to the variation of dipping depths, indicating that the supporting plate is rigid enough to remain unaffected by the liquid.

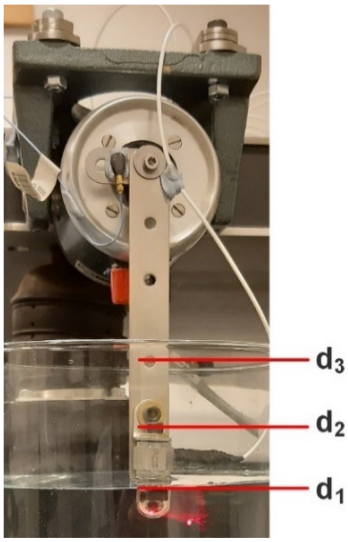

Figure 3.7. Dipping depth variation for the extension plate

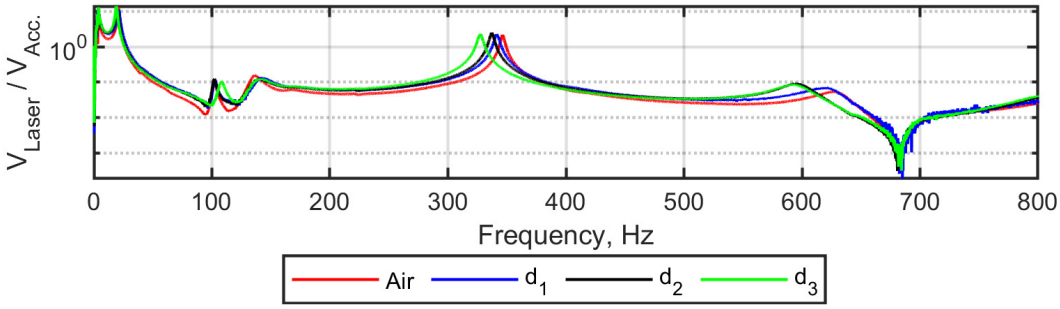

Figure 3.8. FRF of the extension plate for various dipping depth

3.3.3. Nonlinear identification parameters

Identification parameters such as natural frequency and damping values containing nonlinearities are paramount for numerical simulation. Inaccurate procedures for estimating these parameters can lead to erroneous prediction of dynamic responses of a structure. Therefore, the most common method for estimating modal parameters such as the quadrature peak picking method [106] also known as the half-power point method [107], which has been widely implemented in the case of a vibrating beam interacting with liquid in references [27, 108-111], is no longer appropriate for strong nonlinearities. Nevertheless, there are many techniques currently available to extract backbone and damping curves from vibration data. This study considers nonlinear identification parameters based on the time series of transient vibration responses developed by

Londoño [130]. This method is appropriate for this investigation since the beam particularly for the case of vibrating in air can take very long time to reach the steady state.

The backbone curve describes the characteristics of the instantaneous amplitude with respect to instantaneous frequency. The instantaneous frequency, denoted as $f(t_{fi})$, can be assessed from transient vibration data using equation [130],

$$f(t_{fi}) = \frac{1}{(t_{fi+1} - t_{fi-1})} \tag{3.3}$$

where t_{fi} is the time series when the amplitudes cross the zero with $i = [1, 2, 3, \dots]$. The zero-crossing points are demonstrated with blue circle markers in Figure 3.9. The instantaneous amplitude, $A(t_{Ai})$, indicated with red cross markers in Figure 3.9 are estimated by obtaining the local minima and maxima of the decay responses. Since the size of the vector frequency is equal to that of the vector amplitude, the backbone curve is constructed by pairing those vectors.

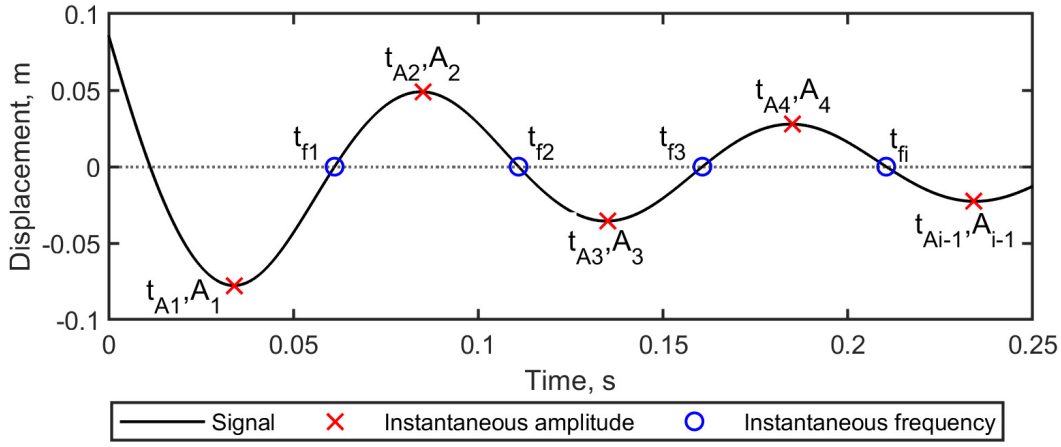

Figure 3.9. Tracking peaks and zero-crossing points of a free vibration response

The damping curve describes the change of the damping ratio with respect to the vibration amplitudes. A linear damping curve is calculated by presuming that the amplitude envelope, $A(t_{Ai})$, can be expressed,

$$A(t_{Ai}) = A_0 e^{-\zeta(t) 2\pi f(t_{fi}) t} \tag{3.4}$$

where A_0 and $\zeta(t)$ define the initial amplitude and the damping ratio, respectively; whereas $f(t_{fi})$ is the instantaneous frequency. The coefficient of the damping ratio, $\zeta(t)$,

can be determined using a linear regression method. For the nonlinear damping, the terms $-\zeta(t)2\pi f(t_{fi})t$ can be replaced with a quadratic or a cubic function depending on the requirement. For the quadratic function, Equation (3.4) can be written as

$$A(t) = A_0 e^{-(k_1 t^3 + k_2 t^2 + k_3 t)} \tag{3.5}$$

where the constants k_1, k_2, and k_3 can be solved, according to reference [131], using the least-square method to give

$$\begin{Bmatrix} \ln|A(t_0)| \\ \ln|A(t_0)| \\ \vdots \\ \ln|A(t_{N-1})| \end{Bmatrix} = \begin{bmatrix} t_0^3 & t_0^2 & t_0 & 1 \\ t_1^3 & t_1^2 & t_1 & 1 \\ \vdots & \vdots & \vdots & \vdots \\ t_{N-1}^3 & t_{N-1}^2 & t_{N-1} & 1 \end{bmatrix} \begin{Bmatrix} k_1 \\ k_2 \\ k_3 \\ \ln|A_0| \end{Bmatrix} \tag{3.6}$$

Note that the terms $\zeta(t)2\pi f(t_{fi})t$ in Eq. (3.4) equal to $k_1 t^3 + k_2 t^2 + k_3 t$ in Eq. (3.6). Therefore, the time series of the damping ratio can be computed by

$$\zeta(t) = \frac{k_1 t^2 + k_2 t + k_3}{2\pi f(t_{fi})} \tag{3.7}$$

Since the beam is theoretically a continuous system with an infinite number of natural frequencies, decaying responses of the beam can include multiple frequencies depending on the initial conditions. This can lead to inaccurate estimation for the instantaneous amplitudes. To alleviate this, the beam must be actuated with a sinusoidal wave at a particular natural frequency until it reaches the steady state condition. This is to isolate the beam vibrating only in one resonant. Once the beam achieves the steady state, the input signal is abruptly stopped, allowing the beam responses to decay with a single frequency. This procedures is often called as the resonance decay method (RDM) [130]. Moreover, in the real measurement, the measured signal can contain some weak frequencies from the sensor, sampling rate and other boundaries. Accordingly, the decaying signal requires a band-pass filter to eliminate unwanted frequencies, leaving only a single frequency in the frequency series.

Also, in the real measurement, it is unlikely to obtain exact zero crossing points with instantaneous amplitudes equal to zero, $A = 0$. Due to the limitation of the sampling rate, the variable t_{fi} is estimated from measurement data with an amplitude approaching to zero, $A \approx 0$. This can lead to a noise in the estimated instantaneous frequency.

Therefore, a linear interpolation method is implemented after applying the band-pass filter to get the exact zero crossing point.

3.3.4. Vibration patterns from image sequences

It is possible to obtain a vibration pattern of a beam vibrating in a medium from camera data. The process begins with selecting the region of interest from an image sequence. Figure 3.10(a) displays a monochrome image of a cantilever beam submerged in water. The size and location of the region of interest in the pixel coordinates must be consistent for all images. Figure 3.10(b) shows the region of interest of the beam. Note that the size of the region has been chosen such a way by considering the maximum displacement of the beam to ensure that the movement of the beam over period of time is within the small region. The cropped monochrome image needs to be converted to a binary image by utilising the "edge" function with the Canny method available in MATLAB [132]. Due to different colour saturation between the beam and the background, this function transforms the edge of the beam with the value 1 and converts the rests with the value 0. Some parts of the converted binary image are displayed in Figure 3.10(b). Note that the black and white pixels represent the value 0 and 1, respectively. The size of the region of interest for this instance is 945-by-80 pixel grids.

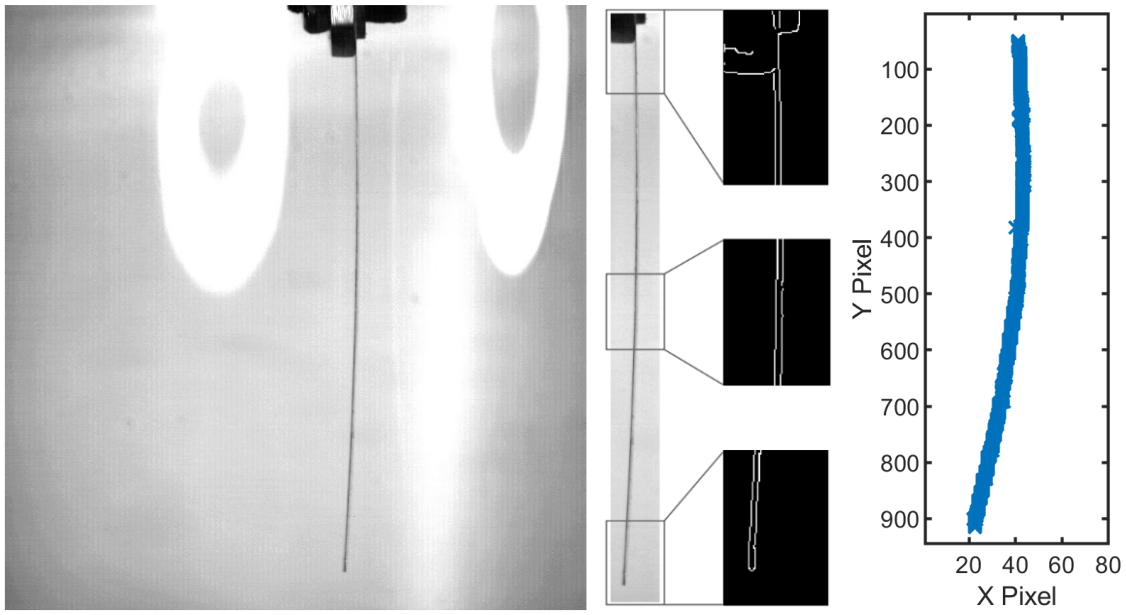

(a) **(b)** **(c)**

Figure 3.10. (a) A monochrome image of a fully submerged beam from the high-speed camera; (b) Converting a monochrome image to a binary image; and (c) Location of the white pixels in the pixel coordinates

From the binary image, the location of the white pixels in the pixel grids can be acquired. It is seen from Figure 3.10(b) that there are two white pixels in each row of the pixel grids due to the edge detection algorithm. For example, two white pixels are found in the coordinate of (40, 70) and (44, 70). To create a vector, the X-pixels must only contain one value. This can be achieved by calculating the mean value of the X-pixels. By averaging the X-pixels for each Y-pixel, this pair of pixel coordinates can be plotted as demonstrated in Figure 3.10(c). From the figure, the X- and Y-pixel represent the beam length, x, and beam displacement, w, respectively.

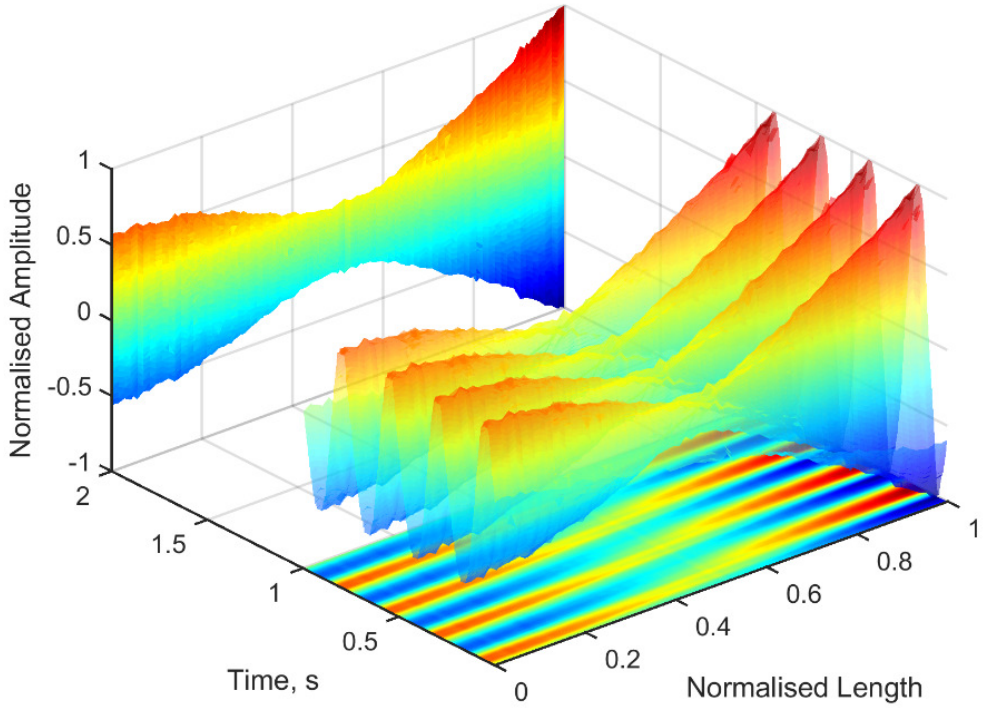

Figure 3.11. A 3D-surface plot representing the displacement with respect to t and x

The procedure for converting a monochrome beam image to a vector of pixel coordinates is implemented for all image sequences. Eventually, this results in a 3D vector of the same length describing the movement of the beam over time, t. Figure 3.11 depicts a collection of pixel coordinates over time acquired from all image sequences. Note that the beam length is normalised with respect to the beam tip. To obtain the displacement value in the metre unit, the beam displacement is normalised with respect to the maximum displacement of the beam tip. This would create a dimensionless value at the tip of the beam oscillating between -1 and 1. The displacement response in the metre unit is achieved by synchronising the dimensionless value with the time series of displacement estimated from the velocity response measured with the laser vibrometer. Moreover, only

two projections from the 3D plot are usable in this study such as the XZ- and XY-plane. The XZ-plane displays the beam envelope with respect to x, and the XY-plane represent the propagating wave or vibration pattern of the beam.

Figure 3.12(a) displays an image of a cantilever beam partly submerged in water. It is seen that refraction occur on the beam image due to different media. The transition area between the air and water creates black pixels in the binary image shown in Figure 3.12(b). By selecting the white pixels that are related to the beam, Figure 3.12(c) depicts the pixel coordinates acquired from the binary image. By post-processing the image sequence of the beam partly submerged in water, this would allow to find the centreline of the beam that vibrates in air and water, which can be used to align the vibration axis of the beam. The discontinuity in the pixel coordinate due to the transition area between the air and water is also removed to create a continuous beam.

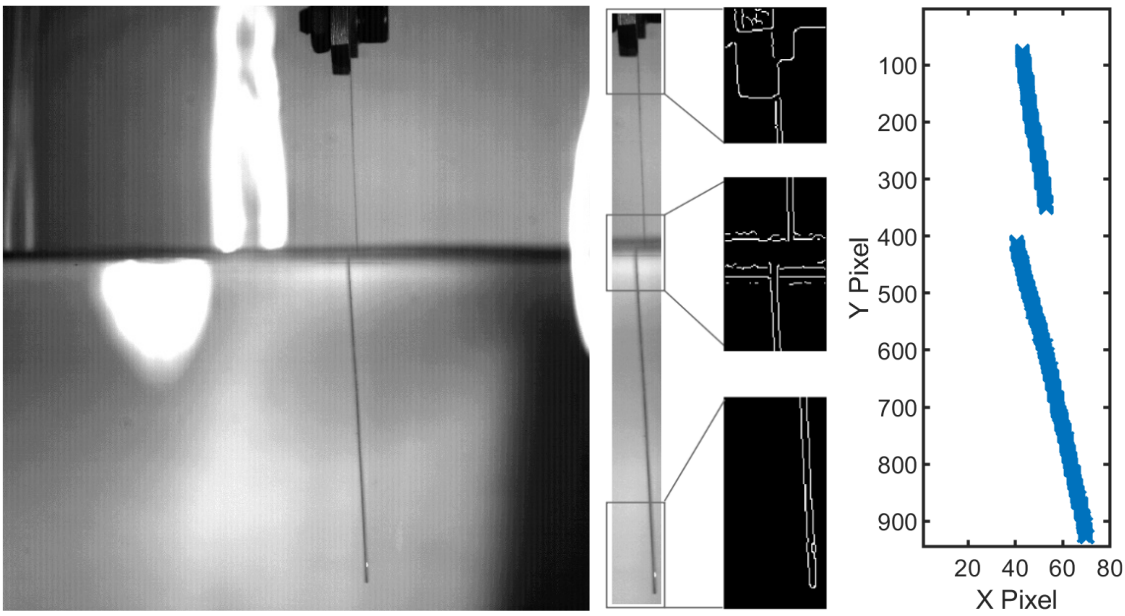

(a) **(b)** **(c)**

Figure 3.12. Procedures for converting an image of the partially submerge beam into data of pixel coordinates

It is worth mentioning that these procedures for converting beam image into pixel coordinates work well for relatively large displacements. However, small displacements can lead to noise in the converted data due to factors such as anti-aliasing filter of the camera, filtering in the "edge" algorithm and the pixel resolution. Consequently, the camera is only used for capturing displacement of the beam with particular amplitudes and frequencies up to 50 *Hz*.

3.4. Test 1: Beam with L = 8 cm

A metal beam with a dimension of 0.08 m, 0.01275 m and 8 x 10^{-5} m for the length, width and thickness, respectively, was used for analyses. The beam density is approximately 7200 kg/m^3 estimated by measuring the beam weight and dividing it with the volume.

3.4.1. Vibrating in air

The frequency response function (FRF) of the beam vibrating in air was obtained by assigning random input signals for the SG/SA to produce white noise signals. The maximum frequency for the random signal was limited to 78.125 Hz to generate a uniform power density for the first two resonant. The time span was set to 20.5 s, resulting in the frequency resolution of 0.049 Hz. The maximum random amplitude was varied arbitrarily to 80 mV, 200 mV and 300 mV. Figure 3.13(a) displays the FRF of the beam tip velocity relative to the base acceleration for various random amplitudes. Note that the dent occurred around 2 Hz is the cut-off frequency for the accelerometer.

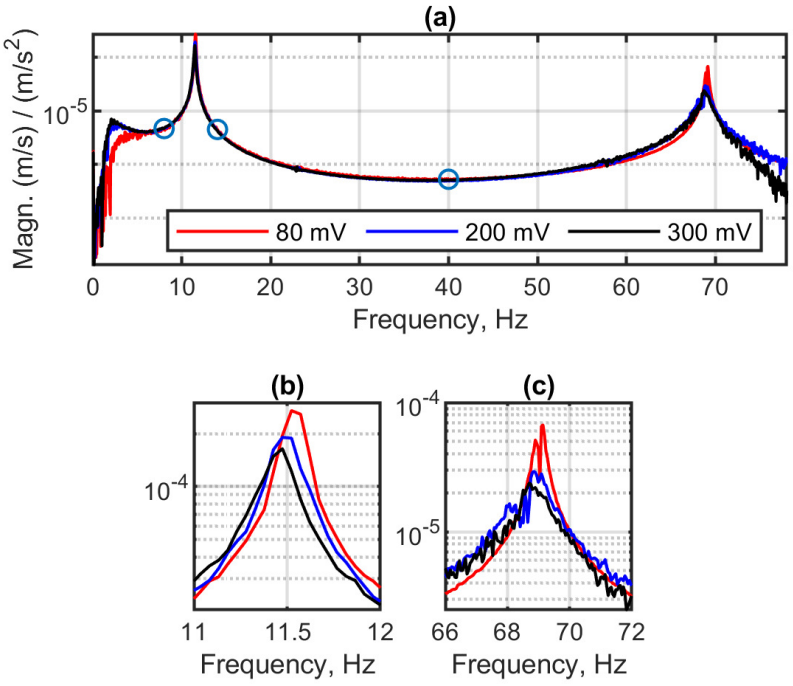

Figure 3.13. (a) FRF of the 8 cm beam vibrating in air. The blue circle markers are the location of the steady state responses; The closer view of (b) the first and (c) second resonant

Figure 3.13(b) shows the closer look of the first resonant. It is observed that the peaks decrease along with increasing forcing amplitudes. In the theory of linear damping described in Section 2.2.6, increasing the base input will proportionally increase the whole beam displacement which makes the peak of the FRF constant regardless the base input amplitude. Therefore, it is believed in this case that the air generates damping for the beam, creating nonlinear phenomena in the FRF. The same incident is also occurred in the second resonant shown in Figure 3.13(c). However, there is a discontinuity in the FRF indicated with a notch around the peak. This will be further investigated with the nonlinear identification parameters.

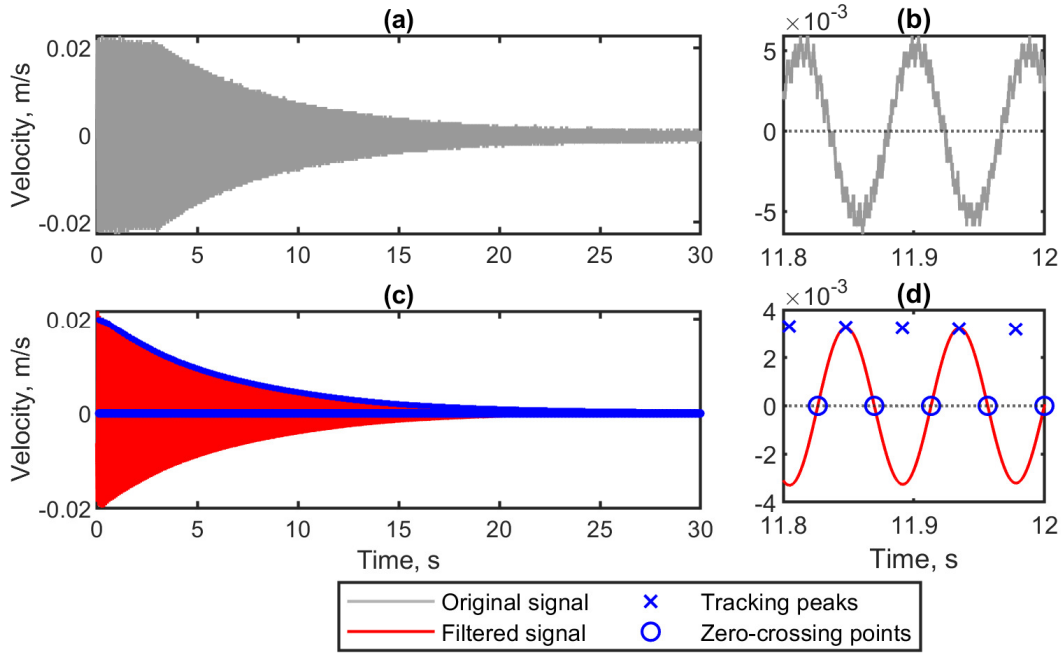

Figure 3.14. (a) Unfiltered signal acquired from experiment; (b) The zoomed section of the original signal; (c) Filtered signal; and (d) The closer view of the filtered signal

The FRF is paramount to determine the RDM for nonlinear identification parameters. To obtain the decay response for the first resonant, the beam was actuated with a sinusoidal wave with the frequency of 11.55 *Hz* and released after reaching the steady state. Figure 3.14(a) displays the RDM at the first resonant with the signal generator amplitude of 5 *mV*. Note that the measurement started after the beam had been running for 60 *s* to ensure the beam reaching the steady state. Figure 3.14(b) displays the zoomed section of the RDM at 11.8 *s* to 12 *s*. It is observed that the signal contains noise from measuring instruments which can make inaccurate estimation for the identification parameter method. Accordingly, a band pass filter was implemented in the frequency

series to isolate the frequency of interest. Figure 3.14(c) and (d) shows the filtered decay response superimposed with the instantaneous amplitudes and zero-crossing points. Note that the steady state part of the RDM signal was removed before applying the band-pass filter.

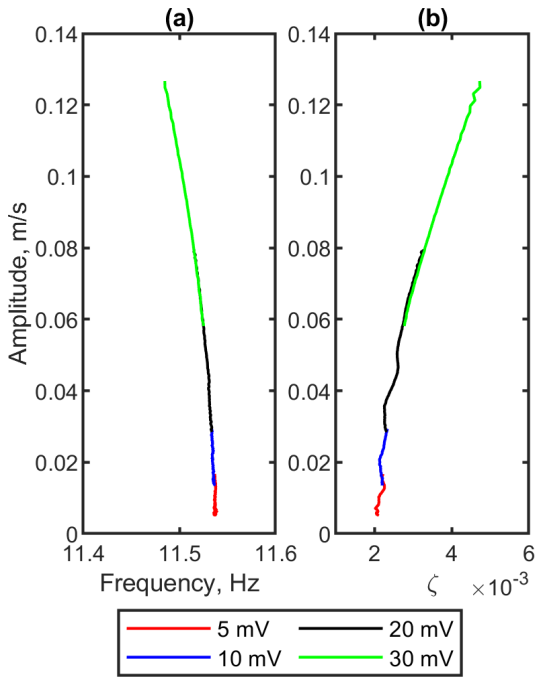

Figure 3.15. (a) Backbone and (b) damping curves of the first resonant

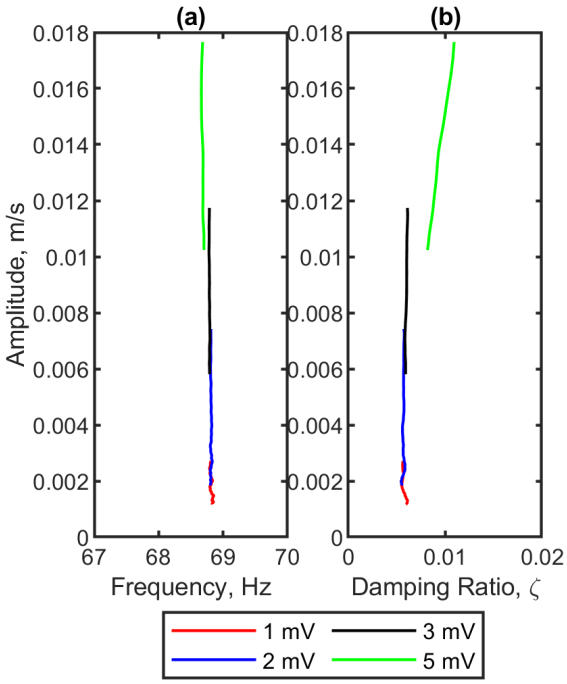

Figure 3.16. (a) Backbone and (b) damping curves of the second resonant

The amplitude of the sinusoidal signal was varied at 5 *mV*, 10 *mV*, 20 *mV* and 30 *mV* to obtain various resonance decay responses for the first natural frequency. This is intended to provide a continuous trendline in the backbone and damping curves. The same procedures for cutting the steady state part of the signal and applying band-pass filters were also implemented to post-process all RDM signals. Figure 3.15(a) and (b) display the backbone and damping curve of the first resonant, respectively. Note that the instantaneous amplitude and frequency were filtered with a moving average filter. It is observed from the backbone curve that there is a weak nonlinearity in the beam for moderately large deflections. This behaviour agrees with the theoretical modelling where nonlinearities due to stretching in the beam deflection can be neglected. Moreover, the damping ratio increases along with increasing velocity amplitudes. The gradient in the damping curve is consistent to the characteristics of the quadratic damping. Therefore, it is believed that beam interacting with air creating a nonlinear behaviour in the FRF.

Figure 3.16 displays the backbone and damping curves of the second resonant. The frequency of the sinusoidal wave for obtaining the RDM was 68.95 *Hz*. The amplitude of the sinusoidal signal was varied at 1 *mV*, 2 *mV*, 3 *mV* and 5 *mV*. The reason for choosing such very low amplitudes is due to the beam that experiences nonlinearities at high amplitudes. At low amplitudes with frequency around 69 *Hz*, the beam undergoes small displacements and damping due to air becomes negligible. Accordingly, the damping is predominantly by the material. This has been demonstrated in the damping curve shown in Figure 3.16 where the first three amplitudes are linear. At 5 *mV*, the damping curve suddenly changes the orientation, forming a positive gradient which creates discontinuities to the previous amplitude. To investigate this, the decay responses of the beam base and the beam tip at 5 *mV* are displayed in Figure 3.17. The Fast-Fourier transform (FFT) analysis of the base acceleration shown in Figure 3.17(b) reveals that the supporting plate also vibrates at the same frequency as the beam. This is an indication that the beam acts as a vibration absorber for the supporting plate. Ultimately, this phenomenon can be related to the notch occurred in the FRF of the second resonant shown in Figure 3.13(c).

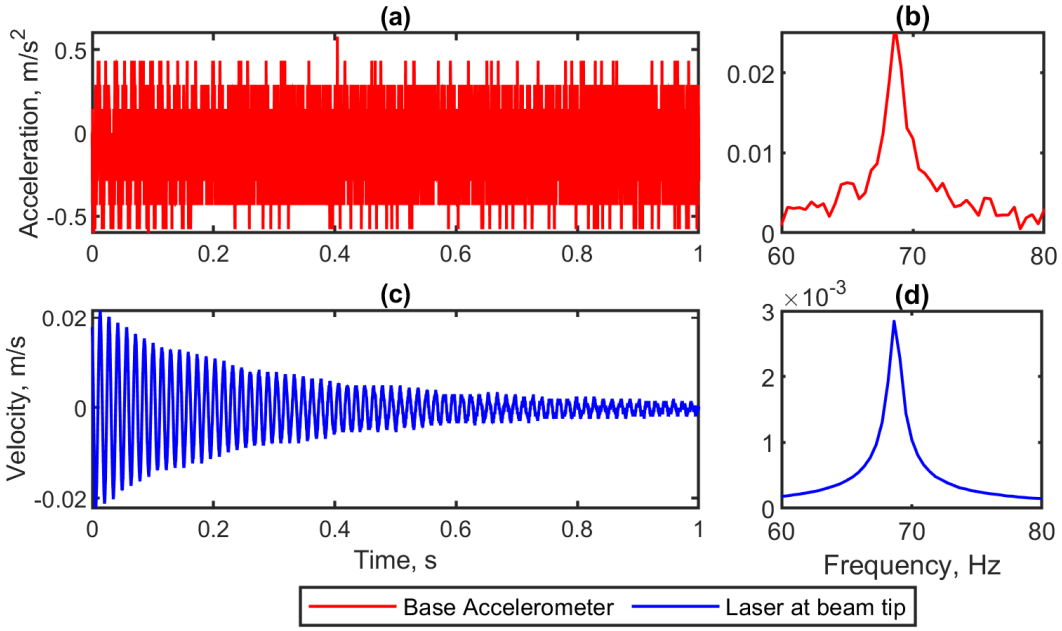

Figure 3.17. (a) Time response and (b) frequency series of the supporting plate; (c) Free vibration and (d) frequency series of the beam

To further investigate modal contribution factors, the beam was excited with a step input signal. At first, the laser vibrometer was pointed out to x = 8 *cm* and recorded the decaying response of the beam shown in Figure 3.18(a). Then, the beam was actuated

again with the laser directed to measure vibration at $x = 7$ *cm*. This process was repeated every 1 *cm* to capture vibration at $x = 6$ *cm* until $x = 0$ *cm*. Using the FFT analysis to transform the time series responses, Figure 3.18(b) presents the frequency responses of the beam at various location along the beam length. It is observed form the figure that the envelopes of the first and second peak, indicated with the red dotted and dashed lines, follow the first and second mode shape of the cantilever beam, respectively. The peaks visible at 150 *Hz* are due to aliasing errors. The third resonant is observed at 195 *Hz* and has very less contribution to the decaying responses, indicated with low peak amplitudes in the frequency series. Some aliasing errors also appeared at 200 *Hz*. Furthermore, the peak distribution follows a consecutive order with the first peak being the highest followed by the second and the third peaks.

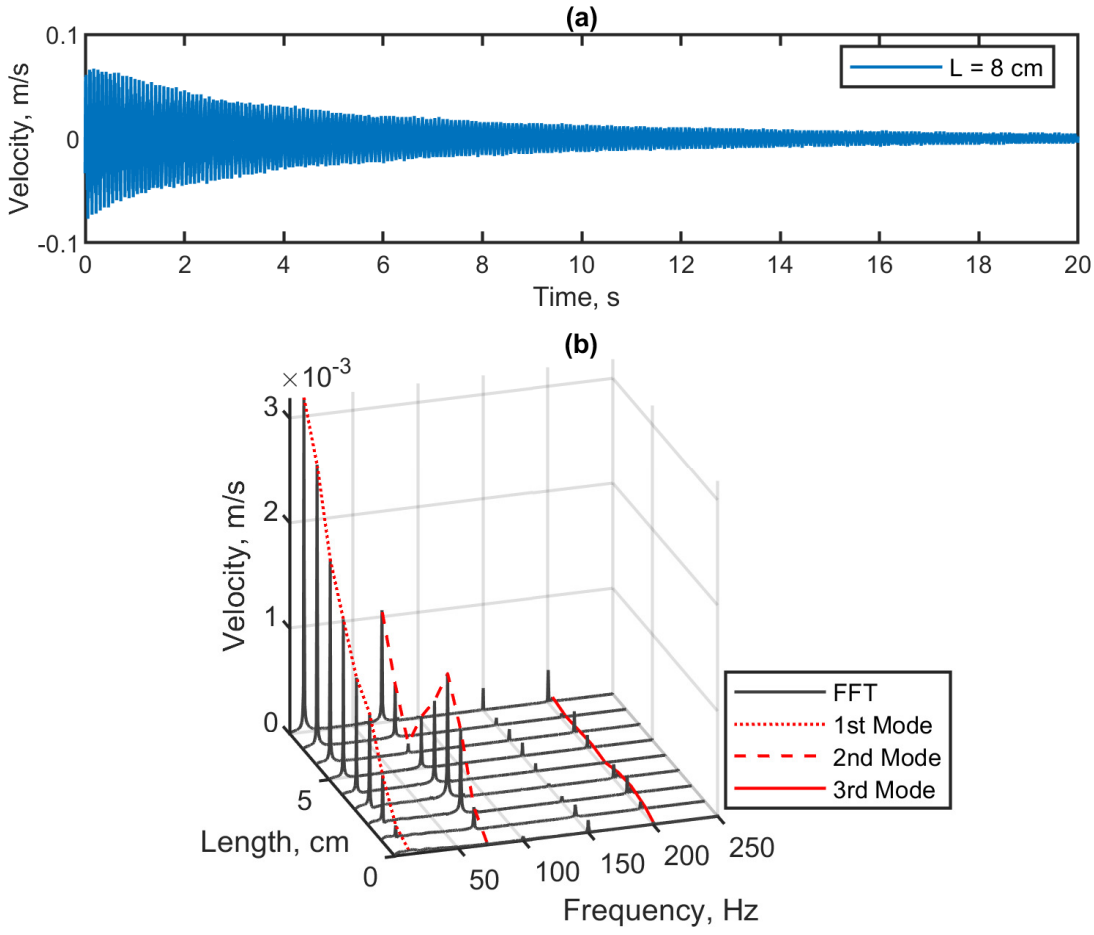

Figure 3.18. (a) Free vibration of the beam vibrating in air; and (b) Frequency series taken every 1 *cm* along the beam length

The steady state responses of the beam vibrating in air for various frequencies are presented in Figure 3.19. Note that the first row represents the vibration pattern of the

beam, and the second row depicts the beam envelope in which the beam envelope was normalised with respect to the maximum amplitude of the base motion. The graphical representation of the beam responses shown in Figure 3.19 demonstrates characteristics of vibration for low damping values, approximately less than 0.8%, as suggested by the damping curve in Figure 3.15(b) and Figure 3.16(b). At f = 8 *Hz*, the beam is mainly influenced by the first resonant. By assuming the term $rp_i \approx 0$ due to $\zeta_i = 0.008$, this results in the beam equation of the form $w_t(x) = \left(A_f + lp_1\varphi_1\right)\sin\omega t$. Accordingly, the beam envelope can be represented with the terms $A_f + lp_1\varphi_1$. Note that, due to the absence of the cosine function in the beam equation, the phase shift between the base input and the beam tip displacement becomes zero. At f = 14 *Hz*, the beam is in the region of the first two resonant. However, the contribution of the second mode shape in the beam equation is still negligible. Since the forcing frequency exceeds the first natural frequency, $\omega_{n1} < \omega$, the variable lp_1 becomes negative due to $(\omega_{n1}^2 - \omega^2)$. Therefore, neglecting the cosine function, the beam equation for this frequency can be expressed with $w_t(x) = \left(A_f - lp_1\varphi_1\right)\sin\omega t$. Moreover, lack of damping not only creates a zero-phase delay between the two tips, but also reduces the amplitude at the node in the beam envelope to zero.

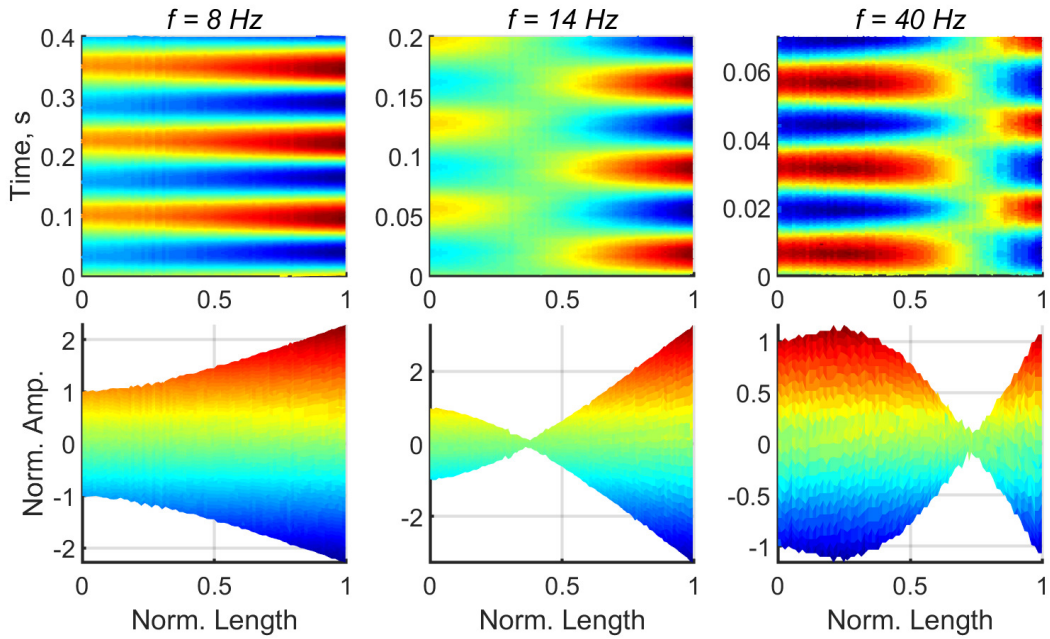

Figure 3.19. Steady state responses of the beam vibrating in air

At f = 40 *Hz*, the second resonant becomes dominant. The beam equation satisfies $w_t(x) = \left(A_f - lp_1\varphi_1 + lp_2\varphi_2\right)\sin\omega t$. Therefore, the node location along the beam

length shifts to the free end of the beam. This is due to the nature of the second mode shape where the zero-crossing point of the beam is located at $0.8L$ demonstrated in Figure 2.2. Moreover, in view of mechanical waves, the beam vibrating in air generates almost pure standing waves due to zero value in the function $V(\beta x)$ expressed in Eq. (3.1). Described in Section 3.2, this can result in the same amplitude of the terms $(\omega t + \beta x)$ and $(\omega t - \beta x)$

3.4.2. Partially submerged in water

A partially submerged beam in a liquid has been of interest by many researchers. This configuration is frequently used in sensors to measure fluid properties such as viscosity and density [55, 57]. Recent development shows that this configuration can also be used as an energy harvester from underwater vibrations [76]. There have been many studies investigating partially submerged beam models both numerically and experimentally to obtain the influence of fluid properties [52, 57, 112] and the dipping depth of the beam [114, 133, 134] on the modal properties. This investigation will expand the study by demonstrating the changes in the FRF due to the dipping depth of the beam.

To obtain the FRF, the amplitude of the random signal was set constant to 100 *mV*. The frequency span of the signal analyser was limited to 250 *Hz*. The dipping depth was increased every 2 *cm*, from 1 *cm* to 7 *cm*. Figure 3.20 displays the FRF of the partly submerged beam for various dipping depth. Note that the FRF magnitude in Figure 3.20 describes the ratio of the base acceleration to the tip acceleration. Since the beam tip was measured by the laser vibrometer which generates velocity responses, the signal analyser automatically derives the signal to obtain acceleration responses. It is seen from the figure that the first resonant of the dipping depth 1 *cm* shifts significantly to 4.6 *Hz*. This value is about 39% of the natural frequency value of the beam vibrating in air. The significant drop in the first resonant, however, is not followed by the second resonant. Dipping the beam 1 *cm* into water only reduces the second natural frequency about 20% from vibration in air. The first resonant becomes independent of the dipping depth function after the beam is immersed 3 *cm*. Once the dipping depth is increased to 7 *cm*, the first and second resonant eventually lead to almost the same percent reduction, about 74% of natural frequencies for vibrating in air. Moreover, it is interesting to see how the third

resonant of the dipping depth 7 *cm*, the green line, appears at the same frequency as the second resonant of the dipping depth 1 *cm*, the red line.

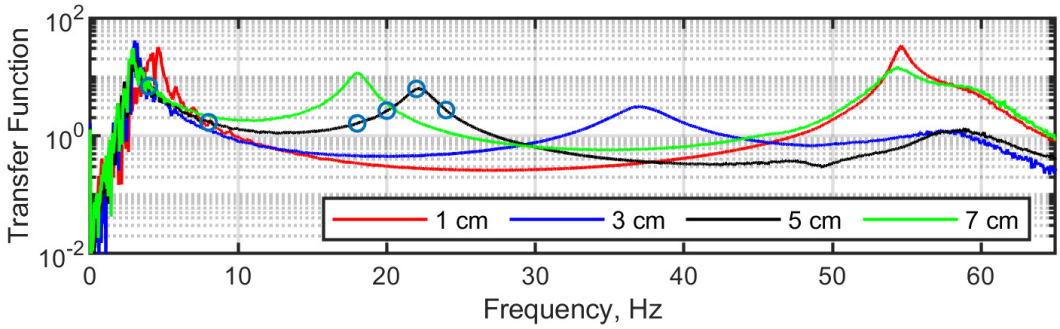

Figure 3.20. FRF of the partially submerged beam for various dipping depth

The transient and steady state responses of the partially submerged beam with particular attention to the tip displacement have been investigated by some researchers [120, 135]. However, characteristics of mechanical waves in partially immersed beam have not been covered in literatures. Therefore, this study will extend the analysis experimentally by investigating the vibration patterns of the beam with the dipping depth of 5 *cm*. Figure 3.21 presents the vibration pattern of the partially submerged beam for some frequencies around the first two resonant. Although the theoretical modelling in Section 2.2 is for fully submerged beam models, some phenomena are still relevant to be correlated with the beam equation. At f = 4 *Hz* for example, the node is in the transition of air and water. It is also seen that the phase shift between the two tips is not exactly 180 degrees. This is due to the influence of damping creating phase delay between the tips. At f = 8 *Hz*, the node displaces to the free end of the beam and the phase shift between the tips becomes almost 180 degrees due to lack of damping contribution in the modal coordinate of the beam equation, described thoroughly in Section 2.2.6. At f = 18 *Hz* and 20 *Hz*, the beam demonstrates travelling waves indicated by a phase delay from the base input to the node. At the resonant, the phase delay increases at some parts of the beam that vibrates in air. It is believed that the fluid absorbs the incoming wave from the base input, creating travelling waves in the dry part of the beam. Furthermore, the notable different colour intensity in the vibration pattern between the dry and the wet parts of the beam at f = 22 *Hz* and 24 *Hz* is due the tip displacement ratio where small input displacements can result in large tip displacements. Furthermore, refraction of light in air and water may also enhance these phenomena.

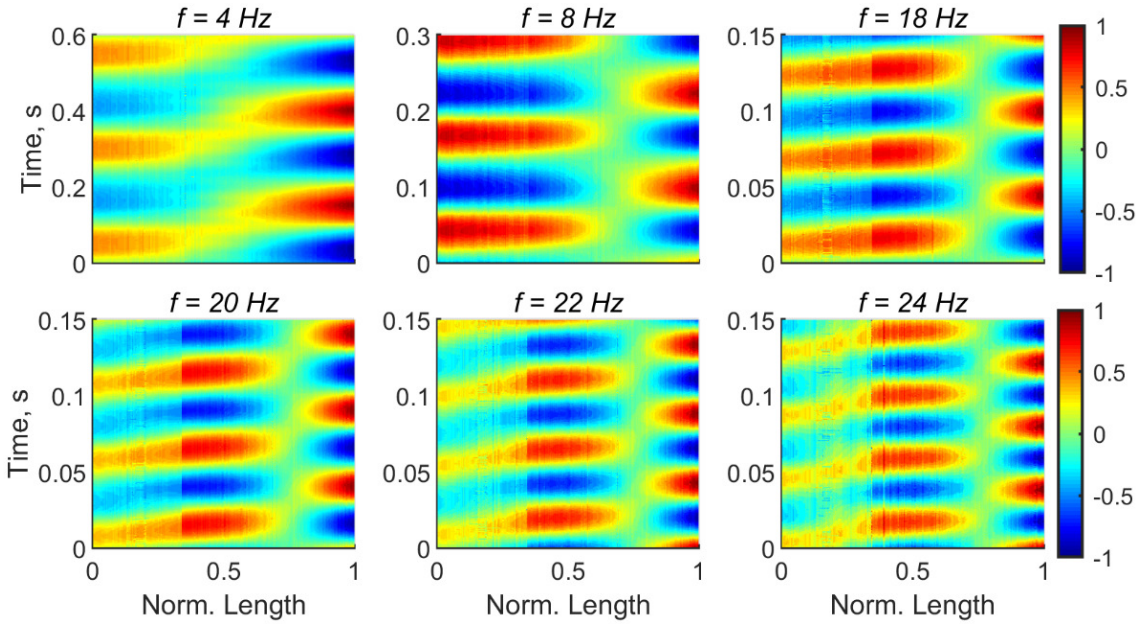

Figure 3.21. Vibration patterns of the partially submerged beam in water

Travelling wave phenomena of the partially submerged beam in water are similar to those of an elastic structure vibrating in vacuum with a spring and a damper attached at a certain location along its length, developed in references [21, 41]. Therefore, the transition of water and air media may induce a spring and damping effect on the beam, preventing reflection waves to occur which can lead to standing waves. Eventually, this demonstration can be used to develop theoretical model to predict the dynamic behaviours of the partially submerged beam.

3.4.3. Fully submerged beam in water

Figure 3.22 presents the FRF of the beam fully submerged in water for various input amplitudes. Note that the FRF magnitude is the ratio of the tip velocity to the base input acceleration. As expected, the FRF magnitude decreases along with increasing the input amplitude. Therefore, the phenomena in the first peak, where the amplitude 80 *mV* generates lower FRF magnitude than 200 *mV* and 300 *mV*, are due to the experimental apparatus such as the sensor, shaker and power amplifier rather than the dynamics of the beam. With low vibration amplitudes and frequencies, the sensors may acquire poor signal-to-noise ratio (SNR). This can result in an inaccurate estimation of the FRF magnitude. Nevertheless, the peaks are in the correct frequency location. For instance, the peak with the amplitude 80 *mV* is obtained at 2.93 *Hz*. By increasing the amplitude to

200 *mV*, this would significantly increase the damping value, shifting the peak location to 2.74 *Hz*.

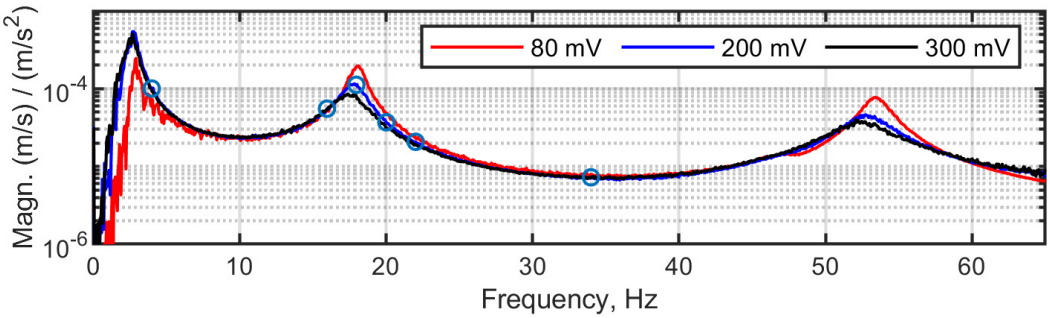

Figure 3.22. FRF of the beam vibrating underwater

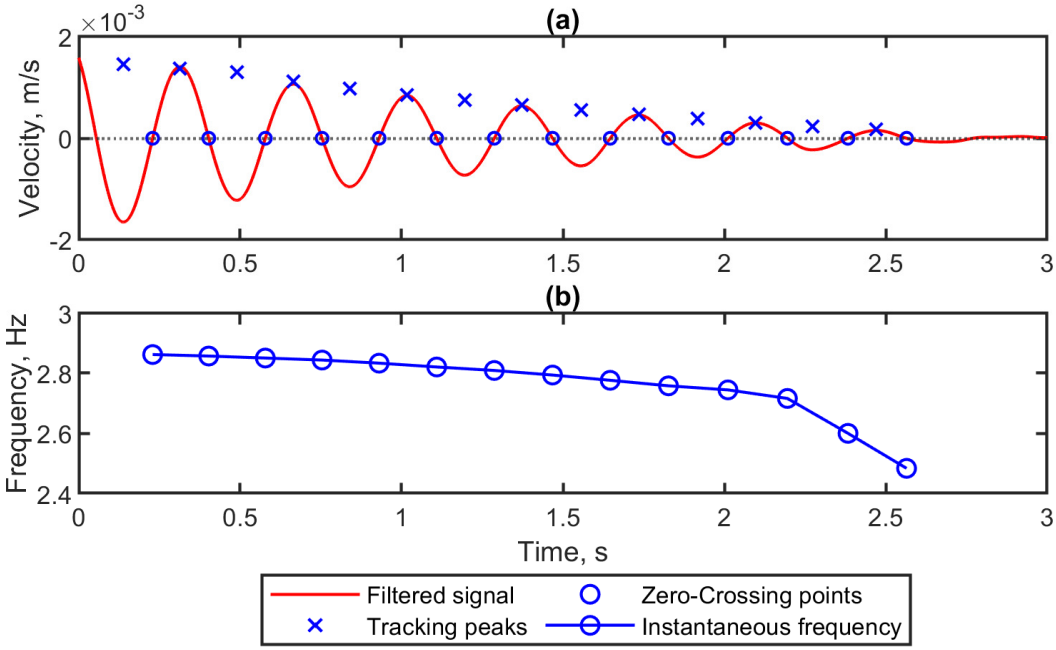

Figure 3.23. (a) Decaying response of the beam underwater, and (b) the instantaneous frequency extracted from the decay response

To obtain the backbone and damping curves, the RDM was conducted by considering the natural frequencies obtained from the FRF. Figure 3.23(a) displays the time series of the filtered decay response for the first resonant generated with the amplitude and frequency of 5 *mV* and 2.75 *Hz*, respectively. The peaks and zero-crossing points are superimposed in the decay responses, indicated with the blue cross and circle markers. Using Eq. (3.3), the instantaneous frequency in time series is presented in Figure 3.23(b). It is observed that frequency value decreases with increasing time. The sudden drop in the frequency value after 2.25 *s* is due to the band-pass filter that reduces the period of the wave. The procedures were repeated for obtaining the decay responses with the

amplitude of the sinusoidal wave gradually increased to 10 *mV*, 20 *mV*, and 30 *mV*. Then, the estimated backbone and damping curves for the first resonant is displayed in Figure 3.24. It is noticed that, due to limitation of the measuring instruments, it is difficult to recover the signal from low amplitudes and frequencies. Therefore, the damping curve phenomena generated with the RDM amplitude of 5 *mV* and 10 *mV* are due to poor SNR and are not associated with the beam responses. Moreover, the damping curve of the first resonant shown in Figure 3.24(b) exhibits a constant value from the amplitude of 3.5E-3 *m*/*s* to 7E-3 *m*/*s*. This, however, requires a further investigation with another nonlinear identification technique based on the steady-state response since the decay responses generated with the amplitude and frequency up to 10E-3 *m*/*s* and 3 *Hz*, respectively, are very limited.

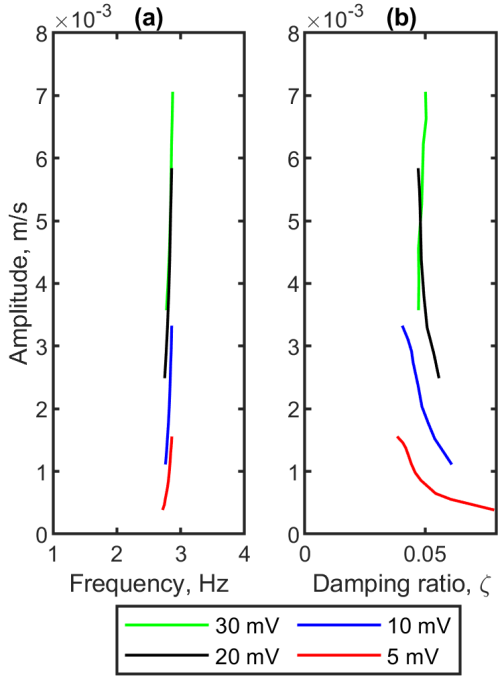

Figure 3.24. (a) Backbone and (b) damping curves of the first resonant

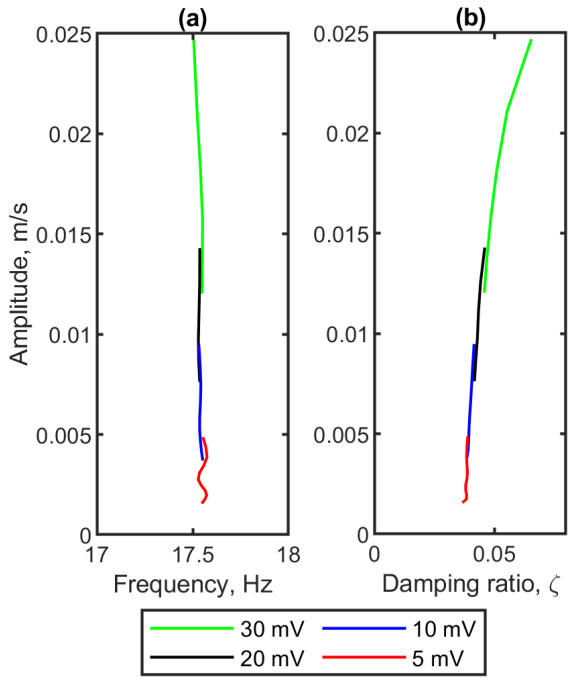

Figure 3.25. (a) Backbone and (b) damping curves of the second resonant

For the second resonant, the RDM frequency was set to 17.55 *Hz* determined from the FRF. The RDM amplitude was varied with the value similar to that of the first resonant. It is noticed that this frequency generates an ideal free vibration signal for the nonlinear identification method. Figure 3.25 presents the backbone and damping curve of the second resonant. Note that the fluctuation in the backbone curve at 5 *mV* is due to noise in the instantaneous frequencies. In general, the backbone curve shown in Figure 3.25(a) demonstrates the characteristic of linear natural frequencies. As expected, the

damping curve exhibits a positive gradient line, indicating that the system is under influenced of quadratic damping [130]. However, the gradient is very large or the change in the damping ratio is very small, meaning that the nonlinearity induced by the quadratic damping is small. Using the 1st order polynomial curving fitting method available in MATLAB, the intercept, $A = 0$, is found at the damping ratio, $\zeta = 0.037$.

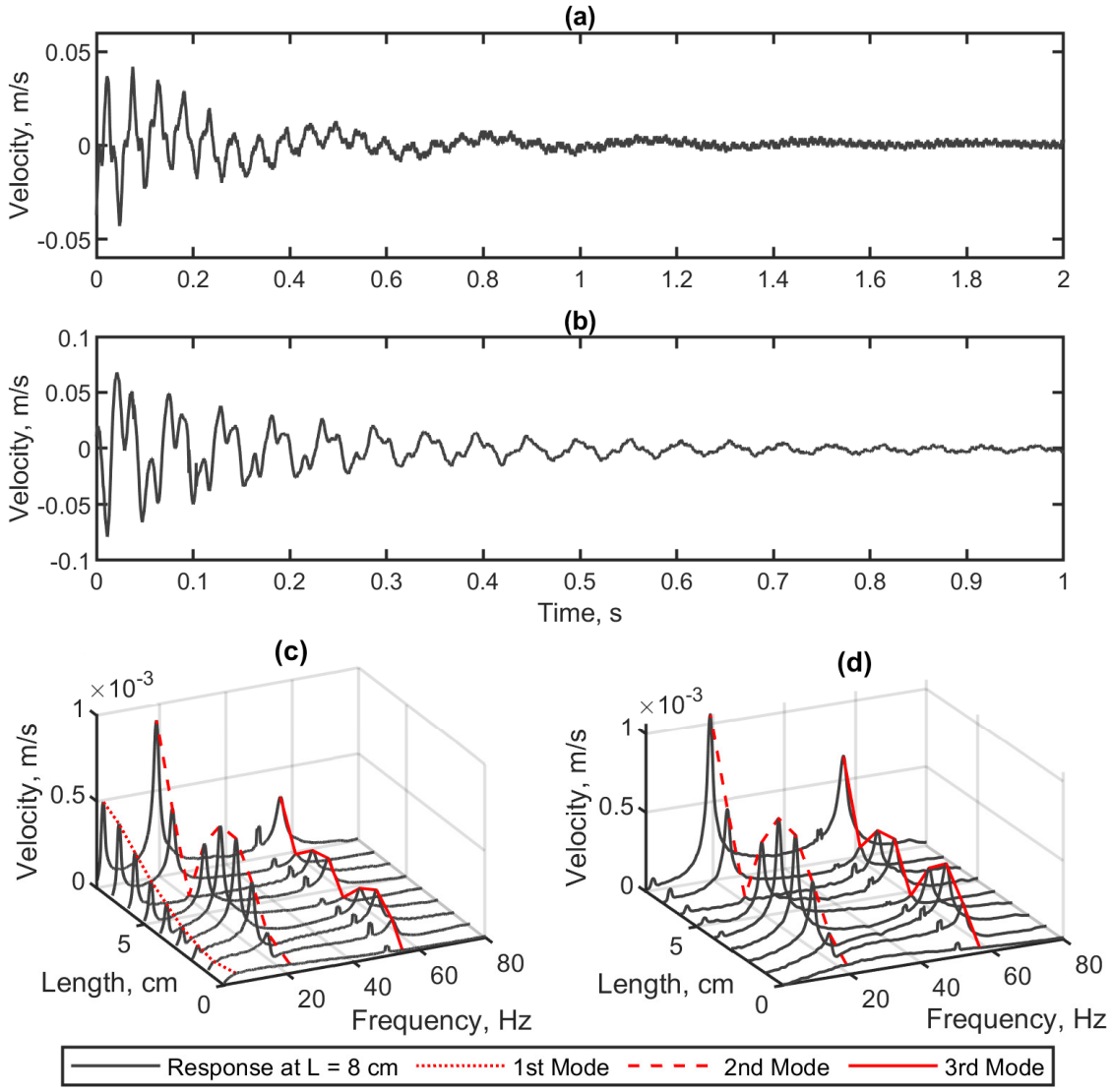

Figure 3.26. Transient responses of the submerged beam at $x = 8$ *cm* due to (a) the step input and (b) the derivative of ramp function input signal; The frequency series obtained along the beam length by inducing (a) the step input and (b) the derivative of ramp function input signals

The same procedure as in Section 3.4.1 was used to obtain the transient response of the fully submerged beam. Figure 3.26(a) and (b) present the transient vibration of the beam at $x = 8$ *cm* generated with the step input and the derivative of ramp function signals,

respectively. It is observed that the beam deteriorates very quickly with amplitudes reaching zero in less than 1 *s*. The FFT analysis for the step function input signal is displayed in Figure 3.26(c). Note that small peaks appeared at 50 *Hz* might be from the measuring instruments rather than the beam. It is interesting to see the modal contribution of the beam where the first three natural frequencies are almost uniformly excited. Based on the visual observation of the free vibration signal shown in Figure 3.26(a), the third resonant may only appear in the very beginning of the signal up to 0.2 *s*. For the rest of the time, the decaying beam oscillation is mostly made of the of the first and second mode shape. Figure 3.26(d) presents the frequency series from the FFT analysis generated with the derivative of the ramp function signal. The input signal may actuate the beam in between the second and third resonant as suggested by the domination of these two peaks in the frequency series. Accordingly, the beam decays with the second resonant, eliminating the influence of the first resonant in the free vibration response.

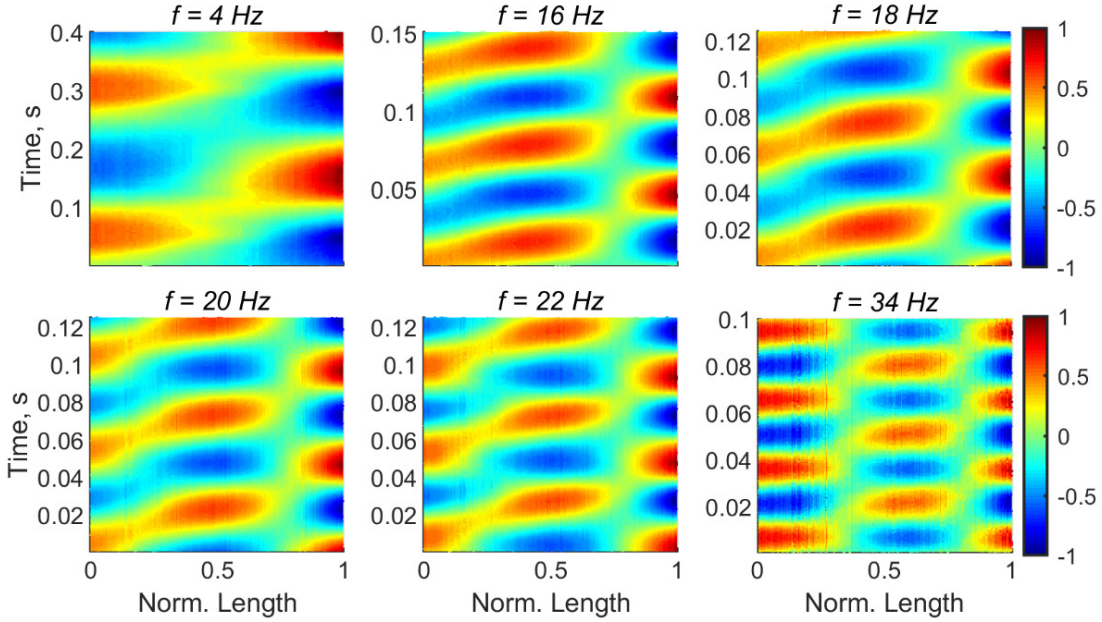

Figure 3.27. Vibration pattern of the fully submerged beam

Figure 3.27 shows steady state responses of the beam for various forcing frequencies. It is noticed that the vibration pattern at $f = 4$ *Hz* for the fully submerged beam is comparable to that of the partially submerged beam. The travelling waves in vibration patterns become clear when the forcing frequency is increased close to the second resonant, demonstrated with $f = 16$ *Hz* and $f = 18$ *Hz* in Figure 3.27. However, the travelling waves are not pure since the maximum vibration amplitude along the beam length is not uniform and the node due to the second mode shape provides discontinuity

in the mechanical waves. After the forcing frequency passes the second resonant, the second node emerges around the quarter of the beam length as suggested with the vibration pattern at $f = 20$ *Hz* in Figure 3.27. The amplitude of the second node reduces with increasing the forcing frequency away from the resonant. Moreover, the amplitude at the node becomes close to zero creating standing wave formations in the beam responses when the forcing frequency is at the lowest FRF magnitude between the two peaks. This incidence is illustrated in Figure 3.27 at $f = 34$ *Hz*.

3.4.4. Influence of fluid viscosity

In the theoretical modelling described in Section 2.2.3, the fluid density determines the damping force on the beam. To investigate the other fluid parameters such as the viscosity on the beam responses, a silicone oil with the chemical formula $(–Si(CH_3)_2O–)_n$ was used as the fluid media. The fluid density for this liquid is 970 kg/m^3 which is comparable to the water density. The refractive index is also almost equivalent to that of the water. However, the viscosity of the silicone oil is approximately 1000 times of that of the water. Figure 3.28 displays the FRF of the beam fully submerged in the silicone oil. The random input signals were generated with the maximum amplitudes of 200 *mV* and 300 *mV*. It is observed from the figure that there is a local maximum point around 9 *Hz*. It is unclear whether the peak is due to the random generated signal or the beam phenomena. Accordingly, the stepped-sine wave signal was used to further investigate phenomena. This would allow to estimate the FRF based on the steady state responses. The frequency was set from 1 *Hz* to 50 *Hz* with the stepping frequency of 1 *Hz*. The amplitude of the signal generator was set constant at 200 *mV*. The results are shown in Figure 3.28 with the dashed blue line and dotted black line for the sweeping direction up and down, respectively. It is seen that the FRF from the stepped-sine wave is superimposed with the random input signal particularly for up to 30 *Hz*. This means that the fluctuation in the FRF magnitude at 9 *Hz* is not caused by noise. Moreover, the vibration pattern will be used not only to elucidate the mechanical wave phenomena, but also to validate whether the peak is a resonant or a normal fluctuation in the FRF magnitude.

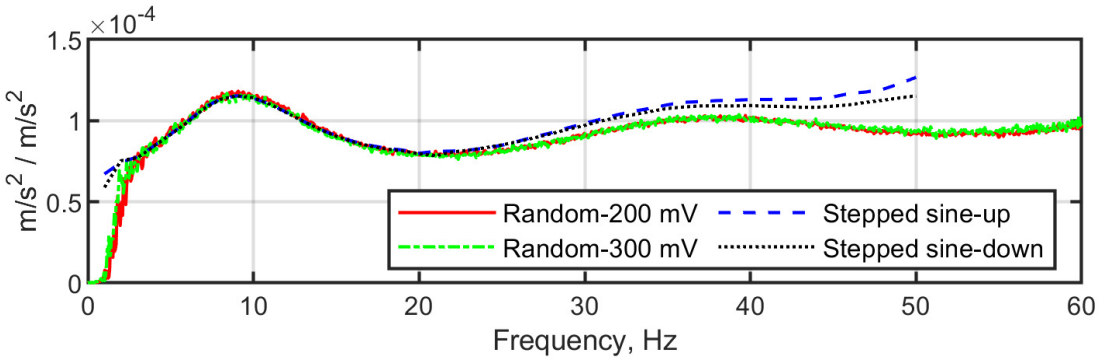

Figure 3.28. FRF of the beam submerged in silicone oil

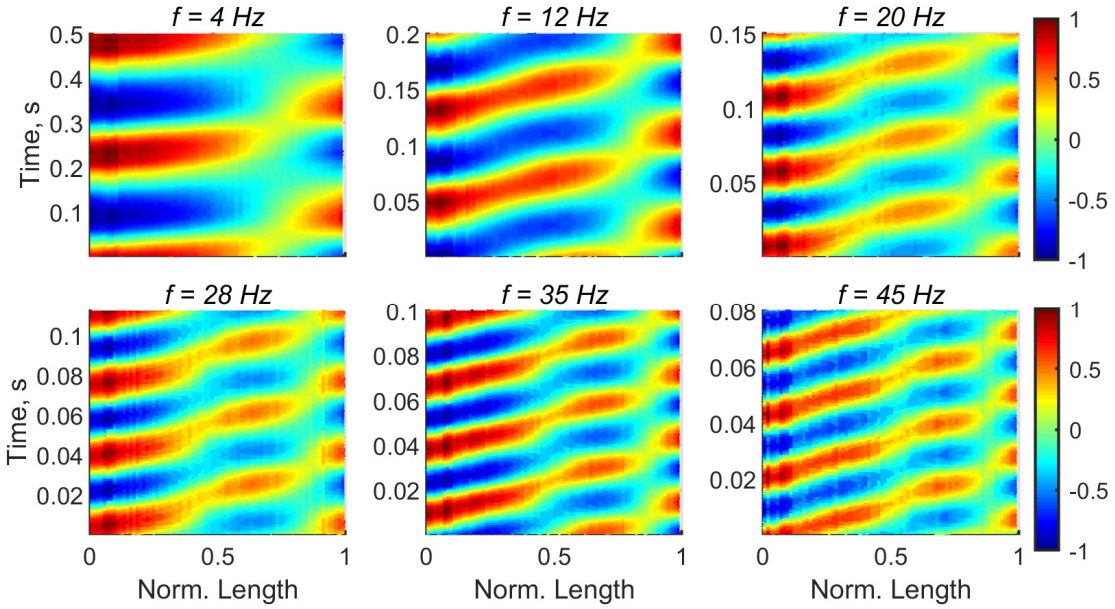

Figure 3.29. Vibration patterns of the beam vibrating in silicone oil

Figure 3.29 presents the steady state responses of the fully submerged beam in silicone oil. It is noticed from the figure that the vibration pattern at $f = 4$ *Hz* demonstrate the beam vibrating in the second mode shape. It is interesting to see how the node location is already close to the free tip of the beam. In comparison, the node location for the beam vibrating in water at this frequency is still around the clamped section of the beam. With increasing the forcing frequency to 12 *Hz*, the node location remains the same. However, the vibration pattern exhibits strong travelling waves. At $f = 20$ *Hz*, the vibration pattern reveals that the beam forming a new node around $0.4L$. This is an indication that the beam was actuated in between the second and third resonant. It is interesting to see how the travelling waves remain consistent with forcing frequencies increased away from the resonant. On the contrary, travelling waves are mostly observed around the resonant for

the case of beam vibrating in water. Moreover, the nodes due to the beam mode shape are unavoidable, even with highly viscous fluid media.

3.5. Test 2: Beam with L = 13.5 *cm*

Since the previous investigation with the 0.8 *cm* beam was limited to the third resonant, the thinner and longer beam were used to further study characteristics of the beam up to the fifth resonant. This would allow to significantly drop the natural frequencies and enhance the contact beam surface to the fluid, increasing the total damping force in the beam. The thickness of the beam was 4 x 10^{-5} *m*, while the total beam length was extended to 0.135 *m*. The beam width was the same as the previous test. The density of the beam was 7200 kg/m^3. Using random input signals, Figure 3.30(a) displays the FRF of the 13.5 *cm* beam vibrating in air for various maximum random amplitudes. It is observed that the first three natural frequencies appear in up to 50 *Hz*. Again, the reason for the first resonant being independent of the input amplitudes, shown in Figure 3.30(a), is due to the frequency location that induces poor SNR for the signal analyser.

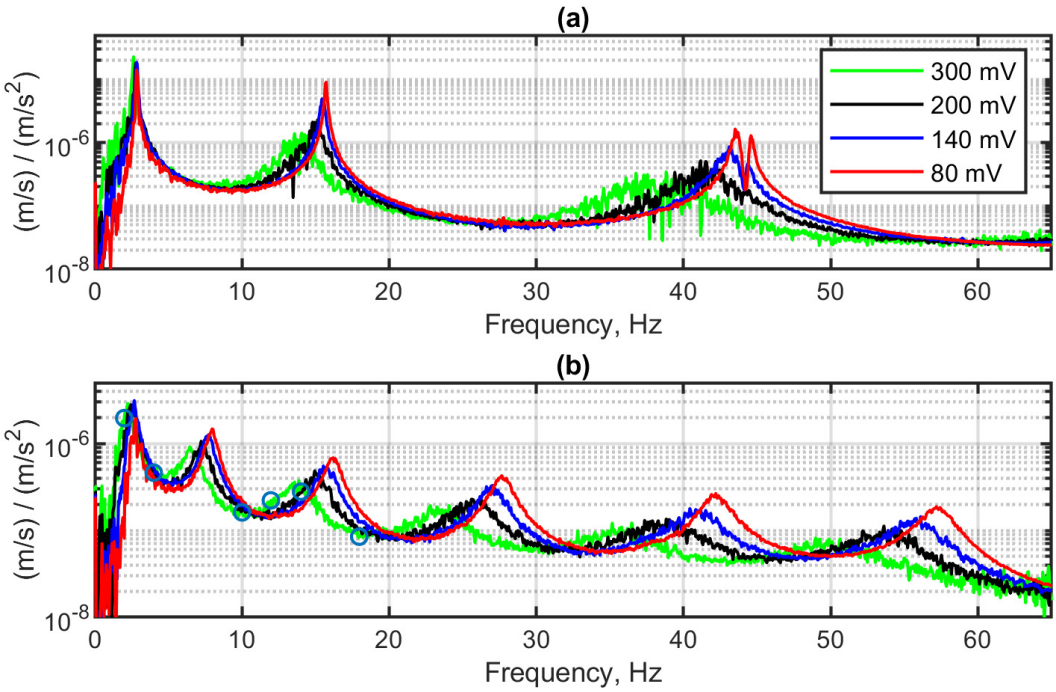

Figure 3.30. FRF of the 13.5 *cm* beam vibrating in (a) air and (b) water

The effect of damping due to air can be seen in the damped second natural frequency shown in Figure 3.30(a) where the peak decreases and shifts to the smaller frequency

along with increasing the forcing amplitudes. The stiffness and damping due to the beam materials are also believed to contribute to these phenomena. Furthermore, there is a discontinuity in the third peak of the amplitude 80 *mV* and 140 *mV*. This occurrence can be related to the nonlinearity described in Section 3.4.1 where the beam acts as dynamic vibration absorbers for the supporting plate. In addition, this is also the reason why the damped natural frequency displaces approximately 5 *Hz* from 80 *mV* to 300 *mV*.

Figure 3.30(b) displays the FRF of the beam fully submerged in water for various maximum random amplitudes. Note that the first peak appeared in the figure is the second resonant. The first resonant is estimated below 1 *Hz* which is in the range of the cut-off frequencies of the sensors. Therefore, there are seven natural frequencies emerged up to 60 *Hz*, making it a good candidate for artificial swimmers. Since the beam possesses low stiffness and high damping characteristics, the amplitudes of the free vibration responses decay very rapidly. Moreover, some peaks are located at low frequencies where the SNR is mostly high. These conditions are not ideal for the nonlinear identification parameter method discussed in Section 3.3.3. Consequently, the backbone and damping curves for this beam configuration are not included in this analysis.

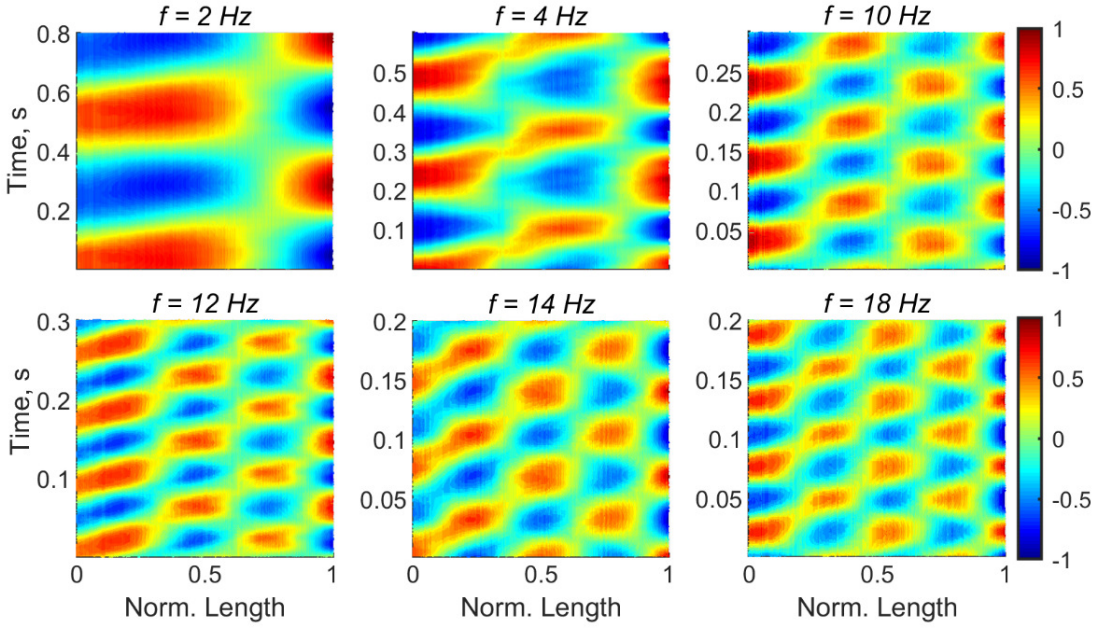

Figure 3.31. Vibration patterns of the long beam submerged in water

Figure 3.31 presents the steady state responses of the 13.5 *cm* beam vibrating in water for various forcing frequencies. The initial presumption that the first peak falls below 1 *Hz* is correct. This has been proved with the presence of a nodal point in the vibration

pattern of the beam at $f = 2$ *Hz*, indicating that the peak at $f = 2.25$ *Hz* is the second resonant. At $f = 4$ *Hz*, the beam vibrates in the third mode shape. At the halfway of the third and fourth resonant, $f = 10$ *Hz*, the beam undergoes vibration in the fourth mode shape. This is demonstrated with three nodal points in the vibration pattern. Eventually, the vibration pattern at $f = 18$ *Hz* demonstrates that the steady state responses are influenced by the fifth mode shape. Although the beam exhibits travelling waves at $f = 12$ *Hz*, the colour intensity in the nodal points of the vibration pattern suggests that the amplitudes at the nodes are considerably lower which may reduce the amplitude of travelling waves.

The 13.5 *cm* beam was also tested in silicone oil media. Figure 3.32 displays the FRF of the fully submerged beam in silicone oil for various input excitations. It is noticed that there is no difference between the random signal of 200 *mV* and 300 *mV*. To further investigate this occurrence, the stepped-sine wave was generated with the frequency range of 1 *Hz* to 50 *Hz* with the linear stepping frequency of 0.25 *Hz* and the sweeping direction "up". The results shows that the amplitude of 80 *mV*, the dashed black line, superimposes with the responses from the random signals. Ultimately, the FRF diverges once the amplitude of the stepped-sine wave is increased to 200 *mV*. Since the beam is highly damped, it is believed that this results in the poor coherence of the base acceleration and beam tip acceleration signals, indicated with the FRF in the order of magnitude of -5. This value is ten times lower than that of the 8 *cm* beam submerged in silicone oil. In addition, the amplitude of 200 *mV* for the stepped sine wave might induce remarkable tip acceleration values, reducing the FRF magnitude. Nevertheless, all measurements follow the similar trendline.

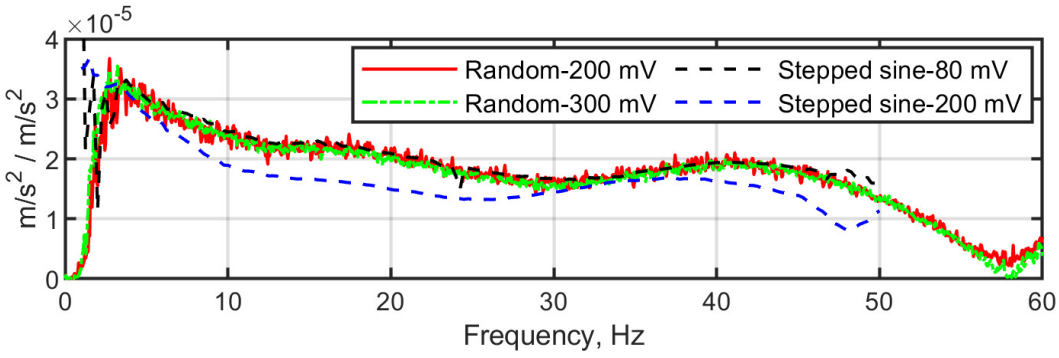

Figure 3.32. FRF of the long beam immersed in silicone oil

Figure 3.33 presents the steady state responses of the fully submerged beam in silicone oil. Note that unsteady state analyses were not conducted due to poor transient signals. The measurement was stopped at $f = 12\ Hz$ due to the very small displacements which makes it difficult to be clearly captured by the high-speed camera. It is seen that the vibration patterns demonstrate travelling waves from $f = 4\ Hz$ to $f = 12\ Hz$. Therefore, increasing the beam length is proven to enhance the phase delay between the base and tip displacement, although this will significantly reduce the displacement amplitude along the beam length as suggested by the vibration patterns which make it difficult to observe the nodes and antinodes.

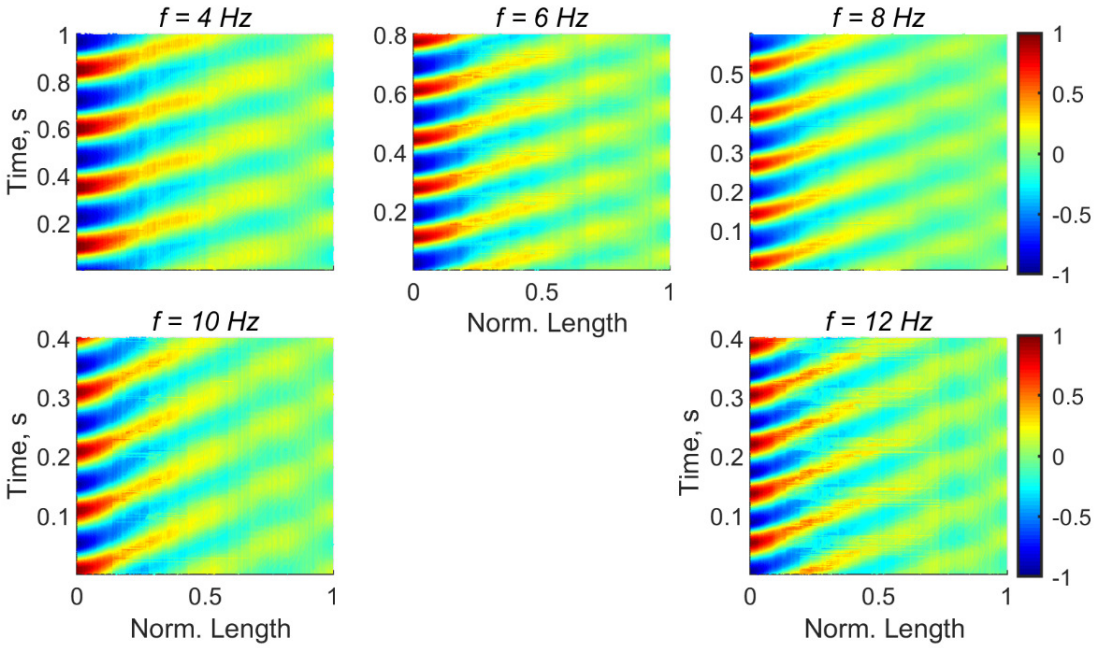

Figure 3.33. Vibration patterns in silicone oil

3.6. Model validation

The comparison of the analytical and experimental data only considers the steady-state responses of the beam. There are two main components to be examined: the beam amplitude over the beam length and the wave propagation over time. These components would provide comprehensive examinations into the accuracy of the spatial and temporal functions of the beam equation approximating the real phenomena. The estimation of the beam envelope is illustrated in Figure 3.34(a) with the black line specified by circle markers. Since the beam undergoes a periodic waveform, the algorithm developed to obtain the beam envelope is based on the detection of local maxima closest to $t = 0\ s$. This is demonstrated in the 3D projection of the beam displacement with respect to x and t

shown in Figure 3.34(b). This technique is beneficial for extracting the envelope of the experimental data, where the periodic wave may contain of multiple frequencies due to noise, creating scattered peak detection over time. Furthermore, by removing the contour map, Figure 3.34(c) depicts the projection of the beam envelope over t, or the top projection of the 3D plot. Note that the straight-line around $x = 0.6L$ is non-existent in the reality. It is a discontinuity due to the algorithm use to post-process the measurements that imposes a time limit of $t = 0.1\ s$ to select the peak. If this limit is exceeded, it considers the following travelling waves. Only the two projections shown in Figure 3.34(a) and (c) are used for validations.

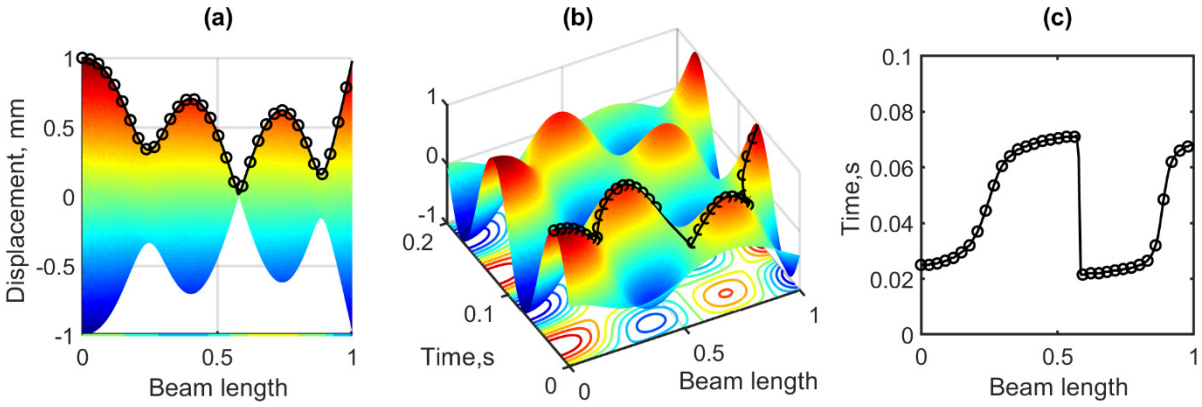

Figure 3.34. Procedures for obtaining the beam envelope and the propagation of the maximum amplitudes over beam length

3.6.1. In water

Some experimental data of the 8 *cm* beam submerged underwater shown in Figure 3.27 are used to compare with data from the analytical model. To simulate the analytical model, the fluid parameters are described as follows: the water density, ρ_f, is 997 kg/m^3 and the drag coefficient, C_d, is 1.8 based on the flat plate model [121]. Due to the ratio of the length to width ratio of the beam, the inertia coefficient, C_m, is 1 based on the estimation in reference [27]. For the solid parameters, the dimension and material properties of the beam are described in Section 3.4. The nonlinear coefficient value for the third resonant, ψ_{333}, is 0.101934. The flexural rigidity, EI, which is the product of the modulus of elasticity and second moment of area, is calculated by rearranging the natural frequency equations derived in Section 2.2.2 to give

$$EI = \frac{\omega_n^2 \mu}{\beta_n^4} \tag{3.8}$$

where μ define as $\rho A + 0.25\pi\rho_f C_m b^2$.

For the case of vibrating in air, the added mass term, $0.25\pi\rho_f C_m b^2$, is approximately zero. Substituting the first two undamped natural frequencies from the FRF shown in Figure 3.13 results in the modulus of elasticity of 1.273 x 10^{-4} $N.m^2$ and 1.159 x 10^{-4} $N.m^2$ for the first and the second resonant, respectively. The discrepancy in the estimated E values for different natural frequencies indicates that there is a nonlinearity in the stress-strain curve of the material. Since the analytical model is derived based on the linear elastic material, the modulus elasticity is presumed to be linear for all natural frequencies. Accordingly, the E values are averaged to give the mean modulus of elasticity of 1.216 x 10^{-4} $N.m^2$. To compare the estimated E value from different fluid media, the first three undamped natural frequencies presented Figure 3.22 are substituted into Eq. (3.8), resulting in the mean E value of 1.442 x 10^{-4} $N.m^2$. The discrepancy between the estimation in air and water is not only due to the nonlinearity on the beam, but also the fluid force approximation developed in the analytical model. It is worth mentioning that the fluid forces, which include the added mass and damping force term, were developed for a fixed rigid body subjected to an oscillating flow. Therefore, the flexural rigidity estimated from the beam vibrating in air will be used to simulate the analytical model.

Figure 3.35 depicts the comparison of the analytical and experimental models at some forcing frequencies. Note that the first column presents the comparison of the beam envelope; the second column demonstrates the envelope location of the analytical model in the 3D plot of the beam amplitude with respect to t and x; and the last column illustrates the wave propagation of the two models. Figure 3.35(a) displays the envelope of the analytical model plotted in the front view of the experimental model generated with $f = 4$ *Hz*. The experimental results are demonstrated in a greyscale colour scheme to prevent ambiguity with the analytical model. It is observed that the envelope of the analytical model provides good approximation for the experimental model. Figure 3.35(b) presents the envelope location of the analytical model in the vibration pattern. By removing the contour map and superimposing with the experimental data, the comparison of the propagation wave of the two models is displayed in Figure 3.35(c). Note that a phase

synchronisation method was used to generate Figure 3.35(c) so that the envelopes of the two models at $x = 0L$ start from $t = 0\ s$.

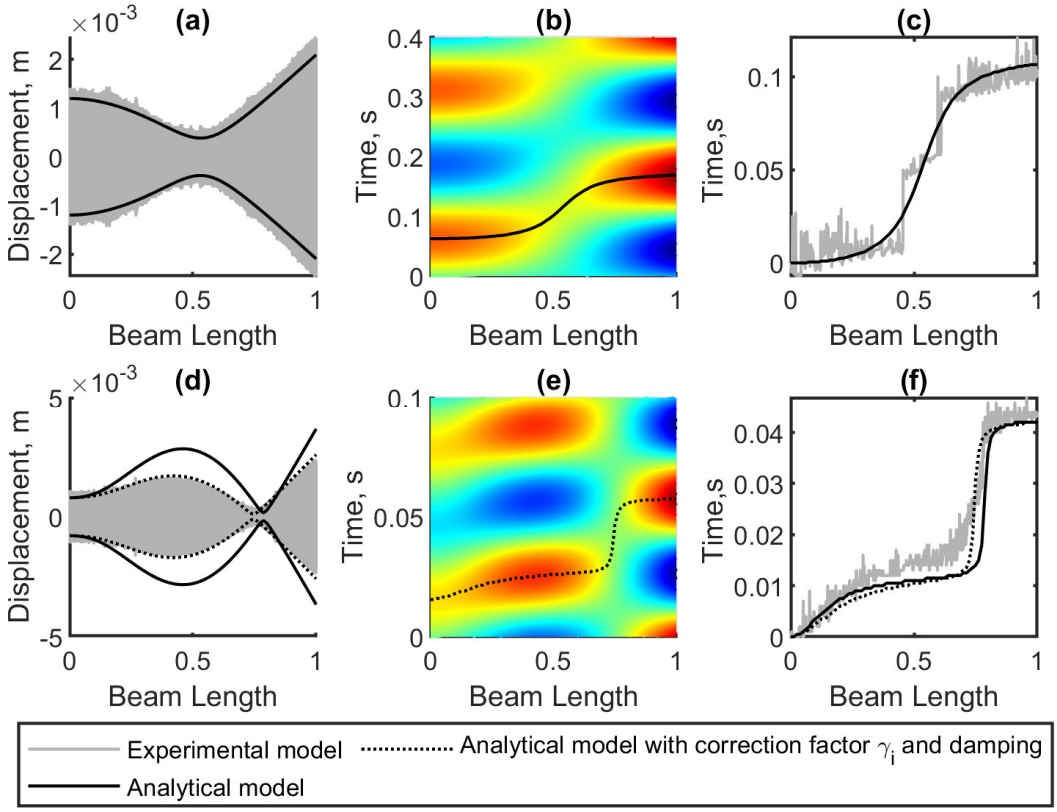

Figure 3.35. Comparison of the analytical and experimental model of the 8 *cm* beam at (a)-(c) $f = 4\ Hz$ and $f = 16\ Hz$

The results shown in Figure 3.35(d)-(f) were generated with the forcing frequency of 16 *Hz*. It is noticed from Figure 3.35(d) that the node location of the analytical model indicated with the solid black line is slightly offset compared to that of the experimental model. Since this frequency is around the second resonant, the nonlinearity in the EI value becomes apparent. Correcting the EI value to fit with the second resonant would create a discrepancy for the lower resonant. The reason for this is due to the relationship of the constant EI to the terms ω_i^2 and β_i^4 in Eq. (2.9). Therefore, a correction factor, denoted with γ_i, is introduced in Eq. (2.9) to give

$$\beta_i^4 = \frac{\mu\omega_i^2}{EI}\gamma_i \tag{3.9}$$

The expression in Eq. (3.9) allows the wave number, β_i, to be varied without altering the natural frequency, ω_i.

Apart from the inaccuracy in the node location, there is also lack of similarity in the amplitude of the envelope which can be caused by the damping approximation in the beam equation. The damping curve obtained from experiments shown in Figure 3.25 demonstrates that the damping is mainly determined by the linear damping with minor nonlinearities due to the quadratic damping function. On the contrary, the total damping force for the analytical model described in Section 2.2.3 is predominantly formed by the quadratic damping. The linear damping, which represents the damping due to material with the value of 0.5%, only accounts for a few proportions in the total damping force. Note that the discrepancy in the envelope becomes notable when the beam is actuated around the resonant. This condition is where the beam generates large displacements, and the cosine part of the beam equation becomes dominant. Eventually, by implementing the correction factors γ_1 = 1 and γ_2 = 1.28 and arbitrarily multiplying the quadratic damping constant, C_{qd}, by two, the envelope of the analytical model indicated with the dashed black line shown in Figure 3.35(d) provides good approximation for the experimental model. In addition, since the natural frequencies of the system remain the same, there are no significant changes for the analytical models in the propagation of the envelope over t shown in Figure 3.35(f).

Figure 3.36 displays the comparison of the analytical and experimental data at the frequency range of the second and third resonant. This is to demonstrate the capability of the analytical model for approximating the development of the second node in the beam envelope. At f = 18 Hz, it is seen that the beam envelopes form a new node in between $x = 0L$ and $x = 0.5L$ as shown in Figure 3.36(a). These phenomena, which include the propagation of the envelope over t shown in Figure 3.36(c), are well predicted by the analytical model. The amplitude at the nodal point reduces with increasing the forcing frequency to 22 Hz, displayed in Figure 3.36(d). Note that the third resonant was considered in the beam equation to simulate the analytical model with the third correction factor, γ_3, set to unity. It is noticed that the correction factors must be re-evaluated when the forcing frequency is increased close to the third resonant to produce the best fit to the experimental model. In addition, the comparison of the beam envelope over time shown in Figure 3.36(f) also shows minor discrepancies for the two models.

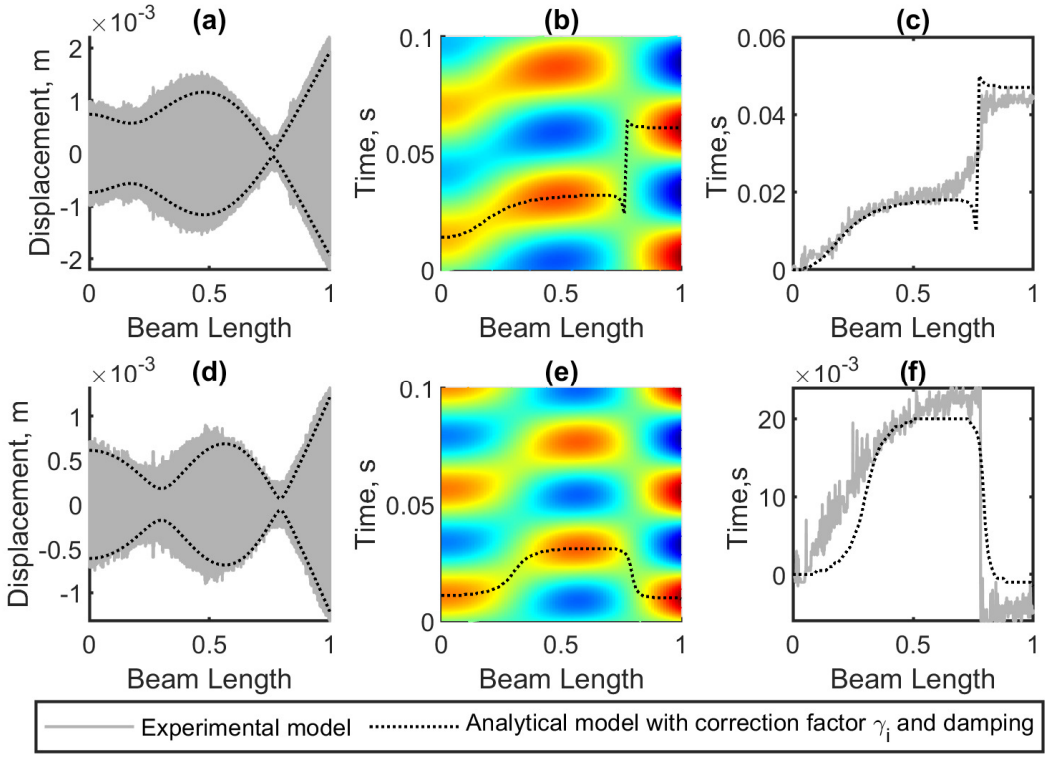

Figure 3.36. Validation of the 8 *cm* beam at (a)-(c) f = 18 Hz and (d)-(f) f = 22 *Hz*

The comparison for the analytical and experimental models for the 8 *cm* beam was limited to 22 *Hz*. To further explore the higher mode, the validation will be carried out with the 13.5 *cm* beam. To calculate the flexural rigidity of the cantilever beam, the first five undamped natural frequencies from the FRF at 300 *mV* of the fully submerged beam shown in Figure 3.30 were substituted into Eq. (3.9). This substitution results in five EI values with the estimated mean value of 2.190 x 10^{-5} $N.m^2$. The mean EI value is rounded to 2.380 x 10^{-5} $N.m^2$ so that the deviation in the higher natural frequencies of the analytical and experimental model are minimum. The first-six nonlinear coefficients, ψ_{jki}, with $j = k = i$ for the modal coordinate equation in Eq. (2.20) are 0.200, 0.175, 0.172, 0.157, 0.158 and 0.159. Following the same procedure for comparing the analytical and experimental models, Figure 3.37 displays the comparison of the beam responses generated with the frequency around the second and third resonant. It is observed that the beam envelope of the analytical model actuated with f = 2 *Hz* shown in Figure 3.37(a) still requires correction factors to fit with the experimental model. The corrections factors of $\gamma_1 = 1$ and $\gamma_2 = 1.25$ were taken arbitrarily and applied to the numerical simulation to shift the node. It is unnecessary to adjust the nonlinear damping value in this case since altering the wave number, β_i, is adequate to approximate the experimental model.

Furthermore, the influence of the correction factor on the propagation of the envelope over time shown in Figure 3.37(c) is minor.

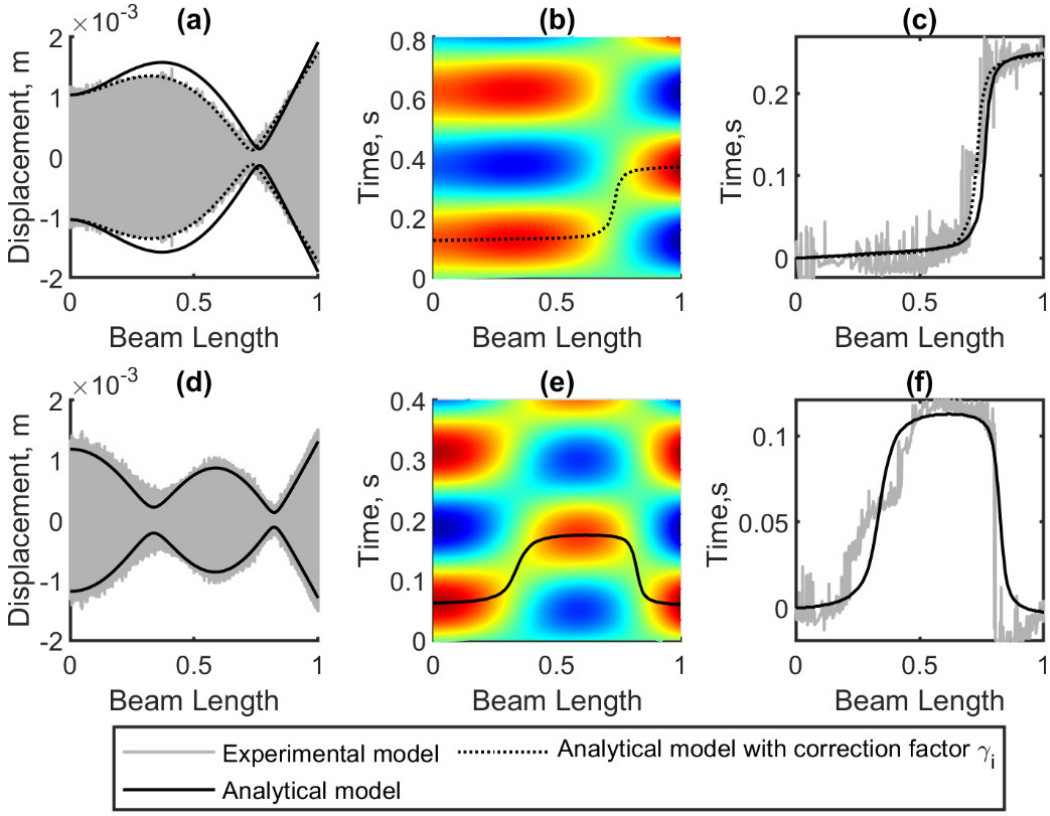

Figure 3.37. Comparison of beam responses with the length of 13.5 *cm* at $f = 2$ *Hz* and $f = 4$ *Hz*

Figure 3.37(d)-(f) depict the beam responses actuated with $f = 4$ *Hz*. At this frequency, the beam vibrates in the third mode shape indicated with the two nodes in the beam envelope shown in Figure 3.37(d). As expected, the analytical model provides very good approximation to the experimental model without correction factors. This may be caused by rounding the mean *EI* value to produce the best fit to the higher natural frequencies. Figure 3.38(a)-(c) displays the beam responses at $f = 10$ *Hz*. It is observed from the nodes in the envelope that the beam vibrates in the fourth mode shape. There is also no notable discrepancy for the two models at $f = 18$ *Hz* that vibrate in the fifth mode shape indicated with the presence of four nodal points in the beam envelope shown in Figure 3.38(d)-(f). Therefore, it is preferred to estimate the *E* value from natural frequencies that are obtained from underwater tests. This would produce more precise prediction to the actual model, particularly for the case of flexible beams where the approximation of the fluid forces tends to break down.

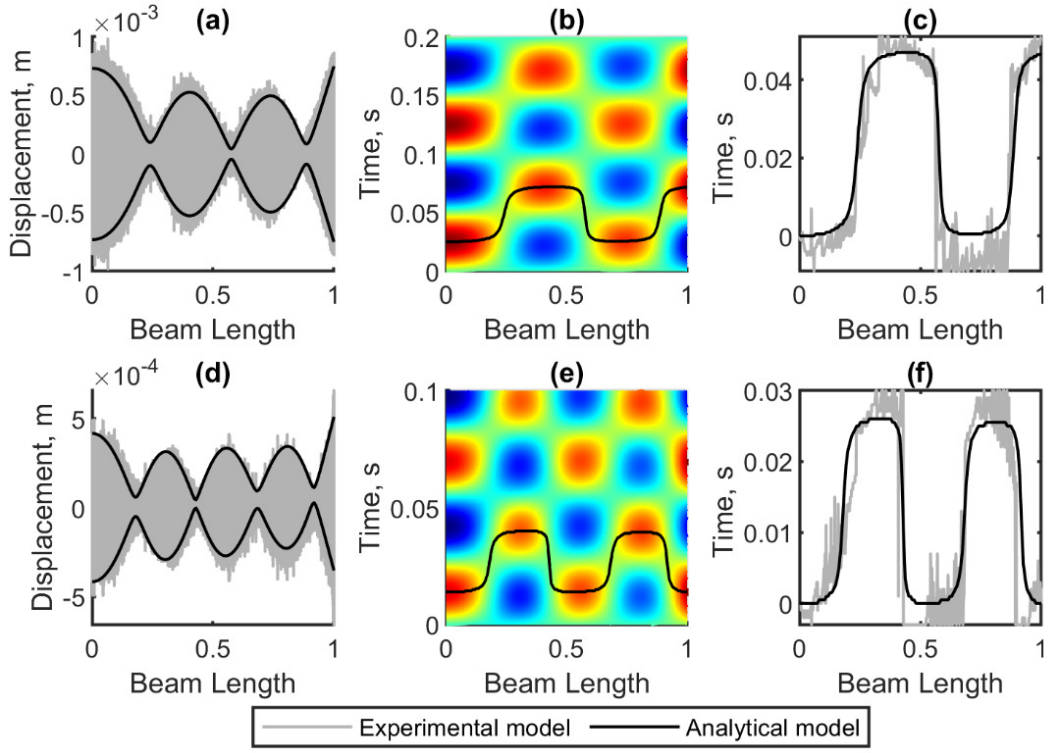

Figure 3.38. Validation of the 13.5 *cm* beam actuated at $f = 10$ *Hz* and $f = 18$ *Hz*

3.6.2. In Silicone oil

It has been demonstrated in Section 3.4.4 that the beam submerged in silicone oil media can perform travelling waves over a wide range of frequencies, even though it is away from resonant. It is also noticed that some nodal points are located in particular locations where it may require a specific manipulation in the beam equation to fit with the experimental model. Therefore, this validation is intended to examine the capability of the Galerkin-based model for fluid structure interaction for approximating the actual model of the beam vibrating in silicone oil. Since the focus is to examine the beam equation, some parameters such as the quadratic damping coefficient, modulus of elasticity and correction factor will be tuned to achieve the desired results. Note that the added mass term, $0.25\pi\rho_f C_m b^2$, in the linear mass per unit length, μ, is kept constant since it has an inversely proportional function to the damping force value in the modal coordinate expressed in Eq. (2.20). Accordingly, the variable E will be varied to alter the ω_n value without changing the damping force. In the reality, the modulus of elasticity of the material is typically constant.

Figure 3.39 displays the comparison of the analytical and experimental model of the 8 *cm* beam vibrating in silicone oil. From the figure, the first row presents the comparison

of the beam envelopes, and the second row displays the propagation of envelopes over time. Figure 3.39(a) presents the comparison of the beam responses actuated with $f = 8$ Hz. To fit with the actual model, the C_{qd} value was altered to 2 times of that of the water. The E value was also reduced to 60 GPa, resulting in the first three natural frequencies of 1.36 Hz, 8.53 Hz and 23.89 Hz, respectively. Therefore, the peak around 9 Hz in the FRF shown in Figure 3.28 is the second resonant of the beam. At $f = 12$ Hz, the coefficient C_{qd} was amplified to 4 times. The correction factors, γ_i, of the first, second and third resonant were 1, 1.28 and 1, respectively. Also, the variable E was tuned to 80 GPa. These parameters can well approximate the maximum amplitude of the experimental model shown in Figure 3.39(b), although there is an inevitable discrepancy occurred in the propagation of the envelope over t.

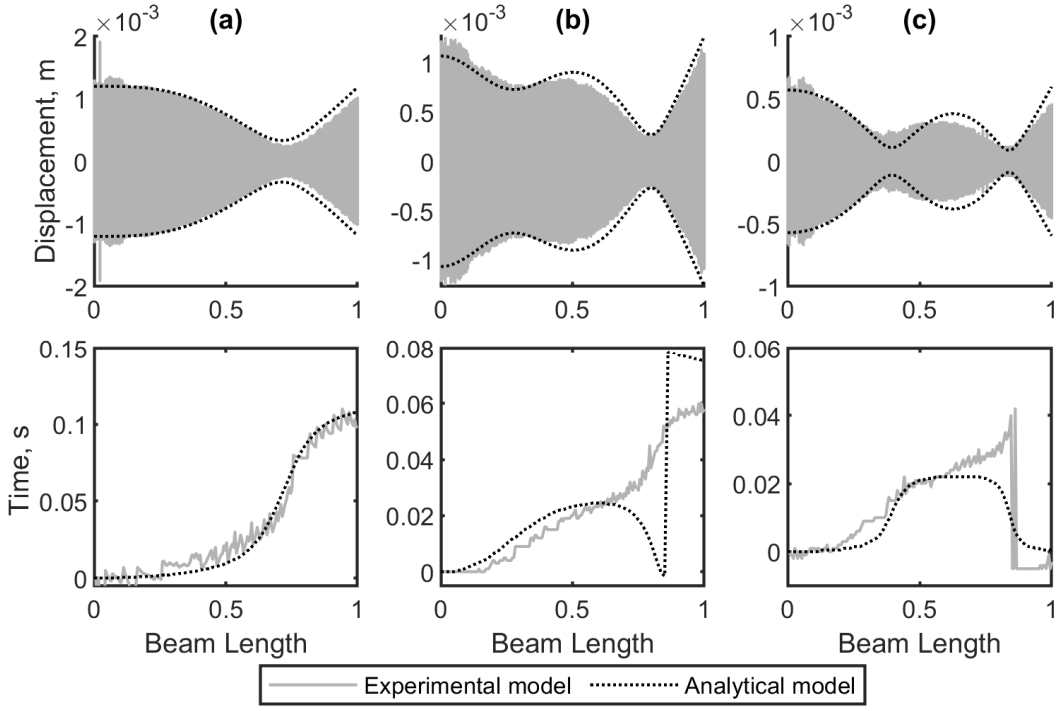

Figure 3.39. Validation of beam responses vibrating in silicone oil at (a) $f = 8$ Hz, (b) $f = 12$ Hz and (c) $f = 20$ Hz

For the forcing frequency of 20 Hz, the modulus of elasticity was set to 100 GPa, and the quadratic damping was 2 times of that of vibrating in water. The comparison of the beam responses for the analytical and experimental models is shown in Figure 3.39(c). It is observed that the analytical models considerably agree to some extent with the experimental model. Eventually, the investigation is limited to $f = 20$ Hz, since higher frequencies require parameter optimisation methods to tune all parameters to achieve the

best estimation to the actual model. Moreover, the 13.5 *cm* beam vibrating in silicone is not included in this analysis since there is no clear nodes and antinodes.

3.7. Discussion on passive travelling waves

It has been demonstrated in the previous section that the nonlinear analytical model can provide good approximation to the actual model. However, it is inconvenient to explain the travelling wave phenomena with the quadratic damping beam model which requires semi-analytical solution methods to solve the equation. Accordingly, a damping correction factor, χ_i, has been introduced in Section 2.2.6 to approximate the quadratic damping terms, allowing the beam equation to be solved using analytical approaches. The linear approximation of the beam equation will be used in this section to explain the passive travelling waves occurred in the beam vibrating in a liquid. The term "passive" for travelling waves refers to the method how the travelling waves are established in a structure which, in this case, are due to the energy dissipation of the beam to the surrounding liquid. This is to distinguish from the term "active" where travelling waves are achieved by active controlling the boundary conditions that are further investigated in the next chapter.

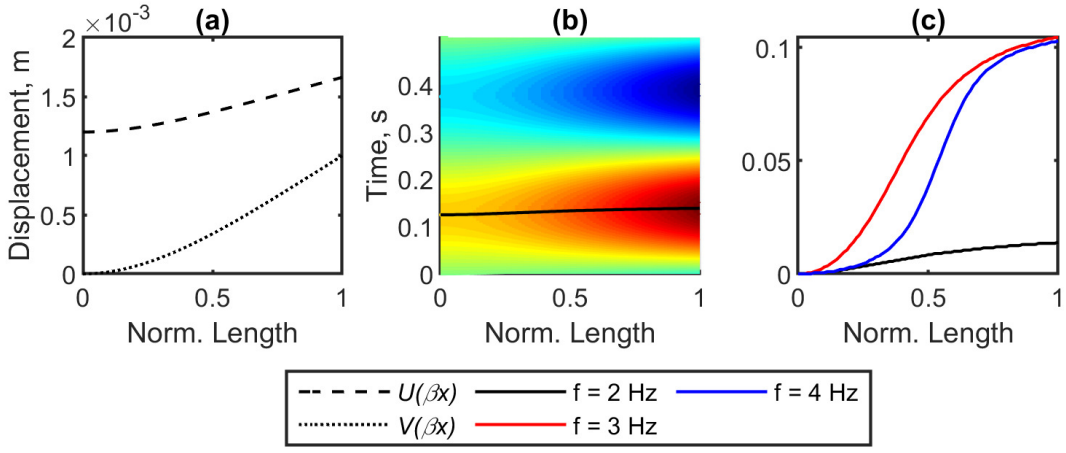

Figure 3.40. (a) The spatial function and (b) the envelope of the 8 *cm* beam vibrating at *f* = 2 *Hz*; (c) Propagation of envelopes for various forcing frequencies

Figure 3.40(a) shows the spatial functions of the 8 *cm* beam actuated with the forcing frequency of 2 *Hz*. It is observed that $U(\beta x)$ forms a linear equation with a non-zero intercept due to the influence of the base motion, A_f. The delay in the displacement response between the two tips, which induce travelling wave pattern, is determined by

the slope $V(\beta x)$. Since the temporal part of $U(\beta x)$ has 90 degrees out of phase to that of the spatial function $V(\beta x)$, the sum of the two functions can create a phase delay along the beam length. Figure 3.40(b) shows the sum of the two spatial functions indicated with solid black line superimposed with the vibration pattern of the beam. It is observed that the delay of the two tips occurs in very short time.

Depending on the slope $V(\beta x)$, the maximum phase delay is achieved when the forcing frequency approaches the natural frequency, $\omega \rightarrow \omega_n$. At this condition, the slope $U(\beta x)$ becomes minimum due to $(\omega_n^2 - \omega^2) \approx 0$ in the term lp_i expressed in Eq. (2.30). Figure 3.40(c) displays the propagation of the beam envelope for various forcing frequencies around the resonant. The phase delay reaches maximum at $f = 3$ *Hz*, then decreases gradually with increasing the forcing frequency, moving away from the resonant. While the influence of the second resonant is still negligible at $f = 4$ *Hz*, the spatial function of the beam satisfies $U(\beta x) = A_f - lp_1\varphi_1$ due to $\omega_n < \omega$. Accordingly, there is a zero-crossing point occurred only in the function $U(\beta x)$ that creates a nodal point in the middle of the beam envelope. This phenomenon can also be seen in the vibration pattern at $f = 4$ *Hz* shown in Figure 3.27. In addition, by assuming the constant slope in the $V(\beta x)$ function, the phase delay increases along with the total beam length. This can make the beam possible to generate maximum travelling waves. However, the wave amplitudes may not be as uniform as the pure travelling waves demonstrated in Figure 3.1.

Unlike the first mode shape, there is a zero-crossing point in the second mode shape that creates a discontinuity in the beam envelope. Figure 3.41(a) displays the spatial functions of the beam generated with $f = 16$ *Hz*. With the contribution of the second resonant, the spatial functions of the beam fulfil the following equations: $U(\beta x) = A_f - lp_1\varphi_1 + lp_2\varphi_2$ and $V(\beta x) = rp_1\varphi_1 + rp_2\varphi_2$. It is noticed that the zero-crossing point for the two spatial functions is in the same location. Increasing the damping will increase the term rp_i and slightly shift the zero-crossing point of $V(\beta x)$. Amplifying the base amplitude, A_f, can also raise the term $U(\beta x)$ which, in turn, displaces the location of the zero-crossing point. These techniques, however, may only increase the amplitude at the nodal point. The zero-crossing point can only be cancelled with a manipulation in the boundary conditions. Figure 3.41(b) presents the envelope at $f = 16$ *Hz*, indicated with the solid black line, that demonstrates travelling waves before discontinued by the node. The

propagation of the envelope over time is visualised separately along with the other forcing frequencies shown in Figure 3.41(c). As anticipated, the gradient line surges with increasing the frequency.

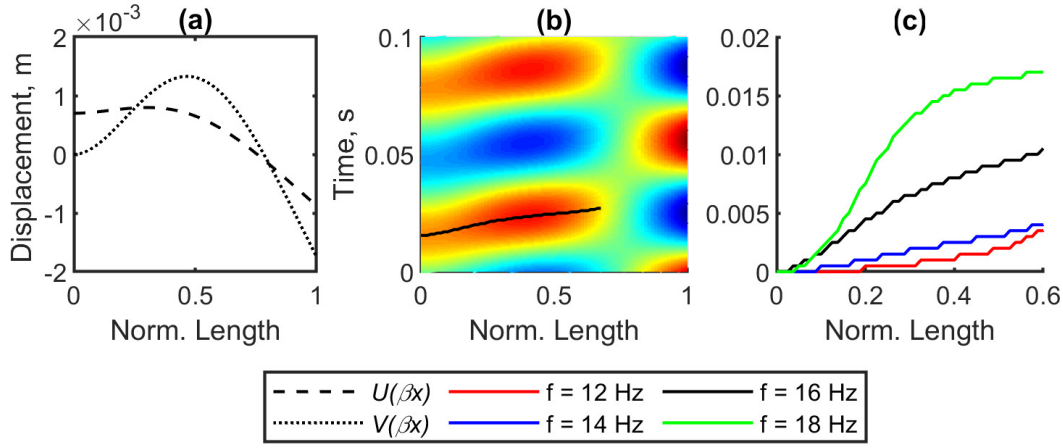

Figure 3.41. (a) The spatial function and (b) the envelope of the 8 *cm* beam vibrating at *f* = 16 *Hz*; (c) Propagation of envelopes for various forcing frequencies around the second resonant

The spatial functions of the 13.5 *cm* beam are used to further investigate the higher resonant. Figure 3.42(a) presents the spatial functions of the beam vibrating in the fourth mode shape at $f = 10$ *Hz*. It is observed that there are 3 zero-crossing points in the function $U(\beta x)$. On the contrary, all values are positive for the function $V(\beta x)$. This might be caused by the strong influence of the term $rp_1\varphi_1$ due to the first resonant value that falls below 1 *Hz*. The minimum amplitude in the beam envelope shown in Figure 3.38(a) occurs at the nodal point of $0.58L$. This location is where the second zero-crossing point of $U(\beta x)$ coincides with the trough of $V(\beta x)$ demonstrated in the plot of spatial functions in Figure 3.42(a). Furthermore, this phenomenon also occurs in the fifth resonant. Figure 3.42(b) presents the spatial functions of the 13.5 *cm* beam vibrating at the fifth mode shape with $f = 18$ *Hz*. It is observed that the intersection of the zero-crossing points between the function $U(\beta x)$ and $V(\beta x)$ are inevitably. When the beam is forced away from resonant, the contribution of $V(\beta x)$ becomes minimum. Accordingly, the amplitude at the nodal points becomes approximately zero which lead to standing wave generation in the beam.

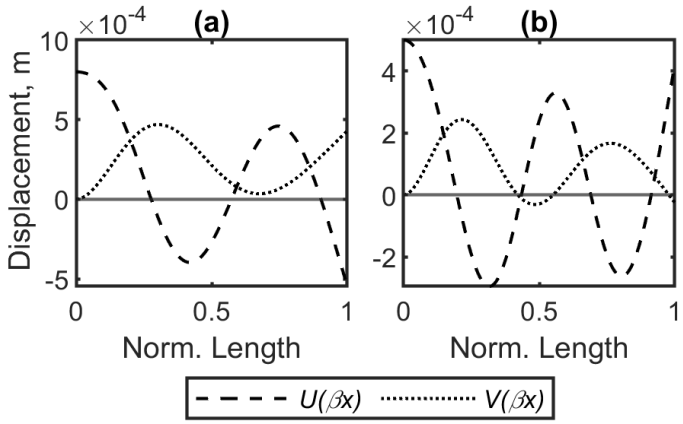

Figure 3.42. Spatial functions of the 13.5 *cm* beam actuated at (a) f = 10 *Hz* and (b) f = 18 *Hz*

3.8. Conclusion

An investigation of travelling waves of a cantilever beam submerged in liquid has been performed under various test conditions. This includes a series of experimental tests to assess the dynamic behaviours of the beam in time and frequency domains. An individual test rig assessment was also performed, assuring no dynamic interaction between the beam and the rig that could affect to the beam responses.

Nonlinearities in the damping and natural frequencies were thoroughly examined by the nonlinear identification parameter method in conjunction with the beam FRF. The damping curves extracted from the transient responses reveal that the presence of water can increase the linear damping ratio by approximately 10 times of the beam vibrating in air. The damping lines also demonstrate high (positive) gradient values, indicating weak nonlinearities in the beam. This is contrast to the modelling assumption, where the quadratic damping function from the drag force estimation creates low (positive) gradient values in the damping curves. Furthermore, the nonlinearity in the stress-strain diagram was identified from the FRF due to variation in the estimation of the modulus of elasticity for different natural frequencies.

The steady state responses of the analytical models have been compared to the experimental model. The analytical models provide good approximation, particularly for the case of vibrating in water. Discrepancies occur when the beam is actuated close to the resonant due to underestimated damping values. A correction factor was also introduced

to manipulate the spatial function, overcoming discrepancies in the validation due to the nonlinear beam properties.

The correlation between the mechanical waves and the linear beam equation has been presented. The travelling wave patterns are achieved due to the fluid damping that creates phase delay along the beam length. In the beam equation, the damping function has a 90-degree out of phase to the base motion. This function contributes the most to the beam equation when the beam is actuated close to the resonant. However, this argument is valid for vibrating in water. For vibrating in viscous fluid such as silicone oil, the experiment shows that the cantilever beam demonstrates travelling waves for wide range frequencies, including away from resonant. Furthermore, the amplitudes of travelling waves are not uniform due to the presence of nodes in the beam envelope. In some cases, this can be alleviated by increasing the forcing amplitudes, altering the damping properties and extending the beam length so that the zero-crossing points of the spatial functions do not intersect in the same location. Finally, this demonstration shows that the Galerkin approximation for FSI model is capable to approximate the beam responses in different fluid viscosities. Although some parameters need to be precisely estimated.

Chapter 4. Influence of travelling waves on the fluid dynamics

4.1. Introduction

This chapter investigates the effect of travelling waves on the fluid dynamics of beams fully submerged in water. The main objective of this study is to examine the time series and mean value of the fluid velocity induced by the submerged beam in various vibration patterns. An experimental investigation is performed to investigate the mean value of fluid velocities produced by a cantilever beam model. A description of the experimental method is provided as well as the techniques used to obtain the experimental data. Two metal beams with different thickness are used to expand the analysis in the range of first two resonant frequencies. The experimental analysis allows to unveil the relationship between the FRF magnitude and the maximum mean fluid velocity.

A 3D numerical simulation capable of performing fluid-structure interaction (FSI) is developed to further explore the relationship of the vibration pattern, beam envelope, the mean fluid velocity, and the fluctuation in the time series of fluid velocity. The mean fluid velocities from the numerical simulation are compared to the experimental data to provide assessment for the numerical model. A thinner beam is also used in the simulation to extend the study into higher modes. Since the travelling waves produced by the cantilever beam are limited around the resonant frequencies, another beam configuration is introduced to induce more travelling waves over wide range of frequencies. The conceptual design of the two-excitation beam model is provided which fulfils a clamped-clamped beam with moving supports. This model generates more uniform travelling waves with constant tip velocity ratio. Finally, a relevant comparison between the two models is discussed and the effect of the vibration pattern on the fluid flow can be obtained.

4.2. Experimental investigation of cantilever beam models

This section describes the experimental study of fluid flow induced by the vibrating beam submerged in water.

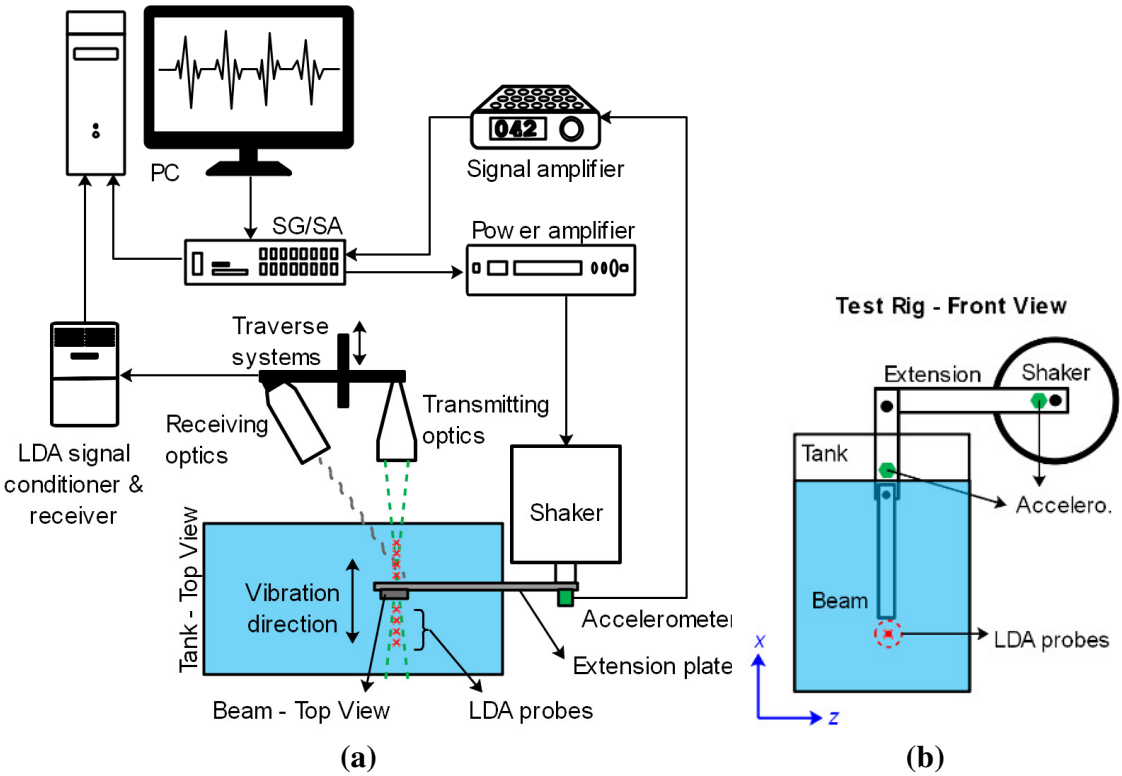

Figure 4.1. The schematic diagram of (a) the test rig and (b) the whole experimental apparatus

4.2.1. Description of apparatus and flow measurement principle

The schematic diagram for investigating fluid flow produced by a cantilever beam vibrating in water is illustrated in Figure 4.1(a). The mechanism to induce vibration in the submerged beam is the same as in Chapter 3. The PicoScope 2405A USB oscilloscope was used to generate sine wave signals for the LDS V201 shaker and record the voltage readings from accelerometer sensors. An L-Shaped plate was used to extend the beam to the desired testing position. The dimension of the plate was estimated such a way to not creating a complex dynamic interaction between the plate and the beam within the frequencies of interest. The beam was submerged into a rectangular glass tank with the size of a 40 x 25 x 25 *cm* filled with approximately 23.5 *L* of water. Note that the *y*- and *z*-axis direction shown in Figure 4.1(a) are for the projection of the test rig including the tank, extension plate and beam. Accordingly, the beam vibrates in the *y*-axis. The more

detailed view of the test rig is depicted in the *XZ*-plane displayed in Figure 4.1(b). Two accelerometers were used to monitor the input signal for the beam: one accelerometer was mounted close to the shaker, and the other accelerometer was attached to the clamped section of the beam. The vibration of the beam in the *y*-direction was expected to generate thrust in the *x*-direction. Therefore, the fluid measurement points were located below the free tip of the beam indicated with the red cross marker shown in Figure 4.1(b).

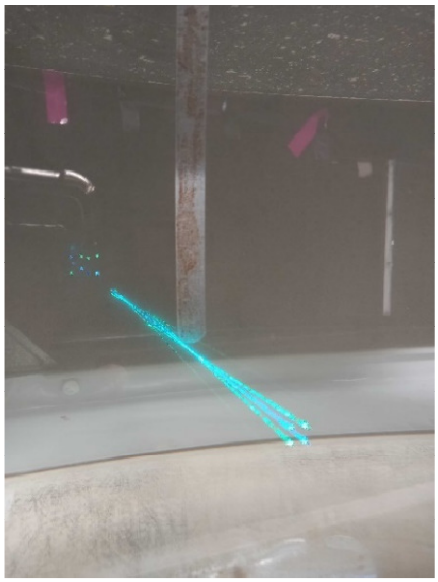

Figure 4.2. Four laser beams coinciding in one location

The fluid velocity around the beam was measured by a Dantec Dynamics two-component Laser Doppler Anemometry (LDA) system. This non-intrusive fluid measurement system mainly consists of laser, transmitting optics, receiving optics and traverse systems. Two diode-pumped solid-state 1*W* lasers with wavelengths of 488 *nm* and 514 *nm* were used to facilitate continuous wave lasers. The transmitting optics, which include laser beam splitters and focussing lenses, were used to diffract laser beams and shift their frequencies. The outputs of the beam splitters were directed with the focussing lens to intersect in the measurement point. Figure 4.2 displays four laser beams that coincide at one point below the beam. All laser beams were oriented at an angle of 2.5°, creating a volume measurement of 2.62 x 0.12 x 0.12 *mm*. The receiving optics, consisting of the lenses, filters and photodiodes, would detect the scattered light due to seeding particles that pass through the probe. The optical lenses for the transmitting and receiving optics were mounted on a Dantec 9041T3332 2D traverse system capable of generating a linear motion with an accuracy of ± 0.01 *mm*. Moreover, the seeding particles used to

scatter the light were silver-coated hollow glass spheres with the mean size of particles 10 μm.

A metal beam material with the length and width of 135 *mm* and 12.75 *mm*, respectively, was used for studying fluid flow around the vibrating structure. The thickness of the beam was varied to expand the analysis. Assuming the clamped section of the beam located in the *xy*-coordinate of (0, 0), Figure 4.3 illustrates the coordinate around the free tip of the beam. Note that the width of the beam is assumed to span along the *z*-axis. Therefore, the beam oscillates in the *y*-direction in the range of positive and negative values. By neglecting the torsional vibration, the transverse vibration of the beam induces fluid flow to the *x*- and *y*-direction. Although the 2D traverse system is capable of scanning the measurement points on the *xy*-plane, the probe locations were kept constant in the *x*-coordinate of 0.140 *m* for safety reasons to prevent reflection due to laser lights hitting the beam surface that could damage the receiving optics. Accordingly, the traverse system was operated to scan the measurement points along the *y*-axis from -0.025 *m* to 0.025 *m*. This location was defined on the basis where strong fluid flow occurred. The location of the fluid measurement in the *xy*-plane is illustrated with red arrows in Figure 4.3.

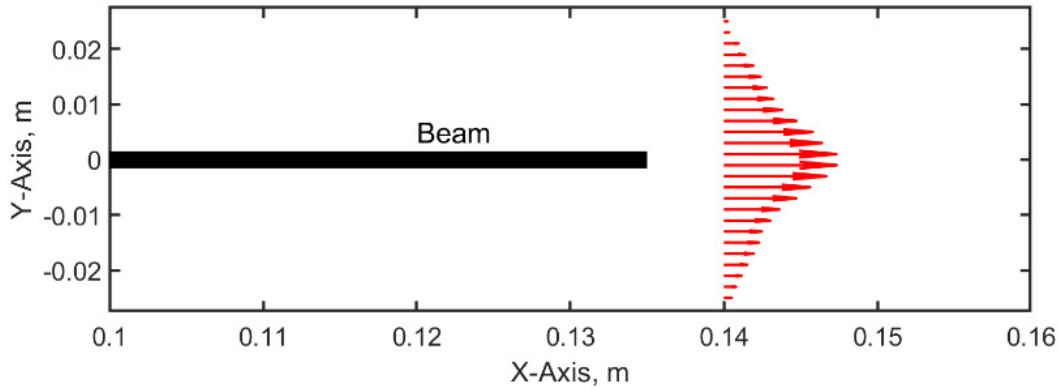

Figure 4.3. Fluid measurement location in the *xy*-plane

Before starting the LDA measurement, the water was stirred gently to distribute the seeding particles. This procedure was performed only if the experiment was suspended for a long time. Then, the beam was actuated with a particular forcing amplitude and frequency for some time not only to ensure the beam reaching steady states, but also to remove the influence of the water circulation due to the stirring process. The laser power was set to 110 *mW*. The laser intensity was regularly calibrated with a Thorlab S121C

standard photodiode sensor in conjunction with a Thorlab PM100USB power and energy meter. The LDA system began to measure fluid flow at the *y*-coordinate of -0.025 *m* which was set as the origin of the traverse system. The two velocity components of the LDA system detect instantaneous velocities of particles in the *x*- and *z*-direction. In an ideal case, the fluid movement in the *z*-axis is negligible and is not the interest of this study. Therefore, only the *x*-velocity component will be used in the analysis.

It is anticipated that the characteristics of velocity in the *x*-direction produced by the vibrating beam fluctuate at a certain velocity value, illustrated with the red solid line in Figure 4.4. Since the LDA collects random sampling of velocity data, the accuracy of the measurement depends on factors such as the sampling time, sampling rate, fluctuation amplitudes and seeding particles. The blue cross markers in Figure 4.4 illustrate the measured velocity by the LDA system. Consequently, the mean velocity from the measurement can be overestimated or underestimated depending on the total data sample. To facilitate adequate samples, the transit time of the traverse system was set to 120 *s* before moving to another measurement location. Since the traverse system was operated to scan 5 *cm* from *y* = -0.025 *m* to *y* = 0.025 *m* with the step size of 2 *mm*, this generated 26 measurement points which took about 1 hour to complete the measurement. Moreover, the rational justification for the transit time will be described in the next section.

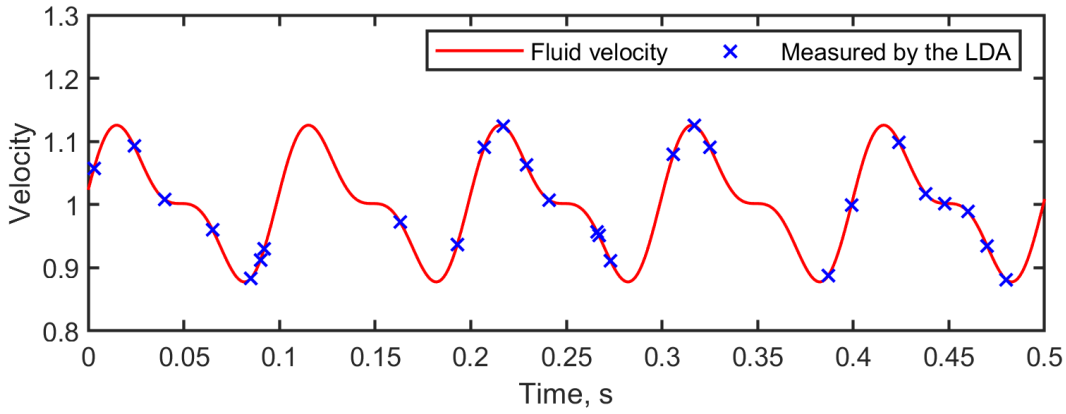

Figure 4.4. Fluid measurement example

4.2.2. Test 1: Beam with the thickness of 0.6 *mm*

The beam used in the fluid investigation had a thickness of 0.6 *mm*. The mass of the beam was 8.718 x 10^{-3} *kg*, resulting in the beam density of 8442 kg/m^3. The modulus of elasticity of the beam was undetermined and will be estimated from the FRF. The

procedures described in Section 3.3 were applied to obtain the FRF with random input signals. The accelerometer was located at the clamped section of the beam to monitor the base input acceleration, while the laser vibrometer was pointed to the free tip of the beam to acquire the velocity responses. Figure 4.5 presents the FRF of the beam vibrating in air and water for various input amplitudes. To generate those data, the frequency span was limited to 600 *Hz* with the maximum random amplitude varied arbitrarily at 400 *mV*, 600 *mV* and 800 *mV*. Note that the signal analyser automatically converted the velocity responses of the beam tip to the acceleration responses, resulting in dimensionless FRF magnitudes. This process might include filtering procedures that could underestimate the magnitude values. However, this should not influence the location of peaks with respect to frequency.

It is observed from the FRF of the beam vibrating in air shown in Figure 4.5 that the beam is rigid indicated with the first resonant frequency located at 24 *Hz*. There is also a notch (discontinuity) in the first peak which can be associated with the interaction of the beam and the supporting plate. This incidence has been thoroughly discussed in Section 3.4.1. The damping ratios for the first three resonant frequencies obtained from the signal analyser are 2.8%, 1% and 0.148%, respectively. It is noticed that the first damping ratio is considerably high. This might be caused by the nonlinearity due to the beam acting as dynamic absorbers of the supporting plate. Substituting the first three natural frequencies from the FRF to Eq. (3.8) results in the flexural rigidity value of 3.95 x 10^{-2} $N.m^2$, 3.92 x 10^{-2} $N.m^2$ and 4 x 10^{-2} $N.m^2$. The mean flexural rigidity is 3.97 x 10^{-2} $N.m^2$, rounded to the nearest integer.

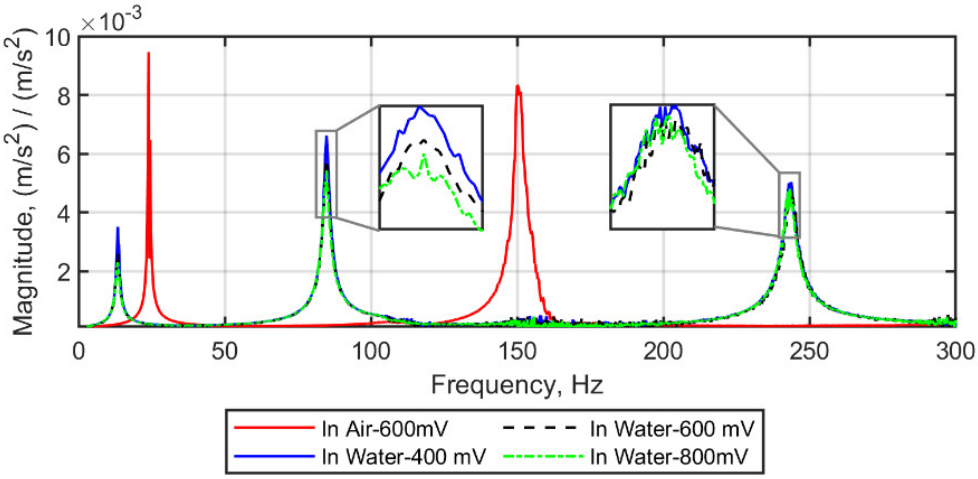

Figure 4.5. FRF of the beam with the thickness of 0.6 *mm* vibrating in different media

For the case of beams vibrating in water, there is a small deviation in the FRF magnitudes due to the variation of input amplitudes shown in Figure 4.5. This can be caused by the properties of the beam where it is 15 times thicker than the previous beam described in Section 3.5. The first three damping ratios extracted from the signal analyser with the amplitude of 600 *mV* are 4.496%, 1.272% and 0.841%. Substituting the first three natural frequencies of 13.48 *Hz*, 84.77 *Hz* and 243 *Hz* to Eq. (3.8) results in the mean modulus of elasticity of 4.48 x 10^{-2} N/m^2. The relative error of the mean E value for the beam vibrating in air and water is 4.6%. This agrees with the presumption in Chapter 3 stating that the approximation of fluid forces works well for estimating the dynamic behaviour of a rigid (solid) structure and tend to break down for flexible structure.

It has been mentioned in Section 4.2.1 that the transit time of the traverse system is paramount in the LDA measurement. To examine the appropriate transit time for the measurement, the beam was arbitrarily actuated with the frequency of 18 *Hz* and the base amplitude of 1.8 *mm*. The transit time was subjectively extended from 60 *s*, 90 *s* to 120 *s*. Figure 4.6 presents the average velocities in the x-direction obtained from the LDA measurement for various transit time. Note that the fluctuation in the velocity profiles was filtered with the *smoothdata* built-in function available in MATLAB. It is observed that all transit time values generate consistent results. Accordingly, the transit time 120 *s* was chosen to investigate the fluid flow for different forcing amplitudes and frequencies to facilitate adequate data samples, particularly at lower frequencies. Furthermore, the effect of water circulation due to stirring the water in the beginning process was also investigated. The dotted green line shown in Figure 4.6 presents the mean fluid velocity measured directly after stirring the water. It is observed that there is no notable discrepancy particularly at the peak with the coordinate of $y = 0$. The deviation occurs on the side of the velocity profile where the flow induced by the beam is minimum. Based on this measurement, it is believed that the fluid flow around the tip is only influenced by the beam and is not affected by water circulation due to the stirring process or reflection from the walls.

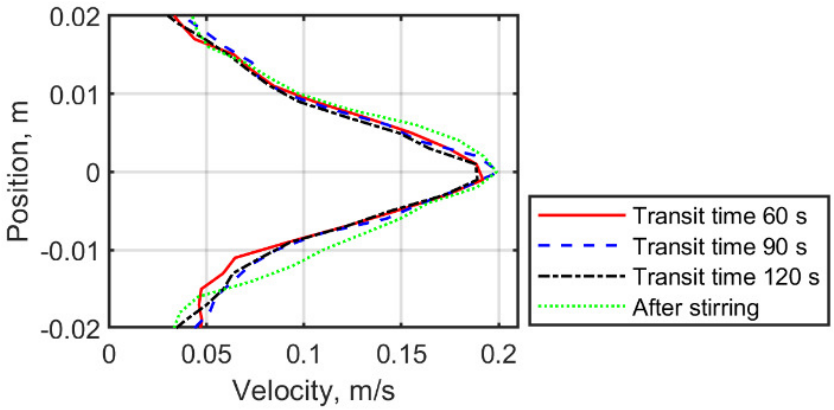

Figure 4.6. Influence of the transit time on the fluid velocity profiles

To further study the fluid flow, the base amplitude was maintained constant at 1.2 *mm*. This value was chosen to significantly generate fluid flow at low frequencies. Due to the limitation of the rig, the maximum forcing frequency was constrained to 35 *Hz* to prevent cavitation or bubble induced by vibrating beam which might affect to the fluid characteristics. The forcing frequencies were varied at 4 *Hz*, 9 Hz, 14 *Hz*, 18 *Hz*, 23 *Hz* and 30 *Hz*. The first three values are to demonstrate the characteristics of mean fluid velocities due to the first mode shape. The other values are to signify the influence of the first and second mode shapes when the beam is developing nodes and the beam tips have 180 degrees phase shift. The location of these forcing frequencies in the beam FRF is illustrated in Figure 4.7.

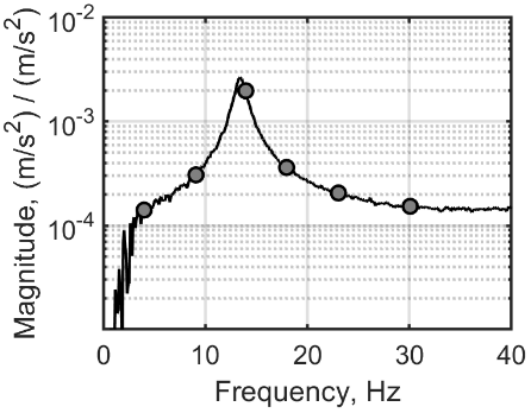

Figure 4.7. Location of fluid investigation in the beam FRF

Figure 4.8 displays the mean velocity from LDA measurements for various forcing frequencies. It is noticed at $f = 4$ *Hz* that the mean fluid velocity oscillates around zero. The fluctuation might be caused by very low velocities produced by the vibrating beam, creating uncertainties in the measurement. The base amplitude at this frequency is

estimated to be approximately 0.03 *m/s*. At 9 *Hz*, the velocity of the base amplitude and the maximum mean fluid is equal which is about 0.07 *m/s*. At the first resonant frequency, $f = 14$ *Hz*, the maximum mean fluid velocity is higher than the base amplitude velocity. It is noticed that the characteristics of the mean fluid velocity follow the trend line of the FRF. This trend line continues to the next regime where the phase shift of the beam tips is about 180 degrees. At $f = 18$ *Hz*, the maximum fluid velocity decreases to 0.12 *m/s* while the base input velocity increases to 0.14 *m/s*. The decrease in the maximum fluid velocity is observed until $f = 23$ *Hz* where the base velocity increase to approximately 0.23 *m/s*. At this frequency, the amplitude at the nodal point in the beam envelope becomes minimum and the phase delay between the two tips is nearly 180 degrees due to lack of damping contribution in the beam equation demonstrated in Section 3.7. However, the maximum fluid velocity rises from 0.1 *m/s* to 0.14 *m/s* at $f = 30$ *Hz*. This phenomenon will be further investigated with another beam dimension to reveal the fluid characteristics until the second resonant.

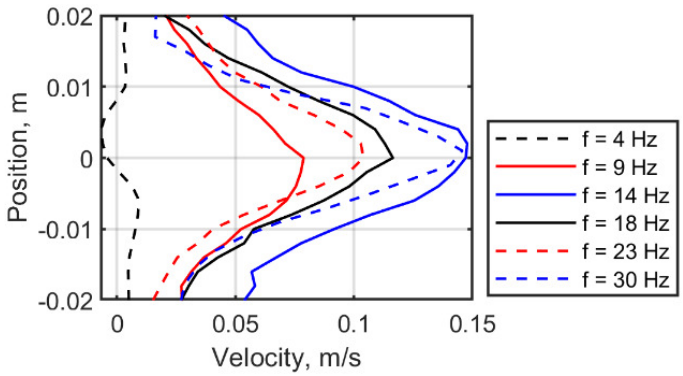

Figure 4.8. Fluid velocity profiles due to variation of forcing frequencies

Figure 4.9 presents the mean fluid velocity for various base amplitude and frequency. At 9 *Hz*, increasing the base velocity from 0.07 *m/s* to 0.11 *m/s* can increase the maximum mean velocity by about 2.5 times. On the contrary, increasing the base velocity at the resonant, $f = 14$ *Hz*, from 0.11 *m/s* to 0.18 *m/s* only improves the maximum fluid velocity about 1.5 times. Moreover, the maximum fluid velocity at $f = 18$ *Hz* also increases approximately 1.5 times when the base input velocity rises about 1.4 times, from 0.14 *m/s* to 0.20 *m/s*. These nonlinear relationships between the base input velocity and the maximum mean fluid velocity can be related to the beam FRF presented in Figure 4.5. At the resonant, the beam tip velocity decreases with increasing the base amplitude due to increasing the damping force. Conversely, the FRF magnitudes at 9 *Hz* and 18 *Hz* are

unchanged due to the variation in the base amplitude. Finally, these findings support the previous analysis for the constant amplitude with variation of forcing frequency where the fluid velocities highly depend on the beam FRF.

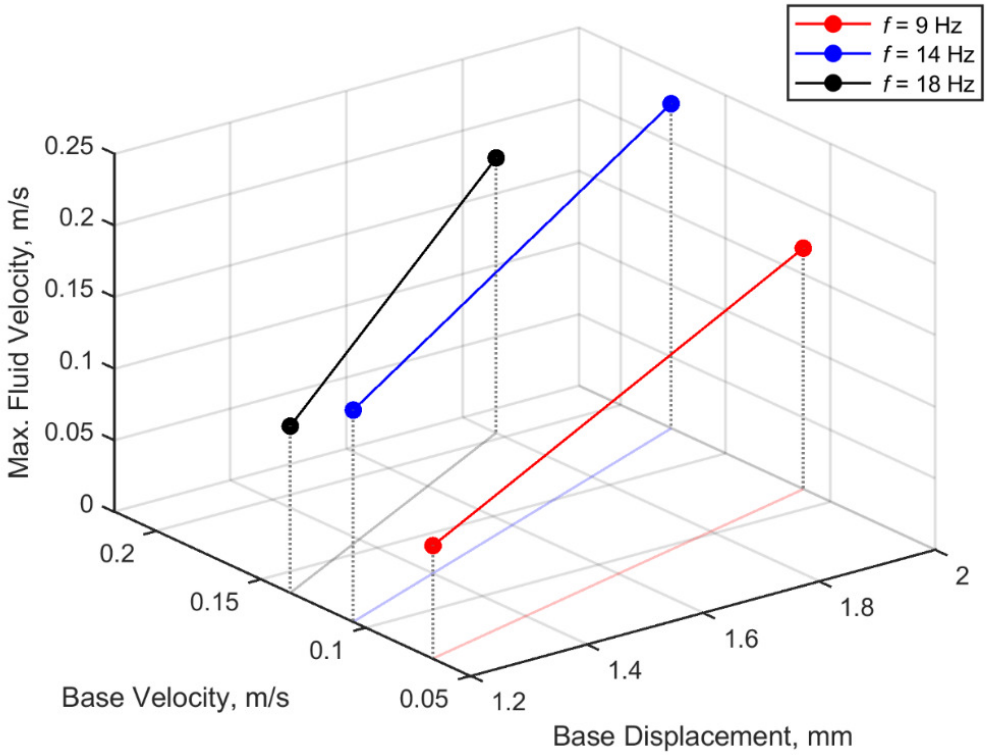

Figure 4.9. Influence of variation in the base amplitudes on the fluid velocity profiles

4.2.3. Test 2: Beam with the thickness of 0.3 *mm*

A metal beam with the thickness of 0.3 *mm* was used to examine the fluid flow between the first and two resonant frequencies. The mass of the beam is 4.457 x 10^{-3} *kg*, which leads to the estimated density of 8631 kg/m^3. The same procedures were applied to obtain the beam FRF. The time and frequency span for the signal analyser were set to 10.24 *s* and 312.5 *Hz* respectively, resulting in the frequency resolution of 0.09766 Hz. Figure 4.10 display the beam FRF in two different media for various forcing amplitudes. It is observed that the first natural frequency for the beam vibrating in air drops to 12 *Hz* due to the thickness reduction. There is no nonlinearity observed in the peak of the first resonant. Using the quadrature pick picking method, the damping ratio is estimated to be 1.22%. The second resonant frequency is located at 75.5 *Hz* with the estimated damping ratio of 2.070%. The second damping ratio may be influenced by the interaction of the beam and the supporting plate which also occur in the other measurement described in

Section 3.4 and 3.5. Substituting these natural frequencies to Eq. (3.8) results in the mean flexural rigidity of 5.10 x 10^{-2} $N.m^2$. For the beam vibrating in water, it is observed that the variation in the base amplitude can significantly change the magnitude at the peaks. The first three natural frequencies are obtained at 4.98 *Hz*, 32.90 *Hz* and 94.80 *Hz*, respectively. The first three damping ratio values at the amplitude of 600 *mV* are estimated about 8.654%, 5.473% and 2.775%, respectively. The mean flexural rigidity for the beam vibrating in water is 4.46 x 10^{-2} $N.m^2$. Accordingly, the relative error of the modulus of elasticity for the beam vibrating in air and water is 9.6%. The error increases due to thickness reduction which makes the beam more flexible than the previous beam with the thickness of 0.6 *mm*.

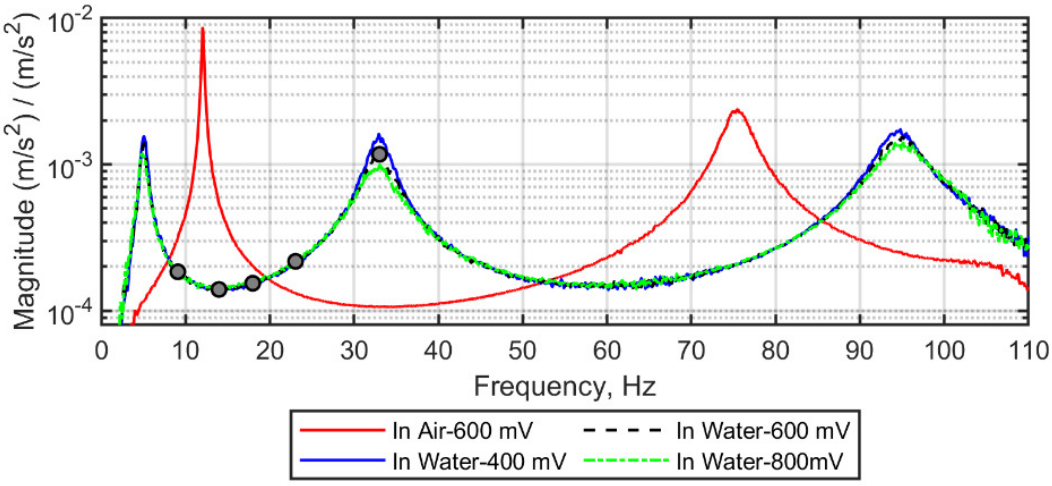

Figure 4.10. FRF of the beam with the thickness of 0.3 *mm* vibrating in air and water

The same LDA setup were used to investigate the fluid characteristics. The fluid measurement location was also located at the *x*-coordinate of 0.140 *m*, or 5 *mm* from the free tip of the beam. The base amplitude was maintained constant at 1.2 *mm*. The forcing frequencies were varied at 9 *Hz*, 14 *Hz*, 23 *Hz*, and 33 *Hz*. The location of these forcing frequencies in the beam FRF is illustrated with the grey circle markers in Figure 4.10. The first three values are intended to obtain the fluid characteristics when the beam is lack of travelling waves due to the minimum contribution of the damping. The last two values are to investigate the fluid flow around the second resonant frequency. In addition, these forcing frequencies are also aimed to provide a fair comparison between the beam with thickness of 0.3 *mm* and 0.6 *mm*.

Figure 4.11 presents the mean fluid velocity obtained from the LDA measurement for various forcing frequencies. As expected, the maximum mean fluid velocities follow

the trend line of the FRF. The least fluid velocity is obtained at 14 *Hz* where this frequency is located at the trough of the first and second peak of the FRF. At 9 *Hz*, the maximum mean fluid velocity is 0.04 *m/s*. At 18 *Hz*, the vibration of the beam only induces the maximum fluid velocity of 0.05 *m/s*. This value is far lower than the beam with the thickness 0.6 *mm*. At $f = 23$ *Hz*, the maximum mean fluid velocity increases to 0.11 *m/s*, which is comparable to the 0.6 *mm* beam. In addition, the fluid velocity value doubles when the beam is actuated at the resonant, $f = 33$ *Hz*. To conclude, the experimental results show that the characteristics of the maximum fluid velocity induced by the submerged cantilever beam have a linear relationship to the beam FRF. On the basis of these data, further investigations utilising numerical simulation will be carried out to obtain the influence of the node in the beam envelope, phase delay between two tips, beam mode shapes and vibration pattern of the beam on the fluid flow.

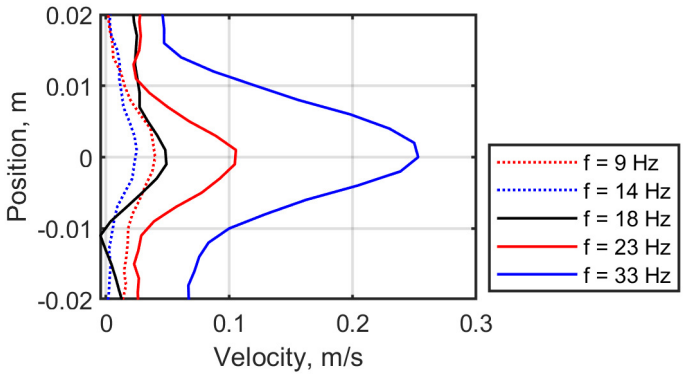

Figure 4.11. Fluid velocity profiles of the beam with the thickness of 0.3 *mm*

4.3. Numerical investigation of cantilever beam models

This section describes numerical investigation of the beam submerged underwater using a 3D Computational Fluid Dynamics (CFD) model. This model allows to examine the time series of fluid velocity at certain locations that can be used to reveal the fluctuation in the fluid generation. Fluctuations in the fluid flow can directly influence the mean fluid velocity.

4.3.1. Model description

This investigation uses the overset mesh method to facilitate the relative motion of the beam. Therefore, the CFD model consists of three domains: the solid (beam), overset

and background domain. These domains are built based on the 3D model using STAR-CCM+. The dimension of the solid domain is taken from the experimental measurement. In the CFD model, the unit of length is represented by the chord length, *c*, rather than in the metre or other units. 1 chord length is equivalent to the total beam length which, in this case, is 0.135 *m*. All parameters related to the unit of length are normalised with respect to the beam length. Accordingly, the thickness of the beam of 0.6 *mm* is equivalent to 0.0044*c*. The symmetry model is used to optimise the computational time. Therefore, the beam width for the CFD model is 0.047*c*, which is half of the experimental model. The geometry of the overset domain is 2*c* x 0.7*c* x 0.1*c* shown in Figure 4.12(a). The solid domain is located at the centre of the overset domain. At this location, the body of the overset domain is cut to the size of the solid domain to provide contact surface between the solid and fluid domains. Furthermore, the geometry of the background domain is 12*c* x 5*c* x 0.5*c* with an arrangement demonstrated in Figure 4.12(a). In addition, the length of the background domain is extended with respect to the free tip of the beam to avoid numerical instabilities occurred in downstream regions.

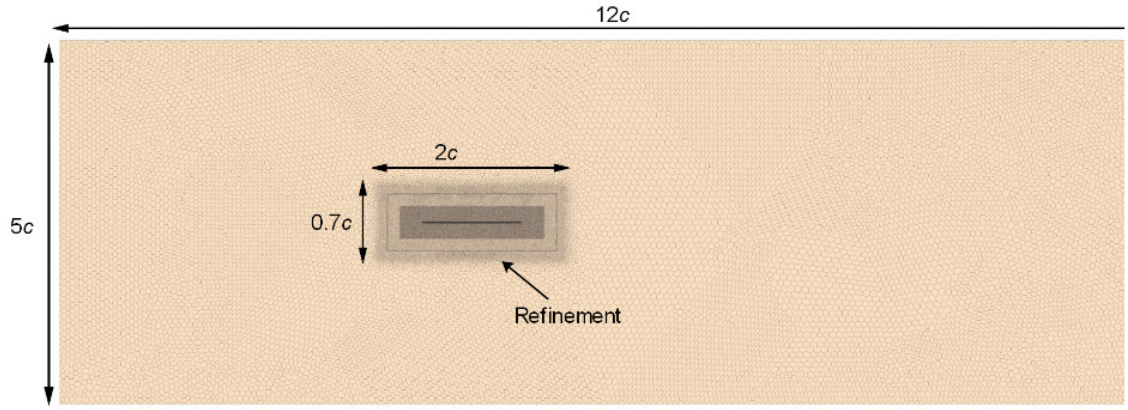

(a)

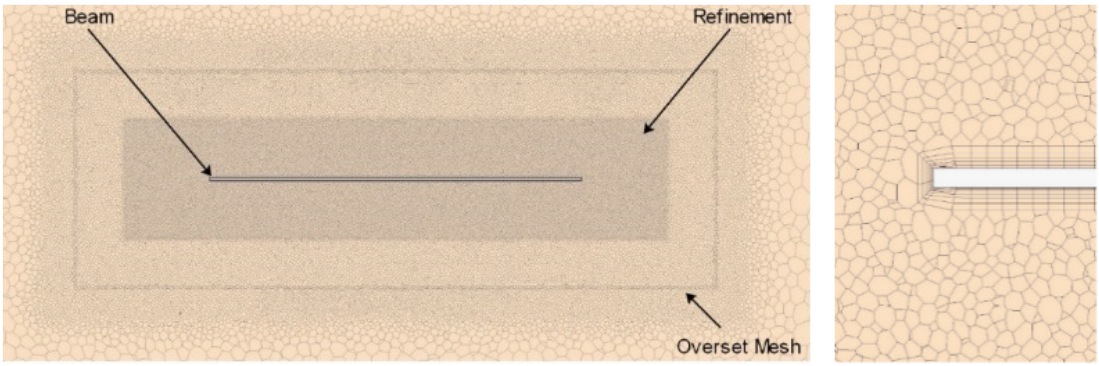

(b) **(c)**

Figure 4.12. (a) Global mesh domain; (b) Overset and background domain; and (c) Closer view of the beam

A 3D based-mesh is constructed with the built-in mesh features available in STAR-CCM+. This FSI problem requires different mesh strategies for the solid and fluid boundaries. For the solid domain, a hexahedral mesher is used to generate a uniform mesh. This is to facilitate a consistent contact interface to the boundary layers of the overset domain, allowing for data mapping between solid and fluid solvers. The meshes for overset and background domain are constructed with an unstructured polygonal mesher and a structured prism layer applied at the solid surface. A base size, which is the parameter to alter the grid density, is assigned for the overset and background meshes. Therefore, the surface, volumetric and refinement control parameters are changed proportional to the variation in the base size value. The surface and volume growth rate are set constant to 1.4 and 1.3, respectively. The surface control is applied to the background domain, allowing the structured mesh to grow from the near-fields of the overset mesh to the far-field of the background boundaries. The far-fields are set to 750% of the base size value. Figure 4.12(a) displays the mesh constructed with the base size value of 1 *mm*.

A part-based refinement is used to create a uniform mesh generation in the transition area of the overset and background domain shown in Figure 4.12(b). This is to ensure that there is no overlap between the two domains. In addition, the volumetric control for this refinement is set to equal to the base size value. Another part-based refinement, demonstrated in Figure 4.12(b), is also used to produce a fine and uniform mesh generation around the solid domain to capture fluid flow. The volumetric control for this fine refinement is set to 50% of the base size value. The prism layer was applied to the near-field boundary of the overset domain. The total prism layer thickness value is 0.0056*c*. The number of layers is constrained to 10 with the prism layer stretching value of 1.4. Figure 4.12 (c) shows the boundary layers in the near-field boundary of the overset domain. In addition, the minimum surface size this mesh is set to 1% of the base size value.

4.3.2. Flow physics and solver

Unsteady FSI simulations are performed in STAR-CCM+. The fluid density is assumed to be unchanged all over the continuum. The segregated flow solver is used to solve the conservation equations of mass and momentum in a sequential manner. The

Reynolds-Averaged Navier-Stokes (RANS) equations with the SST (Menter) $K-\omega$ turbulence model are used for flow computations. The density and dynamic viscosity of water are set to 997.561 kg/m^3 and 8.8871E-4 $Pa\text{-}s$, respectively. All fluid simulation settings, such as the convection scheme, turbulent viscosity, turbulent dissipate rate and under relaxation factor to name but a few, remain as default values. Furthermore, the solid stress model is used to estimate the dynamic responses of the beam under loads. This model is based on the finite element approaches for calculating displacement responses and the corresponding stress and strain. In addition, the solid model is assumed to fulfil the isotropic materials with a linear stress-strain relationship.

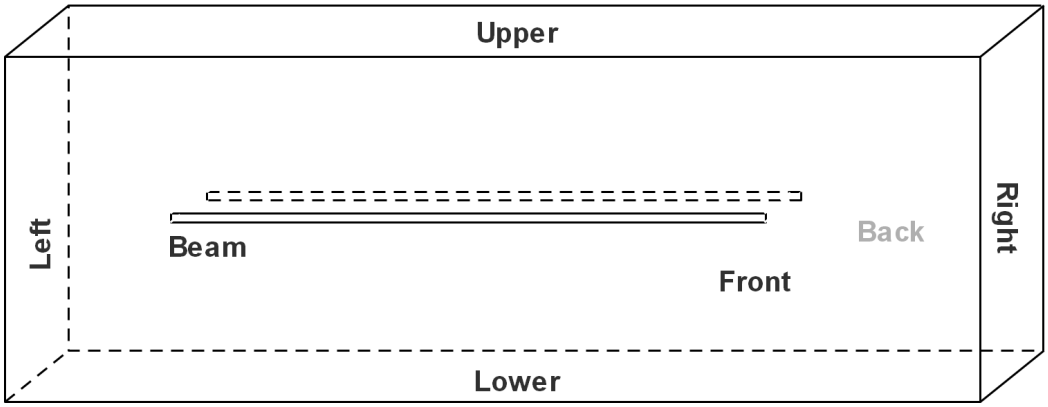

Figure 4.13. Surfaces for assigning boundary conditions

To define the relative motion of the beam in the simulation, the solid displacement module is assigned to the solid domain, allowing the body to deform based on the estimated stress and strain. The morphing module is applied to the overset domain to follow the movement of the beam. The contact surfaces between the solid and overset domain, so-called the solid-fluid interface, are assigned with the mapped contact interface module to exchange displacements and fluid forces every time. This two-way coupling is performed instantly in STAR-CCM+. The outer surfaces of the overset domain that overlaps with the background domain are assigned with the overset mesh module, commonly known as the Chimera or overlapping mesh. Figure 4.13 illustrates the surfaces of the tank domain for assigning boundary conditions. The wall boundary is applied to the upper, lower, left, right and back surface of the tank domain, while the symmetry plane is set to the front surface. The boundary conditions for the solid domain are set to the following configurations: (1) Symmetry plane at the front surface, (2) Free at the top, bottom, back and right surface, and (3) Constraint with prescribed displacement

at the left surface. In addition, the prescribed displacement is used to define the base motion for the beam.

The second order temporal scheme is chosen for the implicit unsteady solver to reduce numerical dissipation and dispersion. A fixed time step is implemented in the simulation. The time step is set to, at least, 1/70 of a period, depending on the operating frequency to reduce the computational cost. Once the beam and fluid responses reach steady states, the simulation is stopped. Therefore, the total time for simulation varies according to frequencies. The simulation is mainly to record the time series of the dynamic responses of the beam and the local velocity around the beam tip. Furthermore, certain criteria are set to ensure that the residuals fall below a certain threshold. The first criterion was that all the main residuals, such as continuity, x-momentum, *y*-momentum and z-momentum, must reach a residual value of 1.0×10^{-4} before progressing to the next time-step. If these criteria cannot be achieved due to convergence issues, then the maximum number of inner iterations is set to 150. Accordingly, the simulation will progress to the next time-step if the number of inner iterations exceeds 150 as a result of not meeting the requirements for the two set criteria.

4.3.3. Grid convergence and validation

A mesh independence study is performed to examine when the fluid flow becomes invariant to the change in the mesh grid. To achieve this, the base size value is assigned with three different numbers such as 0.0015 *m*, 0.001 *m* and 0.00075 *m* which result in the total cell counts for the entire domain of 0.72 mill., 2.15 mill. and 4.89 million cells, respectively. The coarse grid, denoted by G1, is used to provide an initial solution for the simulation. All grids are assessed against the finest grid, G3. Since there is no external flow, the movement of the fluid depends on the displacement of the beam. Therefore, boundary layers become paramount to approximate the transfer of kinetic energy from the beam to the liquid. Inappropriate boundary layer setup can lead to underestimated flow around the structure. Moreover, the bending vibration of the beam can stretch the overset domain which may alter fluid features and generate numerical instabilities. Accordingly, the thickness of the prism layer for the coarse grid is also varied to demonstrate that the fluid flow is already independent of the change in the boundary layers.

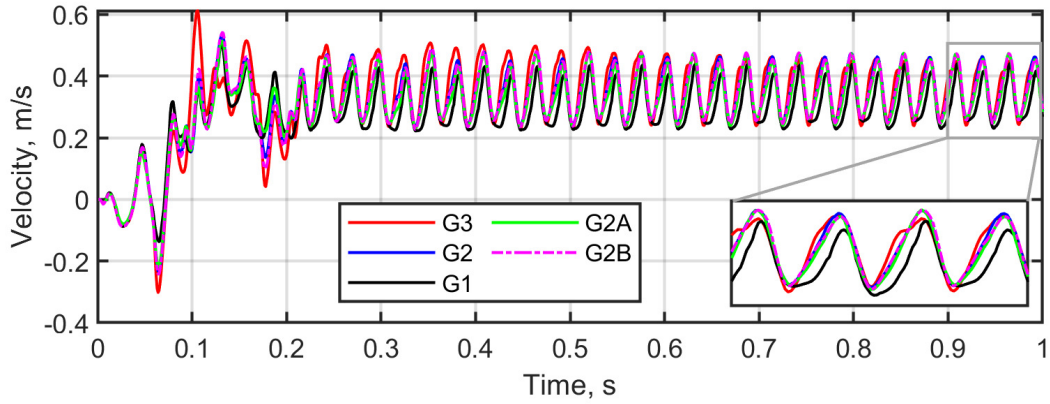

Figure 4.14. Time series of fluid velocities probed at the (x, y) coordinate of (0.137, 0)

The mesh study is conducted by assigning the left surface of the solid domain with a sinusoidal wave with the amplitude and frequency of 1.8 *mm* and 18 *Hz*, respectively. Figure 4.14 displays time series of fluid velocities for various mesh grid at x = 0.137 *m* and y = 0 *m*. As expected, there is a remarkable variation for all grids in the transient responses, particularly up to 0.4 *s*. In the steady state, the mean velocities for G1, G2 and G3 are 0.3159 *m/s*, 0.3604 *m/s* and 0.3646 *m/s*, respectively. the relative error for the mean velocity between the coarse grid, G1, and finest grid, G3, is estimated about 13.36%. The grid G2 can obtaining a low level of variance when compared to the grid G3, while achieving an approximate 44% reduction in the total cell count. Furthermore, the grid G2A and G2B are generated by changing the thickness of the prism layers for the medium grid to 0.0002c and 0.0075c, respectively. It is seen that there is no remarkable discrepancy in the time series of fluid velocity due to the variation in the thickness of boundary layers.

To provide validation, the finest grid G3 is replaced with the experimental data. Figure 4.15 displays the mean fluid velocities at x = 0.140 *m* for various mesh grid. It is observed that the mean velocities for all grids at x = 0.140 *m* and y = 0 *m* drop approximately 44% compared to those at x = 0.137 *m* and y = 0 *m*. An insignificant deviation is also found in the maximum mean velocities for all grids compared to the experimental result. However, the peaks for the coarse grid G1, G1A and G1B are offset from the y = 0 *m*. Moreover, they also demonstrate asymmetrical curves. On the contrary, the grid G2 provides a symmetry average velocity, and the peak is almost superimposed with the experiment data. Therefore, the grid G2 is determined as mesh independent as it produces an accurate resolution and is selected to be used in the fluid investigation.

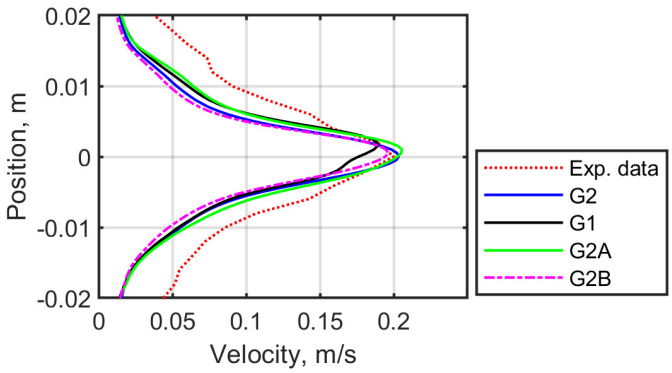

Figure 4.15. Comparison of the mean fluid velocity of the experimental data and numerical simulation

4.3.4. Discussion on the fluid characteristics around the first two resonant frequencies

The numerical simulation is expanded using the grid model G2 to further investigate the fluid characteristics of the 0.6 *mm* beam. The base amplitude is maintained constant at 1.2 *mm*, and the forcing frequency is varied according to the experiment. Figure 4.16 presents the velocity responses of the beam for various frequencies. Note that the first row represents the beam envelope, and the second row demonstrates the propagation of the velocity over time. At $f = 9$ *Hz*, the beam vibrates in the first mode shape with the tip velocity ratio of 2.17. The tip ratio is defined as the ratio of the tip velocity to the base input velocity of the beam. Moreover, the vibration pattern demonstrates a slight phase delay between the tips. At the resonant, $f = 14$ *Hz*, the tip velocity ratio increases to 2.66, and the beam achieves the maximum phase delay. After passing the first peak, the tip ratio decreases to 1.96 at $f = 18$ *Hz*. Although the tip ratio at 18 *Hz* is higher than that at 23 *Hz*, the maximum mean fluid velocity shown in Figure 4.8 demonstrates otherwise. Accordingly, the maximum mean fluid velocity is determined by the beam tip velocity rather than the tip ratio as suggested by the maximum value of the tip velocity at 23 *Hz* exceeding the tip velocity value at 18 *Hz*. A similar phenomenon can also be seen at 14 *Hz* and 30 *Hz* where the two frequencies demonstrate comparable values for the beam tip velocity and the maximum mean fluid velocity. Since the beam at 30 *Hz* vibrates in the second mode shape and the tip ratio is almost unity, it can be concluded that the phase delay and the mode shape do not determine the maximum fluid velocity particularly around the first resonant frequency.

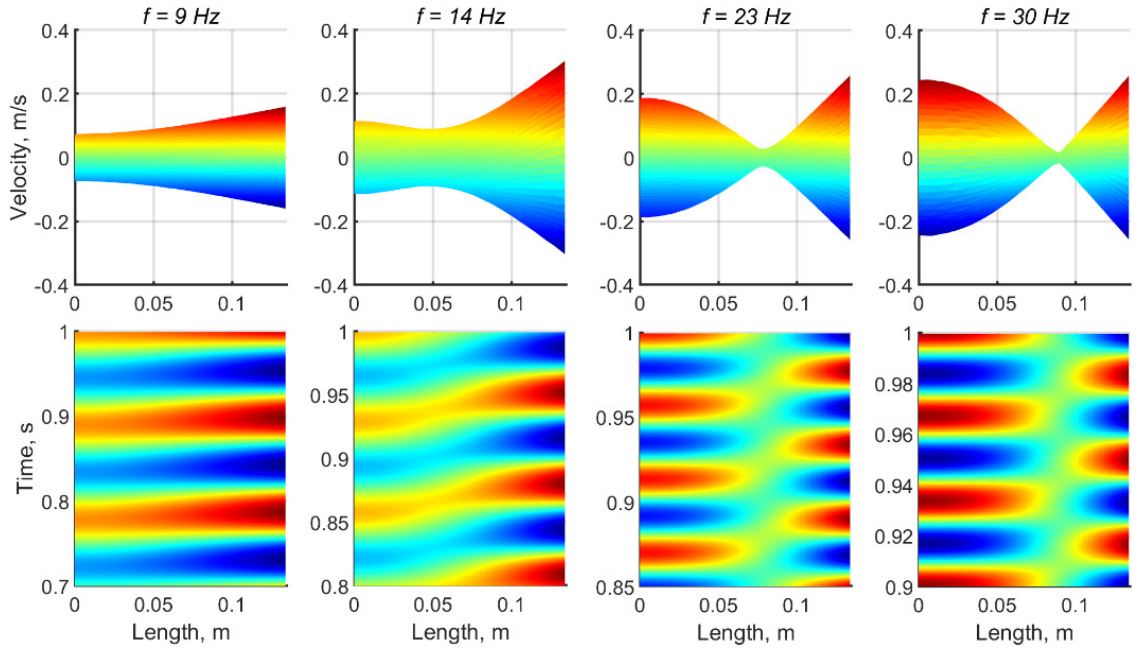

Figure 4.16. Velocity responses of the 0.6 *mm* beam vibrating in water

To obtain the fluid features due to the beam vibrating in the first mode shape, Figure 4.17(a) and (b) present the time series of fluid velocity in the *y*-direction (vertical) and *x*-direction (horizontal) actuated with $f = 9$ *Hz* probed at $x = 0.137$ *m*, respectively. It is noticed by comparing Figure 4.16 and Figure 4.17(a) that maximum velocities of the beam and fluid have 90 degrees phase shift. This indicates that the fluid velocity is directed solely by the displacement of the tip. The highest fluid velocities occur once the tip displacement passes the peak or the trough. With the maximum tip displacement of 2.6 *mm*, the maximum value for the horizontal fluid velocity component shown in Figure 4.17(b) is 0.31 *m*/*s*. However, the maximum mean velocity is estimated to be 0.17 *m*/*s*. At $x = 0.140$ *m*, the horizontal fluid velocity presented in Figure 4.17(b) decreases remarkably about 54%. The maximum mean velocity is approximately 0.076 *m*/*s* which is equal to the maximum mean velocity value obtained from experiments shown in Figure 4.8. The significant drop occurred at 9 *Hz* is due to high tip displacement amplitudes that induce more fluctuation in the fluid velocity. On the contrary, low displacements can promote more uniform fluid generations and reduce the fluctuation in the fluid velocity.

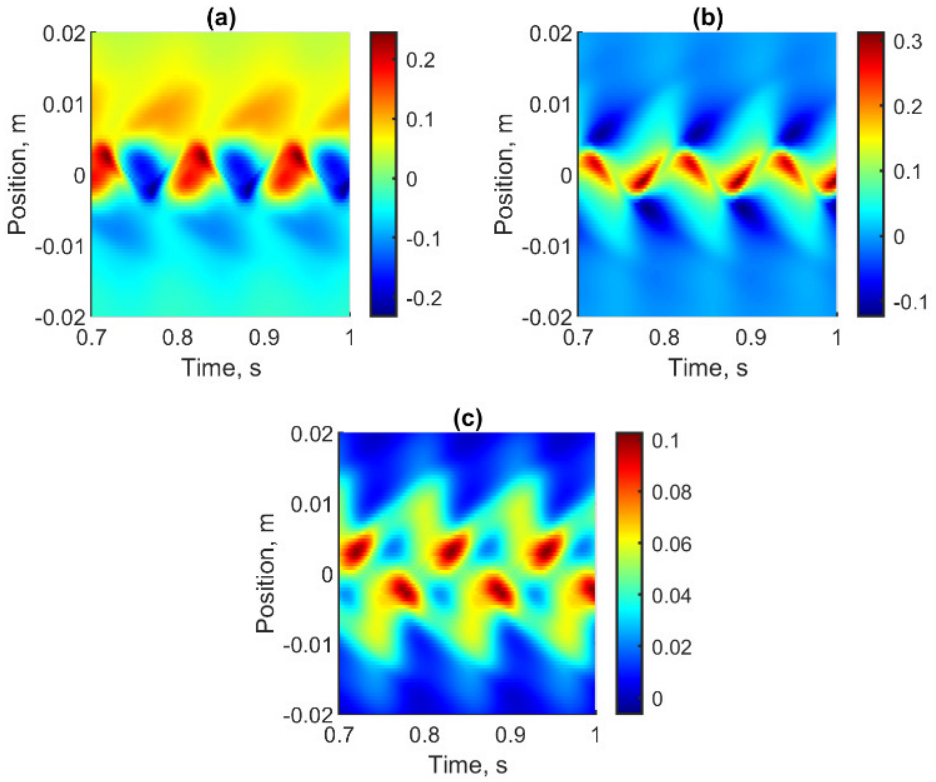

Figure 4.17. Fluid velocity of the 0.6 *mm* beam actuated with 9 Hz probed at (a)-(b) x = 0.137 *m* and (c) x = 0.140 *m*

Figure 4.18(a) presents the characteristics of the horizontal fluid velocity component at x = 0.137 *m* actuated with f = 30 *Hz*. The maximum fluid velocity is obtained about 0.42 *m*/*s*, while the maximum mean velocity drops to 0.3 *m*/*s*. Probed at x = 0.140 *m*, the maximum fluid velocity shown in Figure 4.18(b) only reduces 43% to 0.24 *m*/*s* with the maximum mean fluid velocity of 0.15 *m*/*s*. Therefore, it can be concluded that the amplitude of the tip displacement can influence the fluctuation in the fluid velocity particularly around the first resonant frequency.

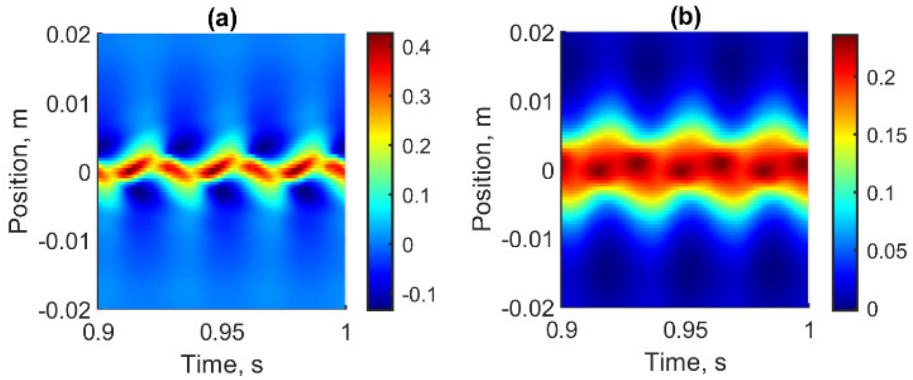

Figure 4.18. Time series of horizontal fluid velocity components at 30 Hz obtained at (a) x = 0.137 *m* and (b) x = 0.140 *m*

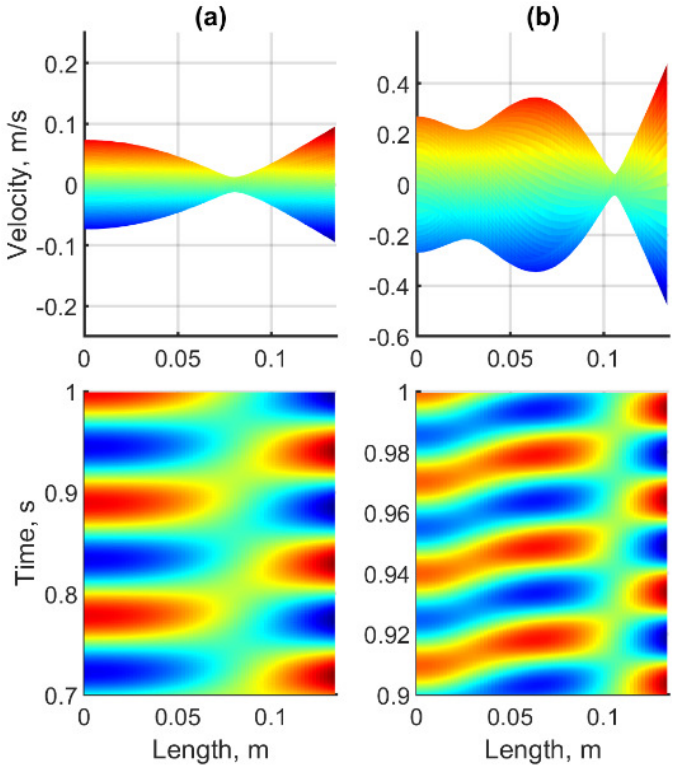

Figure 4.19. Velocity responses of the 0.3 *mm* beam vibrating at (a) 9 *Hz* and (b) 33 *Hz*

The 0.3 *mm* beam is used to further explore the fluid characteristics at the second resonant. The thickness of the solid domain is reduced to $0.0022c$. The mesh configuration follows the grid model G2, and all simulation parameters remain the same as described in Section 4.3.2. The base amplitude is kept constant at 1.2 mm. Figure 4.19(a) displays the beam velocity actuated at $f = 9$ *Hz*. It is observed that the tip ratio is approximately 1.3, and the maximum tip velocity is about 0.1 *m/s*. The tip velocity value is the reason why the fluid velocity of the 0.6 *mm* beam exceeds the 0.3 *mm* beam. At the resonant frequency, $f = 33$ *Hz*, the velocity responses of the beam are presented in Figure 4.19(b). Strong travelling waves are observed in the vibration pattern with the tip velocity ratio approximately 1.78. Furthermore, the time series of fluid flow probed at $x = 0.137$ *m* is displayed in Figure 4.20. Although the fluid demonstrates less fluctuation than the 0.6 *mm* beam, high displacements due to vibrating in the resonant frequency induce more fluctuation in the fluid velocity shown in Figure 4.20(b). With the tip velocity exceeding 0.4 *m/s*, the maximum fluid velocity surges to more than 0.8 *m/s*. However, the maximum mean velocity drops almost 35% to 0.59 *m/s*. This indicates that the tip velocity ratio at the second resonant also influences the fluctuation in the fluid flow. In addition, these

demonstrations reveal that the fluid flow in the first two mode shapes are determined solely by the tip velocity.

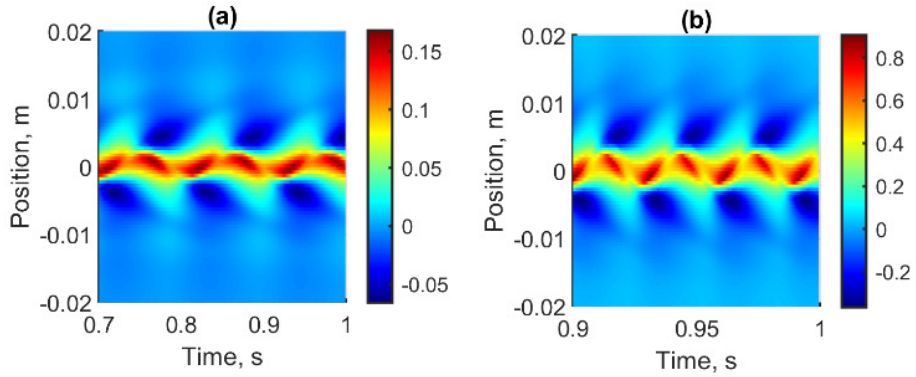

Figure 4.20. Time series of fluid velocity actuated at (a) 9 *Hz* and (b) 33 *Hz*

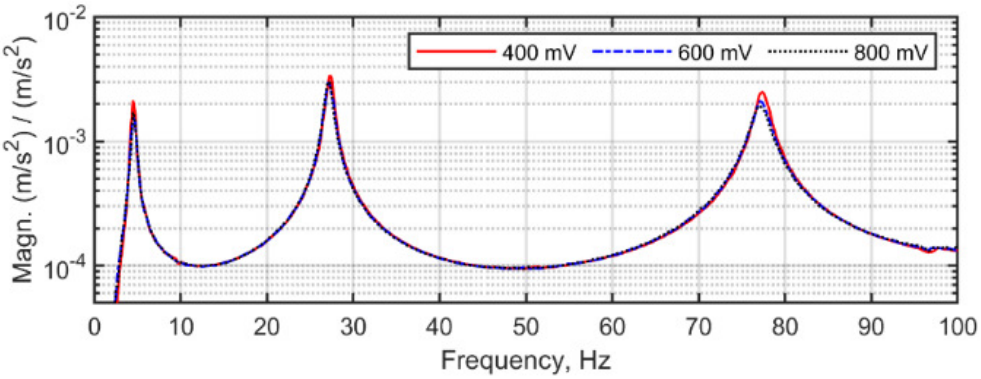

Figure 4.21. FRF of the 0.1 *mm* beam vibrating in air

4.3.5. Higher resonant frequencies

The fluid investigation has been limited to the second resonant. Therefore, a thinner beam is used to explore characteristics of fluid flow up to the fourth resonant. The beam has the thickness of 0.1 *mm* with the same length and width as the previous beam described in Section 4.2. The beam density is estimated to be 8500 kg/m^3. The same procedures were used to obtain the beam FRF. Figure 4.21 presents the FRF of the cantilever beam with the thickness of 0.1 *mm* vibrating in air obtained from experimental measurements with random inputs. The estimated damping ratio values from the first three peaks of the FRF with the amplitude of 600 *mV* are 6.362%, 1.759% and 1.171%, respectively. The damping ratio becomes higher than the other two beams due to damping from materials and interaction with air. The first three natural frequencies are

approximately 4.50 *Hz*, 27.25 *Hz* and 77.25 *Hz*, respectively. Using Eq. (3.8), the mean flexural rigidity is approximately 2.23 x 10^{-4} $N.m^2$.

Note that the first torsional natural frequency for a cantilever beam is typically located between the third and fourth resonant frequency of the bending (transverse) vibration. The torsional vibration may introduce unique fluid phenomena which are not the interest of this study. Accordingly, a 3D modal analysis was carried out using ABAQUS since the experimental apparatus is not capable of performing the FRF for the torsional vibration. The first and second torsional resonant frequencies are obtained at 89.52 *Hz* and 268.55 *Hz*. To obtain the natural frequencies for the beam vibrating in water, the first five natural frequencies, including the torsional resonant, are substituted to Eq. (3.8), resulting in the natural frequency values of 1.23 *Hz*, 7.73 *Hz*, 21.65 *Hz*, 25.08 *Hz* and 42.43 *Hz*. It should be noted that the resonant frequency of 25.08 *Hz* is the torsional vibration of the beam in water.

Numerical simulation is performed using the mesh grid G2 to simulate the dynamic responses of the 0.1 *mm* beam. The thickness of the solid domain of the CFD model is reduced to 0.00074*c*. The simulation parameters are the same as explained in Section 4.3.2. The base amplitude and frequency are taken from the experimental data. Figure 4.22 displays the tip displacement ratio for various forcing frequency obtained from numerical simulation using STAR-CCM+. To investigate the influence of the torsional vibration, the results from numerical simulation are superimposed with the analytical model for transverse vibration of the cantilever beam vibrating in water derived in Chapter 2. The stepped sine waves were implemented to obtain the analytical model with the forcing frequency varied from 0.5 *Hz* to 35 *Hz*. The base amplitude, A_f, were maintained constant at 1.2 *mm*. It is observed that the discrepancy between the two approaches occurs at 18 *Hz* and 23 *Hz*. Since the analytical model only consider the transverse vibration of the beam, the discrepancy can be caused by the influence of the first natural frequency of the torsional vibration on the STAR-CCM+ model. Therefore, the forcing frequency of 18 *Hz* and 23 *Hz* will not be included in the analysis.

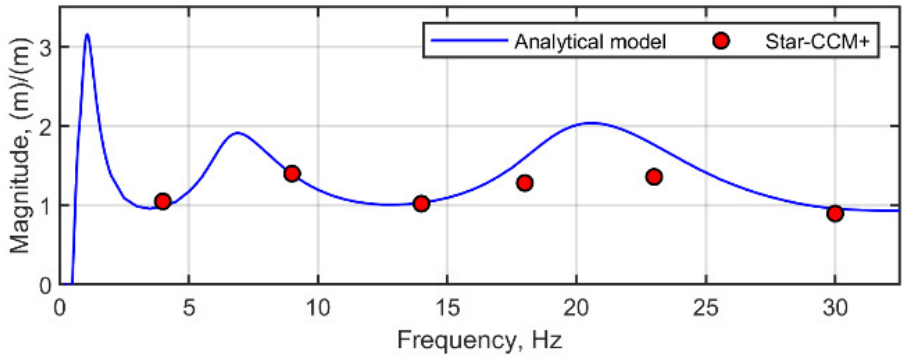

Figure 4.22. The frequency series of the tip displacement ratio of the 0.1 *mm* beam obtained from analytical approaches and numerical simulation

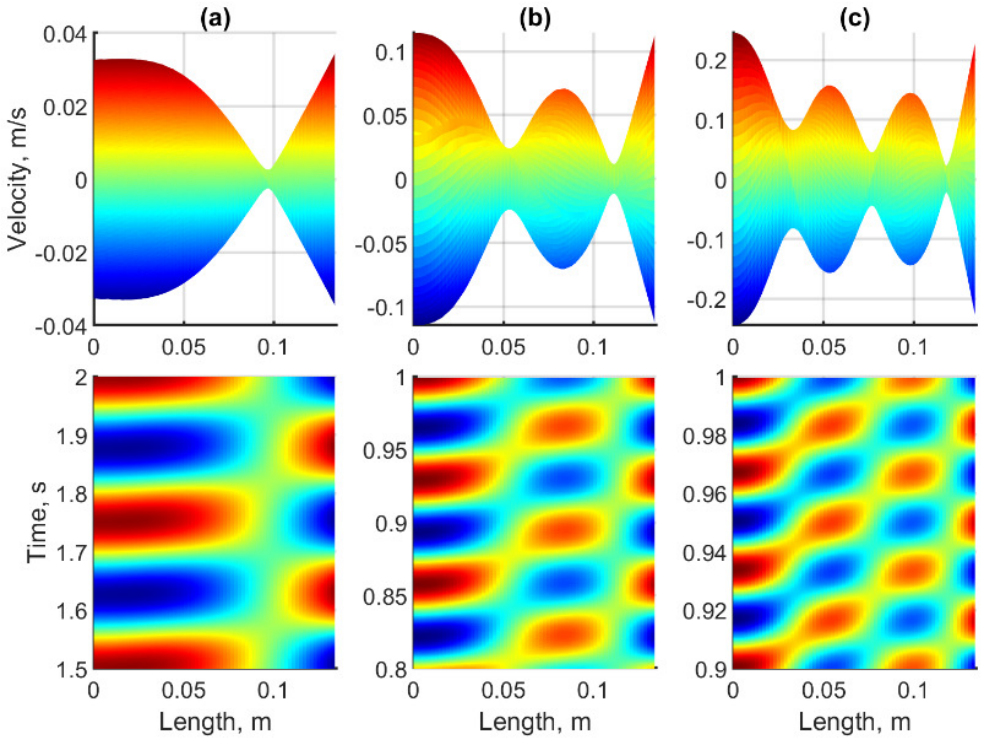

Figure 4.23. Velocity responses of the 0.1 *mm* beam actuated with (a) $f = 4$ *Hz*, (b) $f = 14$ *Hz* and (c) $f = 30$ *Hz*

Figure 4.23 displays the velocity responses of the 0.1 *mm* beam for various forcing frequencies. It is observed that the beam at 14 Hz vibrates in the third mode shape. With the tip velocity about 0.12 m/s, the maximum fluid velocity generated at $x = 0.137$ *m* is 0.23 *m/s*. Note that the fluid velocity is not shown here for brevity. As expected, the fluid velocity demonstrates less fluctuation due to the tip ratio equal to unity. At $f = 30$ *Hz*, the beam vibrates in the fourth mode shape. The vibration pattern also presents strong travelling waves. The maximum fluid velocity at $x = 0.137$ *m* is 0.39 *m/s*, and this value drops 28% to 0.28 *m/s* at $x = 0.140$ *m*. Moreover, the velocity drop at $x = 0.140$ *m* of the

0.1 *mm* beam is lower than that of the 0.6 *mm* beam. However, it is unclear this incident is due to the contribution of the mode shape and/or the vibration pattern. Therefore, further investigation is needed to reveal the influence of those variables on the fluid dynamics.

4.4. Numerical investigation of two-excitation beam models

The travelling waves induced by the cantilever beam models are passive travelling waves. Therefore, it is impractical to compare the effect of travelling waves on the fluid dynamics of the two beams due to inconsistent travelling wave contents over frequencies. In this section, a mechanism to generate active travelling waves is described and the characteristics of vibration in vacuum and water are also presented.

4.4.1. Model description

To facilitate maximum travelling waves over wide range frequencies, each beam tip needs to be actuated with a forcing mechanism that can manipulate the phase of the wave. There are two most common mechanisms used to actuate the beam submerged in liquid: piezoelectric- and magnetic-based actuators. In this study, the magnetic-based actuator is used as the forcing mechanism to control the beam tips. Figure 4.24(a) depicts the schematic diagram of the forcing mechanism for the beam. This arrangement is adopted from a micropump system developed in reference [45]. Permanent magnets are mounted on each beam tip. The other permanent magnets, located outside of the tank, are coupled to a rotating shaft. By rotating the shaft in one direction with a certain frequency, this will reverse the poles of the magnetic fields that can be used to either attract or repel the permanent magnets attached on the beam. This mechanism is equal to giving a periodic oscillation to the beam. The phase delay between the two tips is achieved by adjusting the pole 90-degree out of phase for the permanent magnets that are mounted on the shaft illustrated in Figure 4.24(a). In addition, this non-contact actuation can be miniatured to create artificial swimmers for transport devices.

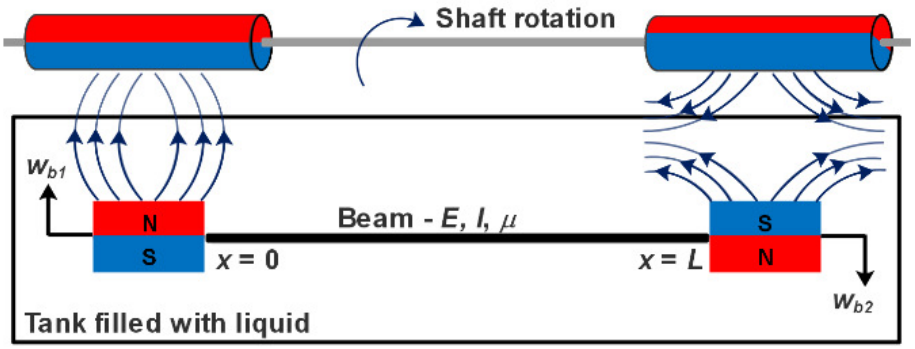

(a)

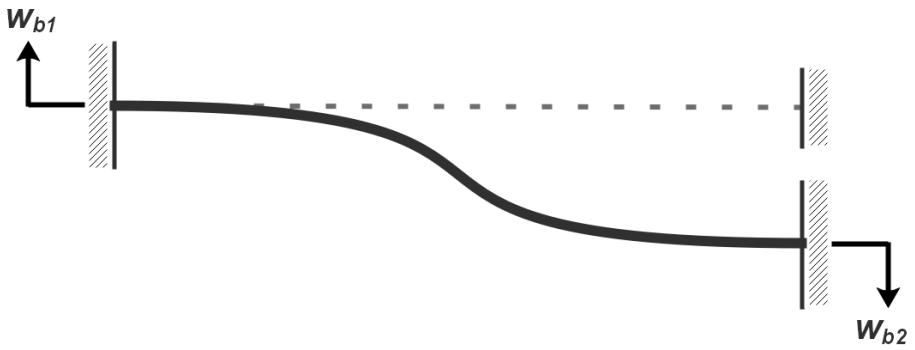

(b)

Figure 4.24. (a) Schematic diagram of the forcing mechanism for the beam, and (b) the simplified representation of the two-excitation beam model

Since the beam is mounted to the permanent magnets which are assumed to be solid, this configuration prevents the slope occurred at the beam tips. Assuming the magnets undergoes rigid body movement without rotation, the beam can be modelled as a fixed-fixed beam with moving supports illustrated in Figure 4.24(b). From the figure, the base input motion for w_{b1} and w_{b2} is defined as $w_{b1} = A_{f1}\sin(2\pi ft + \theta_1)$ and $w_{b2} = A_{f2}\sin(2\pi ft + \theta_2)$. In addition, the first-four values for the terms β_n/L for the clamped-clamped beam configuration are 4.7300, 7.8532, 10.9956 and 14.1372 [106].

4.4.2. Vibrating in vacuum

The 0.1 *mm* beam is used to investigate basic vibration characteristics of the two-excitation beam model up to the fourth resonant frequency. A 3D numerical simulation is performed in STAR-CCM+ with only using the solid domain model to simulate the beam vibrating in vacuum. The solid stress module is implemented in conjunction with the Rayleigh damping model to assign the damping due to material. The damping ratio is

assumed to be constant 0.5% for the first-five resonant frequencies. The natural frequencies are obtained by substituting the β_n value for the clamped-clamped beam, the beam dimension, and its material properties provided in Section 4.3.5 to Eq. (3.8). The first four natural frequencies for this beam configuration vibrating in vacuum are 28.04 *Hz*, 77.28 *Hz*, 151.50 *Hz* and 250.40 *Hz*. Using the surface analogy illustrated in Figure 4.13, the base motion w_{b1} is assigned to the left surface and w_{b2} is applied to the right surface of the solid domain. The base amplitudes A_{f1} and A_{f2} are set constant to 0.5 *mm* to avoid axial stretching of the beam which can induce nonlinearity phenomena. The phase θ_1 and θ_2 are set to 0 and $\pi/2$, respectively. The forcing frequency, ω_f, is varied arbitrarily to investigate the beam responses close and away from resonant frequencies.

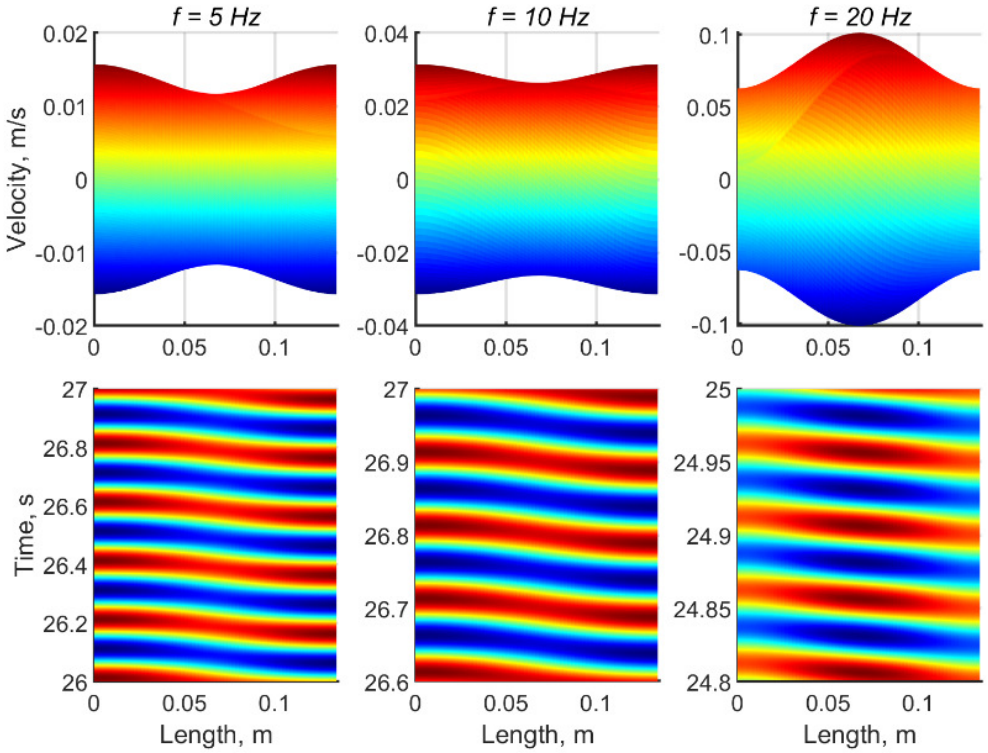

Figure 4.25. Velocity responses of the beam vibrating in the first mode shape

Figure 4.25 presents the velocity responses of the beam actuated around the first resonant frequency. It is observed that this configuration can successfully generate travelling waves. Due to the input parameter θ_1 and θ_2, the waves travel in the negative direction, from x = 0.135 *m* to x = 0 *m*. For this configuration, the tip velocity ratio is always unity. The changes of amplitude only occur in the middle of the beam. With the forcing frequency approaching to the first resonant, the amplitude at the middle of the beam increases shown at f = 20 *Hz* in Figure 4.25. The velocity responses of the beam

actuated between the first and second resonant frequency is displayed in Figure 4.26. It is observed that the waves change to the positive direction, travelling from $x = 0$ *m* to $x = 0.135$ *m*. This is due to the nature of the second mode shape that forms one peak and one trough in the beam envelope with a 180-degree phase shift. At the frequency close to the fist resonant, $f = 30$ *Hz*, the beam demonstrates standing wave patterns. The same case is also observed at the frequency close to the second resonant, $f = 70$ *Hz*, where the node presents at the middle of the beam, creating discontinuity in the propagation wave. On the contrary, the travelling waves are only observed when the forcing frequency is set away from resonant as indicated at $f = 50$ *Hz* shown in Figure 4.26.

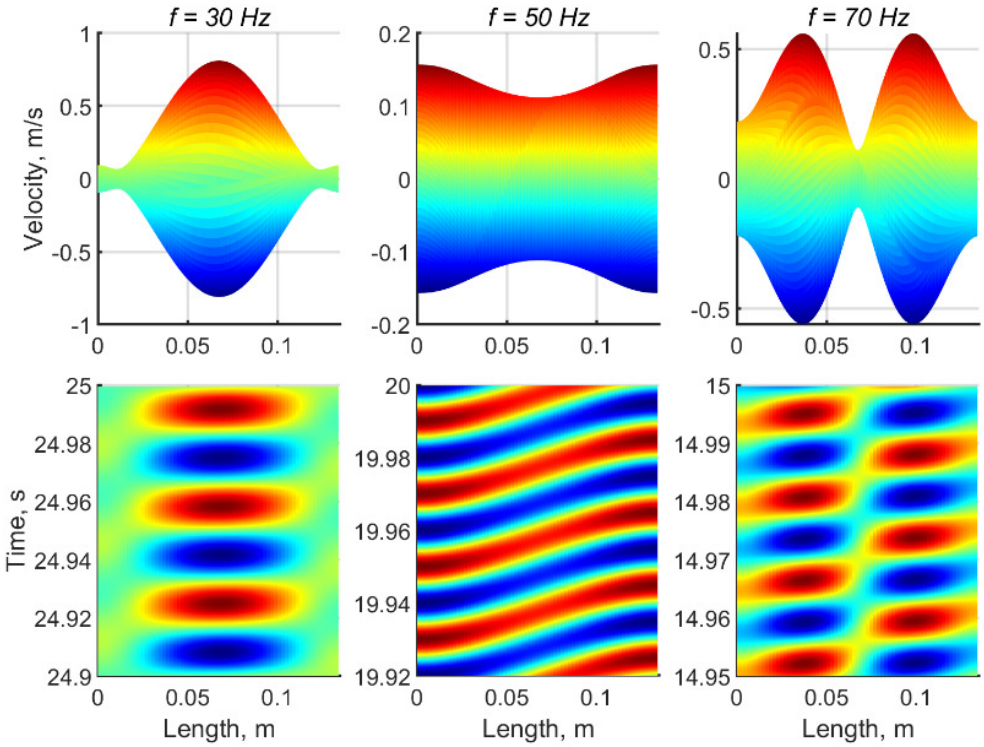

Figure 4.26. Velocity responses of the beam actuated between the first and second resonant

These phenomena can be explained by using the linear approximation of the beam equation in Eq. (2.30). Using the principle of the two-mode summation [21], the beam displacement in this configuration can be expressed as

$$w_t(x,t) = \left(A_{f1}\delta + \sum lp_i\varphi_i\right)\sin(\omega t + \theta_1) + \left(A_{f2}\delta + \sum lp_i\varphi_i\right)\sin(\omega t + \theta_2) + \sum rp_i\varphi_i \cos \omega t \tag{4.1}$$

where $\delta(x)$ is the spatial function of the base motion for the clamped-clamped beam configuration. By setting $\theta_1 = 0$ and $\theta_2 = \pi/2$, the terms $\left(A_{f2}\delta + \sum lp_i\varphi_i\right)$ become in-phase to the damping terms, $\sum rp_i\varphi_i$. When the forcing frequency is set away from the resonant, the terms $\sum rp_i\varphi_i$ become negligible. However, travelling waves are induced due to the contribution of the terms $\left(A_{f2}\delta + \sum lp_i\varphi_i\right)$ in the beam equation from the base motion, w_{b2}. When the beam is actuated close to the resonant, $\omega_n \approx \omega$, the contribution of the terms $\sum lp_i\varphi_i$ becomes minimum. Accordingly, the beam equation is mainly composed of the terms $A_{f1}\delta \sin \omega t$ and $\left(A_{f2}\delta + \sum rp_i\varphi_i\right)\cos \omega t$. The absence of the variable φ_i in the sine function leads to generate the standing wave formation particularly at the middle of the beam where the contribution of the term $A_{f1}\delta$ is minimum.

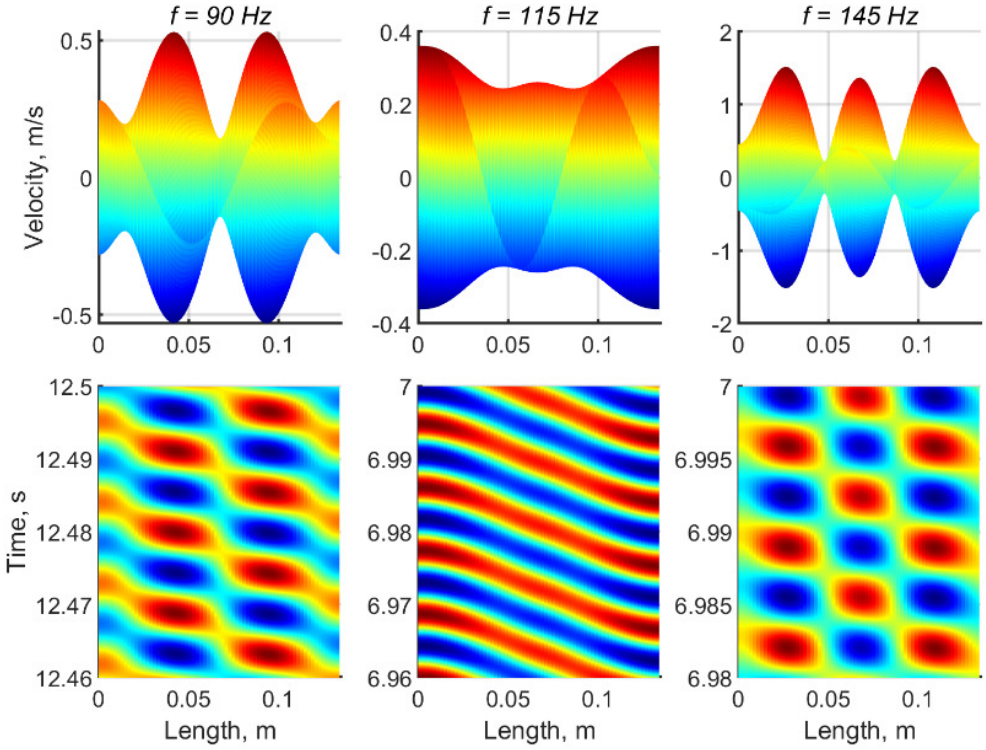

Figure 4.27. Velocity responses of the beam actuated between the second and third resonant

Figure 4.27 presents the velocity responses of the two-excitation beam model actuated between the second and third resonant frequencies. It is noticed that the direction of the waves changes again to the negative direction, from $x = 0.135$ *m* to $x = 0$ *m*. After passing the second resonant, for example at $f = 90$ *Hz*, the beam starts to develop two nodal points in the beam envelope. At halfway of the first and second resonant, $f = 115$ *Hz*, the terms $\left(A_{f1}\delta + \sum lp_i\varphi_i\right)\sin \omega t$ and $\left(A_{f2}\delta + \sum lp_i\varphi_i\right)\cos \omega t$ becomes equal. In

consequence, the amplitudes at the nodes increase, leading to the travelling wave pattern. At the frequency close to the third resonant, f = 145 *Hz*, the amplitudes at the nodes decrease again, indicating the development of the standing wave formation. Furthermore, these phenomena continue to the next region when the beam is actuated between the third and fourth resonant frequencies presented in Figure 4.28. It can be concluded that the travelling waves in the positive direction occur whenever the beam vibrates in an even number of the mode shapes such as $i = 2,4,6, \ldots$.

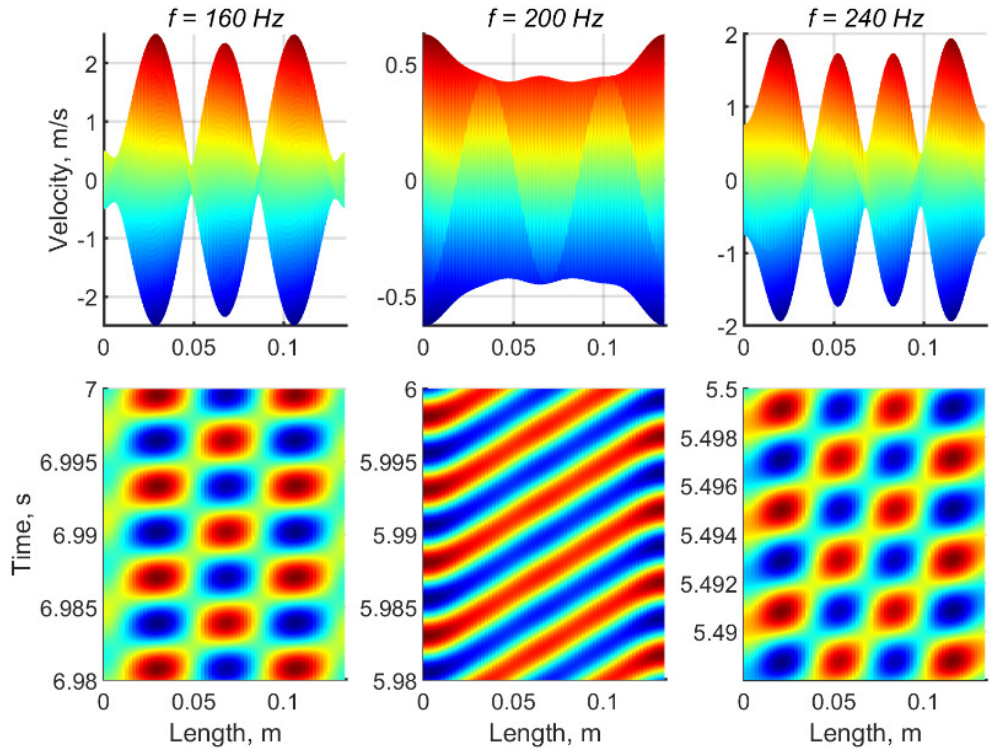

Figure 4.28. Velocity responses of the beam actuated between the third and fourth resonant

4.4.3. Vibrating in water

The analysis for the two-excitation beam model vibrating in water is not only limited to the 0.1 *mm* beam, but also to the other beam models – such as the 0.3 *mm* beam and 0.6 *mm* beam model – to provide a fair comparison to the cantilever beam model. The 3D FSI model and the simulation solvers described in Section 4.3.1 and 4.3.2 are used to perform numerical simulations for the two-excitation beam model. The base input motion for w_{b1} and w_{b2} are applied to the left and right surface of the solid domain, respectively. Using parameters of the 0.6 *mm* beam, the first three natural frequencies for the clamped-clamped beam configuration vibrating in water are approximately 88.88 *Hz*, 244.99 *Hz*,

and 480.29 *Hz*. The forcing frequency is varied based on the cantilever beam model. The base amplitudes for w_{b1} and w_{b2} are set constant to 1.2 *mm*. The phase θ_1 and θ_2 for the base motion are set to $\pi/2$ and 0, respectively, to generate travelling waves in the positive direction propagating from x = 0 *m* to x = 0.135 *m*. All simulation parameters remain default values. Figure 4.29 presents the velocity responses of the 0.6 *mm* beam with the two-excitation model for various forcing frequency. As expected, the beam only vibrates in the first mode shape for the selected forcing frequencies since the first resonant is located at 88.88 *Hz*. It is observed that the two-excitation beam model at 14 *Hz* provides more uniform travelling waves than the cantilever beam shown in Figure 4.16. By comparing the fluid characteristics induced by the two models, it can be used to study the contribution of travelling waves to the fluid flow which will be discussed in the next section.

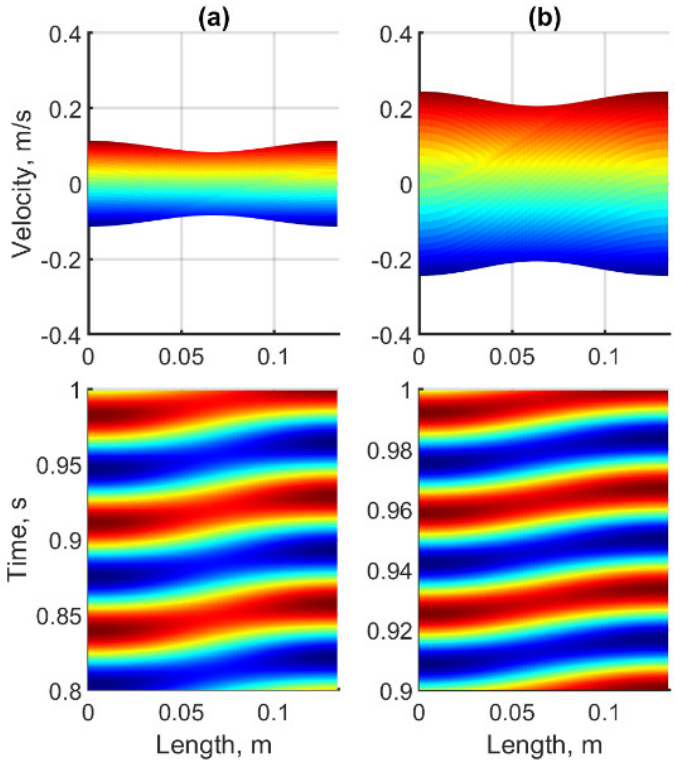

Figure 4.29. Velocity responses of the 0.6 *mm* beam vibrating in water at (a) f = 14 *Hz* and (b) f = 30 *Hz*

The 0.3 *mm* beam is also used for investigating the two-excitation beam model. The first three natural frequencies of the beam vibrating in water for the clamped-clamped beam configuration are 34.65 *Hz*, 95.53 *Hz* and 187.27 *Hz*. In theory, actuating the two-excitation beam model with a moderately large amplitude would shift the damped natural

frequency down. This would allow the beam to vibrate in the second mode shape, particularly at 33 *Hz* which can then be used to compare the responses with the cantilever beam model in the same mode shape. The same CFD model as described in Section 4.3.4 is used to simulate the 0.3 *mm* beam. Figure 4.30 displays the velocity responses of the 0.3 *mm* beam using the two-excitation model for various forcing frequency. It is seen from the figure how the beam develops a node with increasing the frequency. It is also noticed that the peaks at 18 *Hz* and 23 *Hz* are not located at the centre of the beam compared to the beam vibrating in air. Due to the phase input setting, the beam equation at this frequency fulfils the following equation: $w_t = \left(A_{f2}\delta + lp_1\varphi_1\right)\sin\omega t + \left(A_{f1}\delta + lp_1\varphi_1 + rp_1\varphi_1\right)\cos\omega t$. Note that $A_{f1}\delta$ and $A_{f2}\delta$ represent the base motion at x = 0 *m* and x = 0.135 *m*, respectively. Due to strong influence of the damping from the fluid forces, the terms $\left(A_{f1}\delta + lp_1\varphi_1 + rp_1\varphi_1\right)$ in the beam equation becomes dominant which makes the peak offset from the centre of the beam. Furthermore, the beam at 33 *Hz* was actuated by reversing the phase $\theta_1 = \pi/2$ and $\theta_2 = 0$ to maintain the wave in the positive direction.

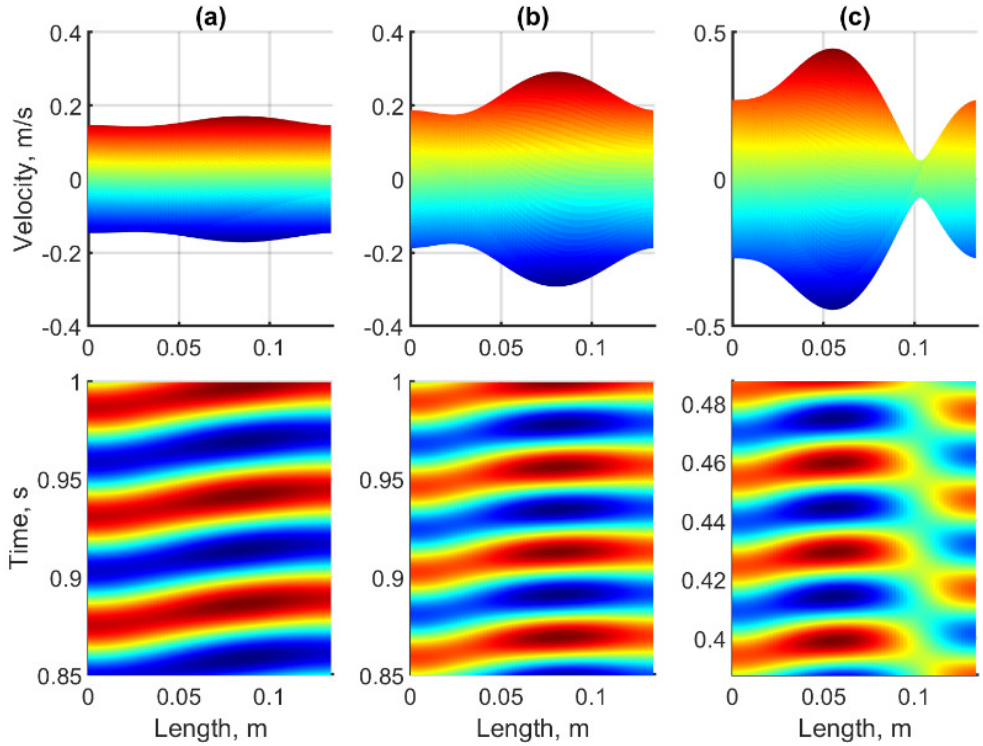

Figure 4.30. Velocity responses of the 0.3 *mm* beam for various forcing frequency

For the 0.1 *mm* beam, the first four natural frequency of the clamped-clamped beam submerged in water are 7.85 *Hz*, 21.65 *Hz*, 42.43 *Hz* and 70.15 *Hz*. There is no resonant

frequency from torsional vibrations in this configuration. Figure 4.31 presents the vibration responses of the two-excitation model for various forcing frequency. Note that the phase of the base input motion was adjusted to generate travelling waves in the positive direction. It is seen that the peak at 4 *Hz* is also offset from the midline of the beam. This is consistent to the previous finding with the 0.3 *mm* beam. At halfway between the first and second resonant, $f = 14$ *Hz*, the amplitudes of the beam envelope are not as uniform as the beam vibrating in vacuum. The amplitude at the node is still low, creating discontinuity in the formation of travelling waves. This incidence also occurs at the frequency halfway between the second and third resonant, $f = 30$ *Hz*, displayed in Figure 4.31. This can be caused by the strong contribution of the fluid forces for the terms $\sum rp_i\varphi_i$ in the cosine part of the beam equation when the beam is actuated away from resonant, preventing pure travelling waves occurred in the beam. Furthermore, the shape of the beam envelope is depended on the direction of travelling waves. In addition, the beam envelope is also no longer symmetry along the beam length compared to the beam vibrating in vacuum.

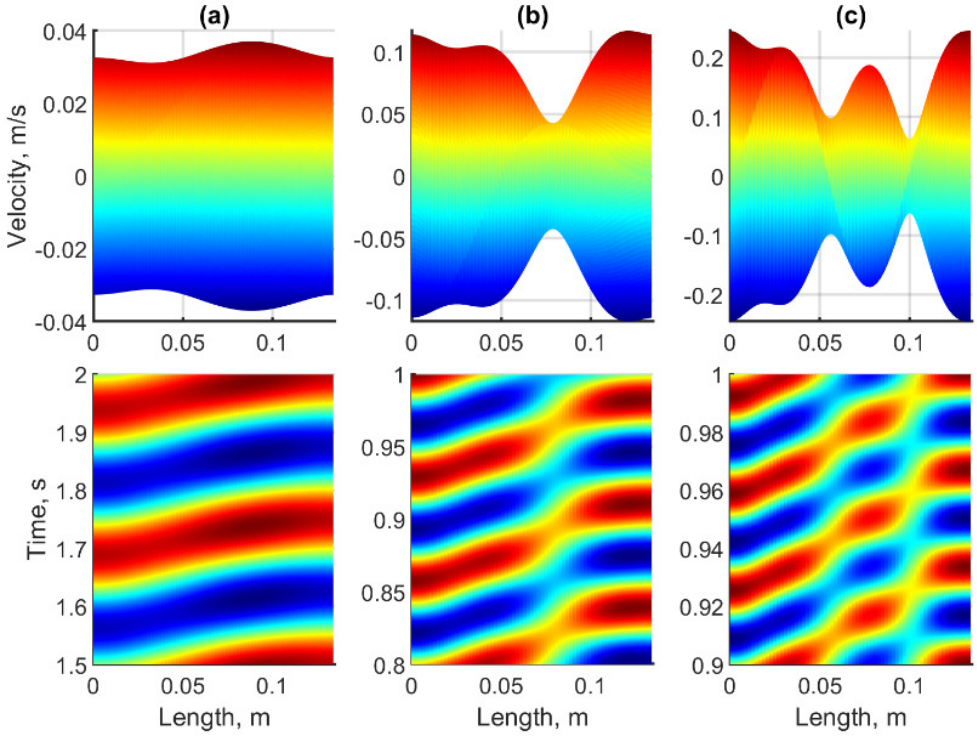

Figure 4.31. Velocity responses of the two-excitation model at (a) $f = 4$ *Hz*, (b) $f = 14$ *Hz* and (c) $f = 30$ *Hz*

4.5. Discussion on the comparison of mean fluid velocities

The mean fluid velocities of the two-excitation beam model for various forcing frequencies are compared to the cantilever beam model. The mean fluid velocities are taken at the coordinate $x = 0.147\ m$ based on Figure 4.3. The comparison of the beam tip velocity estimated from Figure 4.16and Figure 4.29 and is shown in Figure 4.32(a), while the mean fluid velocities of the 0.6 *mm* beam for various forcing frequencies are displayed Figure 4.32(b). The solid and dotted lines represent the results from the cantilever and two-excitation beam model, respectively. It is noticed that the cantilever beam provides higher mean velocities than the two-excitation beam model for the forcing frequency 9 *Hz* to 23 *Hz*. At the first mode shape, the maximum horizontal fluid velocity is determined by the tip velocity rather than the travelling waves. This can be seen from the mean velocity particularly at the forcing frequency of 9 *Hz* and 14 *Hz* where the two models vibrate in the same mode shape. However, the travelling waves may contribute to the less fluctuation in the time series of the fluid velocity. For instance, the maximum mean velocity of the two-excitation model with forcing frequency of 9 *Hz* drops from 0.093 *m*/*s* at $x = 0.136\ m$ to 0.065 *m*/*s* at $x = 0.140\ m$. This is insignificant compared to the cantilever beam model where the maximum mean velocity decreases about 0.09 *m*/*s* for just 4 *mm* away. At 18 *Hz* and 23 *Hz*, the cantilever beam vibrates at the second mode shape with a 180 degrees phase shift between the two tips, while the two-excitation model remains vibrating in the first mode shape. In this case, high generation travelling waves in the two-excitation model do not significantly increase the mean horizontal velocity. Eventually, the mean velocity of the two models superimposes each other at 30 *Hz*. Since the two models have almost identical tip ratio values, this indicates that the presence of travelling waves in the two-excitation beam model does not necessarily generate more fluid flow compared to that of standing waves in the cantilever beam model.

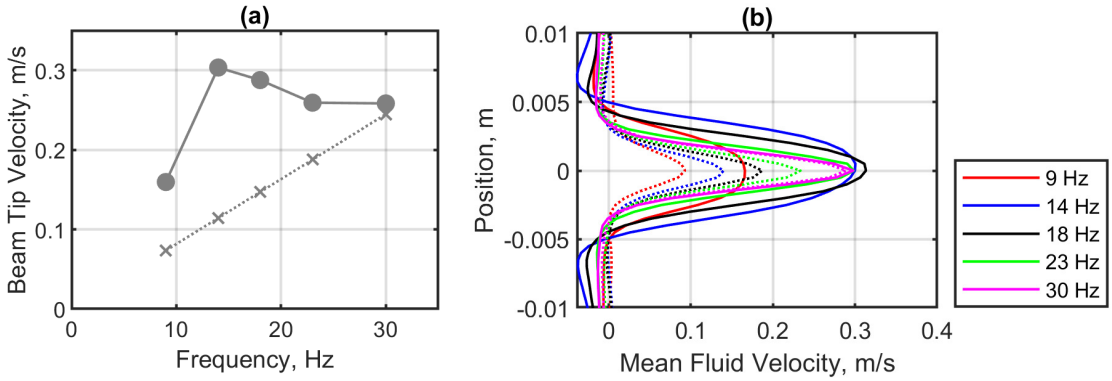

Figure 4.32. (a) The maximum tip velocity of the 0.6 *mm* beam and (b) induced mean fluid velocity; solid lines: the cantilever beam and dotted lines: the two-excitation beam models

The characteristics of induced fluid velocity for the vibrating beam shown, for instance, in Figure 4.17(c) and Figure 4.32(b) are similar to the perturbation flow of swimming fish satisfying the reverse Bénard-von Kármán (rBvK) vortex street [136]. Since the water is propelled rearward at speed V, the fish moves forward with an average velocity, U. Hence, the Strouhal number, St, is used to define oscillating flow due to the fish's motion through the fluid. In animal locomotion, this number is given by [137]

$$St = 2f_s A/U \tag{4.2}$$

where f_s and A are the tail-beat frequency and peak-to-peak oscillation amplitude, respectively. In undulatory swimming, the Strouhal number can vary approximately from 0.1 to 2.0 according to reference [138]. In particular, the optimum number for swimmers utilising body/caudal fins is reported in the range of 0.2 to 0.4 [139]. Since this study considers a cantilever beam subjected to base motion, the forward velocity U becomes nil due to the beam fixed at one extremity. Therefore, the definition of the Strouhal number for animal locomotion becomes irrelevant to be implemented in this study.

In the Bénard-von Kármán (BvK) vortex street, the definition of the Strouhal number is often given by [140],

$$St = f_w D/U \tag{4.3}$$

where f_w and D are the frequency of vortex shedding, $[T^{-1}]$, and characteristic length, respectively This definition can be utilised to assess the time step, Δt, in CFD simulations [141, 142]. In this case, the time period of vortex shedding must be for instance 25 times

of the time step or more, $\Delta t \geq T/25$, in order to capture vortex shedding phenomena in simulation. Thus, an alternative definition of the Strouhal number better suited to examine the time step is given by the following expression $St = U\Delta t/D$. It should be noted that this ratio is the inverse of the Eq. (4.3). In this sense, the value St must be less than unity to observe vortex shedding. This has been implemented in this study by considering U as the induced fluid velocity, for choosing Δt in a way to achieve St below 0.1.

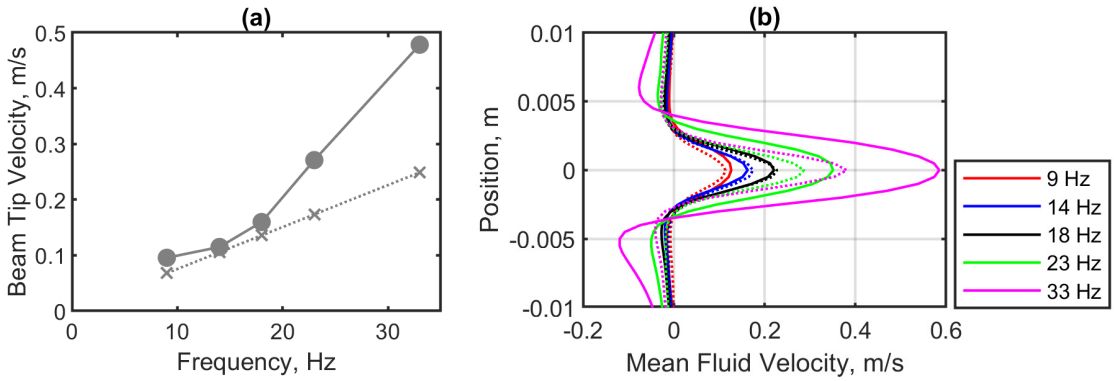

Figure 4.33. Comparison of (a) the maximum beam tip velocity and (b) the induced mean fluid velocity of the 0.3 *mm* beam; solid lines: the cantilever beam and dotted lines: the two-excitation beam models

Figure 4.33(a) presents the beam tip velocity estimated from Figure 4.19 and Figure 4.30; and Figure 4.33(b) displays the mean fluid velocities of the 0.3 *mm* beam for various forcing frequency. Again, the cantilever and two-excitation beam model are indicated with the solid and dotted lines, respectively. It is seen that the mean velocities of the two models are comparable particularly for the forcing frequency of 9 *Hz*, 14 *Hz* and 18 *Hz*. The same phenomenon can also be seen for the cantilever beam at f = 23 *Hz* and the two-excitation beam model at f = 33 *Hz* where these two models generate vibration with an identical tip velocity value of 0.27 *m*/*s*. Based on this instance, it can be concluded for the first two resonant frequencies that the fluid velocity is driven solely by the beam tip velocity. The fluctuation in the time series of fluid velocity is due to high displacement at the tip rather than the vibration pattern. This can be observed, for instance, at f = 33 *Hz* for the cantilever beam model shown Figure 4.33(b) with the magenta solid line where the tip displacement is approximately 2.48 *mm*. high displacement values also induce negative mean velocities on the side of the beam. Considering these phenomena, it can be concluded that the vibration patterns, which can be pure travelling, pure standing, or

hybrid waves, have trivial effect on the maximum fluid velocity, particularly for the first two mode shapes.

Figure 4.34(a) shows the maximum tip velocity of the cantilever beam and two-excitation beam models extracted from Figure 4.23 and Figure 4.31, plotted with respect to frequency. Figure 4.34(b) presents the comparison of horizontal mean velocities at $x = 0.137\ m$ for the cantilever and two-excitation beam model, respectively. Note that the dotted line for $f = 4\ Hz$ is indistinguishable due to superimpose with the solid line. The maximum mean velocity is still determined by the tip velocity for the forcing frequency up to 9 *Hz* or the second resonant. The vibration patterns begin to show their influence on the fluid dynamics at 14 *Hz*. At this frequency, the tip velocity and the tip ratio are equal for both models, while the mean fluid velocity of the two-excitation model outweighs the cantilever beam. This is an indication that the travelling waves begin to show their influence on the induced fluid velocity. Following the same trend, the mean velocity superimposes each other at 18 *Hz*, although the tip velocity of the cantilever beam model is higher than the other. The same incident, where the mean fluid velocity of the two-excitation model exceeds the cantilever beam, can also be seen at $f = 30\ Hz$. Although the two models have a similar tip velocity about 0.23 *m/s* with the tip ratio equal to unity, there is a significant difference in the mean fluid velocity. In addition, the fluid velocity at 23 *Hz* is incomparable since this frequency is located in between the third resonant, 21.65 *Hz*, of the bending vibration and the first resonant, 25.08 *Hz*, of the torsional vibration of the cantilever beam. Therefore, the torsional vibration may contribute to accelerate the fluid, generating higher fluid velocity responses.

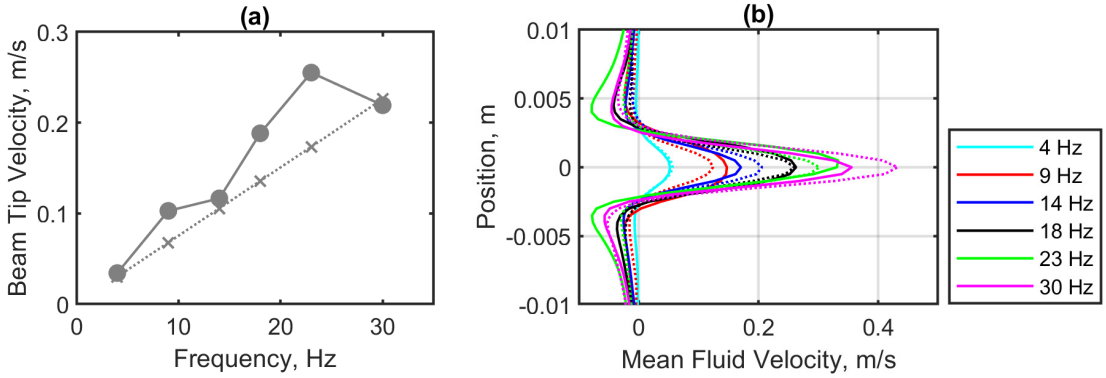

Figure 4.34. (a) The maximum tip velocity of the 0.6 *mm* beam and (b) induced mean fluid velocity; solid lines: the cantilever beam and dotted lines: the two-excitation beam models

4.6. Conclusion

An investigation into fluid dynamics of cantilever beams submerged in liquid has been performed. An experimental rig capable of measuring the mean fluid velocity for various location has been developed. The experimental tests consider two different beam configurations with the thickness of 0.6 *mm* and 0.3 *mm* to explore the characteristics of the first two resonant frequencies. It is found that the maximum induced mean fluid velocity follows the trend line of the FRF magnitude. There is also a nonlinear correlation between the base amplitude and frequency to the induced fluid velocity. To further investigate phenomena from experiments, a 3D numerical simulation has been developed. The comparison between the experimental and numerical models has been presented. The time series analysis from simulation shows that the maximum horizontal fluid velocity is in phase to the displacement of the beam. Furthermore, high displacement ratio between the free tip and base input can affect to the fluctuation in the time series of the horizontal fluid velocity.

The two-excitation beam model has been introduced to generate more uniform travelling waves. This model is capable of generating travelling waves over a wide range of frequencies, although the phase between the beam tips needs to be controlled to achieve travelling waves in the same direction. The influence of travelling waves on the characteristics of fluid flow is investigated by comparing the mean fluid velocity of the cantilever and two-excitation beam model. The simulation reveals that there is no appreciable effect on the fluid velocity due to the presence of travelling waves particularly for the first two modes of the 0.6 *mm* and 0.3 *mm* beams. Accordingly, the induced fluid velocity for these cases is determined by the combination of the tip velocity and displacement of the beam. Moreover, controlling the tip velocity using the two-point excitation beam model can reduce fluctuations in the time series of the fluid velocity.

A more elastic beam with the thickness of 0.1 *mm* was used to investigate the influence of travelling waves up to the fourth resonant frequency. By comparing the one- and two-excitation, it becomes evident that the travelling waves begin to take an effect on the fluid velocity particularly after passing the second resonant. Although the beam tip velocity of the cantilever beam model is higher than or equal to that of the two-excitation beam model, the fluid velocity of the two-excitation model exceeds the cantilever beam

model. To conclude, the relationship between the induced fluid flow and dynamic properties of vibrating beams submerged in liquid is complex than anticipated. Factors such as the tip velocity, mode shape, vibration pattern including standing and travelling waves, fluid viscosity can contribute to the variation in the induced fluid velocity.

Chapter 5. Development of a contactless actuation system for generating passive travelling waves

5.1. Introduction

It has been described in Chapter 3 that passive travelling waves are observed when the beam is actuated at the resonant frequency. Further investigations for fluid dynamics in Chapter 4 also reveal that the tip ratio and tip velocity value are important variables to generate maximum fluid flow. Since these two variables reach maximum values at the resonant frequencies, it is expected that the natural frequencies are designed within the range of the operating frequency of the system. Accordingly, this chapter investigates the non-uniform beam model with a spring mechanism to generate more natural frequencies, actuated with a non-contact actuation method. The main objectives of this study are (1) to use the spring elements to improve the natural frequencies of the beam, (2) to perform parametric study for the non-contact actuation method, and (3) to develop an experimental rig capable of generating passive travelling waves in the frequency of interest.

The dynamic characteristics of the non-uniform beam model, which includes the beam and permanent magnet, are studied by investigating the effect of the spring on the natural frequencies and mode shape of the system. The non-contact actuation method, which involves the interaction of an electromagnet and permanent magnet, are studied by investigating features that promote high mechanical force generation. The relevant application using this type of actuation is also presented in this study. An experimental investigation is also performed to further investigate the conceptual design of the non-uniform beam model. This experimental investigation includes: introducing the structural design for fabrication, characterising the individual components of the experimental rig and evaluating the system's performances.

5.2. Model configuration

Due to the important features of resonant frequencies, a spring mechanism is introduced in the beam system to generate more peaks in the desired frequency region. Figure 5.1 illustrates the configuration of the beam and permanent magnet mounted on a spring element. Note that the springs are connected to the ground which has a fixed displacement. Assuming constant masses for the beam and permanent magnets, the natural frequencies for the spring element in the beam FRF are determined by the spring stiffness, k. Therefore, the stiffness values can be designed such a way to induce more natural frequencies in the selected frequency range.

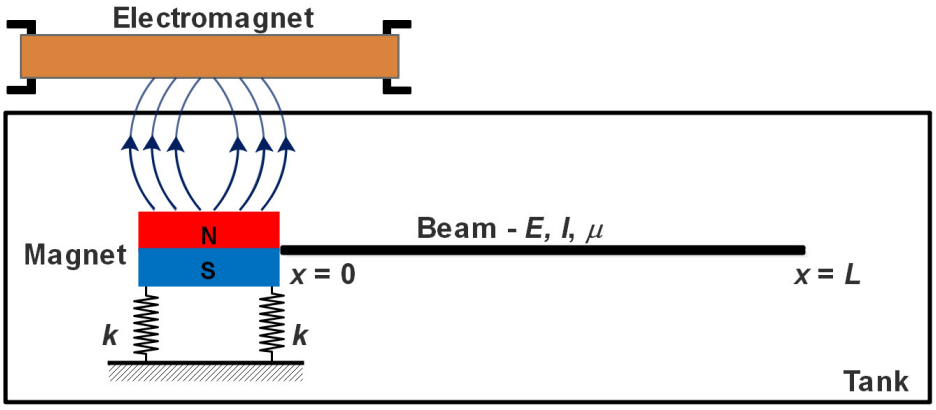

Figure 5.1. An optimal model for generating passive travelling waves

A numerical simulation is performed with ABAQUS to obtain the modal parameters which include the natural frequency and mode shape of the system. The simulation uses a 2D wire model to remove the effect of torsional vibrations since these are not the interest of this study. The magnet and beam are modelled as one beam with non-uniform sections. The spring element is assigned to the boundary conditions at $x = 0$ and $x = l_1$, and only work in the y-direction. The linear perturbation analysis steps are used to evaluate the modal parameters of the system. A neodymium magnet (NdFeB) material with the size of 40 x 20 x 10 mm for the length, width and thickness, respectively, is applied to the magnet section of the non-uniform beam model. The modulus of elasticity, mass density and Poisson's ratio of the magnet material are 160 GPa, 7500 kg/m^3 and 0.30, respectively. Furthermore, the 0.1 mm beam described in Section 4.3.5 is used for the beam section of the non-uniform beam model. In addition, the beam and magnet properties are assumed to satisfy an isotropic, linear and elastic material.

Table 5.1 presents the first eight natural frequencies of the system for various spring stiffness. The coloured cells in the table demonstrate the changes in the natural frequencies of the system due to the variation in the spring element. The first row of the table indicated with "$k = 0$" is the system configuration without the spring mechanism. Therefore, the first three natural frequencies of this configuration are the rigid body motion of the non-uniform beam model. Consequently, the natural frequency for the transverse vibration of the non-uniform beam model starts at the fourth frequency. By setting the stiffness value to 10 N/m, this introduces two frequencies at the second and third resonant. The presence of the natural frequencies of the spring element increases the fourth resonant value of the non-uniform beam model. Furthermore, increasing the stiffness value to 50 N/m also increases the third resonant frequency of the spring to 6.498 Hz. This value becomes comparable to the fourth resonant frequency of the non-uniform beam model without spring mechanism, $k = 0$. In addition, the fourth resonant frequency also displaces to 11.644 Hz from the original location of 6.724 Hz, due to increasing the stiffness of the spring.

Table 5.1. Natural frequencies of the system for various spring stiffness

Mode		**1**	**2**	**3**	**4**	**5**	**6**	**7**	**8**
$k = 0$	**Natural Frequency (Hz)**	0.000	0.000	0.015	6.724	28.688	77.956	151.993	250.851
$k = 10$		0.015	2.571	2.974	7.713	28.718	77.958	151.994	250.851
$k = 50$		0.015	3.878	6.498	11.644	28.856	77.968	151.996	250.852
$k = 250$		0.015	4.297	14.457	22.388	30.419	78.021	152.006	250.855
$k = 500$		0.015	4.351	20.389	26.324	36.188	78.101	152.019	250.859
$k = 750$		0.014	4.369	24.740	27.297	42.902	78.202	152.032	250.863
$k = 1000$		0.013	4.379	26.773	29.389	48.907	78.333	152.047	250.867
$k = 2000$		0.014	4.392	27.363	41.061	67.095	79.683	152.113	250.883
$k = 3000$		0.009	4.397	27.459	50.227	75.139	86.799	152.198	250.901
$k = 5000$		0.011	4.400	27.525	64.719	76.932	109.085	152.469	250.942
$k = 7500$		0.000	4.402	27.555	76.285	80.214	132.103	153.386	251.005
$k = 10000$		0.000	4.403	27.569	76.962	91.907	147.016	158.798	251.086

Figure 5.2 displays the first four mode shapes of the non-uniform beam model with the stiffness variation of $k = 0$ N/m, 10 N/m and 50 N/m. The natural frequency values for these configurations are presented in Table 5.1 with the light green cell colours. It is observed that all configurations perform rigid body motion in the first mode shape. The effect of the spring element can be seen at the second mode shape where the spring mechanism creates a 90-degree phase shift between the two tips. The phase shift between the two tips increases to 180 degrees at the third resonant. In the fourth mode shape, the

non-uniform beam model has an identical mode shape for all spring configurations and the two tips become in-phase. It can be concluded from these plots that the first four mode shapes of the non-uniform beam model have a close similarity to the first two mode shapes of a cantilever beam model presented in Figure 2.2. According to investigation in Chapter 4, the fluid flow of the cantilever beam vibrating in the first two resonant frequencies are determined solely by the tip velocity. Therefore, these low stiffness configurations can assist to generate more fluid velocity by creating three resonant frequencies appeared up to 20 *Hz* that leads to high beam tip velocity.

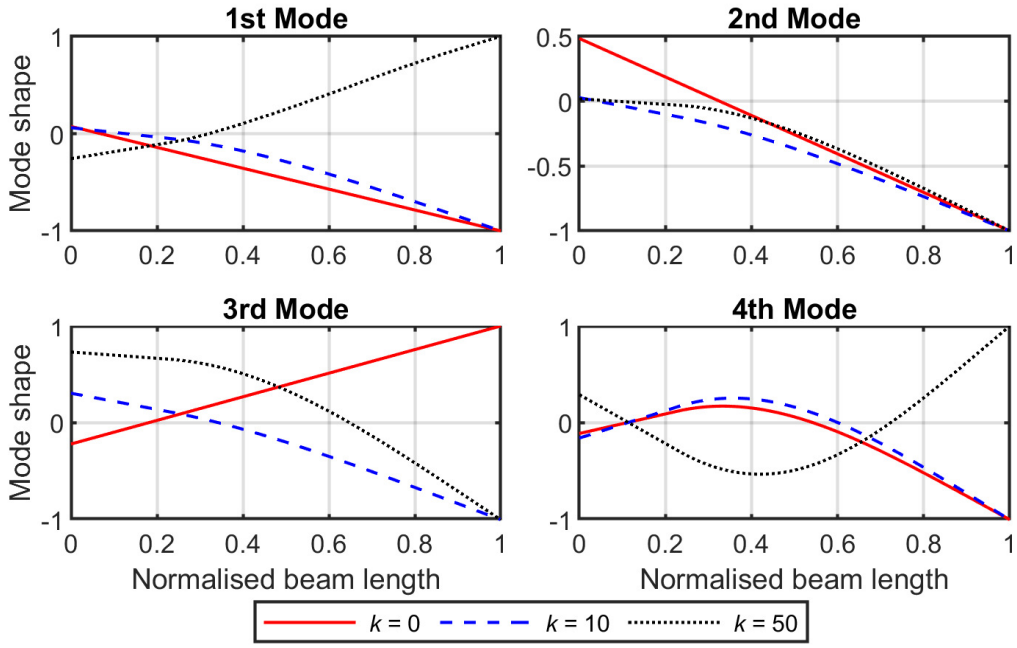

Figure 5.2. The first four mode shapes of the beam with the stiffness variation of $k = 0$ N/m, 10 N/m and 50 N/m

By setting the spring stiffness around 250 N/m to 750 N/m, the changes in the natural frequency values are presented with the light blue cell colours in Table 5.1. It is noticed that the second resonant become invariant to the change in the stiffness value after $k =$ 250 N/m. The significant changes occur in the third to the fifth resonant frequency. Figure 5.3 displays the mode shapes of the non-uniform beam model for various stiffness value. Note that all lines superimpose each other at the second mode shape. It is noticed that the characteristics of the second mode shape of the non-uniform beam model are similar to the first mode shape of the cantilever beam. For the third mode shape, the magnet section of the non-uniform beam model performs rigid body motion due to the contribution of the spring elements, and the beam section of the non-uniform beam model, $x = 0.3L$ to

1L, forms the second mode shape of the cantilever beam model. In the fourth mode shape, the contribution of the spring element is minimum. Therefore, the mode shape of the magnet section becomes close to zero, and the mode shape of the beam section becomes identical, particularly for k = 500 N/m and k = 750 N/m. Furthermore, the spring elements contribute in the fifth mode shape by creating a rigid body rotation for the magnet section of the non-uniform beam model. Accordingly, there are three zero-crossing points in this mode.

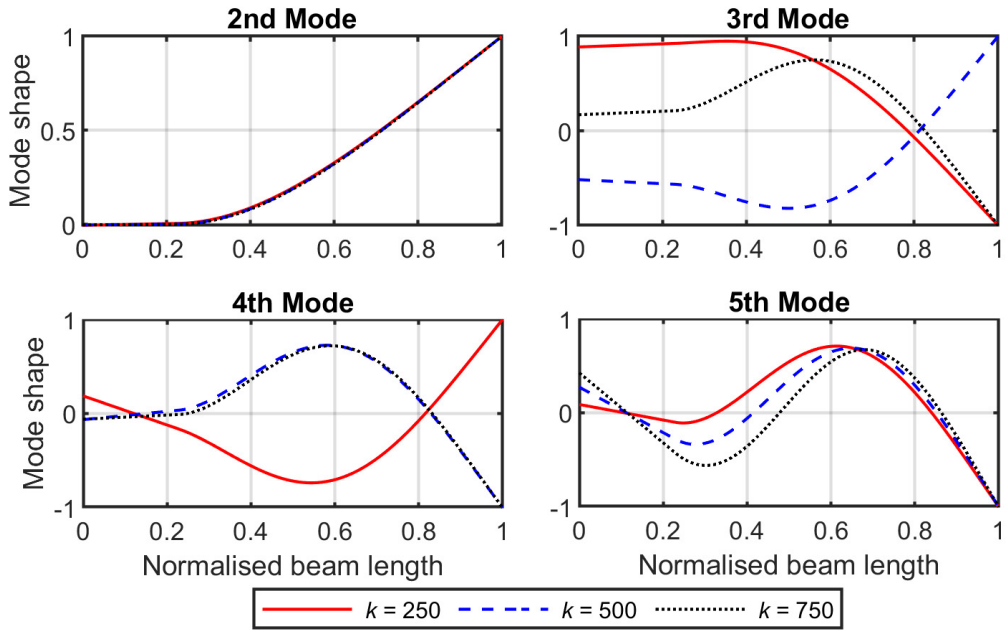

Figure 5.3. The second to fifth mode shapes of the beam with the stiffness variation of k = 250 N/m, 500 N/m and 750 N/m

Further increasing the spring stiffness around 1000 N/m to 3000 N/m, the changes in the natural frequencies are presented with the gold cell colour in Table 5.1. A significant variation in the natural frequencies occurs in the fourth to the sixth resonant. The mode shapes of the non-uniform beam model due to the variation of the spring stiffness are displayed in Figure 5.4. In the third resonant, the mode shape of the magnet section remains zero, while the mode shape of the beam section resembles the second mode shape of the cantilever beam model. In the fourth mode shape, the spring element contributes to a rigid body movement for the magnet. Therefore, the mode shape of the non-uniform beam model is composed of a superposition of the translational motion of the magnet section and the second mode shape of the cantilever beam. In the fifth mode shape, the spring element facilitates a rotational body motion for the magnet. Accordingly, the phase

between the two tips alters from in-phase in the fourth resonant to 180-degree out-of-phase in the fifth resonant. The spring element takes a minor effect in the sixth mode shape, particularly for k = 1000 N/m and k = 2000 N/m. Moreover, it is noticed that the magnet only performs translational and rotational motions in the selected frequency range. This is due to the geometry and the material properties of the beam that creates very high natural frequencies for the transverse vibration.

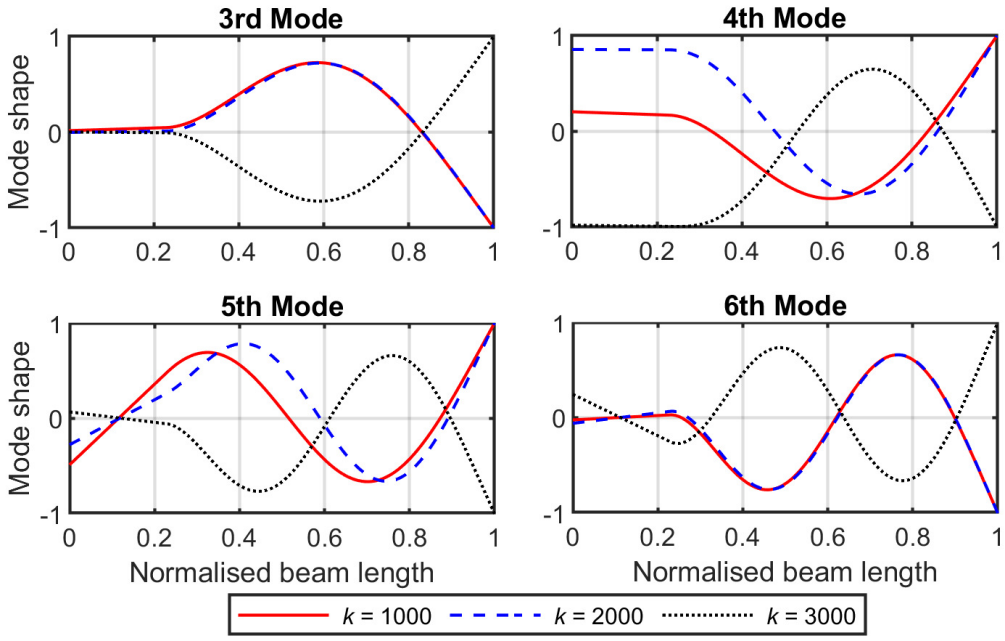

Figure 5.4. The third to sixth mode shapes of the beam with the stiffness variation of k = 1000 N/m, 2000 N/m and 3000 N/m

The last investigation for the non-uniform beam model uses the stiffness values around 5000 N/m to 10000 N/m. The changes in the natural frequencies due to these stiffness values are presented with the light orange cell colours in Table 5.1. The influence of the spring stiffness on the mode shape of the non-uniform beam model is displayed in Figure 5.5. Phenomena where the magnet section undergoes translational and rotational motion are found in the fifth and the sixth mode shapes. Finally, these demonstrations show that the spring element can be used to generate more natural frequencies for the non-uniform beam model in a certain frequency range. In addition, the presence of the spring element and permanent magnet do not alter the mode shape of the beam section significantly. This makes the mode shapes of the beam section for the non-uniform beam model still relevant to the characteristics of the cantilever beam model.

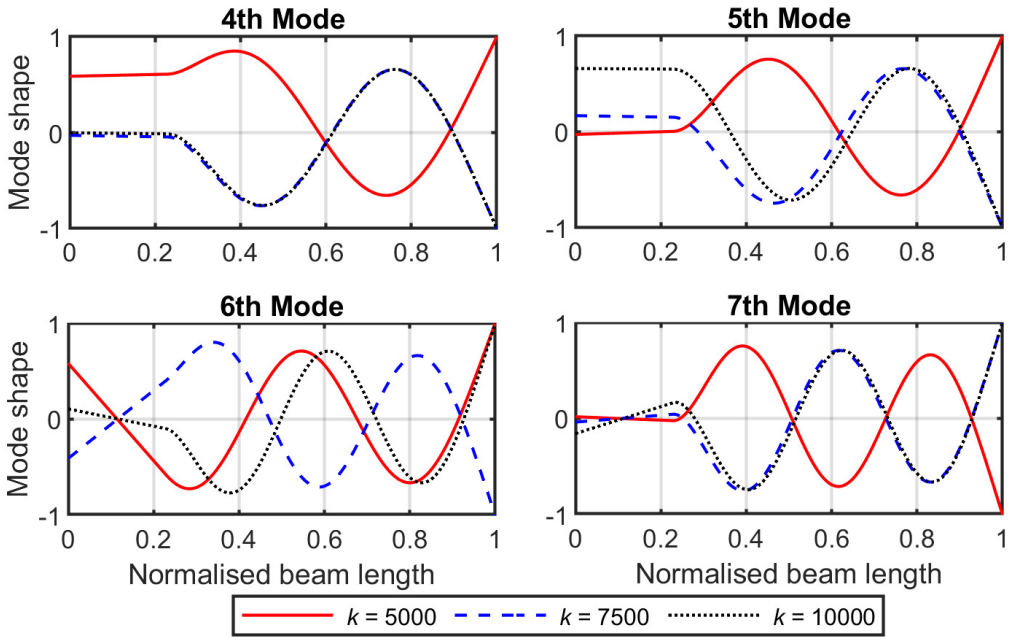

Figure 5.5. The fourth to seventh mode shapes of the beam with the stiffness variation of k = 5000 N/m, 7500 N/m and 10^4 N/m

5.3. Investigation into a non-contact actuation

This section investigates the parameters that enhance mechanical actuation via electro-magnetic interactions: an electromagnetic stator is used to generate the electromagnetic field and permanent magnets connected to the beam are used to induce its oscillation.

5.3.1. Parametric study

The model presented in Figure 5.1 relies on magnetic forces created by the interaction of the electromagnet and permanent magnet. Note that the permanent magnet and coil are interchangeable in terms of magnetic flux. The permanent magnet can be designed such a way to generate the same magnetic properties as the coil. Therefore, for the purpose of investigating the mechanical forces, the permanent magnet that is attached to the beam is replaced by a coil so that many parameters such as the pole orientation, current and number of turns can be altered to study the magnetic fields and flux density around the structure. The dimension of the coil is illustrated in Figure 5.6. The notations *Cl* and *Cw* represent the total length and width of the coil, *Bl* and *Bw* denote the length and width of

the bobbin, whereas *b* and *h* are the width and height of the winding. The fill factor of the coil can be estimated by [a]

$$FF = \frac{\pi . d^2 . n}{4 . b . h} \tag{5.1}$$

where *d* is the wire diameter, and *n* is the number of turns. The maximum fill factor of 90.69% can be achieved by implementing orthocyclic winding methods.

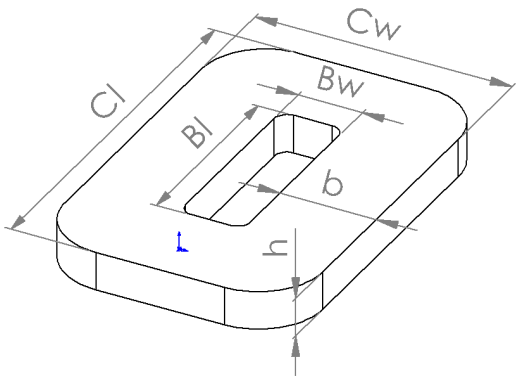

Figure 5.6. Coil dimension

For this investigation, the variable *Cw* and *h* are set constant to 20 *mm* and 5 *mm*, respectively. By setting the maximum fill factor of 0.9069, it is theoretically possible to achieve the maximum cross section for the coil body of 40 mm^2 by utilising the bobbin width of 2 *mm*. Figure 5.7 displays the number of windings estimated by varying the wire diameter and the cross section of the coil body using Eq. (5.1). It is seen that the maximum number of windings is 1800 turns achieved by using the wire diameter of 0.16 *mm*, or equivalent to 34 AWG. Although this wire can produce high number of turns, the maximum current capacity value is very low. Since the magnetic flux are proportional to the current and number of turns, this can limit the magnetic flux generated by this configuration. Moreover, the resistance per unit length for the AWG 34 is very high about 0.8 Ω per metre which can dissipate more electric power. With increasing the wire diameter, the maximum current capacity also increases, while the number of turns and resistance per unit length decrease. Accordingly, the wire diameter needs to be chosen such a way to obtain proportional values between the number of turns and the maximum current capacity to generate maximum magnetic fields. In addition, the number of windings presented in Figure 5.7 will be used as the basis parameter for simulating an interaction of the electromagnet and permanent magnet.

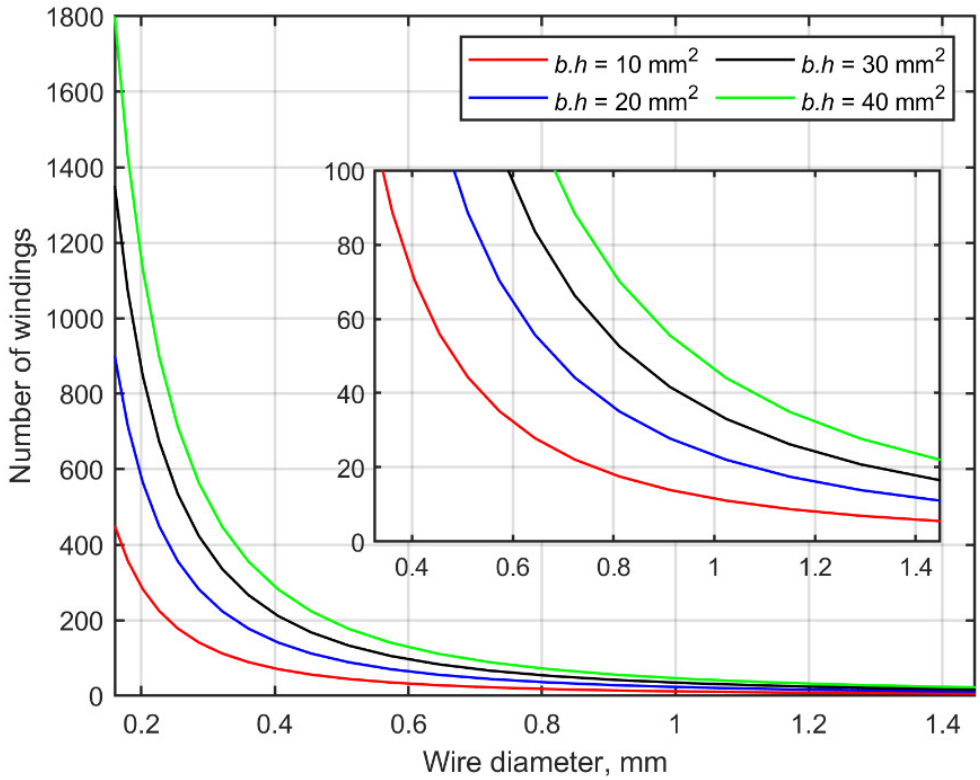

Figure 5.7. Estimated number of windings for various wire diameter and cross section of the coil body

The simulation of the magnetic forces induced by the attraction and repulsion of permanent magnet and electromagnet is performed in EMS – electromagnetic field simulation software provided by EMWorks. Figure 5.8 shows the magnetic circuit models used for investigation. The coil is mounted on a beam made of a non-ferromagnetic material. The type of the coil is the current driven coil. Using the right-hand rule, the surface of the coil opposite of the magnet will create the south pole for the magnetic field. The green arrows on the coil body displayed in Figure 5.8 indicate the current flow direction. An N5214 permanent magnet with the size of 30 x 20 x 12.5 *mm* is used for simulation. According to the SOLIDWORKS's library, this type of magnet is the second strongest magnet with remanence magnetization and coercivity of 1.47 *T* and 819647 *A*/*m*, respectively. This magnet is positioned in-line to the coil surface. The blue arrow shown in Figure 5.8 indicates the coercivity direction which determines the north pole of the magnet. Therefore, the north pole of the magnet will interact with the south pole of the coil, creating attraction forces in the system. The magnet is fixed at a certain location, while the coil and beam are the movable parts which can be displaced to vary the gap between the coil and magnet. The mechanical force is estimated by applying the principle of the virtual work method on the coil body shown with the purple "T" symbol in Figure

5.8. Neither the coil nor the beam is ferromagnetic materials. Therefore, the attraction force only occurs once the current is assigned to the coil.

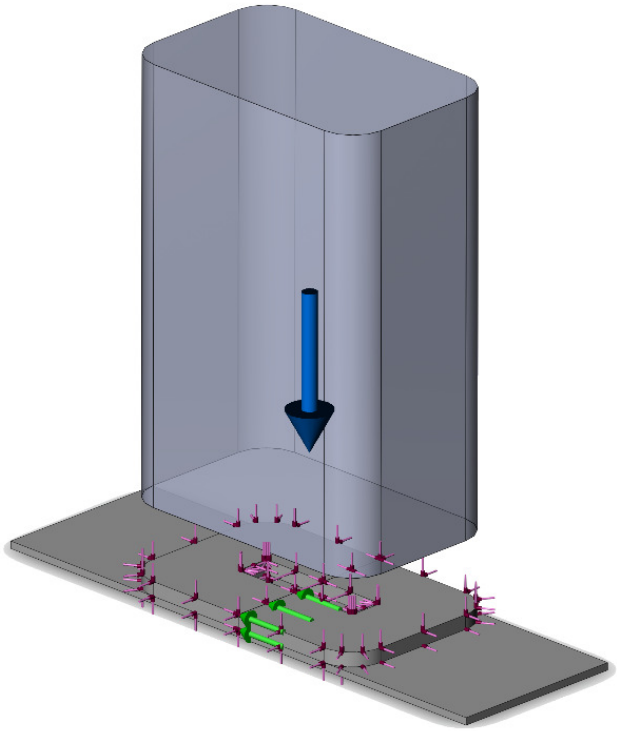

Figure 5.8. Boundary conditions for magnetic simulation

To simulate the attractive forces, the fill factor is set constant to 90.69%. The size of the coil is 20 x 20 x 5 *mm* for variables *Cl*, *Cw* and *h*, respectively. The width of the coil winding, *b*, is constrained to 9 *mm*. Table 5.2 presents forces generated by varying the wire diameter, input current, and gap between the magnet and coil. Note that the positive sign for the force represents an attractive force that pulls the coil upwards close to the magnet. One the contrary, the negative sign indicates a repulsive force that push the coil away from the magnet. As expected, the highest force is obtained at the highest number of windings of 1010 turns for the AWG 31. It is observed that the input current for the coil has a linear relationship to the mechanical force. In addition, the mechanical force also decreases linearly with increasing the gap between the magnet and coil.

Table 5.2. The forces obtained for various wire diameter, gap between the magnet and coil, and input current

AWG	in *mm*	*n*	Gap 2 *mm*			Gap 5 *mm*		
			0.25A	**0.5A**	**0.75A**	**0.25A**	**0.5A**	**0.75A**
18	1.024	49	-0.13201	-0.09604	-0.060071	-0.010825	0.014213	0.039252
21	0.723	99	-0.095306	-0.02263	0.050062	0.014724	0.065314	0.11591
24	0.511	199	-0.021895	0.12424	0.27043	0.065825	0.16753	0.26924
27	0.361	400	0.12497	0.41816	0.71159	0.16804	0.37199	0.576
31	0.227	1010	0.57404	1.3176	2.0628	0.48038	0.99696	1.5139
AWG	**in *mm***	***n***	**Gap 7.5 *mm***			**Gap 10 *mm***		
			0.25A	**0.5A**	**0.75A**	**0.25A**	**0.5A**	**0.75A**
18	1.024	49	0.0046428	0.022123	0.039604	0.0067392	0.019067	0.031394
21	0.723	99	0.02248	0.057798	0.093116	0.019318	0.044224	0.069128
24	0.511	199	0.058155	0.12915	0.20014	0.044475	0.094534	0.14459
27	0.361	400	0.1295	0.27185	0.41419	0.094786	0.19514	0.29547
31	0.227	1010	0.34748	0.70779	1.0681	0.24845	0.50236	0.75613

It is noticed that there are negative force values occurred at the highest wire diameter with the lowest values for the input current and the gap between the magnet and coil. For the AWG 18, the negative force of -0.1320 *N* is obtained at the gap of 2 *mm* and the input current of 0.25*A*. The force decreases to -0.0601 *N* once the input current is increased to 0.75*A*. Following the same trend, the force of -0.0953 *N* is obtained by using the AWG 21 and setting the gap and input current to 2 *mm* and 0.25 *A*. The force decreases to -0.0226 *N* with increasing the input current to 0.50*A*, and eventually becomes positive at 0.75*A*. A similar incident where a negative force becomes positive with increasing input current are also found for the AWG 24. These phenomena may be caused by the low number of turns and input current values in these configurations that may create non-uniform magnetic fields around the coil. Therefore, the north pole of the magnet tends to interact with the north pole of the coil, creating repulsive force for the system. The magnetic fields become more uniform with increasing the input current and the number of turns. Thus, the attraction between the two magnetic poles becomes inevitable.

To further study the influence of coil parameters on the mechanical forces, the total length of the coil, *Cl*, is varied arbitrarily to 0.02 *m*, 0.03 *m* and 0.04 *m*. The coil width, *Cw*, and the winding width, *b*, are set constant to 20 *mm* and 2 *mm*, respectively. Accordingly, the bobbin length, *Bl*, is adjusted to keep the term *b* constant. The total wire length can be estimated by multiplying the average circumference of the coil with the number of turns which can be written as follows

$$L_{total} = 2\left(L_{avg} + W_{avg}\right).n \quad (5.2)$$

where L_{avg} and W_{avg} are the average length and average width of the coil and bobbin. Table 5.3 presents the force generated with 0.25*A* and the gap of 10 *mm*. As expected, increasing the length of the wire by maintaining the cross section of the coil body, $b.h = 40\ mm^2$, can proportionally increase the mechanical force. For the AWG 31, the total wire length of *Cl* = 20 *mm* is 39.51 *m*. The wire length increases to 75.43 *m* when the variable *Cl* is extended to 40 *mm*. Since the resistance per unit length of the AWG 31 is 0.4269 Ω/*m*, the power dissipation with the input current of 0.25A is estimated to be 1.054 *Watt*. This dissipated power doubles to 2.013 *Watt* for *Cl* = 40 *mm*.

Table 5.3. Influence of the variation in the total coil length on the mechanical force

AWG	**in mm**	***n***	**Variation of the total coil length**		
			20 *mm*	**30 *mm***	**40 *mm***
18	1.024	49	0.0067392	0.018867	0.033663
21	0.723	99	0.019318	0.052009	0.084914
24	0.511	199	0.044475	0.11829	0.18742
27	0.361	400	0.094786	0.25087	0.39345
31	0.227	1010	0.24845	0.65591	1.0188

The influence of the attraction and repulsion of the magnet on the mechanical force is studied by altering the flow direction of the input current of the coil. The AWG 28 with 500 turns is selected to simulate the responses of the system. These configurations are chosen on the basis where the number of turns and the maximum current capacity can be maximised to reach 1.5*A*, whilst maintaining the dissipated power at the low level. The length and width of the coil, *Cl* and *Cw*, are set constant to 20 x 20 *mm*. Table 5.4 presents the attractive and repulsive force for various gap and input current. Note that the negative current is used to represent the change in the current flow direction. It is noticed that the repulsive force is lower than the attractive force. This is due to the nature of the molecular magnet arrangement. The unequal poles of the magnet and coil that create attractive forces provide better alignment of the molecular magnetic fields. On the contrary, the repulsion process disrupts the alignment of the molecular magnetic fields which results in the reduction of the intensity of the mechanical force. However, the discrepancy between the attractive and repulsive forces tends to decrease with increasing the gap between the magnet and coil as observed in Table 5.4.

Table 5.4. Attractive and repulsive forces generated with the AWG 28

	Ampere	**Gap 2 *mm***	**Gap 5 *mm***	**Gap 7 *mm***
Repulsion force	-1.50	-2.2898	-1.5007	-1.1359
	-1.25	-1.8922	-1.2445	-0.94402
	-1.00	-1.4952	-0.98849	-0.75212
	-0.75	-1.0986	-0.73253	-0.56025
	-0.50	-0.70265	-0.47665	-0.36839
	-0.25	-0.30719	-0.22086	-0.17655
Attraction force	0.25	0.47934	0.29085	0.20572
	0.50	0.87044	0.54677	0.39614
	0.75	1.261	0.8026	0.58656
	1.00	1.651	1.0583	0.77695
	1.25	2.0406	1.314	0.96732
	1.50	2.4296	1.5696	1.1577

5.3.2. Application to the non-uniform beam model

The mechanical force data of the AWG 28 for various gap and current will be used to obtain the current needed to excite the non-uniform beam model to the desired displacement. The investigation begins with fitting data in Table 5.4 to get the polynomial function of the mechanical force with respect to the input current and gap between the magnet and coil. This is achieved by utilising the polynomial surface fits based on the linear least-square fitting method available in MATLAB. To fit with the simulation data, the total degree of the polynomial for the current and gap is set to 5 and 2, respectively, which results in an equation of the form

$$\begin{aligned} F(x,y) = {} & p_{00} + p_{10}x + p_{01}y + p_{20}x^2 + p_{11}xy + p_{02}y^2 + p_{30}x^3 + p_{21}x^2y \\ & + p_{12}xy^2 + p_{40}x^4 + p_{31}x^3y + p_{22}x^2y^2 + p_{50}x^5 + p_{41}x^4y \\ & + p_{32}x^3y^2 \end{aligned} \tag{5.3}$$

where the terms p are constants, the terms x and y are the current and gap, respectively; whereas $F(x,y)$ is the mechanical force. This equation has the root-mean-square error (RMSE) of 1.637%. Figure 5.9 displays the surface plot of Eq. (5.3) superimposed with the raw simulation data from Table 5.4 represented with the black dot markers. By obtaining the relationship between the force and displacement of the magnet of the non-uniform beam model at a certain frequency, these can be used to evaluate the current value, or the term x, from Eq. (5.3).

This investigation uses the non-uniform beam model described in Section 5.2 with k = 250 N/m. Note that the magnet that is attached on the beam is switched with a small coil to comply with the configuration in Figure 5.8. Accordingly, the electromagnet outside of the tank shown in Figure 5.1 is replaced with a pile of permanent magnets. It should be noted that the magnet and coil are interchangeable in terms of the magnetic fields. A mode-based steady-state dynamic analysis is performed in ABAQUS to obtain the relationship of the force and displacement over a range of frequencies. The frequency span is limited to 50 Hz and the number of frequency points is set to 200. The force of 0.25 N is applied to the vertical direction at the centre of the electromagnet shown in Figure 5.10. A structural-based damping ratio of 0.5% is assigned to the first tenth modes. The other parameters for performing numerical simulation in ABAQUS remain default values.

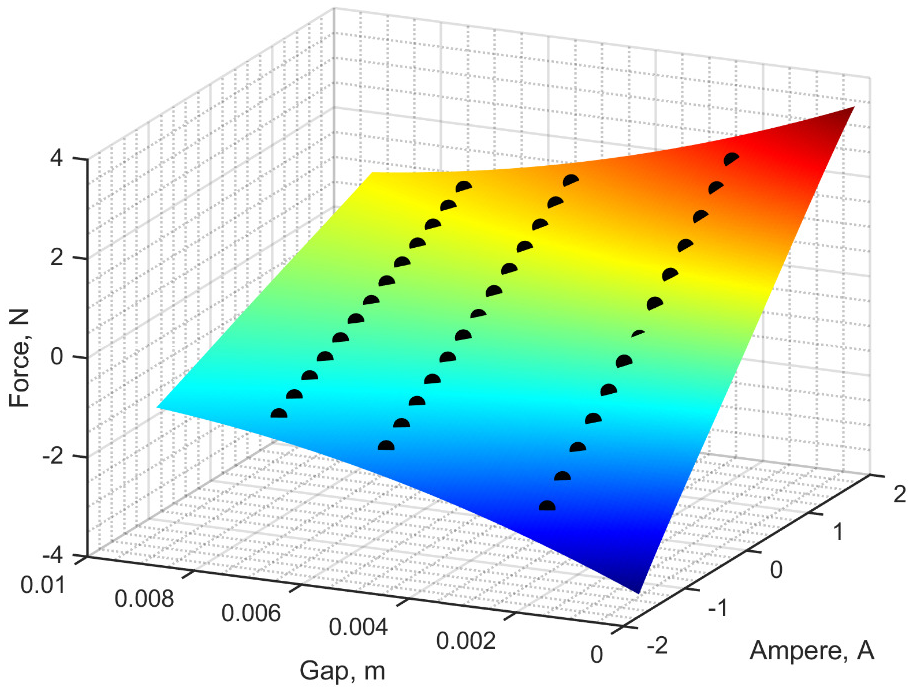

Figure 5.9. Surface plot of mechanical forces generated with the AWG 28

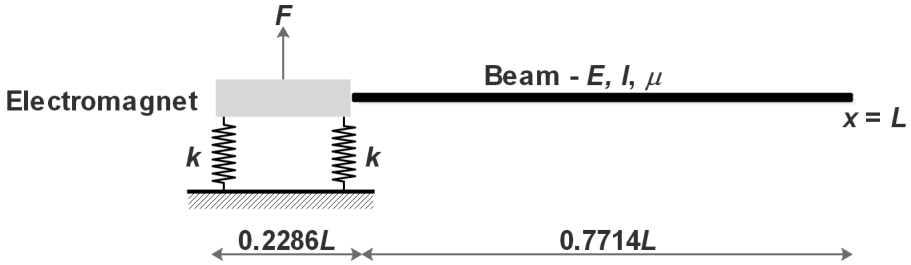

Figure 5.10. Schematic diagram of the non-uniform beam model for performing the steady-state dynamic analysis

Figure 5.11 shows the frequency series of the steady-state displacement responses at the centre of the electromagnet and tip of the beam. It is seen from the responses at the middle of the electromagnet that the magnitude changes to negative after it passes 14.5 *Hz*. Presented in Table 5.1, this frequency is the third resonant for the non-uniform beam model. According to the mode shape shown in Figure 5.3, the third resonant frequency is where the magnet section of the non-uniform beam model performs rigid body motion. Furthermore, the maximum displacement of the electromagnet at this frequency is obtained about 5 *mm* generated with the forcing amplitude of 0.25 *N*. This value is identical to the tip displacement of the beam with a 180-degree phase shift.

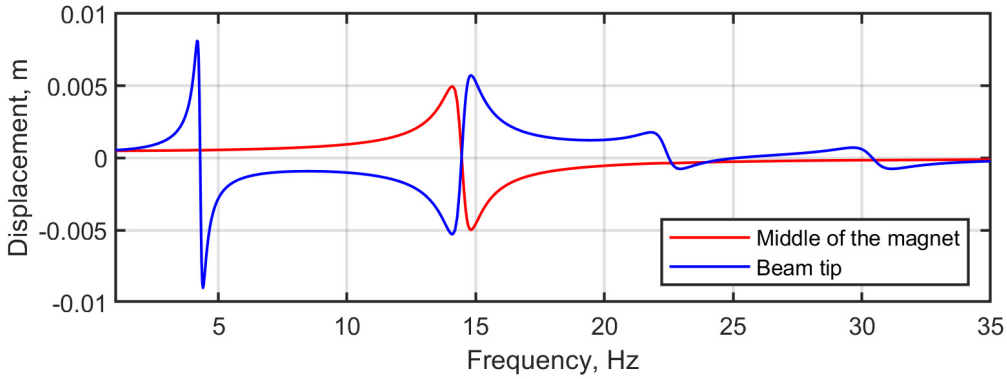

Figure 5.11. Frequency series of the non-uniform beam model actuated with 0.25 *N*

According to Figure 5.11, the displacement of 2.5 *mm* at the middle of the electromagnet can be achieved by actuating the beam with the forcing amplitude and frequency of 0.25 *N* and 13.034 *Hz*, respectively. The time series of the force and displacement at the middle of the electromagnet is presented with the solid red and blue lines in Figure 5.12, respectively. The distance of the electromagnet and permanent magnet at the steady condition is assumed to be 7.5 *mm*. Therefore, the gap between the two magnets oscillates in the range of 5 *mm* to 10 *mm* indicated with the dotted red line colour in Figure 5.12. By substituting the force, $f(x, y)$, and the gap values, x, to Eq. (5.3), this will create a quadratic function of the single variable y. The root of the quadratic equation of the term y determines the responses of the input current for the coil to generate a continuous sinusoidal force along with a variation in the gap values. The time series of the input current used to maintain the sinusoidal force of 0.25 *N* is indicated with the dotted black line in Figure 5.12. It is observed that the magnitude of the input current varies between the attraction and repulsion. In the repulsion process, the gap

between the electromagnet and permanent magnet reaches the maximum value of 10 *mm*. This requires more induced current to generate the maximum repulsive force of -0.25 *N*.

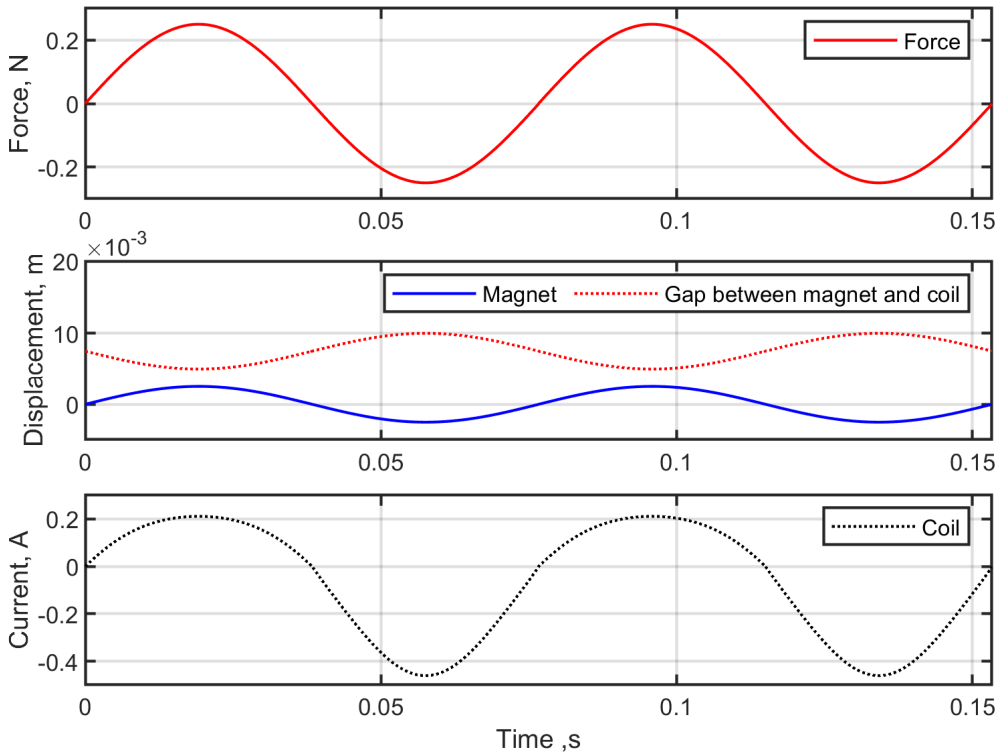

Figure 5.12. Time series of force, displacement of the electromagnet, the gap between the magnets and input current

5.4. Model realisation and fabrication

The physical model for generating passive travelling waves is built and investigated in this section. This experimental-based study includes introducing the conceptual design for fabrication and investigating the individual components that promote travelling waves.

5.4.1. Structural design

The structural design of the experimental rig for developing a non-contact actuation beam model is presented in Figure 5.13. This model, which include the beam, permanent magnet, coils, spring elements and frame, is developed based on the schematic diagram of the non-uniform beam model illustrated in Figure 5.1. Two coils are used and positioned parallel to each other to generate uniform magnetic fields. These coils are used to create attractive forces for one pole of the magnet, and repulsive forces for the other

pole of the magnet at the same time. The permanent magnet, that is attached to the beam, is positioned between the coils utilising springs to maintain its position. This is achieved by using a sandwich arrangement where the magnet and beam are embedded between two plates that are hold together with four bolts in the corners. These bolts also act as the mounting point for the springs. The mechanism for holding the magnet and springs is illustrated in Figure 5.14. Hence the frame purpose is not only to hold the spools in place, but also to hold the springs and the swimmer in place.

The plates for holding the magnet will consist of two 3D printed sheets which will be designed such a way to sandwich the magnet and beam between them. The spool and frame will be made of 3D printed plastics materials. The final design sees the Helmholtz coils being mounted to the inside of the uprights of the frame. The bolts used to fasten the uprights to the frame also provide mounting points for the springs to attach to. To not interfere with the magnetic fields, all fasteners and the beam is made of a non-ferromagnetic material. Furthermore, the springs are made of stainless stell materials which are expected to have trivial effects on the magnetic fields.

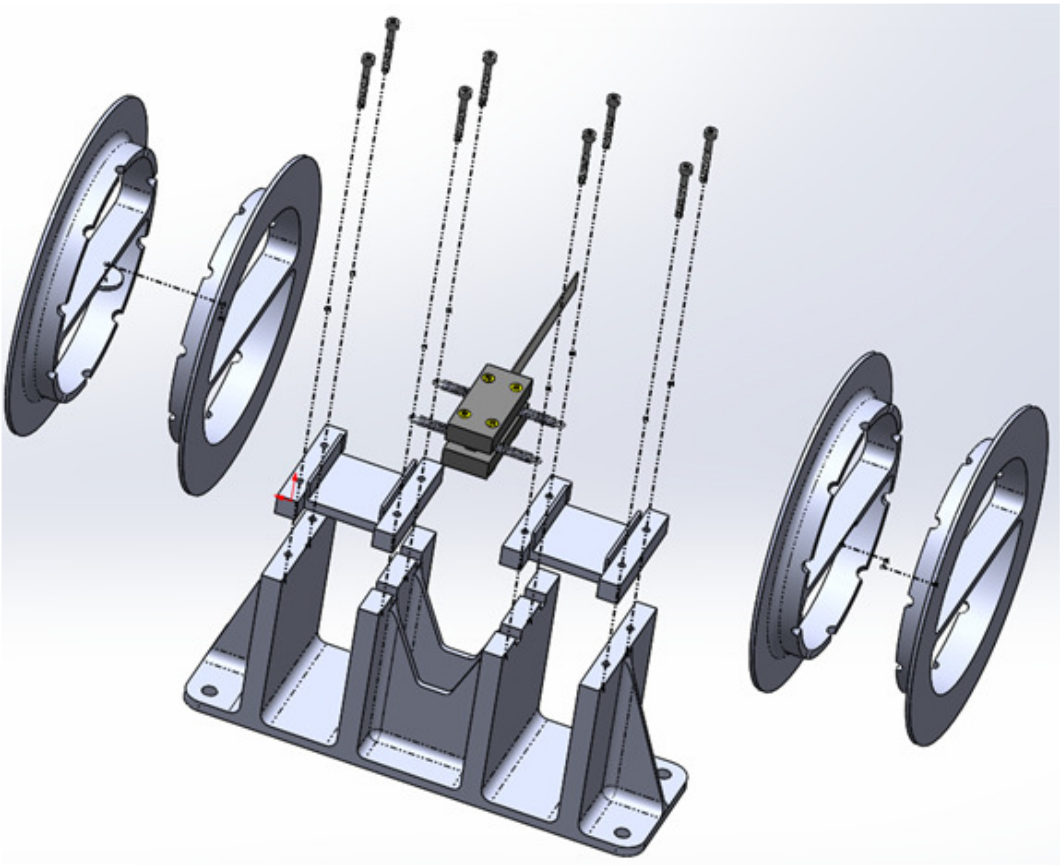

Figure 5.13. Assembly model and presentation

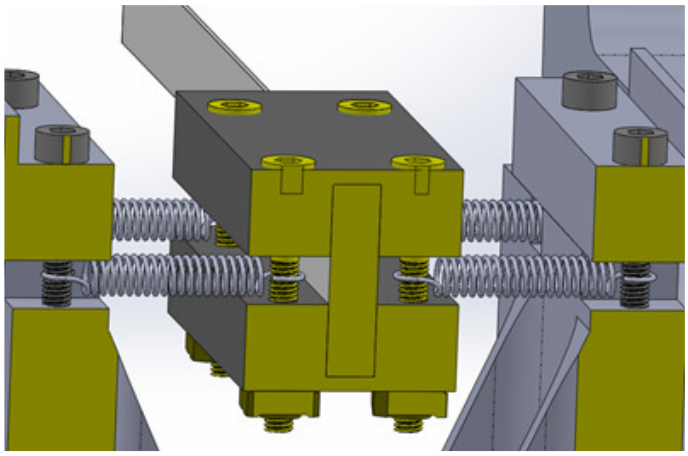

Figure 5.14. Permanent magnet supported by spring elements

Since the coil is based on the air core, the distance between the two coils is paramount for determining the strength of the magnetic fields. The gap between two coils is determined by the thickness of the magnetic head, elongation of the springs and space for adjusting the parts. The thickness of the head of the beam, including the magnet and plates, is 20 *mm*. The minimum elongation of the springs is about 12 *mm*. These geometrical constraints dictate that the minimum distance between the coils is about 40 *mm*, but to allow for changes to the design this distance was made to be 60 *mm*. In order to generate a homogeneous field in the region of interests, it has been estimated that the coils required a minimum radius of 60 *mm*. The spool has been designed to hold approximately 1000 turns of wire. This design choice has determined the thickness and width of the spool as well as its outside diameter. Estimations of these design parameters have been made by assuming an even distribution of the wire around the spool. With 1000 windings the optimum distribution is roughly 30 windings across by 30 layers of winding. A 0.5 *mm* copper wire would require the spool to house a coil with a section of 15 *mm* x 15 *mm*. This assumes that the wire is wrapped in the most space-efficient way, which is unlikely to be achieved. Therefore, safety factors have been applied to determine the width and the height of the spool, which have been dimensioned to be 20 *mm* and 30 *mm* respectively.

5.4.2. Individual characteristics of the beam and electromagnet

The parts involving the spool and frame were made using a Makerbot Replicator + FDM 3D printer with a polylactic acid (PLA) filament specified by 10–20% infill. Figure 5.15 shows the Helmholtz coils that are mounted on the frame. Note that heat resistant

and electric insulation tapes are used to isolate the wires. The coil was built by wrapping the wire approximately 800 turns around the spools. The wire diameter is 0.51 *mm* which results in the total resistance of 32 Ω and 25 Ω for each coil. The discrepancy in the resistance values is due to the by inhomogeneity in the copper and wild winding process for wrapping the coil. To avoid phase shift between the two coils caused by different resistance values, these coils are connected in series, leading to the total resistance of 56.5 Ω. The coils are powered by the 48-Watt LDS PA25E power amplifier. This amplifier is the same device used to investigate the vibration pattern of the beam using the vibration shaker described in Section 3.3.

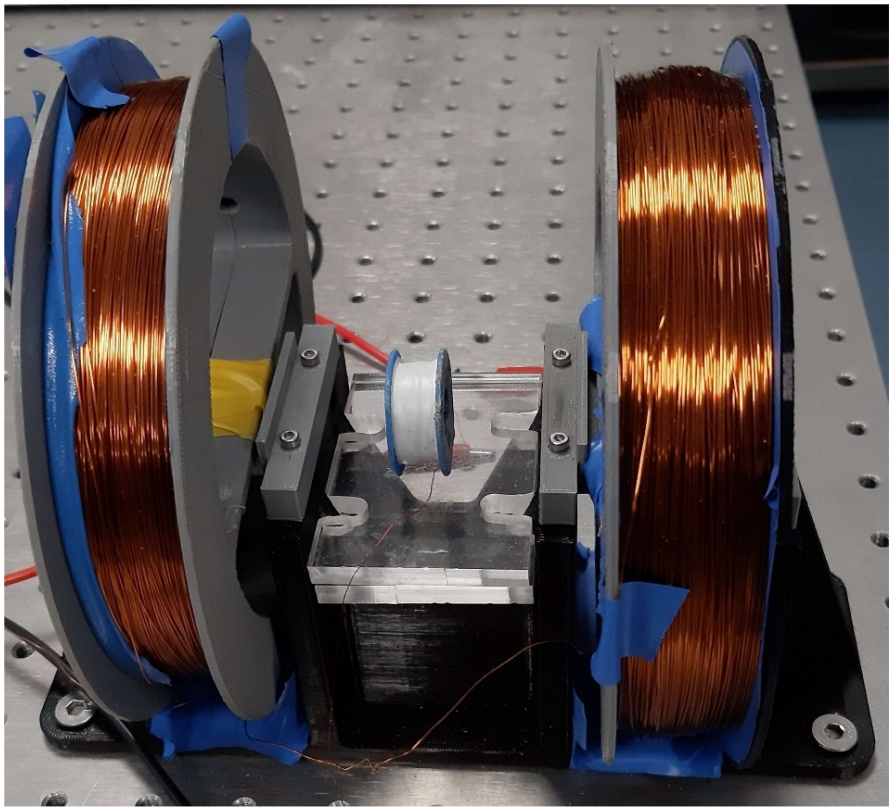

Figure 5.15. Characterising magnetic fields

To characterise the magnetic fields, a small coil shown in Figure 5.15 is positioned between the two coils. This arrangement is comparable to a single-phase air core transformer in which the small and big coil represent the secondary and primary windings, respectively. The SignalCalc Ace signal generator in conjunction with the Quattro hardware platform is used to generate and manipulate input signals for the big coils. Since the output signal from Quattro is typically low, the power amplifier magnifies the voltage to the desired values. The characteristics of the magnetic fields induced by the coils are obtained by examining the voltage reading from the small coil and the output of the signal

generator. The signal analyser estimates the transfer function of the two signals over a range of frequencies.

A random signal with the maximum amplitude of 0.707 *V* was assigned to the signal analyser. The gain for the power amplifier was set to 3. The first test used the receiver coil with the wire diameter of 0.2 *mm* wrapped about 1000 turns around the bobbin. This results in the total resistance of 45.2 Ω. To obtain a variation in the measurement results, the second test was performed with the receiver coil that has the wire diameter of 0.41 *mm*. With 600 turns, the total resistance for this coil is about 3 Ω. Note that the size of the bobbin for the second test is slightly bigger than the first test. Figure 5.16 presents the frequency responses of the first and the second tests indicated with the red and blue solid lines, respectively. The magnitude of the frequency response is a dimensionless value describing the voltage ratio of the receiver coil to the signal generator. As expected, the magnitude of the second test is higher than the first test. This agrees with the investigation in Section 5.3.1 where extending the surface of the coil can reduce leakage in the magnetic flux that leads to higher mechanical force generation. Furthermore, it is observed from the figure that the transfer function is frequency dependent particularly for the frequency up to 300 *Hz*.

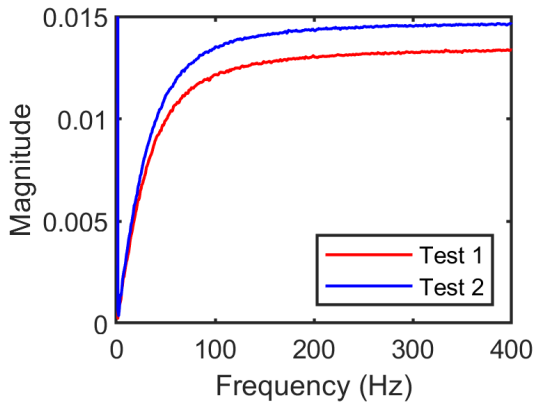

Figure 5.16. Frequency responses of the transfer function of the coil receiver to the signal generator

The characteristics of the beam are examined before incorporating the beam into the system. The same procedures as in Section 3.3.1 were applied to obtain the beam FRF. To assess the natural frequencies, the beam was mounted on an LDS V406 shaker specifically for vibration and mechanical shock testing. This type of shaker uses an LDS PA500L power amplifier to amplify the input voltage signal. The beam was clamped at

one tip and free on the other tip. The PCB Piezotronics 352C22 ceramic shear accelerometer was mounted on the clamped section of the beam, while the Polytec PDV100 laser vibrometer was pointed to the free tip of the beam. Figure 5.17 displays the configuration for characterising the beam. Note that the characteristics of the accelerometer and laser vibrometer have been provided in Section 3.3.2. In addition, the reading voltage from the accelerometer is enhanced by the PCB Piezotronics 428C signal conditioner.

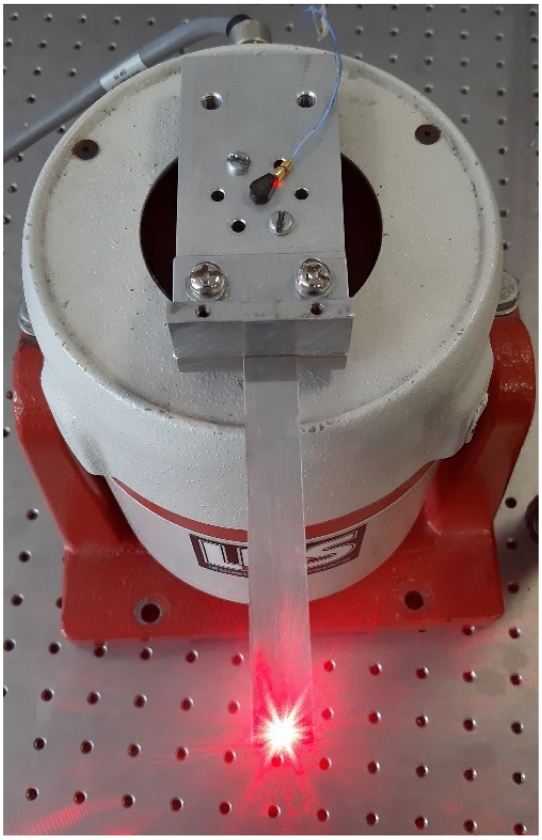

Figure 5.17. Configuration for measuring the beam FRF

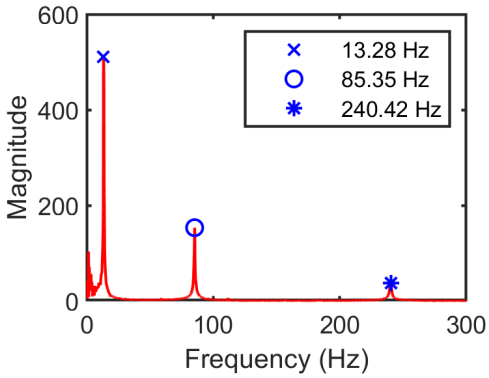

Figure 5.18. FRF of the beam for the frequency up to 300 Hz

The output voltages from the sensors are connected to Quattro to estimate the FRF of the beam using the SignalCalc Ace signal analyser. Random input signals with the maximum amplitude of 0.707 V were applied to the shaker to uniformly excite the modes. The beam is made of a non-ferromagnetic material with the size of $149.65 \times 15.2 \times 0.4$ mm for the length, width and thickness, respectively. Figure 5.18 presents the beam FRF for the frequency up to 300 Hz. The FRF magnitude has a dimensionless value describing the ratio of the acceleration of the beam tip to the base. Note that the velocity responses from the laser vibrometer is derived with respect to time by the signal analyser to get the

acceleration response. Therefore, the spike around zero in the beam FRF is due to the cut-off frequency of the sensors and the filtering process of the signal analyser. In addition, it is observed from the figure that there are two peaks for frequency up to 300 Hz indicated with the marker symbol “x”, “o” and “*”, representing the first three resonant frequencies, respectively.

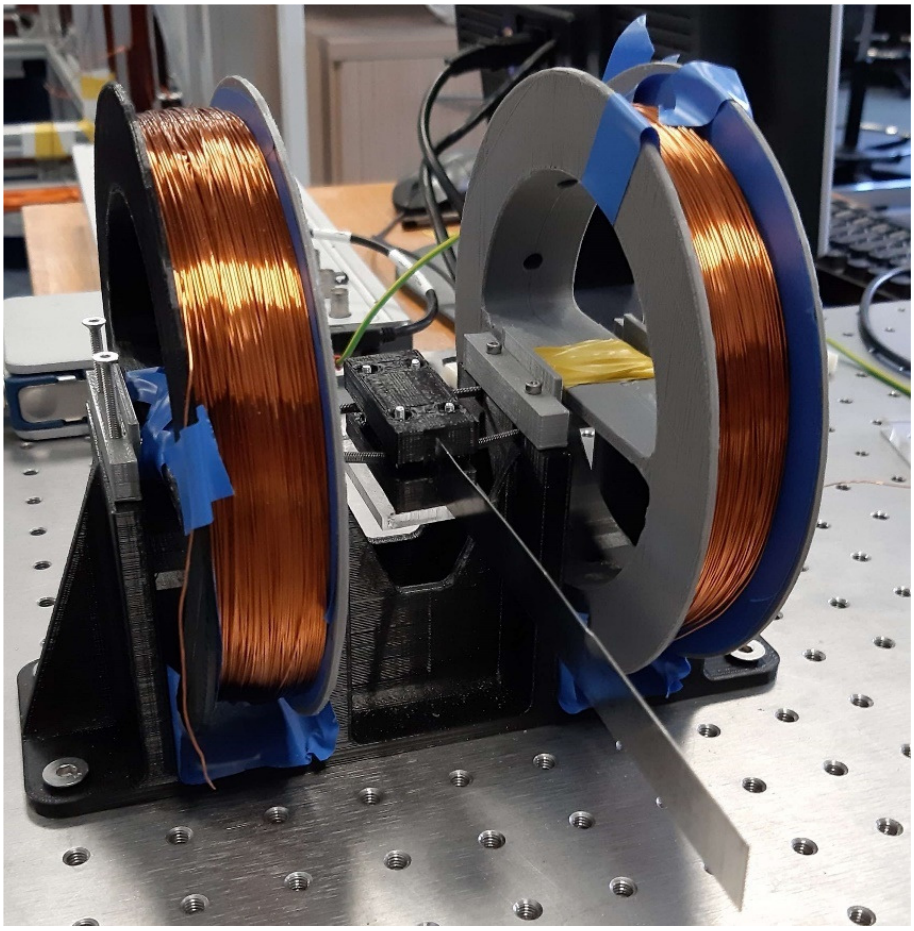

Figure 5.19. Assembled system

5.4.3. Assembly and testing

The plates to sandwich the beam and magnet were printed using the same PLA filament as it satisfied the required stress resistance with 10% infill. An N52 neodymium magnet with the dimension of 40 x 20 x 5 *mm* was used. This type of permanent magnet is the most powerful magnet and readily available in the market with the pull strength of 15.1 *kg*. The spring has a spring rate of 210 *N*/*m* with an initial tension of 0.66 *N*. Figure 5.19 displays the assembled system for generating passive travelling waves with a non-contact actuation. The same procedures as in Section 5.4.2 were applied to estimate the

FRF of the experimental rig. The laser vibrometer was directed to measure the tip velocity of the beam. However, the accelerometer sensor was no longer used since the head of the magnet experiences strong magnetic fields that might affect to the readings. Accordingly, the output voltage from the signal generator, before amplified by the power amplifier, was connected to Quattro. Since the two signals have different measurement units, the gains in the signal analyser were set to unity. This would allow for the analyser to estimate the voltage of the laser vibrometer compared to that of the output from the signal generator.

Figure 5.20 shows the beam FRF generated with the random input amplitude of 0.707 *mV*. It is seen that the FRF magnitude is more than unity. This is due to the output voltage from the laser vibrometer that is higher than that of the signal generator. However, the scale of the FRF magnitude should not affect to the location of the natural frequencies of the system. It is observed that there are five peaks indicated with the marker symbols appeared up to 150 *Hz*. The blue and green maker colours represent the resonant frequencies of the springs and the non-uniform beam model, respectively. As expected, the first resonant of the beam model shown in Figure 5.18 displaces from 13.28 *Hz* to 19.53 *Hz* due to the presence of the spring elements and the magnet. The second resonant of the springs, which represents the rotational motion of the magnet according to the mode shape analysis in Section 5.2, is located in between the first and second resonant of the beam. The presence of springs and the permanent magnet makes the second resonant frequencies of the beam displaces from the original location of 85.35 *Hz* to 98.24 *Hz*. In addition, it is believed that the peak appeared between the first resonant of the beam and the second resonant of the spring shown with the black triangle marker in Figure 5.20 is the natural frequency for the torsional vibration of the non-uniform beam model.

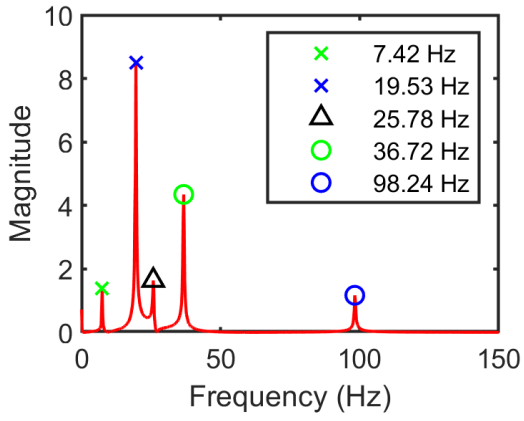

Figure 5.20. Beam FRF describing responses of the beam tip to the input signal

To investigate the torsional vibration of the model, the laser vibrometer was directed to measure velocity responses in different locations along the beam width. Figure 5.21(a) shows the times series of velocity measured at the tip of the beam with the forcing frequency of 25.75 *Hz*. Note that a phase synchronisation method with respect to the input signal was applied to the velocity responses. This is due to the limitation of the laser vibrometer that can only measure one (point) location at one time. From the figure, the width = 7.6 *mm* refers to the measurement of the laser vibrometer at the middle of the beam. This location can be seen from the laser pointer shown in Figure 5.17. The width = 0 *mm* and 15.2 *mm* indicate that the laser beam is pointed to measure the surface close to the edges the beam.

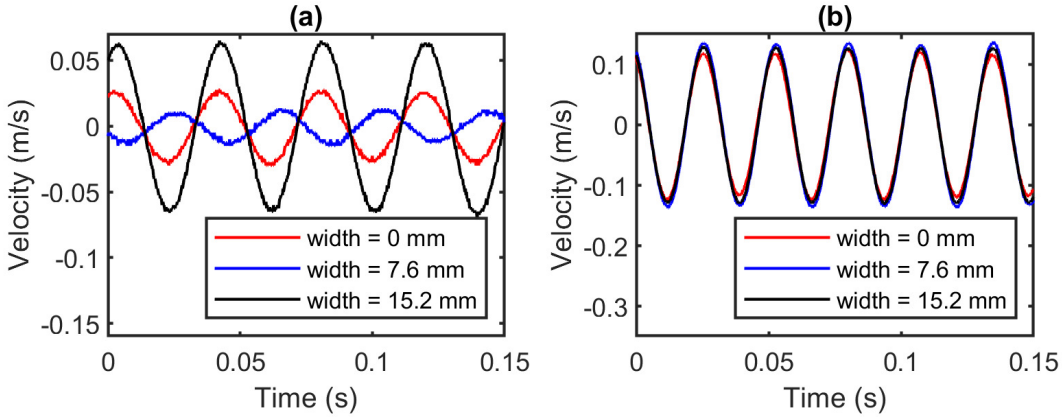

Figure 5.21. Time responses measured along the beam width for various frequencies

It is observed from Figure 5.21(a) that there are discrepancies both in the phase and amplitude of the velocity responses. This agrees to the first presumption that the third peak is the torsional vibration of the non-uniform beam model. For comparison, the same procedures were applied to measure the velocity responses along the beam width with the forcing frequency equal to the fourth resonant value of 36.72 *Hz*. The results are presented in Figure 5.21(b). It is observed from the figure that the velocity responses are all in-phase over time. Nevertheless, there are small discrepancies in the velocity amplitudes at this frequency which can be caused by manufacturing imprecision of the head, bad positioning of the swimmer and non-uniformity of the magnetic fields. Furthermore, this discrepancy becomes obvious at the natural frequency for the torsional vibration.

According to the steady-state responses of the beam, it was observed that the amplitude of the signal generator needs to be carefully tuned particularly around the natural frequencies to avoid the springs reaching the maximum deflection. To illustrate

these phenomena, Figure 5.22(a) and (b) show the steady-state responses of the beam vibrating at 19.53 *Hz* generated by setting the amplitude of the signal generator to 300 *mV* and 400 *mV*, respectively. The responses from the laser vibrometer indicated with the blue lines are presented in the voltage unit so that those can be compared with the signal generator, indicated with the red lines in Figure 5.22. It is seen that there is a distortion around the peaks for the amplitude of 400 mV that leads to subharmonic phenomena in the beam responses due to the maximum compression of the springs.

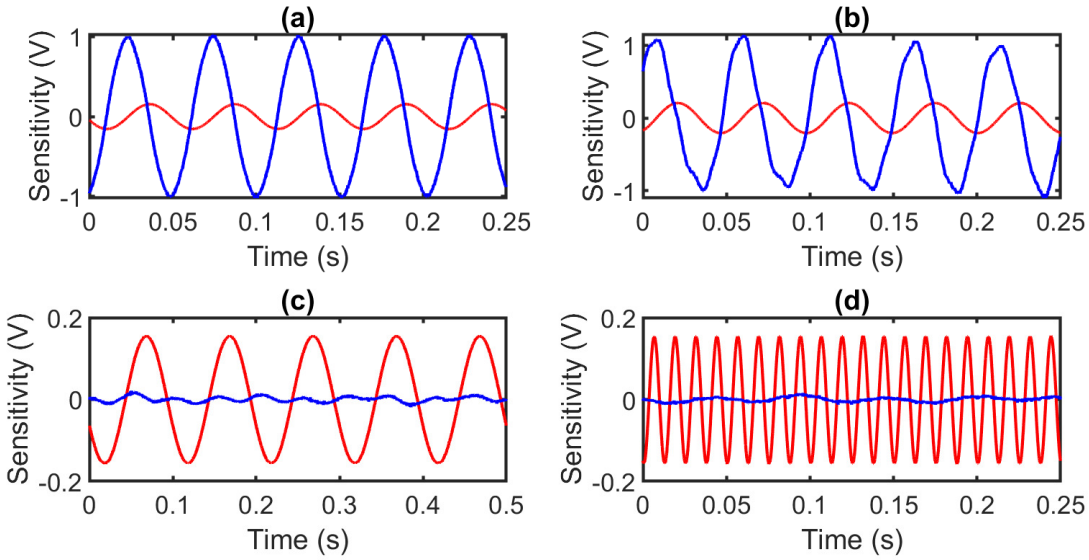

Figure 5.22. Dynamic responses of the non-uniform beam model for various forcing frequency. The red lines are voltages from the signal generator and the blue lines are responses from the laser vibrometer.

At frequencies away from resonant, the beam responses become very small, requiring more power to increase the mechanical force. However, the interaction of the permanent magnet and electromagnet as the forcing mechanism can reach saturation points that make the beam responses are independent to the change in the input voltage. This phenomenon can be seen from the beam responses vibrating at 10 *Hz* in Figure 5.22(c), generated by assigning the amplitude of the signal generator to 1 *V* and setting the gain for the power amplifier to the maximum level. Note that the data used to plot the figure have not been scaled from the vertical scale of the digital oscilloscope. Accordingly, the limit of the Y-axis is in the range of -0.2 *V* to 0.2 *V*, rather than -1 *V* to 1 *V*. It is seen from the figure that applying the maximum voltage for the coils does not alter the responses of the beam. The same phenomena are also found when the beam is actuated at 80 *Hz* shown in Figure

5.22(d). Although the input voltage was set to the maximum value, the velocity responses are very small in this frequency with poor signal-to-noise ratio.

It is believed that the non-linear beam model with the springs can generate irregular movement once the model is submerged in liquid. This is due to the hanging position of the beam that can create many degree-of-freedom due to the fluid flow. Accordingly, an acrylic plate is used to support the head of the non-uniform beam model to avoid structural torsion and rigid body motion in the vertical direction (up and down). Figure 5.23 shows the assembled model of the head support integrated in the rig. This design will avoid rotation of the head around the axis of the beam. The bottom of the head is also covered with the same material to create smooth contact between the surfaces. The purpose of this support is also to limit the vertical movement of the swimmer, reducing the effects of imbalance of the centre of mass and/or improper positioning of spring.

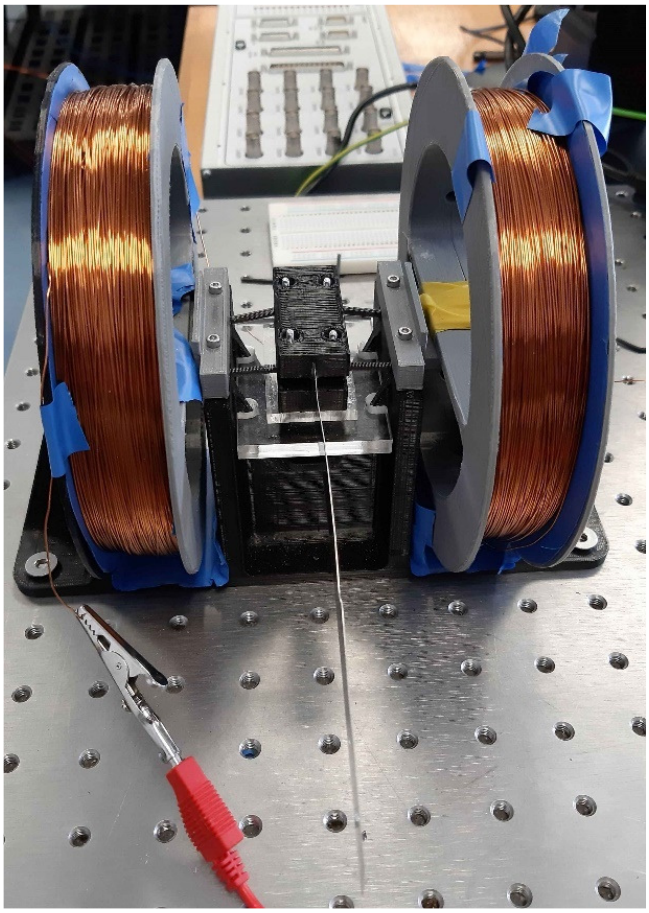

Figure 5.23. The beam with a head support

To evaluate the beam FRF, random input signals with the amplitude of 10 V were applied to the signal generator. The gain for the power amplifier was set to the maximum

level to overcome the friction force due to the contact surface between the head and acrylic plate. Figure 5.24 presents the FRF of the non-uniform beam model with the head support. Note that FRF magnitude described the voltage ratio of the laser vibrometer to the output of the signal generator. It is seen that the first two natural frequency values obtained from this measurement are similar to those appeared in Figure 5.18. A slight discrepancy in the second resonant value is caused by the length of the clamped section of the beam. The non-uniform beam model requires 5 *mm* of the beam length to fully engage with the head's slot. Therefore, the optimal length for the beam to perform vibration is 144.5 *mm*. Furthermore, the influence of the springs and torsional rotation on the beam FRF is no longer existed.

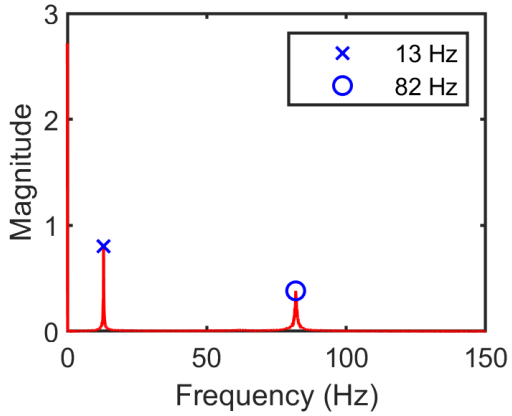

Figure 5.24. Beam FRF with the head support

To further investigate the absence of the spring on the beam FRF, the steady-state responses of the beam for various forcing frequencies are shown in Figure 5.25. Note that the red lines represent the output voltage from the signal generator, while the blue lines represent the velocity responses at the tip of the beam. The velocity response in Figure 5.25(a) is generated with the forcing frequency of 7.5 *Hz*. It is seen that the signal contains multiple frequencies. These multiple frequency phenomena disappear, and a clear sinusoidal signal is obtained when the beam is actuated at the first resonant frequency, f = 13 *Hz*, as shown in Figure 5.25(b). Further increasing the frequency to f = 19.5 *Hz* and 25.75 *Hz* shown in Figure 5.25(c) and (d), the velocity responses become more complex, and the frequency content is far richer than anticipated. Based on this occurrence, it is believed that there is not enough force generated by magnetic fields to counter the static friction force of the surface, leading to stick condition of the head of the non-uniform beam model. Therefore, the magnetic fields induce vibration through the whole frame rather than the head of the beam. This was clearly observed in the experimental test where

the stick state in the beam results in shaking a whole rig (including the holder and the coils). Finally, this stick state condition can be correlated to the absence of the spring element in the beam FRF presented in Figure 5.24.

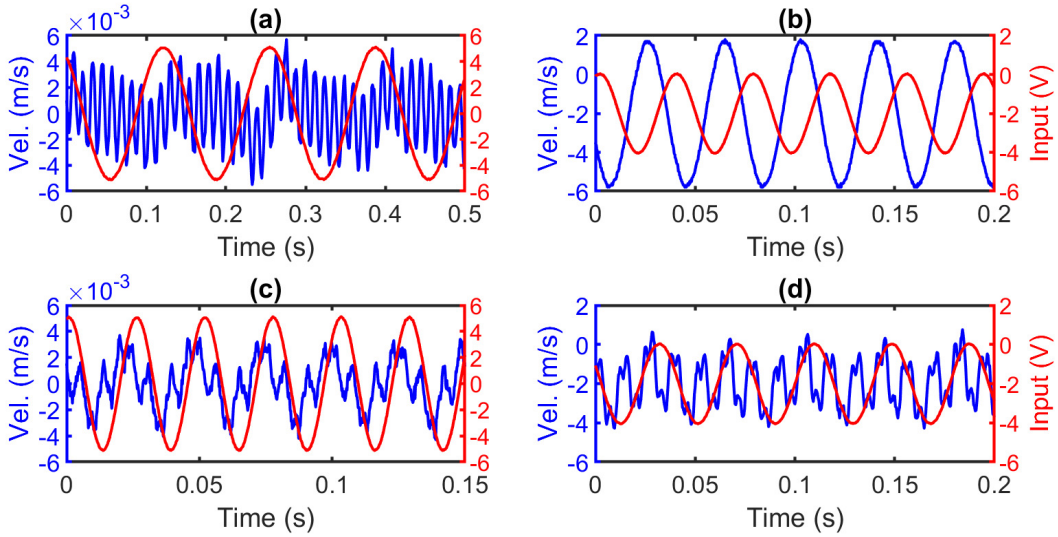

Figure 5.25. Time series at stick conditions for various forcing frequency

To achieve the slip condition, an arbitrary initial force was given to the beam to overcome the static friction force between two surfaces. Since the movement of the beam was not visible around the natural frequency using random input signals, the input was changed to sinusoidal waves. This, however, would give a strong peak in the forcing frequency in the FRF of the signal analyser that can attenuate the influence of the modes. Accordingly, a noise signal was superimposed to the sine wave to excite all the modes in the frequency range of interest and therefore generate a frequency response function. This method was first validated in the proper shaker that was used for evaluating the natural frequency of the beam described in Section 5.4.2. From the measurement, both the sinusoidal input with noise and random input, not shown here for brevity, give the same resonant frequencies with good repeatability. Although there is a discrepancy in the FRF magnitude compared to the other input signal, this should not affect the natural frequency values of the system.

Figure 5.26 presents the FRF of the beam with the head support generated by using sinusoidal input signals. It is seen that the beam FRF contains noisy signals with inconsistent pattern for various forcing frequency. The measurements were also repeated by adding lubricants as well as adjusting the percentage of the noise input levels with the

purpose to remove the noisy signal and unveil the modes, but the friction between two acrylic surfaces creating unwanted noise resulted in indeterminate FRF patterns.

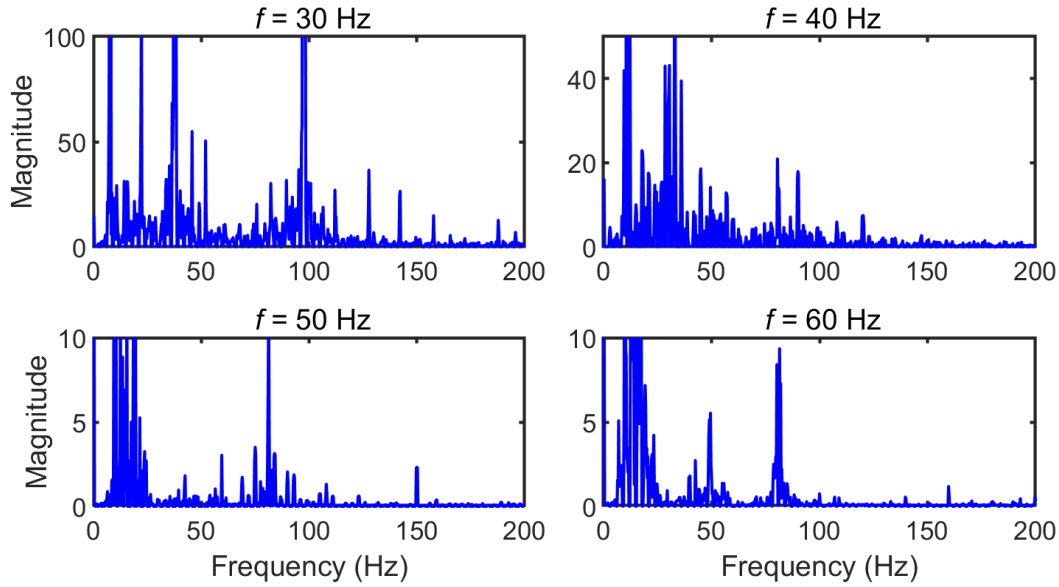

Figure 5.26. FRF of the beam with head support at slip condition

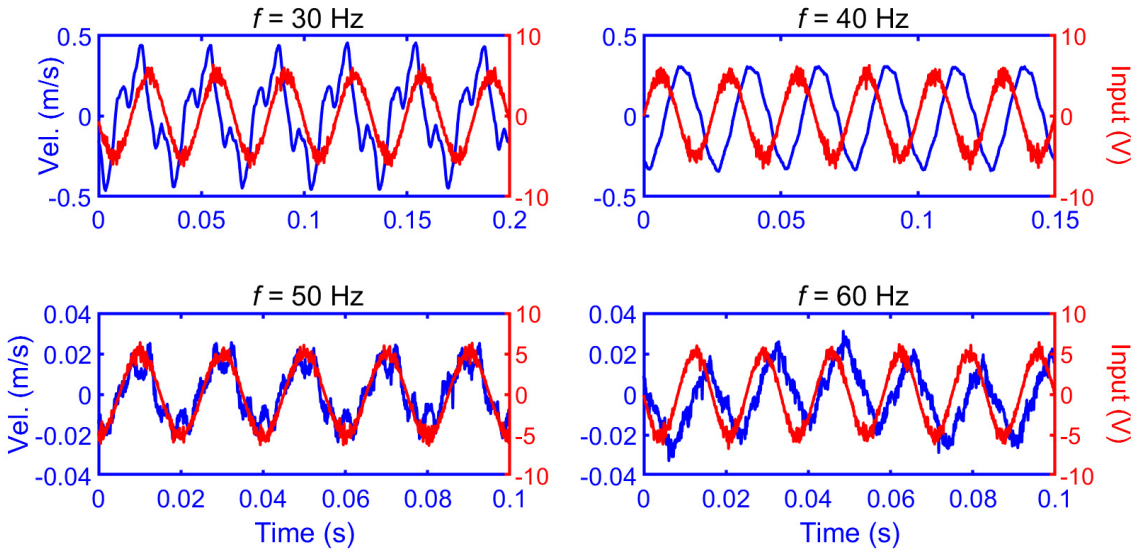

Figure 5.27. Time series of the beam with head support at slip conditions

Further investigations were carried out by probing output signals from the laser vibrometer and signal generator with respect to time using a digital oscilloscope shown in Figure 5.27. The notches and sharp peaks in the time series from the figures demonstrate the presence of stick-slip condition in the swimmer dynamics. The stick state occurs when the swimmer changes the displacement direction, resulting in the sharp peaks and troughs in the velocity responses. These time series plots also reveal that the damping caused by the friction of two surfaces is high enough to make the response of

the beam not strongly correlated to the input signal. With increasing the forcing frequency, the beam exhibits very small displacements and the influence of the spring become negligible. Therefore the well identifiable peak close to 100 *Hz* at the frequency of 50 *Hz* and 60 *Hz* presented in Figure 5.26 become more similar to those observed in Figure 5.18 and Figure 5.23 where the beam can be considered clamped at one end.

5.5. Conclusion

A conceptual design of a non-uniform beam model capable of generating more natural frequencies in the frequency of interest has been presented. The permanent magnet that is mounted on the one tip of the beam has also been considered in the analysis. The influence of the springs has been examined by considering different stiffness values. Depending on the stiffness values, the presence of the spring not only increases the number of natural frequencies, but also displaces the resonant values of the beam. From the mode shape analysis, the magnet is stiff enough to not perform torsional and bending vibrations. Accordingly, the spring introduces two motions for the magnet: the translational (rigid body) motion and rotational motion.

Investigation into the mechanism of the non-contact actuation has been performed. The parametric study of the electromagnet and permanent magnet includes: varying the gap, input current, total length of the coil, and wire diameter. It is expected that the coil has the maximum number of turns within the allowable space to increase the mechanical force. In a confined space, this can be achieved by decreasing the wire diameter. However, this can lead to increase the dissipated electrical power. The other way to increase the mechanical force is to extend the total surface of the coil which results in the increasing the total length of the coil. The mechanical forces also tend to be higher in the attraction than the repulsion particularly when then gap between the electromagnet and permanent is close. Furthermore, a demonstration for determining parameters to generate appropriate force for actuating the beam at the desired amplitude and frequency has been performed. Since the gap between the beam and electromagnet varies depending on the displacement beam amplitude, the input current needs to be manipulated with a different magnitude for the positive and negative values to generate a constant forcing amplitude.

The experimental model for the non-uniform beam with springs actuated by the magnetic fields has been developed. As expected, the assembled model has five natural

frequencies appeared up to 150 *Hz*: two natural frequencies from the springs, the other two from the beam, and one frequency contributed by the torsional vibration. To restrict the motion of the beam, an acrylic plate is introduced to support the magnet. However, this introduces complex dynamic responses in the beam such as the stick and slip condition, multiple frequencies in the signal, and subharmonic phenomena in the time series.

Chapter 6. Conclusions and future work

This chapter summarises the key findings from this study which can be divided into three categories: (i) Dynamic behaviours of a cantilever beam submerged in liquid; (ii) Characteristics of fluid flow of a submerged beam; and (iii) Development of a non-uniform beam model with a non-contact actuation method. Recommendations for future work are then discussed to further the development of the beam submerged in liquid for transport devices.

6.1. Conclusions

As discussed in Chapter 1, the work presented aims to contribute to the development of controllable devices capable of self-propulsion. This is achieved by investigating the structural travelling waves induced through electromagnetic actuation and their coupling with the fluid surrounding them. The key aspect in which this has been achieved are summarised below.

6.1.1. Dynamic properties of the beam

The initial phase of this study was to derive analytical models for obtaining the dynamic responses of a cantilever beam submerged in liquid. In Chapter 2, the deflection of the beam was approximated by using the Euler-Bernoulli equation and the presence of the fluid was integrated into the beam equation using the Morison's equation. The temporal solution based on the Galerkin approximation results in nonlinear coefficients and complex modal interactions for each resonant frequency. The discussion in this chapter highlights the limitation associated to these phenomena, using two lumped-mass systems to demonstrate the responses with numerical solutions. It has been shown that the cross-coupling modal terms introduce multiple-frequency in the steady-state responses of the submerged beam model. However, it has also been demonstrated that the

multiple frequency responses can be minimised without loss of generality by removing the cross-coupling modal terms for $j \neq k \neq i$. In addition, this chapter has demonstrated that a key aspect in simplifying the methodology of this technique is to linearise the quadratic damping term that provide mathematical convenience for correlating the beam parameters and beam responses.

While the previous discussion focussed on the beam equation, Chapter 3 addressed the derivation of the beam equation into the mechanical wave equation that leads to standing, travelling and hybrid waves. The accuracy of the nonlinear beam equation was thoroughly examined by comparing the responses with the experimental model. It has been demonstrated that the analytical model provides good approximation for predicting the real phenomena particularly for the beam submerged in water. Although the limitation of the analytical approaches arises from the estimation of fluid forces and elastic properties of the beam, the correction factors for the damping and spatial term can effectively refine the accuracy of the analytical approaches. Furthermore, the correction factors also present the opportunity to flexibly model the beam submerged in different fluid media.

The findings related to the vibrational properties of the beam from experiments are outlined in Chapter 3. Particular attention was given to the characteristics of the damping ratio extracted using the nonlinear identification parameter from experiments which exhibited high gradient values in the damping curves. It is further concluded that the discrepancy in the responses of the analytical model arises because of the relative contributions to the damping due to the fluid. Furthermore, a series of experimental investigations demonstrating the formation of travelling waves in different beam configurations are also presented. These experimental observations highlight the importance of operating in proximity of the natural frequency in the properties of travelling waves that are associated to the phase delay between the two tips and the beam amplitude at the node(s). This investigation was expanded by using the linear approximation model to provide detailed explanation to such phenomena. The analytical approaches suggest that the phase delay along the beam length in proximity of the natural frequency is due to the superposition of two main variables in the beam equation: the base input motion and damping parts, having a 90-degree phase shift. The superposition also

results in increasing the beam amplitude at the nodes since the two variables have different zero-crossing points along the beam length.

6.1.2. Fluid flow characteristics

Chapter 4 focusses on the influence of travelling waves on the characteristics of fluid flow generated by a cantilever beam submerged in water. An experimental investigation using the cantilever beam model was performed to illustrate the dependence of fluid dynamics on the beam responses. Particular attention was given to the variation of the forcing amplitude and frequency of the beam around the first two resonant frequencies in which the mean fluid velocities are determined by the trend line of the FRF magnitude of the beam. This study was expanded by using numerical simulations to obtain the time series of fluid velocity around the structure. The results suggest that the free tip velocities of the beam dictate the mean fluid velocity values. The demonstration also shows that large displacements result in higher fluid velocity. However, this can induce fluctuations in the flow field which with a consequent reduction in the fluid mean velocity. The numerical simulation using a thinner beam is also presented to obtain mean fluid velocities up to the fourth resonant frequencies. Through these investigations the importance of the dynamic properties of the beam on the induced velocity was demonstrated: important dynamic characteristics include tip velocity, tip ratio and pattern induced in the fluid flow.

Following this discussion, a beam configuration capable of maintaining constant tip velocity and tip ratio is introduced. This is achieved by manipulating the boundary conditions for each tip of the beam which would also allow to generate maximum travelling waves over a wide range of frequencies. The key motivation for using this model is to limit the independent variables of the beam such as the tip velocity and tip ratio. This would allow for comparison between the two-excitation beam and cantilever beam model to be made for examining the influence of travelling waves on the fluid flow. To provide more fundamental insight into the abilities and shortcomings of this beam configuration, the effect of the modification in the boundary conditions on the linear approximation of the beam equation derived in Chapter 2 is presented. The dynamic behaviours of this model vibrating in vacuum are also considered which exhibited pure travelling waves on the beam responses when actuated away from resonant frequencies.

Initially, the investigation of the two-excitation beam model submerged in water focusses on the first two resonant frequencies. It has been demonstrated by comparing the two models that the fluid velocity is independent of the changes in the vibration patterns of the beam. The discussion in this observation highlights the dependency of the fluid velocity on the beam tip velocity in these frequency ranges. Further investigation using the thinner beam demonstrates that the fluid flow becomes responsive to the vibration patterns after the third resonant frequencies. Finally, these observations outline which beam properties influence the most to the fluid flow around the first four resonant frequencies.

6.1.3. Development of a non-uniform beam model

The work of Chapter 5 undertook a fundamental investigation into the non-uniform beam model, focussing on the analysis of spring elements and electromagnetic actuation. It was noted that the main motivation for their use is their ability to provide more natural frequencies within the frequency of interest. The conceptual design of the system was initially outlined. To provide more insight into the abilities of the system, Chapter 5 considers the modal analysis of the non-uniform beam model which includes the analysis of the natural frequencies and mode shapes for various stiffness value. The motivation for doing so is that it demonstrates the changes in the dynamic properties of the non-uniform beam model due to the spring elements.

The interaction of the electromagnet and permanent magnet was also observed. It has been demonstrated that the number of turns, input current and extending the coil's surface can increase the performance of the actuation model. These variables are dictated by the wire diameter of the coil in which the size selection of the wire depends on the allowable maximum current, winding space and electrical power dissipation. It was further demonstrated that the attraction and repulsion process can result in different force magnitudes. Furthermore, the application of this technique to produce a sinusoidal force for actuating the non-uniform beam model to vibrate in the desired displacement value was also highlighted.

This investigation was expanded by developing an experimental rig based on the conceptual design of the non-uniform beam model. It has been demonstrated by experimental modal analyses that the torsional vibration also presents in the frequency of

interest. Effort to minimise this effect has been presented, though it consequently introduces other nonlinear phenomena that lead to increasing the electrical power consumption and reducing the efficiency of the system. Furthermore, the discussion in this experimental analysis outlines a number of benefits and limitations associated with the experimental rig of the non-uniform beam model.

6.2. Recommendations for future work

With respect to the current development, the areas proposed for future work are presented below.

- The analytical model derived in Chapter 2 was limited to the fully submerged beam model. The development of analytical models by considering the beam partially submerged in liquid is needed to facilitate a wide range of applications.
- The implementation of the analytical approaches is currently limited to approximate the dynamic responses of the beam in water. For the other fluid media such as silicone oil, it requires correction factors which are tuned subjectively to fit with the experiments. These correction factors can be used as the basis to further develop parameters that can elucidate the influence of the fluid forces on the beam properties.

- The nonlinear identification parameters described in Chapter 3 considers the identification method based on free vibration responses. The investigation becomes limited since the decay responses tend to deteriorate very quickly. Therefore, further investigation using forced vibration responses such as the CONCERTO and FORCEVIB method is necessary to examine the damping curves of the submerged beam. This would allow to expand the damping characteristics that leads to provide more accurate estimation for the analytical model.

- This study is limited to the forcing frequency up to the fifth resonant. Accordingly, the travelling waves at high frequencies needs to be examined in which some assumptions in the analytical models may break down. In addition, the investigation also needs to consider the miniaturisation of the system to develop micro-devices capable of self-propulsion

- The fluid investigation in this study only considers a uniform beam model. The rotation at one tip of the beam was restricted. The investigation was limited to the fourth resonant frequency. In addition, no external flow was applied to the analysis. Further investigation needs to consider the non-uniform beam model which includes the beam and permanent magnet. The rotational motion of the magnet needs to be considered in the analysis. The characteristics of fluid flow at higher resonant frequencies are also necessary to be studied. In addition, the external fluid flow can be included on the fluid investigation of a vibrating beam to expand the analysis.

- The development of the experimental rig for the non-uniform beam model with spring mechanism using a non-contact actuation method presented in Chapter 5 was limited to the application of a system vibrating in air. Further investigation requires the system to be submerged in liquid. The experimental rig also requires another mechanism that capable of providing a support for the head of the magnet to avoid torsional vibration and vertical vibration, whilst maintaining the function of the springs as these components can induce more natural frequencies in the operating frequency.

Appendix A. List of Publications

List of Publications

The contents of this dissertation have been partially published, or in the process of being published, and presented in related conferences.

A.1 Journal Publications

- Syuhri S.N.H., Zare-Behtash H., Cammarano A. (2020) Investigating the influence of fluid-structure interactions on nonlinear system identification. *Vibration*, Vol. 3, Issue 4, page 521-544. https://doi.org/10.3390/vibration3040032
- Syuhri S.N.H., Zare-Behtash H., Cammarano A. Travelling waves of cantilever beams. *Smart Materials and Structures*, Under preparation for submission.
- Syuhri S.N.H., Pickles D., Zare-Behtash H., Cammarano A. Influence of travelling waves on the fluid dynamics of a beam submerged in water. *Journal of Fluids and Structures*, Under preparation for submission.

A.2 Conference Proceedings and Presentations

- Syuhri S.N.H., McCartney A., Cammarano A. Development of an experimental rig for emulating undulatory locomotion. International Modal Analysis Conference (IMAC) XXXVIII, Houston, Texas, USA, 2020.
  Proceedings: Nonlinear Structures & Systems, Volume 1. Conference Proceedings of the Society for Experimental Mechanics Series. Springer, Cham. https://doi.org/10.1007/978-3-030-47626-7_37
- Syuhri S.N.H., Zare-Behtash H., Cammarano A. Experimental characterisation of structural travelling wave induced thrust. International Modal Analysis Conference (IMAC) XLI, Austin, Texas, USA, 2023 (to be presented).

Bibliography

1. Lauga, E. and T.R. Powers, *The hydrodynamics of swimming microorganisms.* Reports on Progress in Physics, 2009. **72**(9). http://dx.doi.org/10.1088/0034-4885/72/9/096601.
2. Machin, K.E., *Wave Propagation along Flagella.* Journal of Experimental Biology, 1958. **35**(4): p. 796-806. http://dx.doi.org/10.1242/jeb.35.4.796.
3. Gray, J., *Studies in Animal Locomotion.* Journal of Experimental Biology, 1933. **10**(1): p. 88-104. http://dx.doi.org/10.1242/jeb.10.1.88.
4. Tytell, E.D. and G.V. Lauder, *The hydrodynamics of eel swimming*. Journal of Experimental Biology, 2004. **207**(11): p. 1825-1841. http://dx.doi.org/10.1242/jeb.00968.
5. Borazjani, I., *Numerical simulations of fluid-structure interaction problems in biological flows*. 2008: University of Minnesota.
6. Hultmark, M., M. Leftwich, and A.J. Smits, *Flowfield measurements in the wake of a robotic lamprey.* Experiments in Fluids, 2007. **43**(5): p. 683-690. http://dx.doi.org/10.1007/s00348-007-0412-1.
7. Graham, J.B., et al., *Surface and Subsurface Swimming of the Sea Snake Pelamis Platurus.* Journal of Experimental Biology, 1987. **127**(1): p. 27-44. http://dx.doi.org/10.1242/jeb.127.1.27.
8. Feeny, B.F. and A.K. Feeny, *Complex Modal Analysis of the Swimming Motion of a Whiting.* Journal of Vibration and Acoustics, 2013. **135**(2). http://dx.doi.org/10.1115/1.4023056.
9. Cui, Z., et al., *Complex modal analysis of the movements of swimming fish propelled by body and/or caudal fin.* Wave Motion, 2018. **78**: p. 83-97. http://dx.doi.org/10.1016/j.wavemoti.2018.01.001.
10. Cheng, J.Y., T.J. Pedley, and J.D. Altringham, *A continuous dynamic beam model for swimming fish.* Philosophical Transactions of the Royal Society of London. Series B: Biological Sciences, 1998. **353**(1371): p. 981-997. http://dx.doi.org/10.1098/rstb.1998.0262.
11. Lighthill, M.J., *Note on the swimming of slender fish.* Journal of Fluid Mechanics, 1960. **9**(2): p. 305-317. http://dx.doi.org/10.1017/s0022112060001110.
12. Videler, J.J., *Fish swimming*. Vol. 10. 1993: Springer Science & Business Media.

13. Wu, T.Y.-T., *Swimming of a waving plate.* Journal of Fluid Mechanics, 1961. **10**(3): p. 321-344. http://dx.doi.org/10.1017/s0022112061000949.
14. Ramananarivo, S., R. Godoy-Diana, and B. Thiria, *Passive elastic mechanism to mimic fish-muscle action in anguilliform swimming.* Journal of The Royal Society Interface, 2013. **10**(88). http://dx.doi.org/10.1098/rsif.2013.0667.
15. Godoy-Diana, R. and B. Thiria, *On the diverse roles of fluid dynamic drag in animal swimming and flying.* Journal of The Royal Society Interface, 2018. **15**(139). http://dx.doi.org/10.1098/rsif.2017.0715.
16. Piñeirua, M., R. Godoy-Diana, and B. Thiria, *Resistive thrust production can be as crucial as added mass mechanisms for inertial undulatory swimmers.* Physical Review E, 2015. **92**(2). http://dx.doi.org/10.1103/PhysRevE.92.021001.
17. Piñeirua, M., B. Thiria, and R. Godoy-Diana, *Modelling of an actuated elastic swimmer.* Journal of Fluid Mechanics, 2017. **829**: p. 731-750. http://dx.doi.org/10.1017/jfm.2017.570.
18. Ramananarivo, S., R. Godoy-Diana, and B. Thiria, *Propagating waves in bounded elastic media: Transition from standing waves to anguilliform kinematics.* EPL (Europhysics Letters), 2014. **105**(5). http://dx.doi.org/10.1209/0295-5075/105/54003.
19. Ramananarivo, S., B. Thiria, and R. Godoy-Diana, *Elastic swimmer on a free surface.* Physics of Fluids, 2014. **26**(9). http://dx.doi.org/10.1063/1.4893539.
20. Raspa, V., et al., *Vortex-induced drag and the role of aspect ratio in undulatory swimmers.* Physics of Fluids, 2014. **26**(4). http://dx.doi.org/10.1063/1.4870254.
21. Malladi, V.V.N.S., *Continual Traveling waves in Finite Structures: Theory, Simulations, and Experiments*. 2016, Virginia Polytechnic Institute and State University: Blacksburg, Virginia.
22. Musgrave, P.F., *Electro-hydro-elastic modeling of Structure-Borne Traveling Waves and their application to aquatic swimming motions.* Journal of Fluids and Structures, 2021. **102**. http://dx.doi.org/10.1016/j.jfluidstructs.2021.103230.
23. Malladi, V.V.N.S., et al., *Investigation of propulsive characteristics due to traveling waves in continuous finite media*, in *Bioinspiration, Biomimetics, and Bioreplication 2017*. 2017.
24. Calisti, M., G. Picardi, and C. Laschi, *Fundamentals of soft robot locomotion.* Journal of The Royal Society Interface, 2017. **14**(130). http://dx.doi.org/10.1098/rsif.2017.0101.

25. Smits, A.J., *Undulatory and oscillatory swimming.* Journal of Fluid Mechanics, 2019. **874**. http://dx.doi.org/10.1017/jfm.2019.284.
26. Erturk, A. and G. Delporte, *Underwater thrust and power generation using flexible piezoelectric composites: an experimental investigation toward self-powered swimmer-sensor platforms.* Smart Materials and Structures, 2011. **20**(12). http://dx.doi.org/10.1088/0964-1726/20/12/125013.
27. Shahab, S., D. Tan, and A. Erturk, *Hydrodynamic thrust generation and power consumption investigations for piezoelectric fins with different aspect ratios.* The European Physical Journal Special Topics, 2015. **224**(17-18): p. 3419-3434. http://dx.doi.org/10.1140/epjst/e2015-50180-1.
28. Fernández-Prats, R., et al., *Large-amplitude undulatory swimming near a wall.* Bioinspiration & Biomimetics, 2015. **10**(1). http://dx.doi.org/10.1088/1748-3190/10/1/016003.
29. Demirer, E., *Bio-inspired locomotion using oscillating elastic plates*. 2021, Georgia Institute of Technology.
30. Shelton, R.M., P. Thornycroft, and G.V. Lauder, *Undulatory locomotion of flexible foils as biomimetic models for understanding fish propulsion.* Journal of Experimental Biology, 2014. http://dx.doi.org/10.1242/jeb.098046.
31. Yeh, P.D., *Fast and efficient locomotion using oscillating flexible plates*. 2016, Georgia Institute of Technology.
32. Cen, L. and A. Erturk, *Bio-inspired aquatic robotics by untethered piezohydroelastic actuation.* Bioinspiration & Biomimetics, 2013. **8**(1). http://dx.doi.org/10.1088/1748-3182/8/1/016006.
33. Shahab, S. and A. Erturk, *Underwater Dynamic Actuation of Macro-Fiber Composite Flaps With Different Aspect Ratios: Electrohydroelastic Modeling, Testing, and Characterization*, in *Volume 2: Mechanics and Behavior of Active Materials; Integrated System Design and Implementation; Bioinspired Smart Materials and Systems; Energy Harvesting*. 2014.
34. Shahab, S. and A. Erturk, *Experimentally Validated Nonlinear Electrohydroelastic Euler-Bernoulli-Morison Model for Macro-Fiber Composites With Different Aspect Ratios*, in *Volume 8: 27th Conference on Mechanical Vibration and Noise*. 2015.
35. Shahab, S. and A. Erturk, *Coupling of experimentally validated electroelastic dynamics and mixing rules formulation for macro-fiber composite piezoelectric*

structures. Journal of Intelligent Material Systems and Structures, 2016. **28**(12): p. 1575-1588. http://dx.doi.org/10.1177/1045389x16672732.

36. Nisar, A., et al., *MEMS-based micropumps in drug delivery and biomedical applications*. Sensors and Actuators B: Chemical, 2008. **130**(2): p. 917-942. http://dx.doi.org/10.1016/j.snb.2007.10.064.
37. Nelson, B.J., I.K. Kaliakatsos, and J.J. Abbott, *Microrobots for Minimally Invasive Medicine.* Annual Review of Biomedical Engineering, 2010. **12**(1): p. 55-85. http://dx.doi.org/10.1146/annurev-bioeng-010510-103409.
38. Wang, Y.-N. and L.-M. Fu, *Micropumps and biomedical applications – A review.* Microelectronic Engineering, 2018. **195**: p. 121-138. http://dx.doi.org/10.1016/j.mee.2018.04.008.
39. Ogawa, J., et al., *Development of liquid pumping devices using vibrating microchannel walls.* Sensors and Actuators A: Physical, 2009. **152**(2): p. 211-218. http://dx.doi.org/10.1016/j.sna.2009.04.004.
40. Liu, G. and W. Zhang, *Travelling-Wave Micropumps*, in *Microbial Toxins*. 2017. p. 1-19. http://dx.doi.org/10.1007/978-981-10-2798-7_29-1.
41. Zhang, W., et al., *Travelling-wave piezoelectric micropump with low resistance microchannel.* Electronics Letters, 2011. **47**(19). http://dx.doi.org/10.1049/el.2011.2035.
42. Afrasiab, H. and M.R. Movahhedy, *Treatment of the small time instability in the finite element analysis of fluid structure interaction problems*. International Journal for Numerical Methods in Fluids, 2013. **71**(6): p. 756-771. http://dx.doi.org/10.1002/fld.3684.
43. Afrasiab, H., M.R. Movahhedy, and A. Assempour, *Proposal of a new design for valveless micropumps*. Scientia Iranica, 2011. **18**(6): p. 1261-1266. http://dx.doi.org/10.1016/j.scient.2011.11.023.
44. Afrasiab, H., M.R. Movahhedy, and A. Assempour, *Fluid-structure interaction analysis in microfluidic devices: A dimensionless finite element approach.* International Journal for Numerical Methods in Fluids, 2012. **68**(9): p. 1073-1086. http://dx.doi.org/10.1002/fld.2592.
45. Ye, W., et al., *Travelling wave magnetic valveless micropump driven by rotating integrated magnetic arrays*. Micro & Nano Letters, 2014. **9**(4): p. 232-234. http://dx.doi.org/10.1049/mnl.2014.0022.

46. Yu, H., et al., *Design, fabrication, and characterization of a valveless magnetic travelling-wave micropump.* Journal of Micromechanics and Microengineering, 2015. **25**(6). http://dx.doi.org/10.1088/0960-1317/25/6/065019.
47. Li, C., et al., *Recent progress in drug delivery.* Acta Pharmaceutica Sinica B, 2019. **9**(6): p. 1145-1162. http://dx.doi.org/10.1016/j.apsb.2019.08.003.
48. Abiev, R.S., *Modern state and perspectives of microtechnique application in chemical industry.* Russian Journal of General Chemistry, 2013. **82**(12): p. 2019-2024. http://dx.doi.org/10.1134/s1070363212120237.
49. Ehrfeld, W., V. Hessel, and H. Lehr, *Microreactors for Chemical Synthesis and Biotechnology — Current Developments and Future Applications*, in *Microsystem Technology in Chemistry and Life Science*. 1998. p. 233-252. http://dx.doi.org/10.1007/3-540-69544-3_10.
50. Zhang, T. and Q.-M. Wang, *Valveless piezoelectric micropump for fuel delivery in direct methanol fuel cell (DMFC) devices*. Journal of Power Sources, 2005. **140**(1): p. 72-80. http://dx.doi.org/10.1016/j.jpowsour.2004.07.026.
51. Hironari, T., S. Koichi, and N. Shintaro, *An active micro reactor system with integrated fluid control devices for chemical synthetic process*, in *2008 IEEE/ASME International Conference on Advanced Intelligent Mechatronics*. 2008. p. 43-48.
52. Abassi, W., A. El Baroudi, and F. Razafimahery, *Vibration Analysis of Euler-Bernoulli Beams Partially Immersed in a Viscous Fluid.* Physics Research International, 2016. **2016**: p. 1-14. http://dx.doi.org/10.1155/2016/6761372.
53. Ghanbari, M. and G. Rezazadeh, *A MEMS-based methodology for measurement of effective density and viscosity of nanofluids*. European Journal of Mechanics - B/Fluids, 2021. **86**: p. 67-77. http://dx.doi.org/10.1016/j.euromechflu.2020.12.003.
54. Ghommem, M., V. Puzyrev, and F. Najar, *Fluid sensing using microcantilevers: From physics-based modeling to deep learning.* Applied Mathematical Modelling, 2020. **88**: p. 224-237. http://dx.doi.org/10.1016/j.apm.2020.06.051.
55. Hossain, A., A. Mishty, and A. Mian, *Numerical analysis for design optimization of microcantilever beams for measuring rheological properties of viscous fluid.* Finite Elements in Analysis and Design, 2013. **68**: p. 1-9. http://dx.doi.org/10.1016/j.finel.2013.01.002.
56. Rezazadeh, G. and M. Ghanbari, *On the Mathematical Modeling of a MEMS-Based Sensor for Simultaneous Measurement of Fluids Viscosity and Density.* Sensing and Imaging, 2018. **19**(1). http://dx.doi.org/10.1007/s11220-018-0213-z.

57. Riesch, C., et al., *Characterizing Vibrating Cantilevers for Liquid Viscosity and Density Sensing*. Journal of Sensors, 2008. **2008**: p. 1-9. http://dx.doi.org/10.1155/2008/697062.

58. Hou, J., et al., *Damage Identification Based on Adding Mass for Liquid–Solid Coupling Structures*. Applied Sciences, 2020. **10**(7). http://dx.doi.org/10.3390/app10072312.

59. Alunda, B.O. and Y.J. Lee, *Review: Cantilever-Based Sensors for High Speed Atomic Force Microscopy.* Sensors, 2020. **20**(17). http://dx.doi.org/10.3390/s20174784.

60. Rogers, B., et al., *Tapping mode atomic force microscopy in liquid with an insulated piezoelectric microactuator.* Review of Scientific Instruments, 2002. **73**(9): p. 3242-3244. http://dx.doi.org/10.1063/1.1499532.

61. Chon, J.W.M., P. Mulvaney, and J.E. Sader, *Experimental validation of theoretical models for the frequency response of atomic force microscope cantilever beams immersed in fluids*. Journal of Applied Physics, 2000. **87**(8): p. 3978-3988. http://dx.doi.org/10.1063/1.372455.

62. Green, C.P. and J.E. Sader, *Torsional frequency response of cantilever beams immersed in viscous fluids with applications to the atomic force microscope.* Journal of Applied Physics, 2002. **92**(10): p. 6262-6274. http://dx.doi.org/10.1063/1.1512318.

63. Green, C.P. and J.E. Sader, *Frequency response of cantilever beams immersed in viscous fluids near a solid surface with applications to the atomic force microscope.* Journal of Applied Physics, 2005. **98**(11). http://dx.doi.org/10.1063/1.2136418.

64. Kiracofe, D. and A. Raman, *Quantitative force and dissipation measurements in liquids using piezo-excited atomic force microscopy: a unifying theory.* Nanotechnology, 2011. **22**(48). http://dx.doi.org/10.1088/0957-4484/22/48/485502.

65. Sader, J.E., *Frequency response of cantilever beams immersed in viscous fluids with applications to the atomic force microscope*. Journal of Applied Physics, 1998. **84**(1): p. 64-76. http://dx.doi.org/10.1063/1.368002.

66. Van Eysden, C.A. and J.E. Sader, *Frequency response of cantilever beams immersed in viscous fluids with applications to the atomic force microscope: Arbitrary mode order.* Journal of Applied Physics, 2007. **101**(4). http://dx.doi.org/10.1063/1.2654274.

67. Van Eysden, C.A. and J.E. Sader, *Frequency response of cantilever beams immersed in compressible fluids with applications to the atomic force microscope.* Journal of Applied Physics, 2009. **106**(9). http://dx.doi.org/10.1063/1.3254191.
68. Alexeev, A., J.M. Yeomans, and A.C. Balazs, *Designing Synthetic, Pumping Cilia That Switch the Flow Direction in Microchannels.* Langmuir, 2008. **24**(21): p. 12102-12106. http://dx.doi.org/10.1021/la801907x.
69. Dryden, A. and M. Ballard, *Numerical investigation of a biomimetic elastic valve for microfluidic pumping.* Journal of Fluids and Structures, 2021. **103**. http://dx.doi.org/10.1016/j.jfluidstructs.2021.103265.
70. Gomez, M., D.E. Moulton, and D. Vella, *Passive Control of Viscous Flow via Elastic Snap-Through.* Physical Review Letters, 2017. **119**(14). http://dx.doi.org/10.1103/PhysRevLett.119.144502.
71. Jiao, S. and M. Liu, *Snap-through in Graphene Nanochannels: With Application to Fluidic Control.* ACS Applied Materials & Interfaces, 2020. **13**(1): p. 1158-1168. http://dx.doi.org/10.1021/acsami.0c16468.
72. Kim, H., et al., *Flow-induced periodic snap-through dynamics.* Journal of Fluid Mechanics, 2021. **913**. http://dx.doi.org/10.1017/jfm.2021.57.
73. Wagg, D. and S. Neild, *Nonlinear Vibration with Control.* Solid Mechanics and Its Applications. 2015.
74. Cellini, F., et al., *Effect of hydrodynamic interaction on energy harvesting in arrays of ionic polymer metal composites vibrating in a viscous fluid.* Smart Materials and Structures, 2014. **23**(4). http://dx.doi.org/10.1088/0964-1726/23/4/045015.
75. Cha, Y., et al., *Energy harvesting from a piezoelectric biomimetic fish tail.* Renewable Energy, 2016. **86**: p. 449-458. http://dx.doi.org/10.1016/j.renene.2015.07.077.
76. Cha, Y., H. Kim, and M. Porfiri, *Energy harvesting from underwater base excitation of a piezoelectric composite beam.* Smart Materials and Structures, 2013. **22**(11). http://dx.doi.org/10.1088/0964-1726/22/11/115026.
77. Liao, W.-H., S. Shahab, and A. Erturk, *Electrohydroelastic dynamics of macro-fiber composites for underwater energy harvesting from base excitation*, in *Active and Passive Smart Structures and Integrated Systems 2014*. 2014.
78. Gabai, R. and I. Bucher, *Generating Traveling Vibration Waves in Finite Structures*, in *Volume 2: Automotive Systems; Bioengineering and Biomedical*

Technology; Computational Mechanics; Controls; Dynamical Systems. 2008. p. 761-770.

79. Byoung-Gook, L. and P.I. Ro, *An object transport system using flexural ultrasonic progressive waves generated by two-mode excitation.* IEEE Transactions on Ultrasonics, Ferroelectrics and Frequency Control, 2000. **47**(4): p. 994-999. http://dx.doi.org/10.1109/58.852083.
80. Bucher, I., et al., *Experimental travelling waves identification in mechanical structures.* Mathematics and Mechanics of Solids, 2017. **24**(1): p. 152-167. http://dx.doi.org/10.1177/1081286517732825.
81. Hariri, H., Y. Bernard, and A. Razek, *A traveling wave piezoelectric beam robot.* Smart Materials and Structures, 2014. **23**(2). http://dx.doi.org/10.1088/0964-1726/23/2/025013.
82. Hariri, H., Y. Bernard, and A. Razek, *Dual piezoelectric beam robot: The effect of piezoelectric patches' positions.* Journal of Intelligent Material Systems and Structures, 2015. **26**(18): p. 2577-2590. http://dx.doi.org/10.1177/1045389x15572013.
83. Musgrave, P.F., M.I. Albakri, and A.A. Phoenix, *Guidelines and procedure for tailoring high-performance, steady-state traveling waves for propulsion and solid-state motion.* Smart Materials and Structures, 2021. **30**(2). http://dx.doi.org/10.1088/1361-665X/abd3d7.
84. Musgrave, P.F., et al., *Generating Structure-Borne Traveling Waves Favorable for Applications*, in *ASME 2020 Conference on Smart Materials, Adaptive Structures and Intelligent Systems*. 2020.
85. Kuribayashi, M., S. Ueha, and E. Mori, *Excitation conditions of flexural traveling waves for a reversible ultrasonic linear motor.* The Journal of the Acoustical Society of America, 1985. **77**(4): p. 1431-1435. http://dx.doi.org/10.1121/1.392037.
86. Gabai, R. and I. Bucher, *Excitation and sensing of multiple vibrating traveling waves in one-dimensional structures.* Journal of Sound and Vibration, 2009. **319**(1-2): p. 406-425. http://dx.doi.org/10.1016/j.jsv.2008.06.013.
87. Tanaka, N. and Y. Kikushima, *Active Wave Control of a Flexible Beam. Proposition of the Active Sink Method.* JSME international journal. Ser. 3, Vibration, control engineering, engineering for industry, 1991. **34**(2): p. 159-167. http://dx.doi.org/10.1299/jsmec1988.34.159.

88. Ghenna, S., et al., *Modelling and control of a travelling wave in a finite beam, using multi-modal approach and vector control method*, in *2015 Joint Conference of the IEEE International Frequency Control Symposium & the European Frequency and Time Forum*. 2015. p. 509-514.
89. Gabay, R. and I. Bucher, *On Vibrating Traveling Waves Actuation, Sensing, and Tuning in Finite Structures*, in *Design Engineering and Computers and Information in Engineering, Parts A and B*. 2006. p. 809-817.
90. Blanchard, A., et al., *Mode complexity in a harmonically forced string with a local spring–damper and transitions from vibrations to waves.* Journal of Sound and Vibration, 2015. **334**: p. 282-295. http://dx.doi.org/10.1016/j.jsv.2014.08.033.
91. Blanchard, A., et al., *Damping-induced interplay between vibrations and waves in a forced non-dispersive elastic continuum with asymmetrically placed local attachments.* Proceedings of the Royal Society A: Mathematical, Physical and Engineering Sciences, 2015. **471**(2176). http://dx.doi.org/10.1098/rspa.2014.0402.
92. Minikes, A., et al., *On the sensing and tuning of progressive structural vibration waves.* IEEE Transactions on Ultrasonics, Ferroelectrics, and Frequency Control, 2005. **52**(9): p. 1565-1576. http://dx.doi.org/10.1109/tuffc.2005.1516029.
93. Païdoussis, M.P., *Fluid-Structure Interactions*. 2016.
94. Nakamura, T., et al., *Flow-induced vibrations: classifications and lessons from practical experiences*. 2013: Butterworth-Heinemann.
95. Tuck, E.O., *Calculation of unsteady flows due to small motions of cylinders in a viscous fluid.* Journal of Engineering Mathematics, 1969. **3**(1): p. 29-44. http://dx.doi.org/10.1007/bf01540828.
96. Van Eysden, C.A. and J.E. Sader, *Resonant frequencies of a rectangular cantilever beam immersed in a fluid.* Journal of Applied Physics, 2006. **100**(11). http://dx.doi.org/10.1063/1.2401053.
97. Green, C.P. and J.E. Sader, *Small amplitude oscillations of a thin beam immersed in a viscous fluid near a solid surface.* Physics of Fluids, 2005. **17**(7). http://dx.doi.org/10.1063/1.1995467.
98. Ahsan, S.N., *Modulation Of Hydrodynamic Forces On Oscillating Submerged Structures In Viscous Fluids*. 2018, University of Nevada: Reno.
99. Alben, S. and M. Shelley, *Coherent locomotion as an attracting state for a free flapping body.* Proceedings of the National Academy of Sciences, 2005. **102**(32): p. 11163-11166. http://dx.doi.org/10.1073/pnas.0505064102.

100. Bidkar, R.A., et al., *Nonlinear aerodynamic damping of sharp-edged flexible beams oscillating at low Keulegan–Carpenter numbers.* Journal of Fluid Mechanics, 2009. **634**. http://dx.doi.org/10.1017/s0022112009007228.
101. Falcucci, G., et al., *Transverse harmonic oscillations of laminae in viscous fluids: a lattice Boltzmann study.* Philosophical Transactions of the Royal Society A: Mathematical, Physical and Engineering Sciences, 2011. **369**(1945): p. 2456-2466. http://dx.doi.org/10.1098/rsta.2011.0062.
102. Ahsan, S.N. and M. Aureli, *Finite amplitude oscillations of flanged laminas in viscous flows: Vortex–structure interactions for hydrodynamic damping control.* Journal of Fluids and Structures, 2015. **59**: p. 297-315. http://dx.doi.org/10.1016/j.jfluidstructs.2015.09.010.
103. Aureli, M., M.E. Basaran, and M. Porfiri, *Nonlinear finite amplitude vibrations of sharp-edged beams in viscous fluids.* Journal of Sound and Vibration, 2012. **331**(7): p. 1624-1654. http://dx.doi.org/10.1016/j.jsv.2011.12.007.
104. Phan, C.N., M. Aureli, and M. Porfiri, *Finite amplitude vibrations of cantilevers of rectangular cross sections in viscous fluids.* Journal of Fluids and Structures, 2013. **40**: p. 52-69. http://dx.doi.org/10.1016/j.jfluidstructs.2013.03.013.
105. Shahab, S. and A. Erturk, *Electrohydroelastic Euler–Bernoulli–Morison model for underwater resonant actuation of macro-fiber composite piezoelectric cantilevers.* Smart Materials and Structures, 2016. **25**(10). http://dx.doi.org/10.1088/0964-1726/25/10/105007.
106. Inman, D.J., *Engineering Vibrations*. Fourth ed. 2013: Pearson.
107. Rao, S.S., *Mechanical Vibration*. 5th ed. 2010: Pearson.
108. Hosoya, N., et al., *Dynamic characterizations of underwater structures using noncontact vibration tests based on nanosecond laser ablation in water: evaluation of passive vibration suppression with damping materials.* Journal of Vibration and Control, 2017. **24**(16): p. 3714-3725. http://dx.doi.org/10.1177/1077546317710158.
109. Kohtanen, E.A. and R.B. Davis, *Hydroelastic damping of low aspect ratio cantilevered plates.* Journal of Fluids and Structures, 2019. **90**: p. 315-333. http://dx.doi.org/10.1016/j.jfluidstructs.2019.06.015.
110. Wang, Y., M. Masoumi, and M. Gaucher-Petitdemange, *Damping analysis of a flexible cantilever beam containing an internal fluid channel: Experiment,*

modeling and analysis. Journal of Sound and Vibration, 2015. **340**: p. 331-342. http://dx.doi.org/10.1016/j.jsv.2014.12.014.

111. Xiu, H., R.B. Davis, and R.C. Romeo, *Edge clearance effects on the added mass and damping of beams submerged in viscous fluids*. Journal of Fluids and Structures, 2018. **83**: p. 194-217. http://dx.doi.org/10.1016/j.jfluidstructs.2018.08.016.
112. Hossain, A., L. Humphrey, and A. Mian, *Prediction of the dynamic response of a mini-cantilever beam partially submerged in viscous media using finite element method.* Finite Elements in Analysis and Design, 2012. **48**(1): p. 1339-1345. http://dx.doi.org/10.1016/j.finel.2011.08.004.
113. Hossain, A. and A. Mian, *Numerical Analysis to Predict Dynamic Response of Mini Cantilever Beam Submerged in Viscous Fluids*, in *Volume 11: Nano and Micro Materials, Devices and Systems; Microsystems Integration*. 2011. p. 1-6.
114. Vu, V.H., et al. *Effect of added mass on submerged vibrated plates*. in *Canadian Machinery Vibration Association (CMVA 7)*. 2007.
115. Labuschagne, A., N.F.J. van Rensburg, and A.J. van der Merwe, *Comparison of linear beam theories*. Mathematical and Computer Modelling, 2009. **49**(1-2): p. 20-30. http://dx.doi.org/10.1016/j.mcm.2008.06.006.
116. Zhang, X., D. Thompson, and X. Sheng, *Differences between Euler-Bernoulli and Timoshenko beam formulations for calculating the effects of moving loads on a periodically supported beam.* Journal of Sound and Vibration, 2020. **481**. http://dx.doi.org/10.1016/j.jsv.2020.115432.
117. Morison, J.R., J.W. Johnson, and S.A. Schaaf, *The Force Exerted by Surface Waves on Piles*. Journal of Petroleum Technology, 1950. **2**(05): p. 149-154. http://dx.doi.org/10.2118/950149-g.
118. Tari, H., *On the parametric large deflection study of Euler–Bernoulli cantilever beams subjected to combined tip point loading*. International Journal of Non-Linear Mechanics, 2013. **49**: p. 90-99. http://dx.doi.org/10.1016/j.ijnonlinmec.2012.09.004.
119. Avirovik, D., et al., *Theoretical and experimental correlation of mechanical wave formation on beams.* Journal of Intelligent Material Systems and Structures, 2016. **27**(14): p. 1939-1948. http://dx.doi.org/10.1177/1045389x15615967.
120. Ma, C., et al., *Fluid structure interaction analysis of flexible beams vibrating in a time-varying fluid domain.* Proceedings of the Institution of Mechanical Engineers,

Part C: Journal of Mechanical Engineering Science, 2020. **234**(10): p. 1913-1927. http://dx.doi.org/10.1177/0954406220902163.

121. Buchak, P., C. Eloy, and P.M. Reis, *The Clapping Book: Wind-Driven Oscillations in a Stack of Elastic Sheets.* Physical Review Letters, 2010. **105**(19). http://dx.doi.org/10.1103/PhysRevLett.105.194301.
122. Blevins, R.D. and R. Plunkett, *Formulas for natural frequency and mode shape.* Journal of Applied Mechanics, 1980. **47**(2): p. 461.
123. Sarpkaya, T., *Force on a circular cylinder in viscous oscillatory flow at low Keulegan—Carpenter numbers.* Journal of Fluid Mechanics, 2006. **165**(-1). http://dx.doi.org/10.1017/s0022112086002999.
124. Aureli, M. and M. Porfiri, *Low frequency and large amplitude oscillations of cantilevers in viscous fluids.* Applied Physics Letters, 2010. **96**(16). http://dx.doi.org/10.1063/1.3405720.
125. Syuhri, S.N.H., H. Zare-Behtash, and A. Cammarano, *Investigating the Influence of Fluid-Structure Interactions on Nonlinear System Identification.* Vibration, 2020. **3**(4): p. 521-544. http://dx.doi.org/10.3390/vibration3040032.
126. Ferrier, L., *Investigation on the Aerodynamic Performance of Cycloidal Rotors with Active Leading-Edge Morphing*, in *School of Engineering*. 2020, University of Glasgow: Glasgow, UK.
127. *Simcenter STAR-CCM+ Documentation Version 2020.2*. 2020: Siemens Digital Industries Software.
128. Zienkiewicz, O.C. and R.L. Taylor, *The Finite Element Method for Solid and Structural Mechanics*. Sixth ed. 2006, Oxford, UK: Butterworth-Heinemann.
129. Dassault_Systèmes. *Abaqus 2016 Online Documentation*. 2015 [cited 2022; Available from: http://130.149.89.49:2080/v2016/index.html.
130. Londoño, J.M., S.A. Neild, and J.E. Cooper, *Identification of backbone curves of nonlinear systems from resonance decay responses.* Journal of Sound and Vibration, 2015. **348**: p. 224-238. http://dx.doi.org/10.1016/j.jsv.2015.03.015.
131. Sumali, H. and R.A. Kellog. *Calculating Damping from Ring-Down Using Hilbert Transform and Curve Fitting*. in *4th International Operational Modal Analysis Conference (IOMAC)*. 2011. Istanbul, Turkey.
132. The MathWorks, I. *Image Processing Toolbox: User's Guide (R2019B)*. Available from: https://uk.mathworks.com/help/releases/R2019b/images/ref/edge.html.

133. Ergin, A. and B. Uğurlu, *Linear vibration analysis of cantilever plates partially submerged in fluid.* Journal of Fluids and Structures, 2003. **17**(7): p. 927-939. http://dx.doi.org/10.1016/s0889-9746(03)00050-1.
134. Kwak, M.K. and D.-H. Yang, *Free vibration analysis of cantilever plate partially submerged into a fluid.* Journal of Fluids and Structures, 2013. **40**: p. 25-41. http://dx.doi.org/10.1016/j.jfluidstructs.2013.03.005.
135. Shao, M., et al., *Effects of Time-Varying Fluid on Dynamical Characteristics of Cantilever Beams: Numerical Simulations and Experimental Measurements.* Mathematical Problems in Engineering, 2020. **2020**: p. 1-18. http://dx.doi.org/10.1155/2020/6679443.
136. Eloy, C., *Optimal Strouhal number for swimming animals*. Journal of Fluids and Structures, 2012. **30**: p. 205-218. http://dx.doi.org/10.1016/j.jfluidstructs.2012.02.008.
137. Borazjani, I., et al., *Optimal specific wavelength for maximum thrust production in undulatory propulsion.* Plos One, 2017. **12**(6). http://dx.doi.org/10.1371/journal.pone.0179727.
138. van Weerden, J.F., D.A.P. Reid, and C.K. Hemelrijk, *A meta-analysis of steady undulatory swimming*. Fish and Fisheries, 2014. **15**(3): p. 397-409. http://dx.doi.org/10.1111/faf.12022.
139. Taylor, G.K., R.L. Nudds, and A.L.R. Thomas, *Flying and swimming animals cruise at a Strouhal number tuned for high power efficiency.* Nature, 2003. **425**(6959): p. 707-711. http://dx.doi.org/10.1038/nature02000.
140. Katopodes, N.D., *Free-Surface Flow: Environmental Fluid Mechanics*. 2019, Oxford, UK: Butterworth-Heinemann.
141. Alam, M.M., Q. Zheng, and K. Hourigan, *The wake and thrust by four side-by-side cylinders at a low Re.* Journal of Fluids and Structures, 2017. **70**: p. 131-144. http://dx.doi.org/10.1016/j.jfluidstructs.2017.01.014.
142. Qiu, Q., et al., *Optimal evaluation of time step size in numerical simulation for two-dimensional flow sensing*. Cluster Computing, 2017. **22**(S3): p. 5379-5396. http://dx.doi.org/10.1007/s10586-017-1250-4.